COO-2245-11TR

VELOCITY MEASUREMENTS IN EDGE SUBCHANNELS OF WIRE WRAPPED LMFBR FUEL ASSEMBLIES

Y. B. Chen, K. Ip, N. E. Todreas

Department of Nuclear Engineering

September, 1974

Department of Nuclear Engineering
Massachusetts Institute of Technology
Cambridge, Massachusetts 02139

AEC Research and Development

Contract AT(11-1)-2245

U. S. Atomic Energy Commission

DISCLAIMER

ABSTRACT

Velocity profile in the edge subchannel of a 61 wire wrapped pin bundle with a 12-inch axial wire pitch was measured. The experiments were performed in water at both laminar and turbulent regimes. In both cases the axial velocity seem to have developed fully within the 2nd axial pitch while the transverse velocity still appears to be developing in the 2nd pitch. The axially averaged transverse gap velocity was found to be about 13% and 10% of the bundle average velocity for the turbulent and laminar flow cases respectively. The average edge subchannel axial velocity was found to be about 1.04 and 1.19 times the bundle average velocity for the turbulent and laminar case respectively.

The experiments were repeated with a 6-inch axial wire pitch. The axially averaged transverse gap velocity is 21% and 17% of the bundle average velocity for the turbulent and laminar flow cases respectively. The average edge subchannel axial velocity remains about the same as for the 12" pitch case with 1.02 and 1.24 for turbulent and laminar respectively.

ACKNOWLEDGEMENTS

The Authors wish to express their sincere gratitude to all people who assisted during the preparation of this report and the research that supported it. In particular, to the following people:

To Messrs. Jon Ferguson, Dennis Buckley and Saeed Jabbawy who labored initially to establish the velocity measuring system.

To Messrs. Thomas Eaton, Alan Hanson and Ehsan Khan, for their valuable advice on our problems.

To Mr. Pedro Carajilescov for his helpful suggestions and comment on Appendix A and during the conduct of the measurements.

To Mr. Joseph Caloggero and Mr. Fred Johnson of the Engineering Project Laboratory, who helped set up the flow loop and test bundles. Their laborious efforts made an extremeny important contribution to this work.

To Mr. Francis Woodworth and the staff of the Nuclear Reactor Machine Shop of MIT for their help with the test bundles and instrumentation.

Financial support by the U.S.A.E.C. under contract No. AT(11-1)-2245 is also sincerely acknowledged.

TABLE OF CONTENTS

LIST OF TABLES AND FIGURES

Nomenclature

A	bundle flow area
c	velocity of light
C	correction factor for voltage drop in the integrating circuit
d	fringe spacing
D	diameter of laser beam, referred to e^{-2} intensity point
D_e	hydraulic diameter
D_f	distance across the flat
D_p	pin diameter
D_w	wire diameter
D_{ph}	diameter of pinhole in front of photomultiplier
E	electric field intensity
f_D	doppler frequency
f_i	frequency of incident beam
f_r	friction factor
f_s	frequency of scattered beam
f_1	doppler frequency measured at 45° from axial axis
f_2	doppler frequency measured at -45° from the axial axis
Δf	frequency broadening
F	focal length of optical unit
g_c	conversion factor
i_D	doppler current
ID	inside diameter

n	index of refraction
$\hat{n}$	unit vector
n_{fringe}	number of fringes within the measuring volume
OD	outside diameter
P	ratio of transverse to axial velocity
P_ℓ	laser power
r	ratio of V_1 to V_2
Re	Reynolds number
S	beam separation distance
T	temperature
u	velocity in X-direction
u'	root mean square value of velocity u
V_A	axial velocity
V_A'	axial velocity averaged over one edge subchannel at one plane
$\bar{V}_A$	pitch average axial velocity
V_B	bundle average (or bulk) velocity
V_T	transverse velocity
$\bar{V}_T$	pitch average transverse velocity
V_1	velocity component measured at 45° from axial axis
V_2	velocity component measured at -45° from axial axis
λ	wavelength of light
θ	intersection angle of two incident beams
ρ	density of the fluid
μ	viscosity

2A	small diameter of measuring volume
2B	smallest diameter of measuring volume
2C	largest diameter of measuring volume

CHAPTER I

INTRODUCTION

Subchannel coolant temperature differences occur in Liquid Metal Cooled Fast Breeder Reactor (LMFBR) fuel assemblies for geometrically symmetric subchannels due to neutron flux gradients between subchannels. This temperature imbalance causes a difference in expansion in the fuel assembly duct walls. Consequently, the duct will tend to bow with the convex curvature being in the higher neutron flux direction. Additionally, the effect of irradiation - induced temperature - dependent stainless steel growth in the fast fluence greatly magnifies the bowing phenomenon. The swirl flow in the edge subchannels caused by the helical wires tends to decrease the temperature imbalance and the bowing effect.

Several investigators [1], [2], have already done some preliminary velocity flow measurements using salt injection, and dye injection method in 91 pin wire wrapped bundles. Local velocity measurements have also been made [3] in 7 pin wire wrapped bundles. The measurements made in this study are the first local velocity determinations in edge subchannels of pin bundles large enough, 61 pins, to have swirl flows

characteristic of LMFBR bundles. The measuring instrument used in this experiment was the Laser Doppler Anemometer (LDA). The greatest advantage of this method is that it introduces no probe within the flow channel to disturb the flow. For the very small geometry of the edge subchannels this is probably the only method to make direct local velocity measurement with very good accuracy. Appendix A gives brief explanation of the principles of operation of the Laser Doppler Anemometer.

This report presents the experimental measurements of the axial and transverse components of coolant velocity in the edge subchannels of 61 pin wire-wrapped assembly. In addition the detailed axial velocity distribution in the edge subchannel was also measured to evaluate the flow split prediction by hydraulic-diameter concept. The reactor designer may use these results to evaluate parameters utilized in thermal hydraulic codes used to predict the coolant temperature fields in wire wrapped fuel bundles.

CHAPTER 2

EXPERIMENTAL APPARATUS

The experiment was performed in the Engineering Project Laboratory (EPL) at MIT. The large reservoir at EPL can supply sufficient water under various operating conditions to make the experiment possible.

The following sections describe the hydraulic facilities and instruments used in this experiment.

2.1 Hydraulic Facilities

A schematic diagram of the overall arrangement of the 61 fuel pin bundle flow loop, and milk injection system is shown in Fig. 2.1. The individual components will be discussed in the following sections.

2.1.1 61 Fuel Pin Bundle

The test bundle consists of 61 wire-wrapped rods (shown in Fig. 2.2) arranged on a triangular pitch in a hexagonal housing. The hexagonal flow housing is composed of two machined aluminum (Type 2024) pieces and two 7/8 inch thick plexiglas faceplates which when bolted together defined a hexagonal internal cross section as shown in Fig. 2.3. The complete construction details of the flow housing are shown in Fig. 2.4.

The wire wrap was attached to the pins by silver brazing at each end under a tensile force in excess of 10 pounds. The wire was tacked to the pin surface at intermediate points along the pin length by a solder substitute (Formula 32 by DAP Inc.). This method can closely control the location of wire wrap. The pins are 0.25 in. OD and 50 in. long stainless steel solid rods and are wrapped with 0.0625 inch diameter stainless steel spacer wire yielding a nominal pitch to diameter ratio of 1.25. Two sets of pins were used in the experiment, one with a 12-inch axial wire pitch, one with a 6-inch axial wire pitch.

Eighteen rods were painted a flat black to eliminate the problem of laser light reflection from the shiny steel surface. These eighteen rods make up the two rows of rods adjacent to the two plexiglas faces of the hexagonal housing. Each rod was fixed at the bottom of the bundle by support pins passing through two 0.125 inch drilled holes as shown in Fig. 2.4. The assembled bundle was within the dimensional tolerances of Figure 2.4 and no compression of the pins by the hexagonal housing was observed. The test section was bolted between upper and lower plenums as shown in Fig. 2.5.

Vibration of the bundle is relatively minor. It consists of a small steady state component due to the vibration of the building floor by the pumps and another component due to the flow oscillation in the exit line from the upper plenum. Both components depend largely on the flow rate delivered by the pump. Since in this experiment the operating flow rate is quite low (< 25 GPM) the vibration was judged small and negligible.

During the initial three months of operation, a white crud was gradually built up between wire and rods and at the corners of the flow housing. At first it was thought that this was due to the white milk powder injected into the fluid stream to provide the scattering particles for the Laser Doppler Anemometer. But when the bundle was disassembled for cleaning, it was discovered that the problem was extensive corrosion of the aluminum portions of the hexagonal flow housing. This had occurred despite anodization of the aluminum surfaces. Examination of the corroded faces showed severe pitting below apparent surface scratches in the axial direction. These surfaces were remachined to a depth of about 1/16 inch to assure that all corrosion and pitting was removed. This remachining required the construction of two new plexiglas faceplates

to maintain the proper geometry. The remachined aluminum surfaces were then treated by hard anodization with a dichromate seal. In spite of the better surface protection the corrosion still reoccurred very quickly. The problem was determined to be galvanic corrosion due to contact between the aluminum flow housing and the stainless steel rods, wires, and support pins. To stop the galvanic corrosion, contact between the two dissimilar metals was broken by coating the aluminum flow housing with a smooth epoxy film. This epoxy film was sprayed on the metal surface and then baked hard. Several coats were applied to obtain a thicknes of 6 mils. The bundle was reassembled and has since operated quite successfully. Only a small amount of corrosion was experienced at the corners of flow housing due to the difficulty in coating the sharp edges.

2.1.2 Loop and Milk Injection System

Figure 2.1 shows the schematic diagram of the test loop. Two pumps are connected so that each pump can be operated individually or both pumps operated simultaneously either in series or in parallel. It was decided to connect these two 20 hp pumps this way in order to provide a wide range of flow conditions.

City water is sucked from the large underground reservoir by the pump(s). This large reservoir of about 55,000 gallons can supply water without any temperature change. The water was chemically tested and the composition of impurities is presented in Table 2.1. A bypass valve is used to control the flow rate in the bundle. During the test period, a large quantity of air bubbles were observed in the bundle. These bubbles made velocity measurement by the laser doppler method impossible. The loop was carefully checked for air leaks but none were found. The source of the bubbles was finally found to be cavitation at the globe valve in the bypass line. The problem was solved by dumping the bypass line to the canal directly instead of returning it to the intake line.

For different operating flow rates, three different flowmeters are used to assure the accuracy of flowmeter readings. Flow rates ranging from 2 GPM to 200 GPM can be obtained. In this experiment two rotameters were used. Calibration was done by the stop watch and weigh tank technique. The curves are shown in Fig. 2.6. The difference between the calibration curve and manufacturer specification is within 2%.

During the first author's work,a milk injection system was used to increase the concentration of scattering particles in the water for the laser

doppler measurement. Powdered milk was first mixed with hot water in the mixer and then pumped into the large tank. High pressure was applied to inject the mixture into the main loop. The detail arrangement is also shown in Fig. 2.1. Since the water loop in this experiment was a once-through system, continuous milk injection was required. Just before the start of the second author's experiment, the loop was modified from an open loop to a partially closed loop. Both the inlet and outlet of the loop were directed into a large tank that communicated with the canal which supplied fill and makeup water. Powdered milk used as the seeding material was mixed in the tank before the start of each run.

2.1.3 Rectangular Test Section

A simple rectangular test section was built to check the operation of measurement system. The test section consisted of one 28 inch long, half inch wide square brass tube and two plexiglas faceplates. Eighteen inches from the entrance two plexiglas faceplates were bolted together with brass tube to form a 1-1/4" high by 1/2" wide window for entrance and exit of the laser beams. Figure 2.7 shows a detailed view of the rectangular test section.

2.2 Instrumentation

A complete list of instruments used in this experiment is shown in Table 2.2. Functions of individual instruments are described in the following sections.

2.2.1 Optic System[4]

The optical arrangement for this experiment, the differential mode with backscattering, is shown in Fig. 2.8. The laser beam from a Spectra Physics Model 125A He-Ne laser, without etalon, is first split into two beams by DISA 55L01 optical unit. The two beams are then focused to a point within the flow channel by using a 13 cm focal length lens. Scattered light from the measuring point is picked up by an RCA-7265 photomultiplier. A high voltage supply provides power for the photomultiplier. The anode current of photomultiplier is monitored by an anode current meter.

The laser,optical unit, and photomultiplier are mounted on an aluminum plate as shown in Fig. 2.9. This plate is supported above a column knee and table assembly whose carriage will provide three dimensional travel of the entire system. The measuring point is positioned within the flow channel by moving the

carriage containing the laser, optical unit, and photomultiplier as an integral unit. The axial travel of the carriage is not sufficient for travel along the whole length of the bundle. Thus two sets of pillars were designed to put between the carriage and the aluminum plate. This arrangement makes the velocity measurement in the whole bundle possible.

2.2.2 Signal Processing System [5]

A DISA 55L35 frequency tracker was used to measure the local instantaneous velocity in the bundle. Fig. 2.10 is a block diagram of the tracker. The incoming signal from the photomultiplier, at a frequency which varies with time, first passes through the preamplifier to increase the signal level and filter out noise outside the selected frequency range. Then the signal is combined with the output of a voltage-controlled local oscillator (V.C.O.) in the mixer. The output signal at the difference frequency is narrow-band filtered by intermediate frequency stage A, i.e., I.F./A to remove as much noise as possible, passed through limiter I to remove amplitude fluctuations inherent in the doppler signal, and then passed to a sensitive frequency discriminator. This provides a d.c. output u proportional to the I.F. frequency deviation from

a fixed center value f_o. After suitable smoothing with a long time constant T_o, and d.c.amplification, the resulting error voltage v is fed back to the control input of the V.C.O. The result of the feedback is that, provided a suitable value of loop gain is chosen, the oscillator frequency tracks the doppler signal maintaining a nearly constant difference equal to f_o. The resultant voltage v provides an electrical analogue of the instantaneous doppler frequency of flow velocity.

An oscilloscope and spectrum analyzer were used to monitor the output of the preamplifier. This was very helpful in optical alignment to optimize the signal and to provide a check on the magnitude and quality of the doppler signal.

2.2.3 Signal Recording System

The two output sockets of the tracker are in parallel and carry the instantaneous analog output voltage which was registered on both a digital voltmeter (after passing an integrating circuit) and true RMS voltmeter.

The integrating circuit has six different time constants ranging from 1 sec. to 90 sec. and is shown in Fig. 2.11. The digital voltmeter reading corresponds to the mean velocity of the flow. Turbulent intensity

information is contained in the reading of RMS voltmeter. An X-Y plotter was also used occasionally to record the velocity fluctuation with time. This record was very useful in studies conducted to determine when the flow in specific subchannel locations passed from laminar to turbulent as the Reynolds Number was increased.

The complete layout of the instrumentation is shown in Fig. 2.12.

TABLE 2.1 COMPOSITION OF IMPURITIES IN CITY WATER*

Impurities	Composition (mg/liter)
Chloride	40
Ammonia	few
Nitrate	few
Sulphate	small

* Tested in February 1974 by KENT LABORATORIES , Waltham, Massachusetts.

TABLE 2.2 DESCRIPTION OF EQUIPMENT

UNIT	MANUFATURER	MODEL NO.	SERIAL NO.
He-Ne LASER	SPECTRA PHYSICS	125A	N/A
EXCITER	SPECTRA PHYSICS	261	3147308
CAVITY EXTENSION	SPECTRA PHYSICS	325	N/A
OPTICAL UNIT	DISA	55L01	N/A
PHOTOMULTIPLIER	RCA	7265	N/A
HIGH VOLTAGE SUPPLY	NORTHEAST SCIENTIFIC	RE-3002	345
ANODE CURRENT METER	E-H RESEARCH LAB	240	A-0126
DOPPLER SIGNAL PROCESSOR	DISA	55L02	170
OSCILLOSCOPE	TEKTRONIX	541	5560
DIGITAL VOLTMETER	HEWLETT-PACKARD	405AR	006-00979
RMS VOLTMETER	DISA	55D35	456
OSCILLOSCOPE	HEWLETT-PACKARD	141B	1225A01016
PLUG IN SPECTRUM ANALYZER	NELSON-ROSS	235	N/A
X-Y RECORDER	MOSELEY	2D	N/A

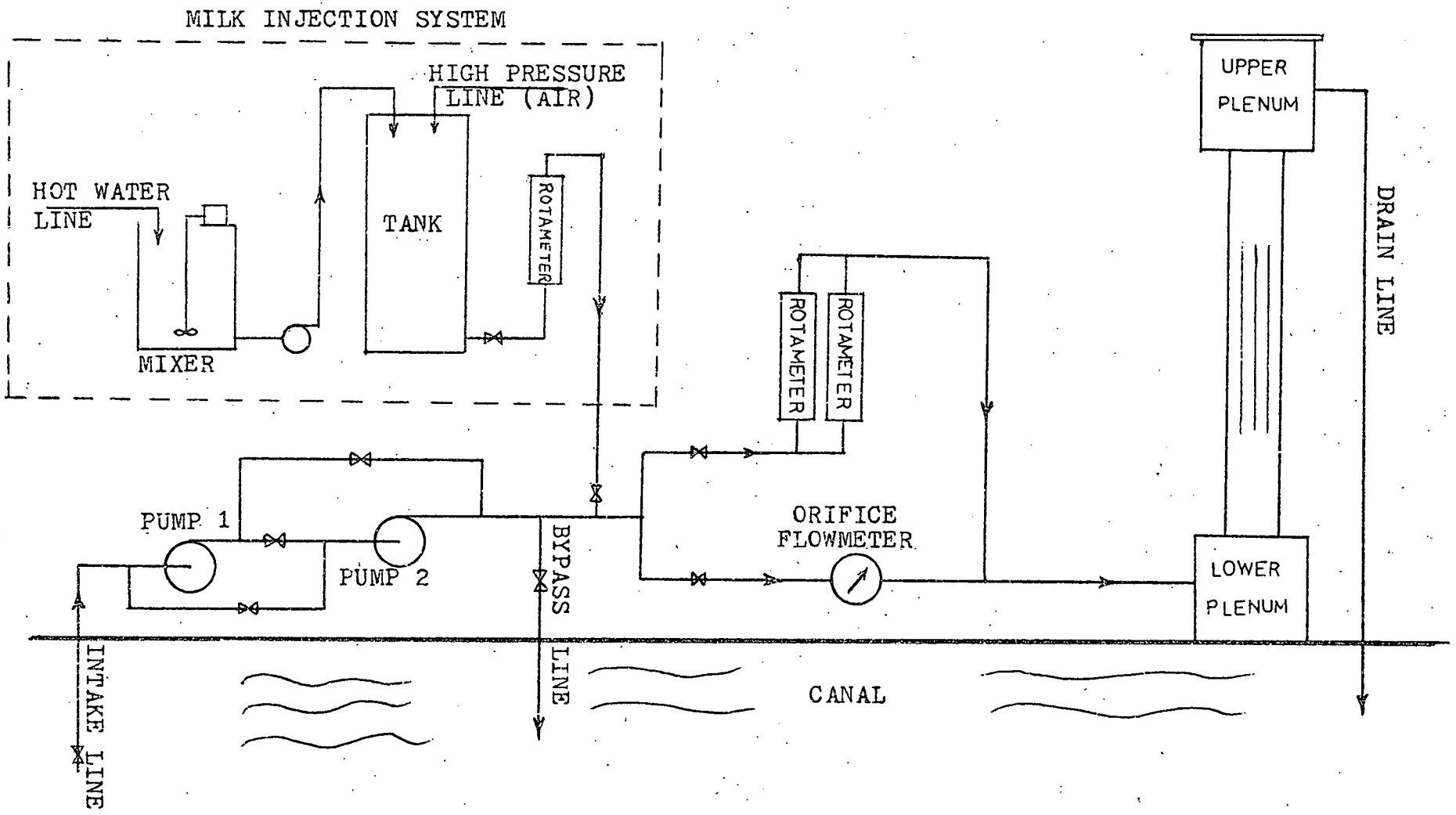

FIGURE 2.1 FLOW SCHEME FOR 61 FUEL PIN BUNDLE

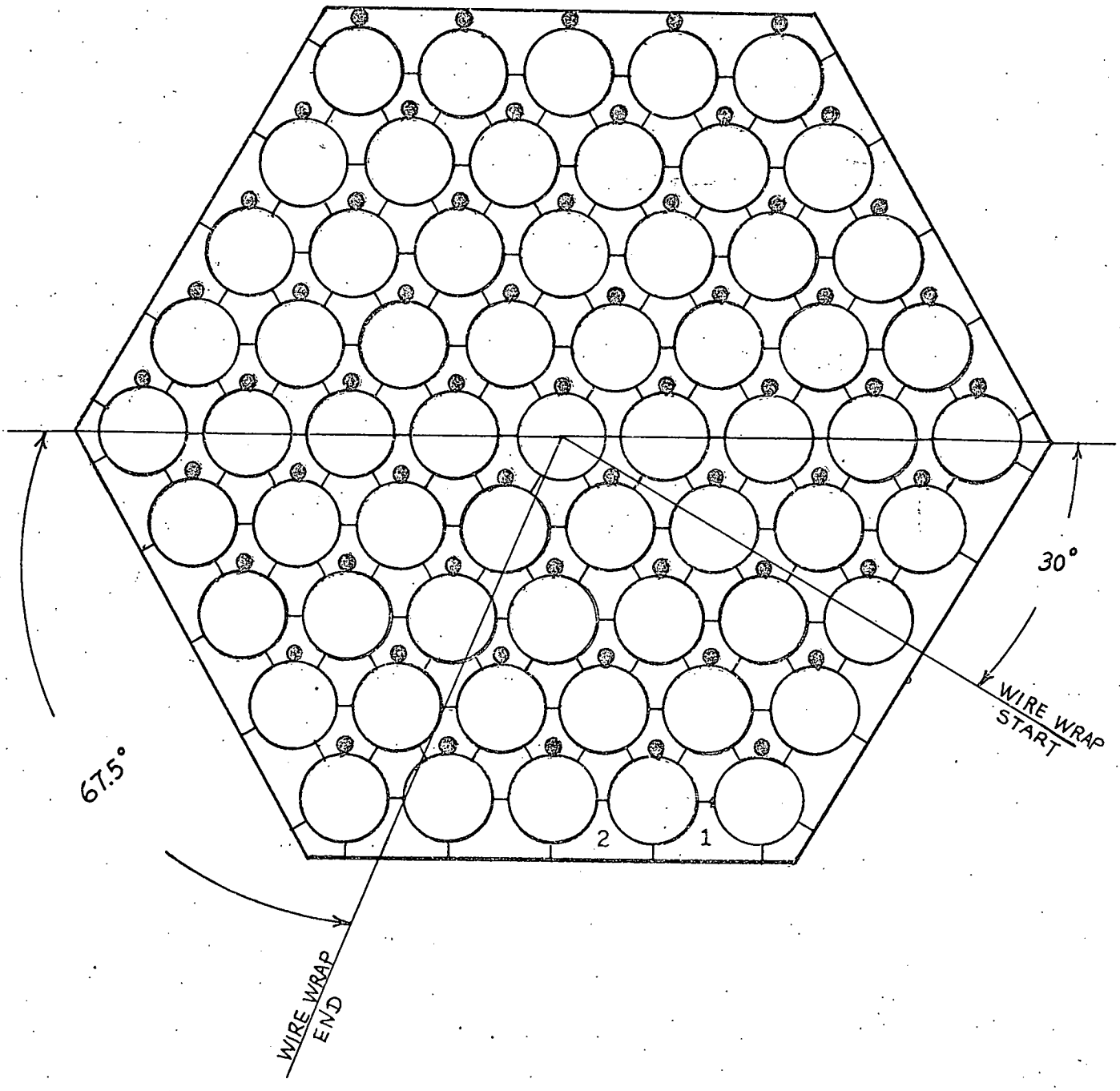

FIGURE 2.2 CROSS SECTIONAL SKETCH OF TEST SECTION

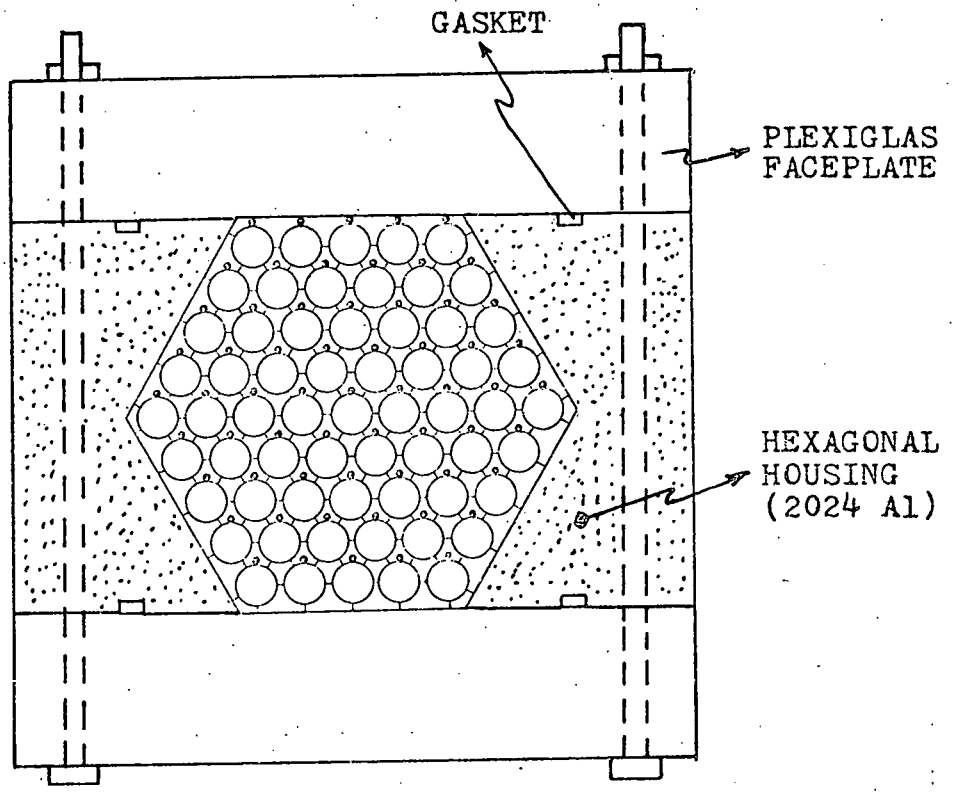

FIGURE 2.3 TEST SECTION CONSTRUCTION DETAILS

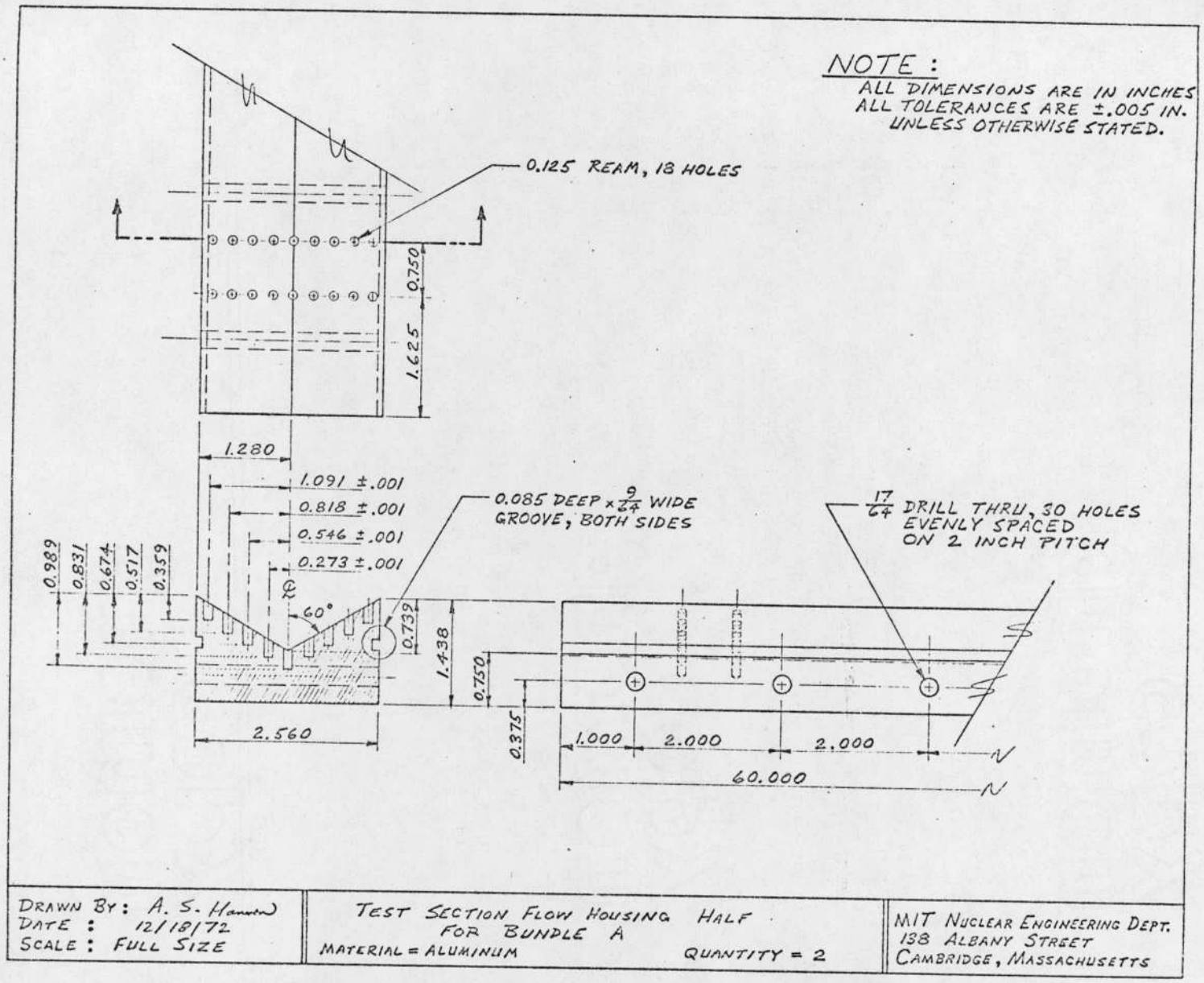

FIGURE 2.4 CONSTRUCTION DETAILS OF THE HEXAGONAL FLOW HOUSING

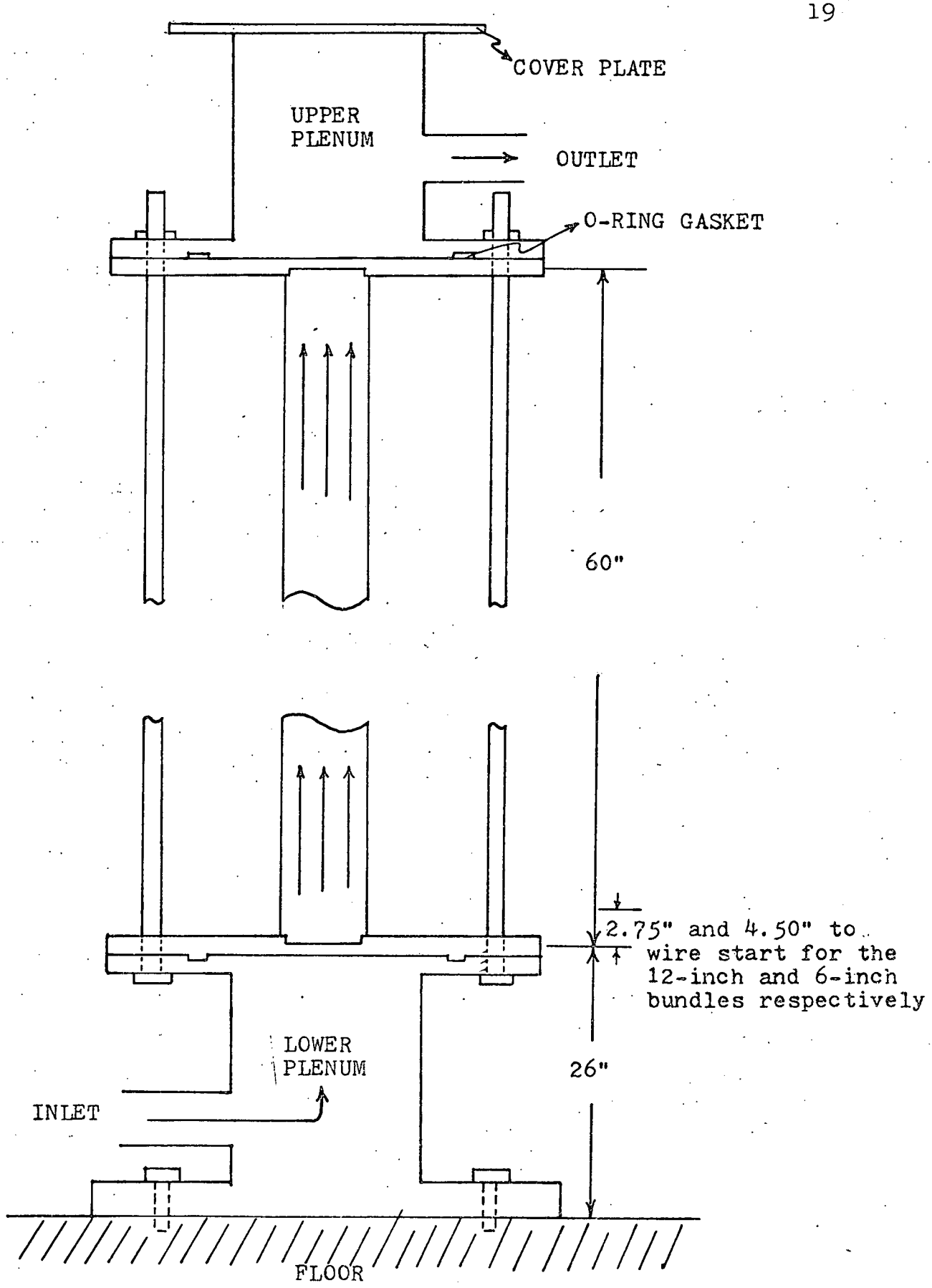

FIGURE 2.5 SCHEMATIC DIAGRAM OF 61 FUEL PIN BUNDLE

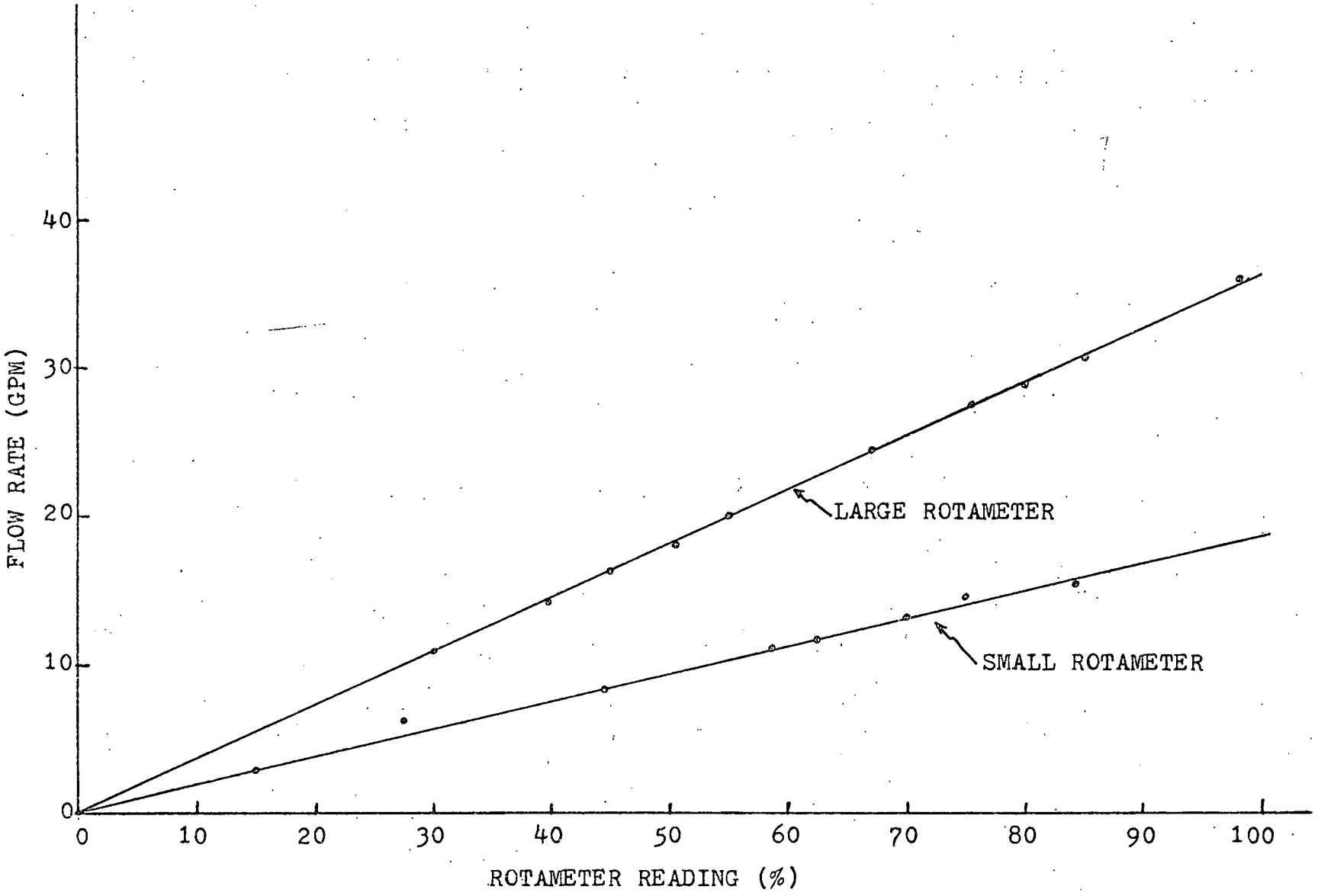

FIGURE 2.6 SMALL AND LARGE ROTAMETER CALIBRATION CURVES

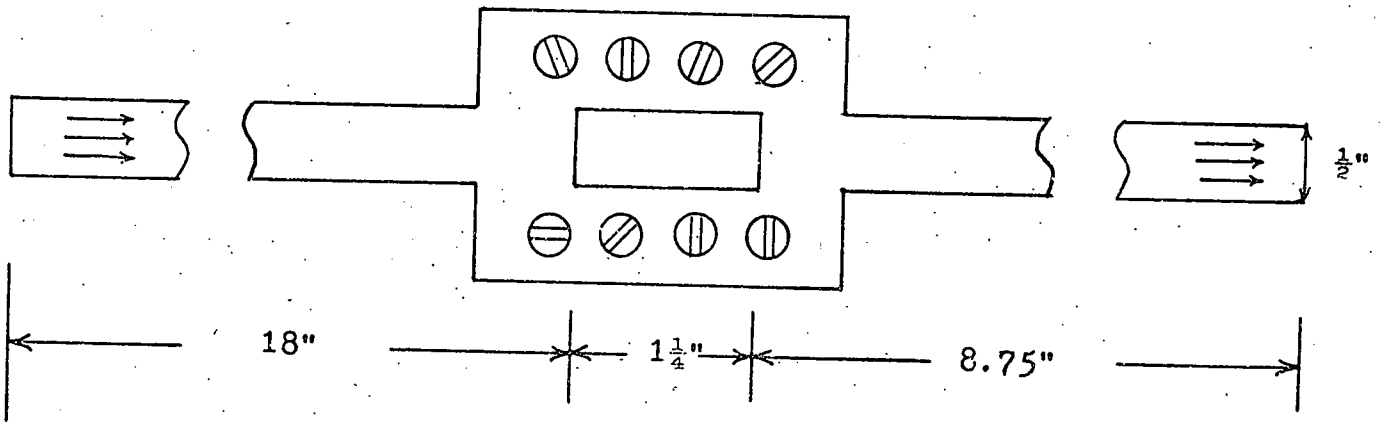

FIGURE 2.7 SCHEMATIC DIAGRAM OF RECTANGULAR TEST SECTION

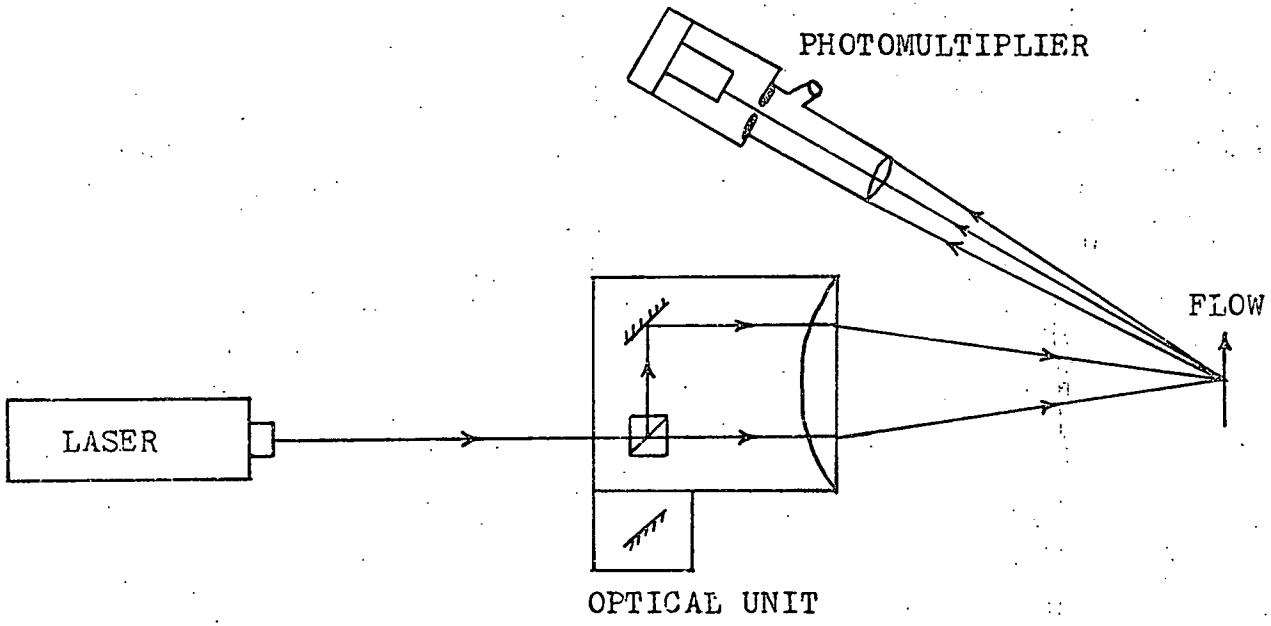

FIGURE 2.8 LDA OPTIC SYSTEM LAYOUT

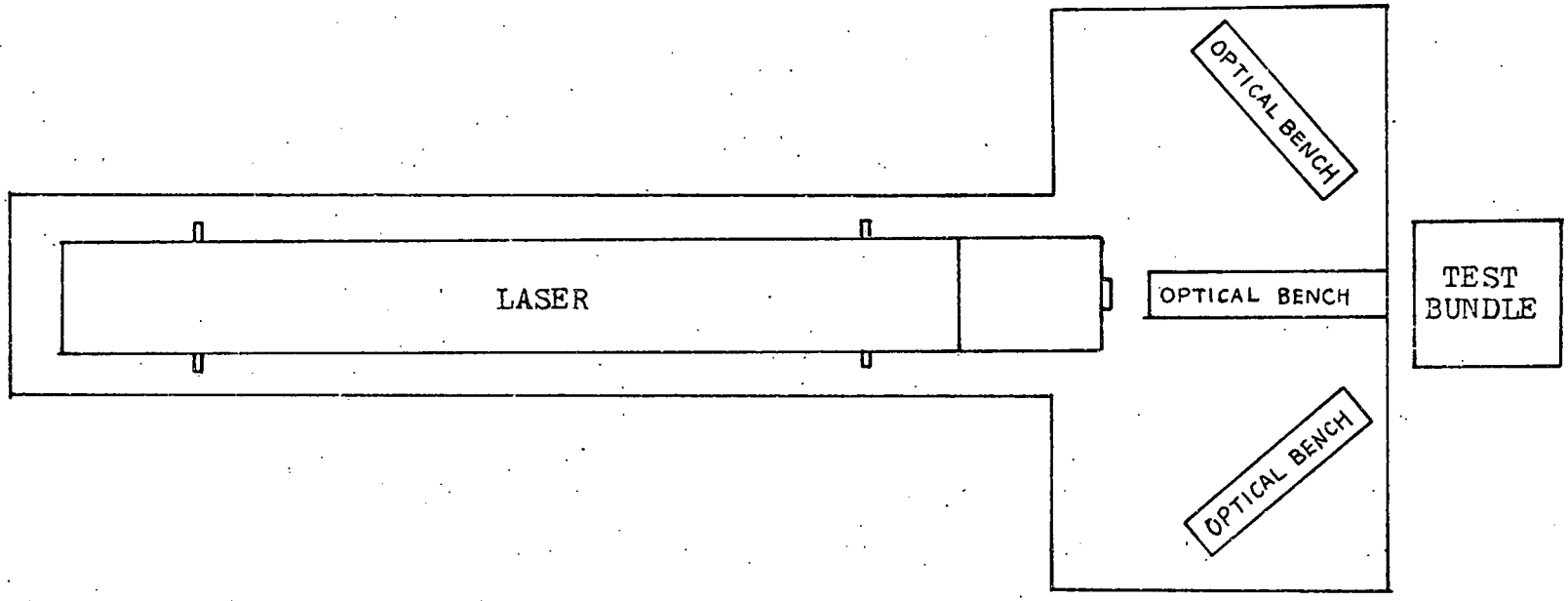

FIGURE 2.9 TOP VIEW OF TEST EQUIPMENT PLATFORM

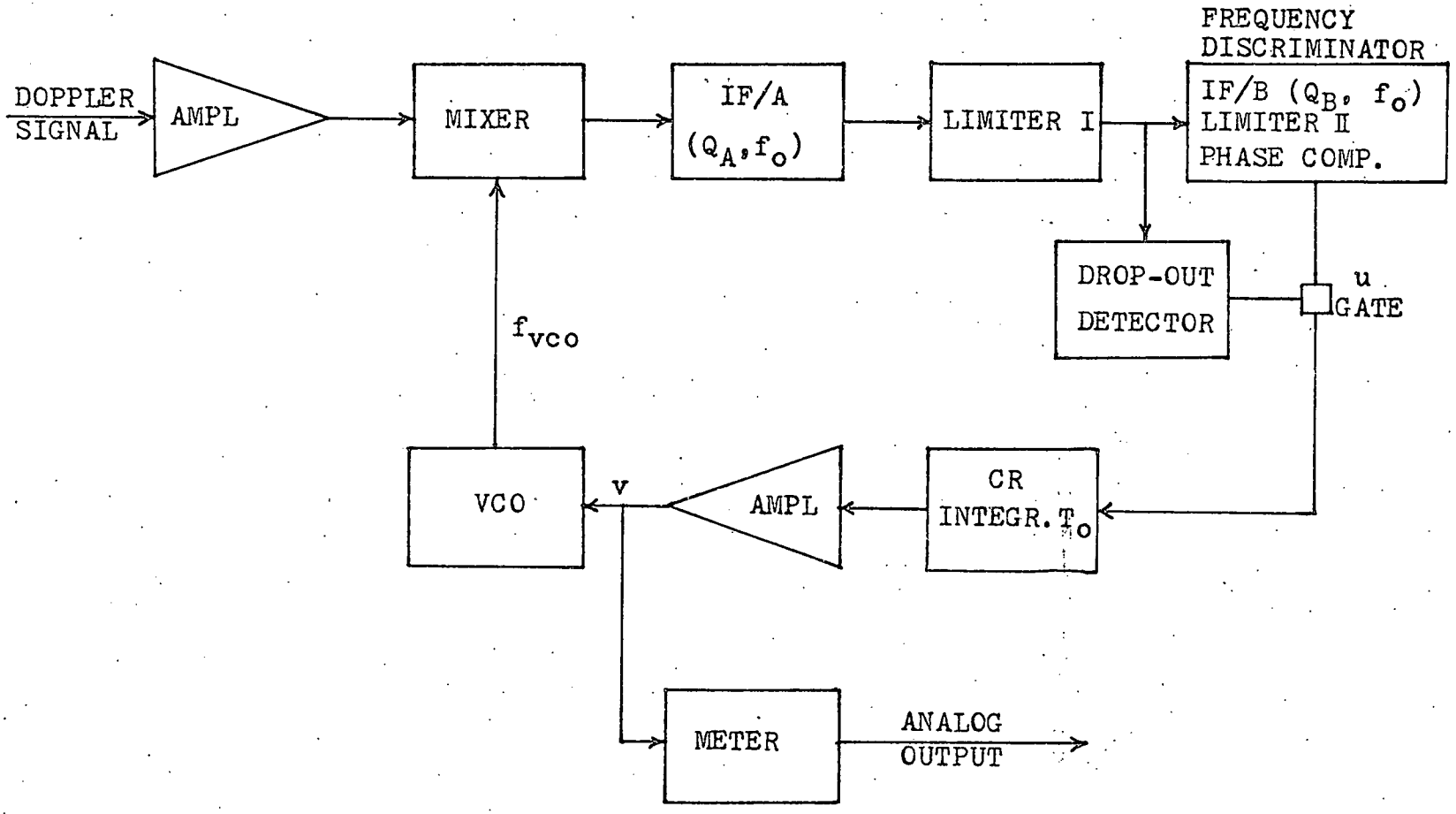

FIGURE 2.10 BLOCK DIAGRAM OF THE TRACKER

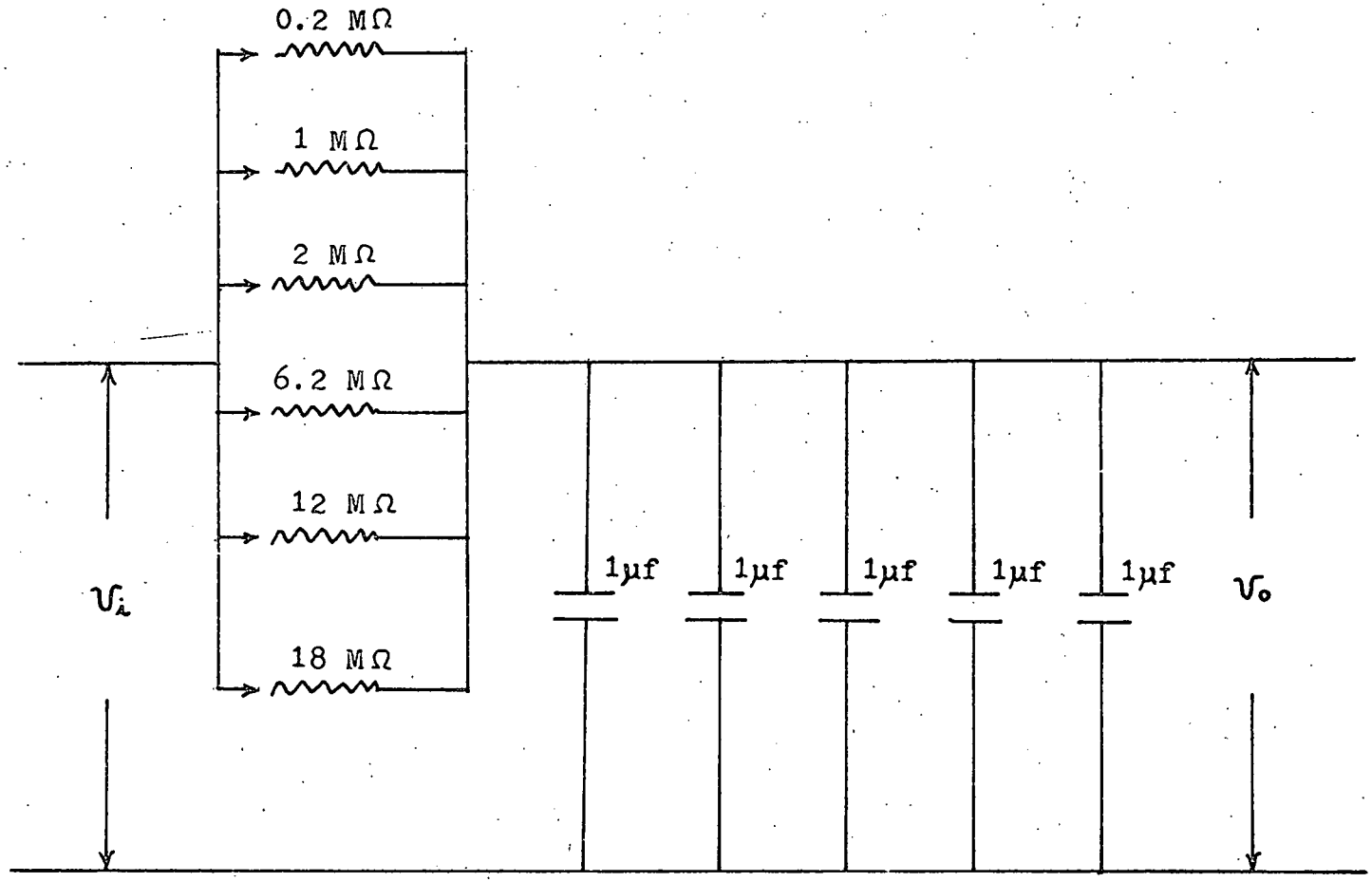

FIGURE 2.11 INTEGRATING CIRCUIT

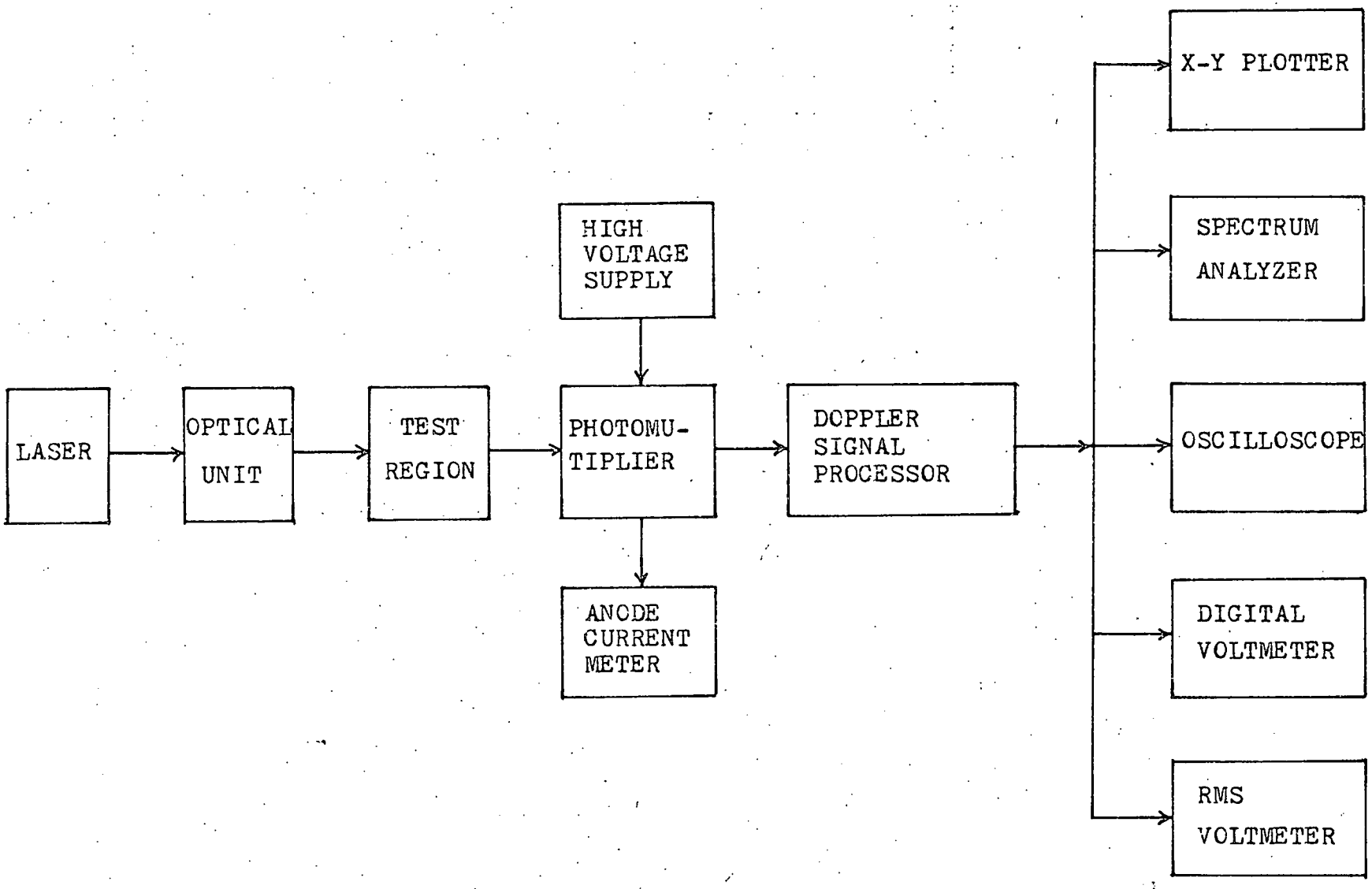

FIGURE 2.12 LAYOUT OF EQUIPMENT

CHAPTER 3

EXPERIMENTAL PROCEDURES

The detailed procedures used by the first author are presented in Appendix H. During the second author's experiment, the loop was modified to a partially closed loop. Thus no milk injection was needed. Rather, powdered milk used as the seeding material was mixed in the tank before the start of each run. In addition, the milk concentration was monitored by directing a laser beam through a sample of the milk solution within a 1-1/2 inch wide plexiglas container. The milk concentration was defined as the percent of laser beam power reduction achieved when directed through the sample. It was found that data acquisition was reasonably easy when the milk concentration was above 40%. Usually during the run, the milk concentration was kept between 50 to 60% which gave good signal to noise ratio. The quality of the signal also depended on the Reynolds number and laser power. Figure 3.1 shows the minimum laser power required as a function of Reynolds number.

In the velocity measurements conducted to determine the flow split, only the axial component of the flow was measured. This was achieved by rotating the optical unit such that the plane in which the two emerging parallel beams from the optical unit was in the axial direction.

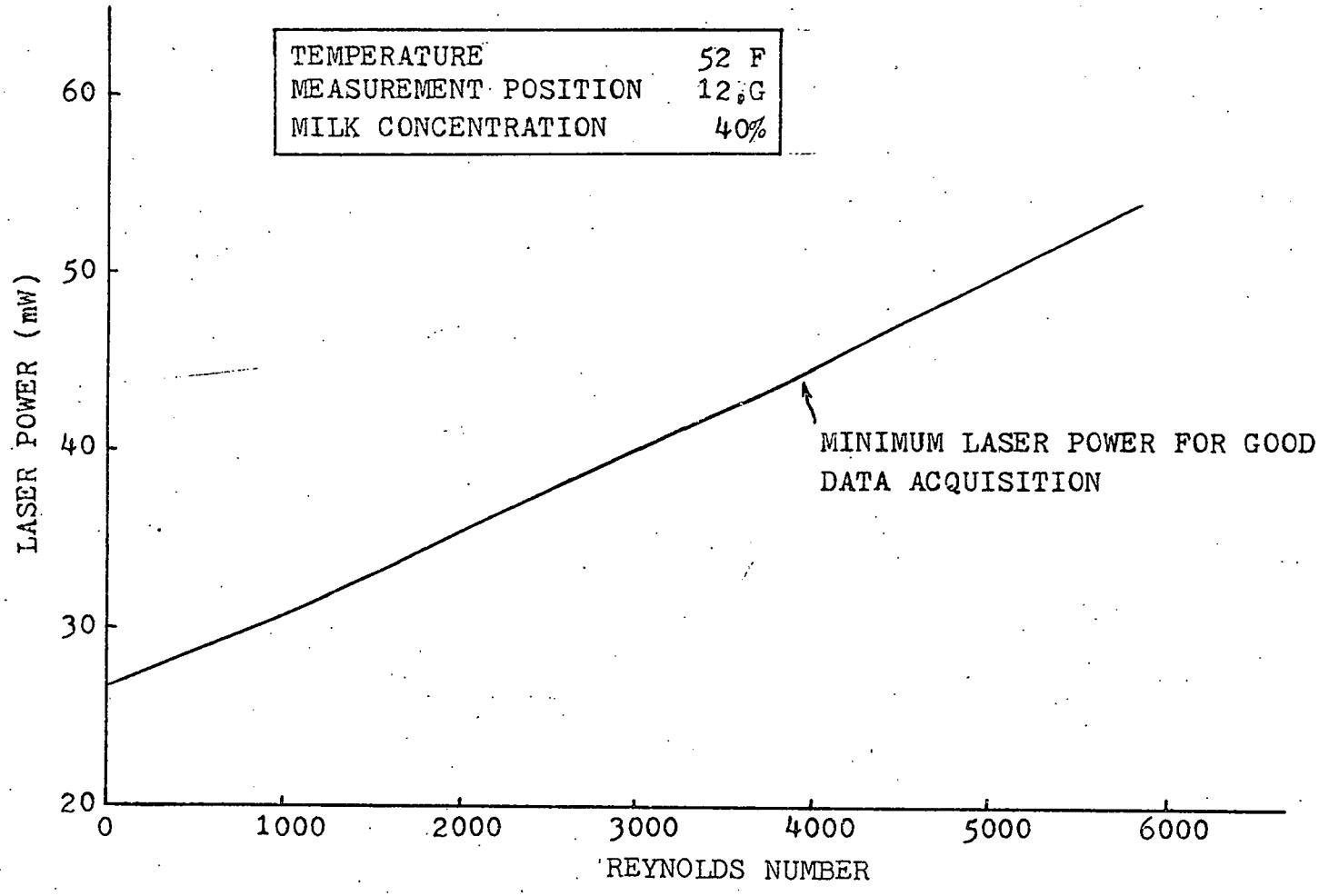

FIGURE 3.1 LASER POWER VERSUS REYNOLDS NUMBER FOR BACKSCATTERING MEASUREMENT OF EDGE SUBCHANNEL VELOCITY

CHAPTER 4

EXPERIMENTAL RESULTS

Several preliminary experiments were conducted before making the measurements in the bundle. The results of these exploratory experiments are included in Appendix I.

4.1 Turbulent Intensity Measurements

The turbulent intensity versus Reynolds number in the edge subchannel was first measured in order to determine the transition Reynolds number in the wire wrapped bundle. The result is shown in Figure 4.1. The subchannel Reynolds number is calculated from the hydraulic diameter concept in which the presence of the wire is considered by including half of a wire over one axial pitch distance. (See Appendix J for details.) The decrease in turbulent intensity at higher Reynolds number is primarily due to the different sensitivity of the tracker reading within the same frequency range. In reality, we should get a smooth horizontal line in turbulent regime.

4.2 Axial and Transverse Velocity versus Axial Position

The experiments were run between temperatures of 50° to 70°F principally due to seasonal change of the canal temperature. Since the flow rate of the loop was fixed, the Reynolds number increased with increasing temperature. The Reynolds numbers for laminar and turbulent flow ranged from 460 to 640 and 3270 to 4500 respectively.

Due to the small nominal but large variation of transverse velocity, the optical unit is oriented to +45° and -45° from axial as shown in Fig. D.1. The transverse and axial velocities were obtained by vector addition. The possible error in the transverse velocity determined by this indirect method is high as explained in Chapter 6 but this is the only possible way to measure the transverse velocity because of the limitation of the tracker when operated without a frequency shifter.

The results are presented in the following two sections. Both the axial and transverse velocities are normalized to the bulk bundle velocity. Fig. 4.2 shows the measuring locations of the data presented in this chapter. In both the 6-inch and 12-inch axial pitch bundles, the wire wrap starts at 30° below plane 2. An axial sketch of the test section geometry is shown in Fig. 2.5.

4.2.1 12-inch Wire Axial Pitch Bundle

4.2.1.1 Laminar, Figures 4.3 to 4.12

4.2.1.2 Turbulent, Figures 4.13 to 4.22

4.2.2 6-inch Wire Axial Pitch Bundle

4.2.2.1 Laminar, Figures 4.23 to 4.30

4.2.2.2 Turbulent, Figures 4.31 to 4.38

4.3 Flow Split

These measurements were made in subchannel 2, see Fig. 2.2. During these measurements the temperature was kept at about 70°F and hence the laminar and turbulent Reynolds number are 640 and 4500 respectively.

4.3.1 12-inch Wire Axial Pitch Bundle

4.3.1.1 Laminar, Figures 4.39 to 4.46

4.3.1.2 Turbulent, Figures 4.47 to 4.54

4.3.2 6-inch Wire Axial Pitch Bundle

4.3.2.1 Laminar, Figures 4.55 to 4.62

4.3.2.2 Turbulent, Figures 4.63 to 4.70

Note the values in the squares on the flow split data diagrams are the measured values at the center of each square. This value is reported in voltage which is proportional to the doppler shift frequency which is in turn proportional to the axial velocity at the measuring point. The bundle average velocity has an equivalent of 3.68 and 4.36 volts in turbulent and laminar regimes respectively.

4.4 Detailed Axial and Transverse Velocity Distribution in Edge Subchannels - LAMINAR FLOW

Axial and transverse velocity profiles in two edge subchannels at eight different wire locations have been obtained. Both the axial and transverse velocity are normalized to the bulk bundle velocity and are shown in Figures 4.71 to 4.86. The plane number is assigned according to Figure 4.2.

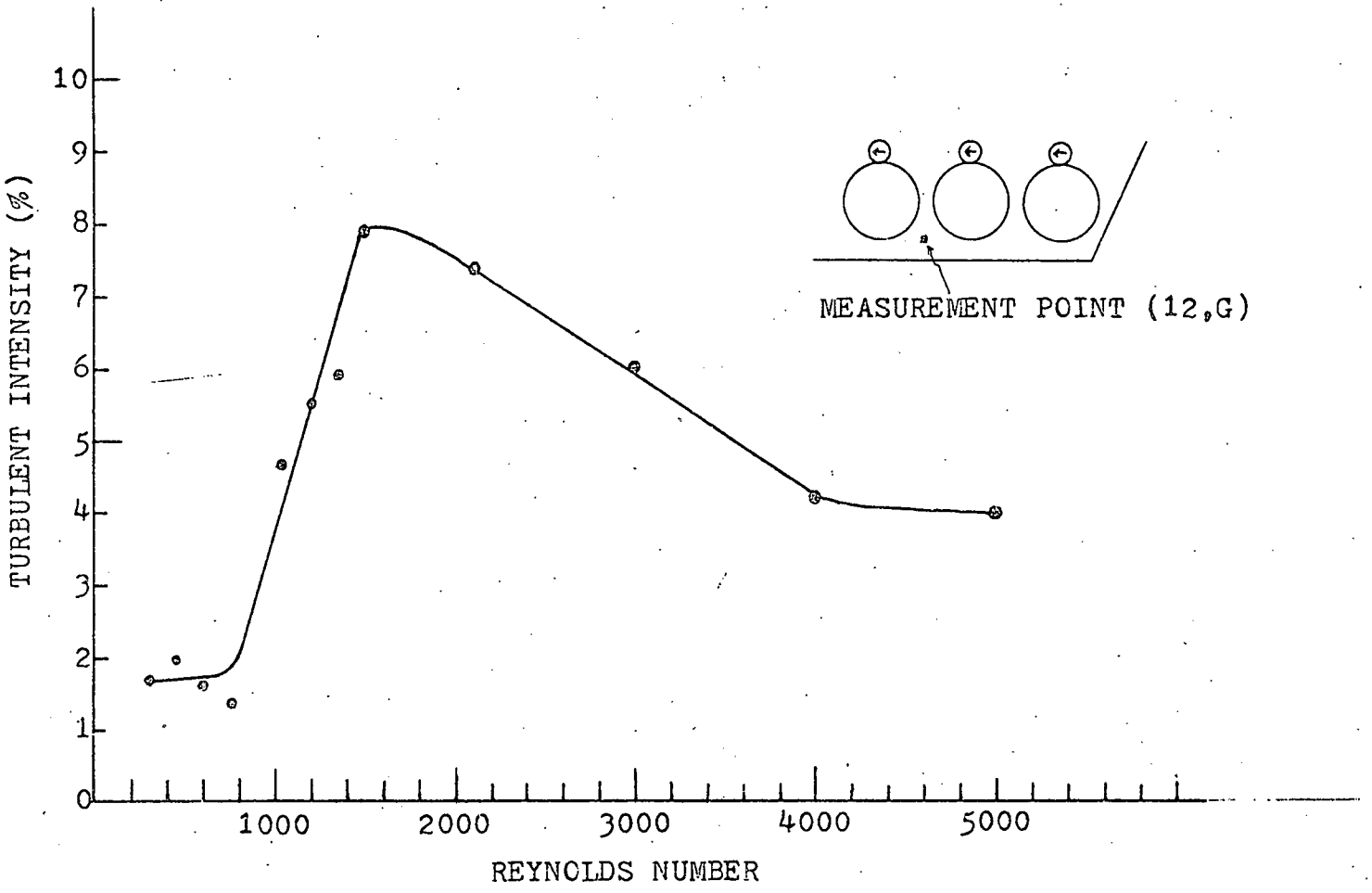

FIGURE 4.1 TURBULENT INTENSITY MEASUREMENT IN THE BUNDLE

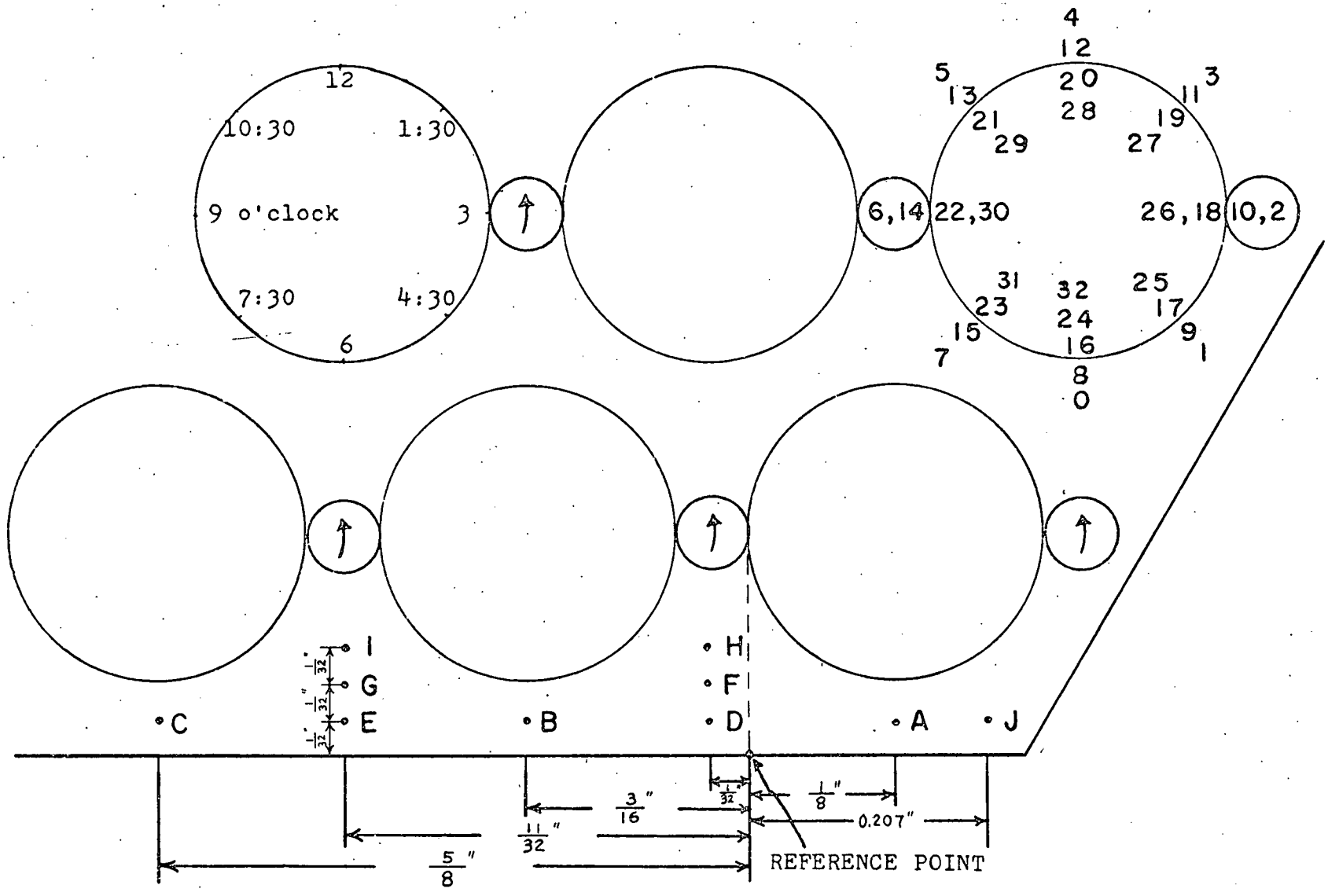

FIGURE 4.2 LOCATIONS OF MEASURING POINTS

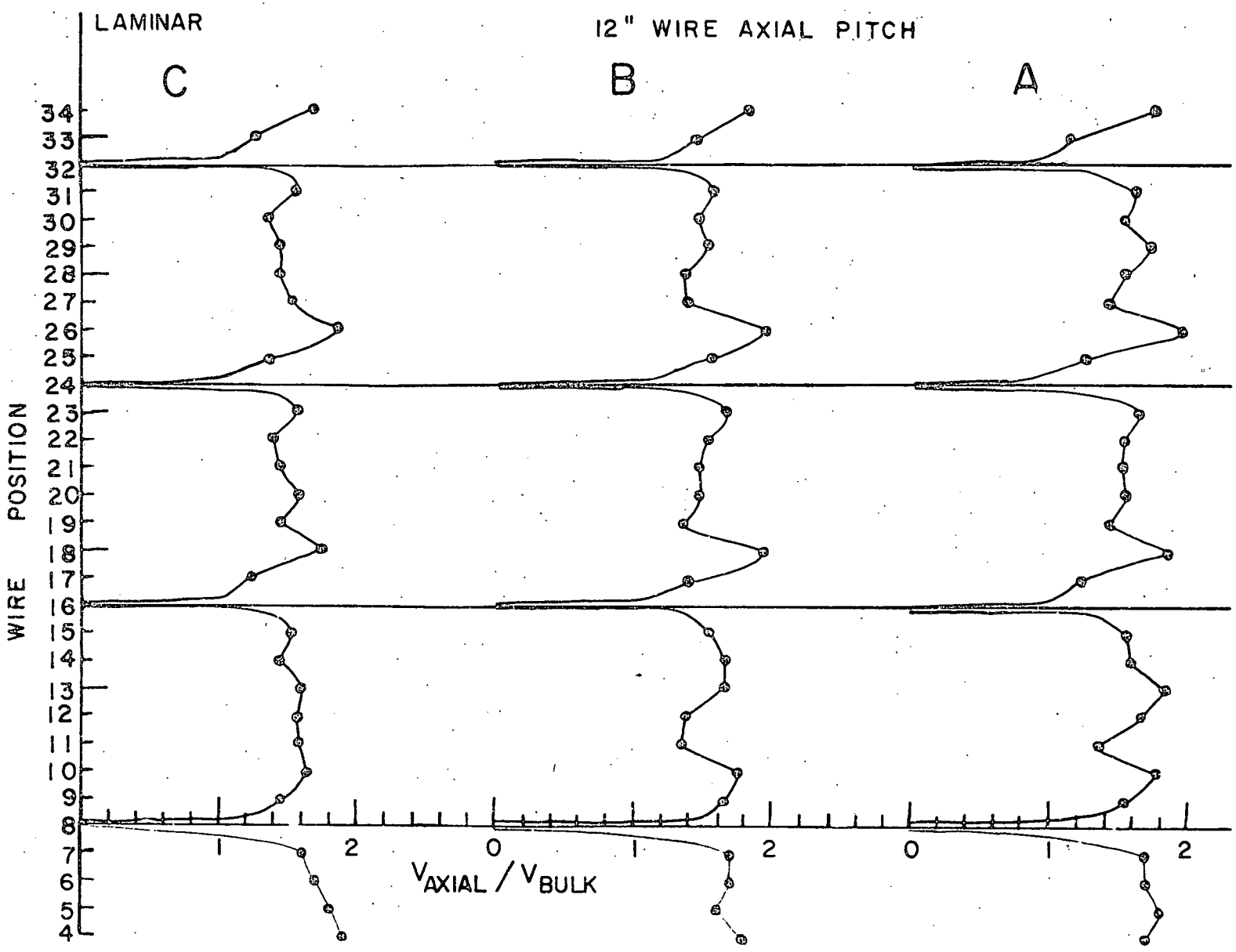
LAMINAR
12" WIRE AXIAL PITCH
C
B
A
WIRE POSITION
34
33
32
31
30
29
28
27
26
25
24
23
22
21
20
19
18
17
16
15
14
13
12
11
10
9
8
7
6
5
4
1
2
0
1
2
0
1
2
V_{AXIAL} / V_{BULK}

FIGURE 4.3

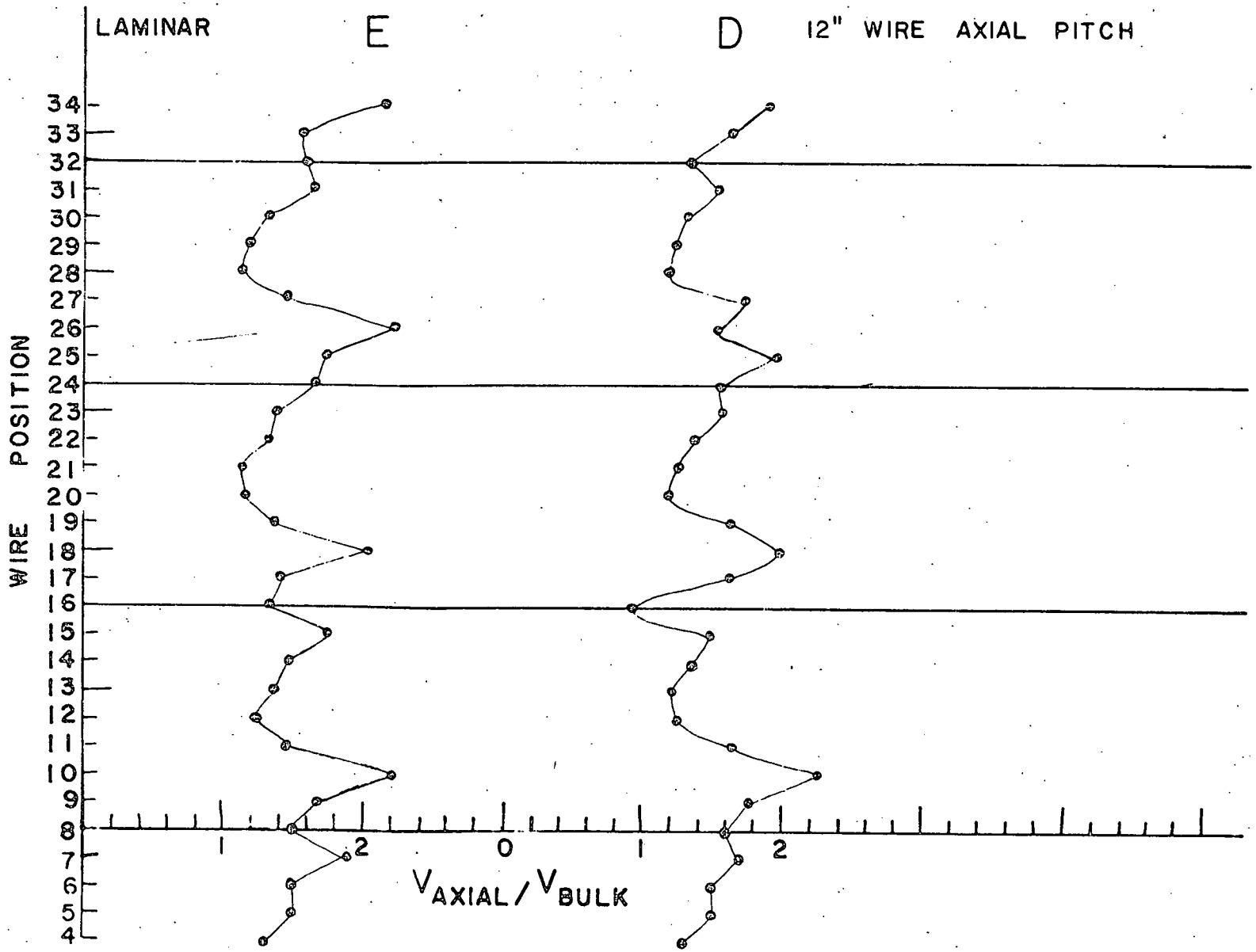
LAMINAR
E
D
12" WIRE AXIAL PITCH
WIRE POSITION
34
33
32
31
30
29
28
27
26
25
24
23
22
21
20
19
18
17
16
15
14
13
12
11
10
9
8
7
6
5
4
2
1
0
1
2
VAXIAL / VBULK

FIGURE 4.4

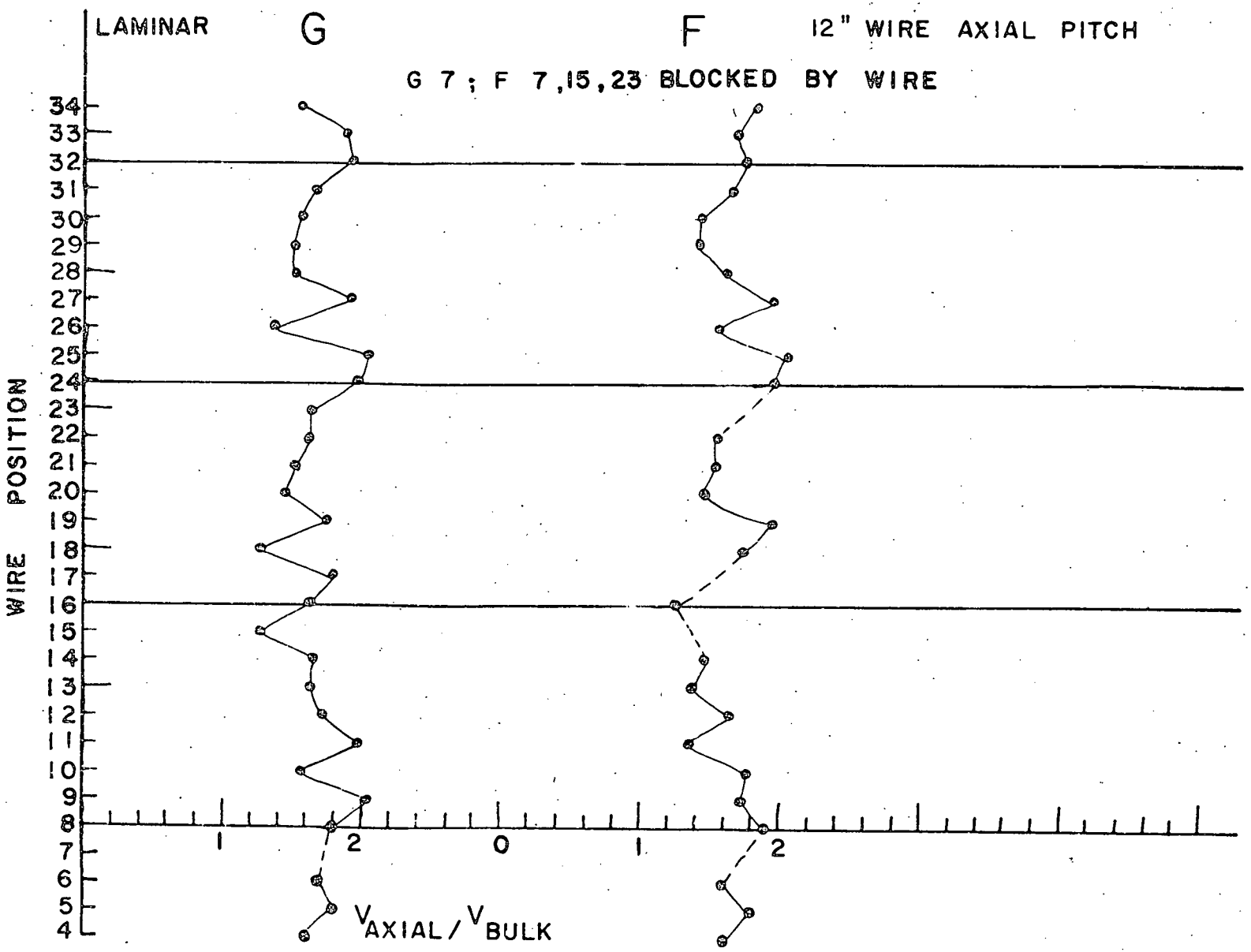
LAMINAR
G
F
12" WIRE AXIAL PITCH
G 7 ; F 7,15,23 BLOCKED BY WIRE
WIRE POSITION
34
33
32
31
30
29
28
27
26
25
24
23
22
21
20
19
18
17
16
15
14
13
12
11
10
9
8
7
6
5
4
1
2
0
1
2
V_{AXIAL}/V_{BULK}

FIGURE 4.5

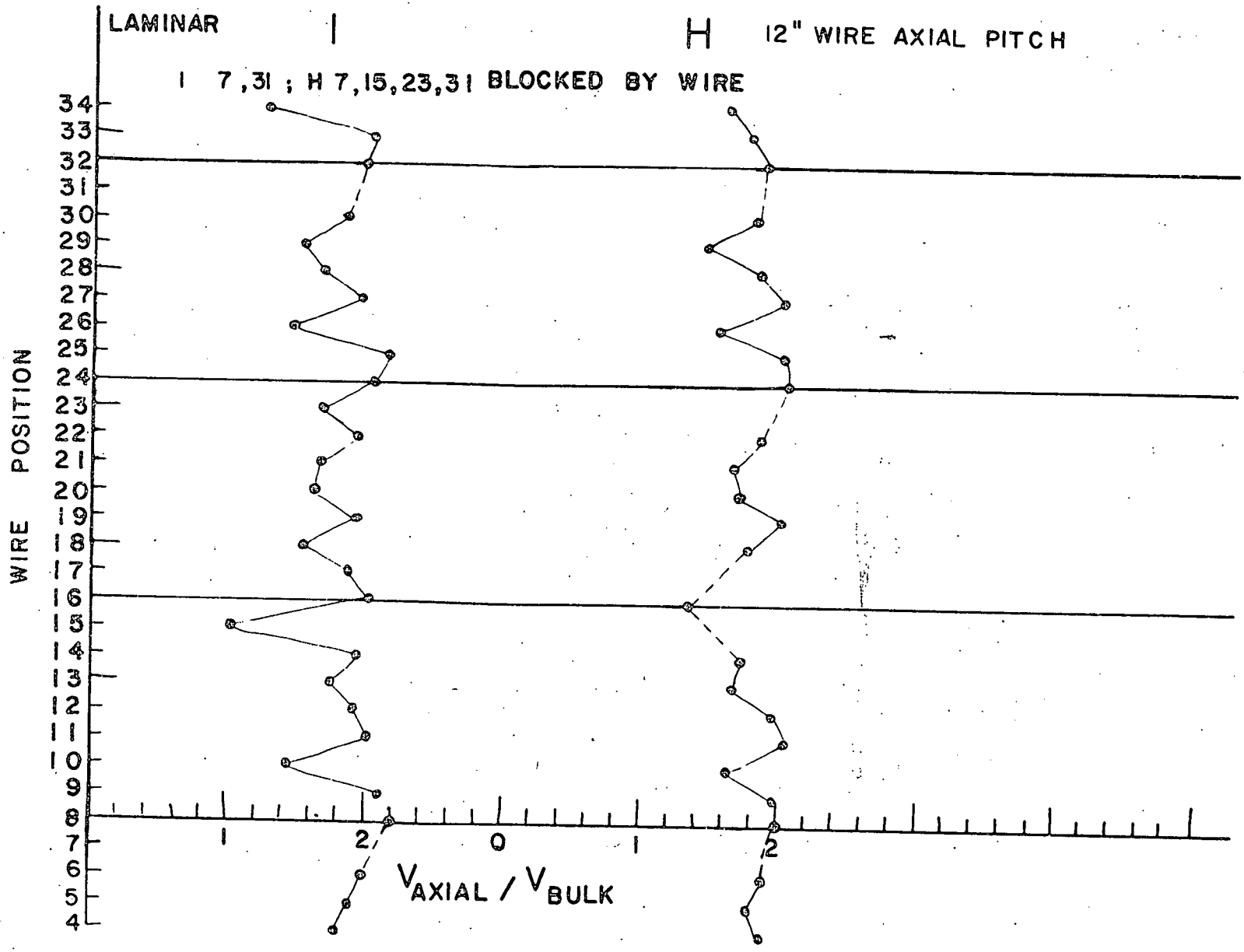
LAMINAR
I
H
12" WIRE AXIAL PITCH
I 7,31 ; H 7,15,23,31 BLOCKED BY WIRE
WIRE POSITION
34
33
32
31
30
29
28
27
26
25
24
23
22
21
20
19
18
17
16
15
14
13
12
11
10
9
8
7
6
5
4
1
2
0
1
2
VAXIAL / VBULK

FIGURE 4.6

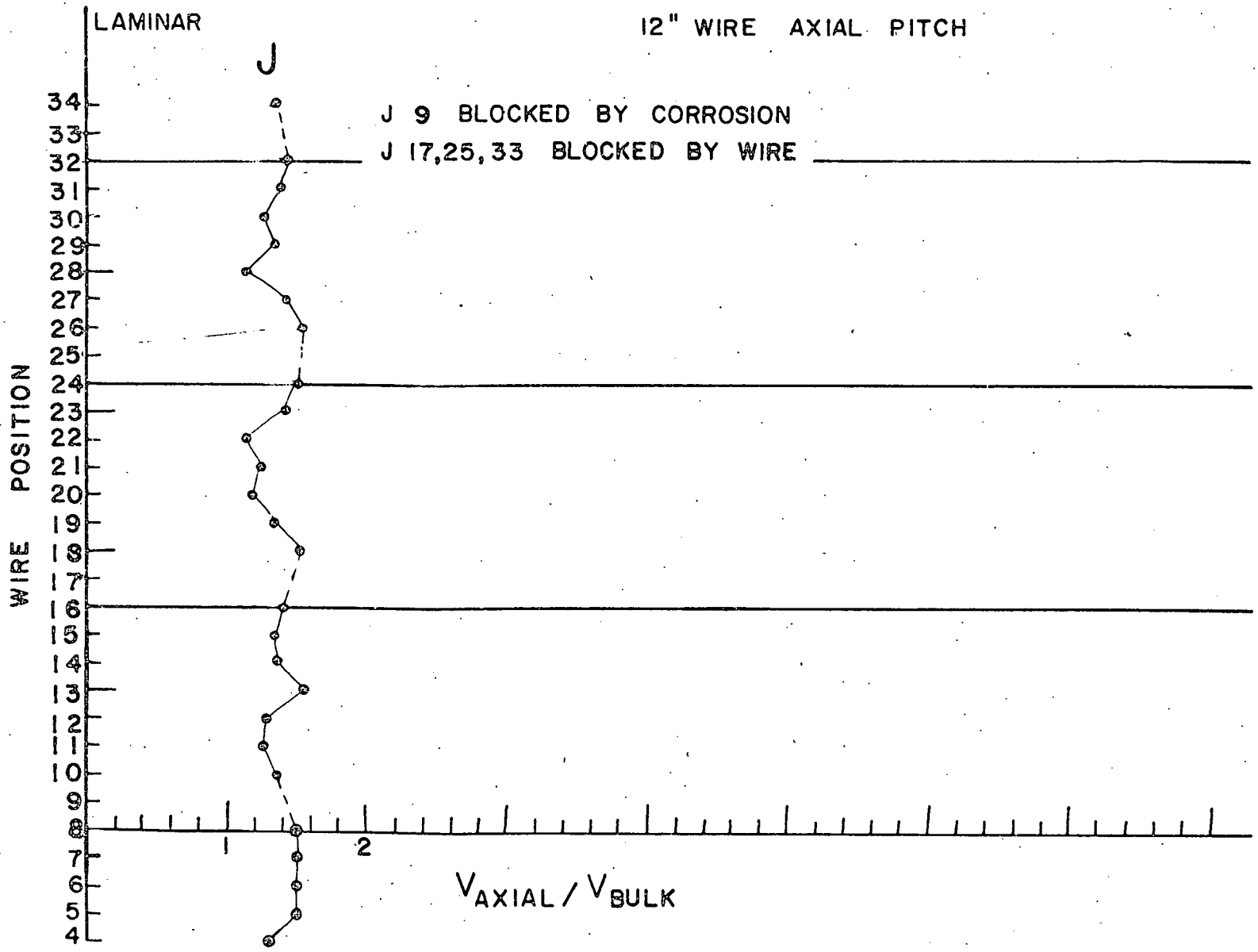
LAMINAR
12" WIRE AXIAL PITCH
J
J 9 BLOCKED BY CORROSION
J 17,25,33 BLOCKED BY WIRE
WIRE POSITION
34
33
32
31
30
29
28
27
26
25
24
23
22
21
20
19
18
17
16
15
14
13
12
11
10
9
8
7
6
5
4
1
2
V_{AXIAL} / V_{BULK}

FIGURE 4.7

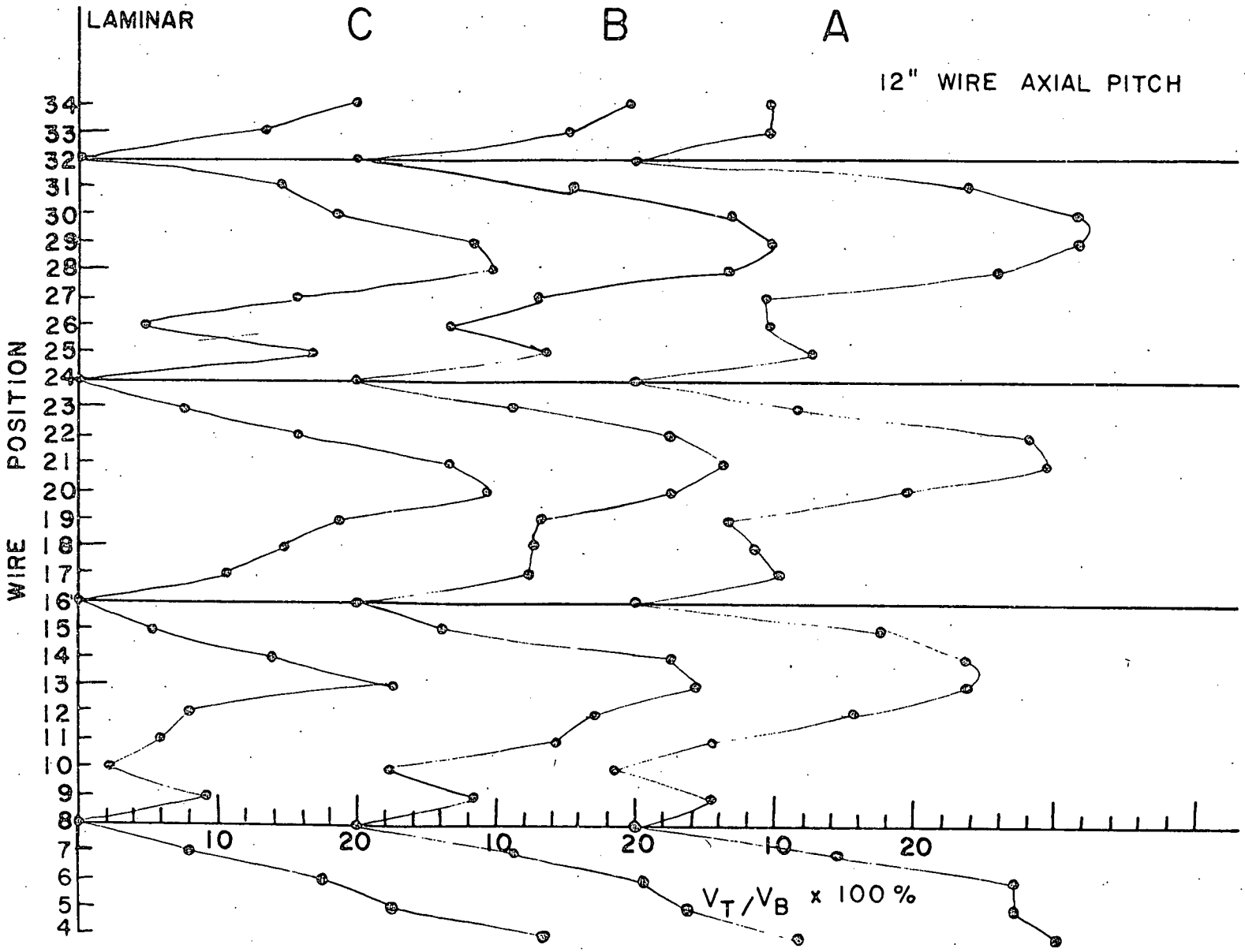
LAMINAR
C
B
A
12" WIRE AXIAL PITCH
WIRE POSITION
34
33
32
31
30
29
28
27
26
25
24
23
22
21
20
19
18
17
16
15
14
13
12
11
10
9
8
7
6
5
4
10
20
10
20
10
20
V_T/V_B x 100 %

FIGURE 4.8

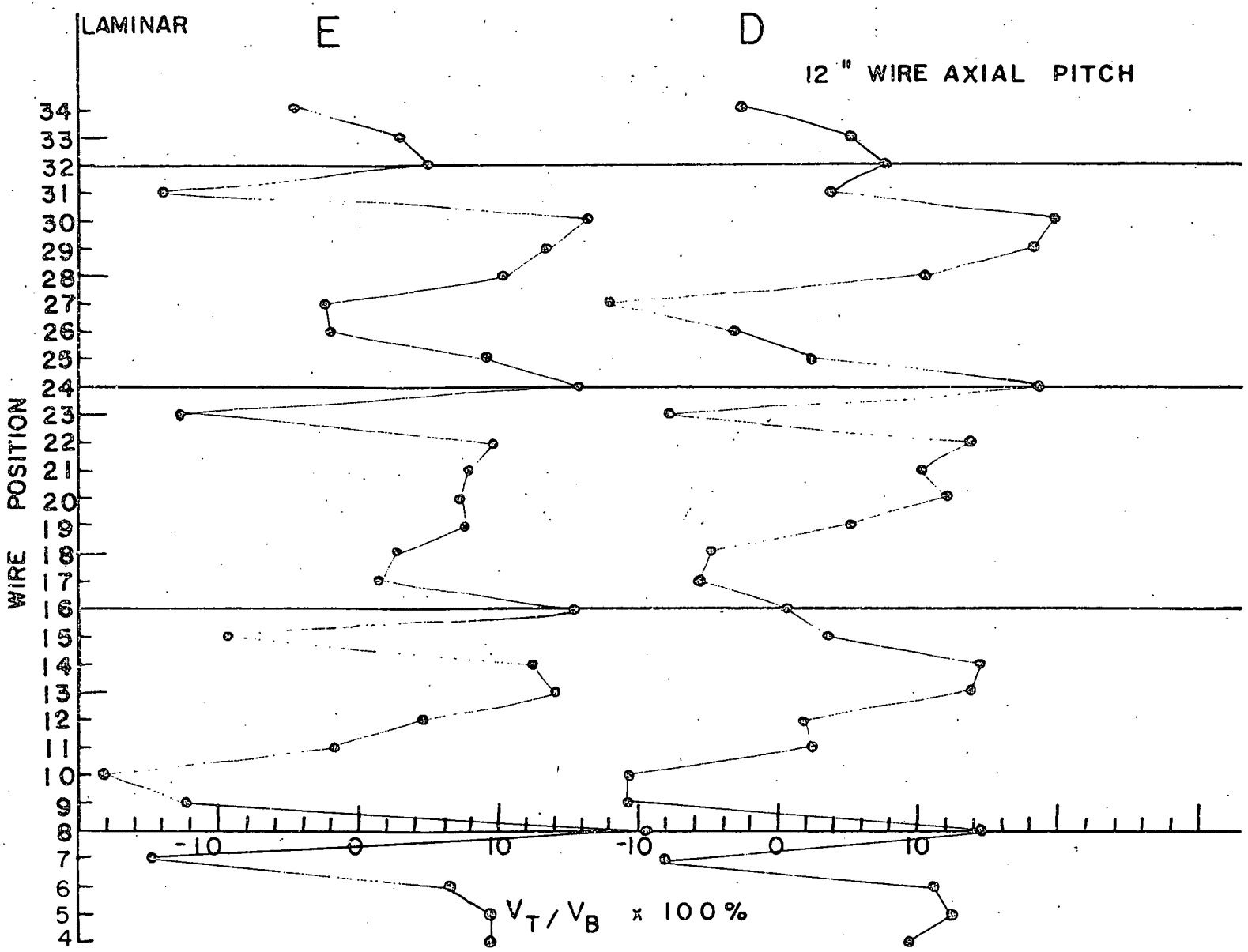
LAMINAR
E
D
12 " WIRE AXIAL PITCH
WIRE POSITION
34
33
32
31
30
29
28
27
26
25
24
23
22
21
20
19
18
17
16
15
14
13
12
11
10
9
8
7
6
5
4
-10
0
10
-10
0
10
V_T / V_B x 100%

FIGURE 4.9

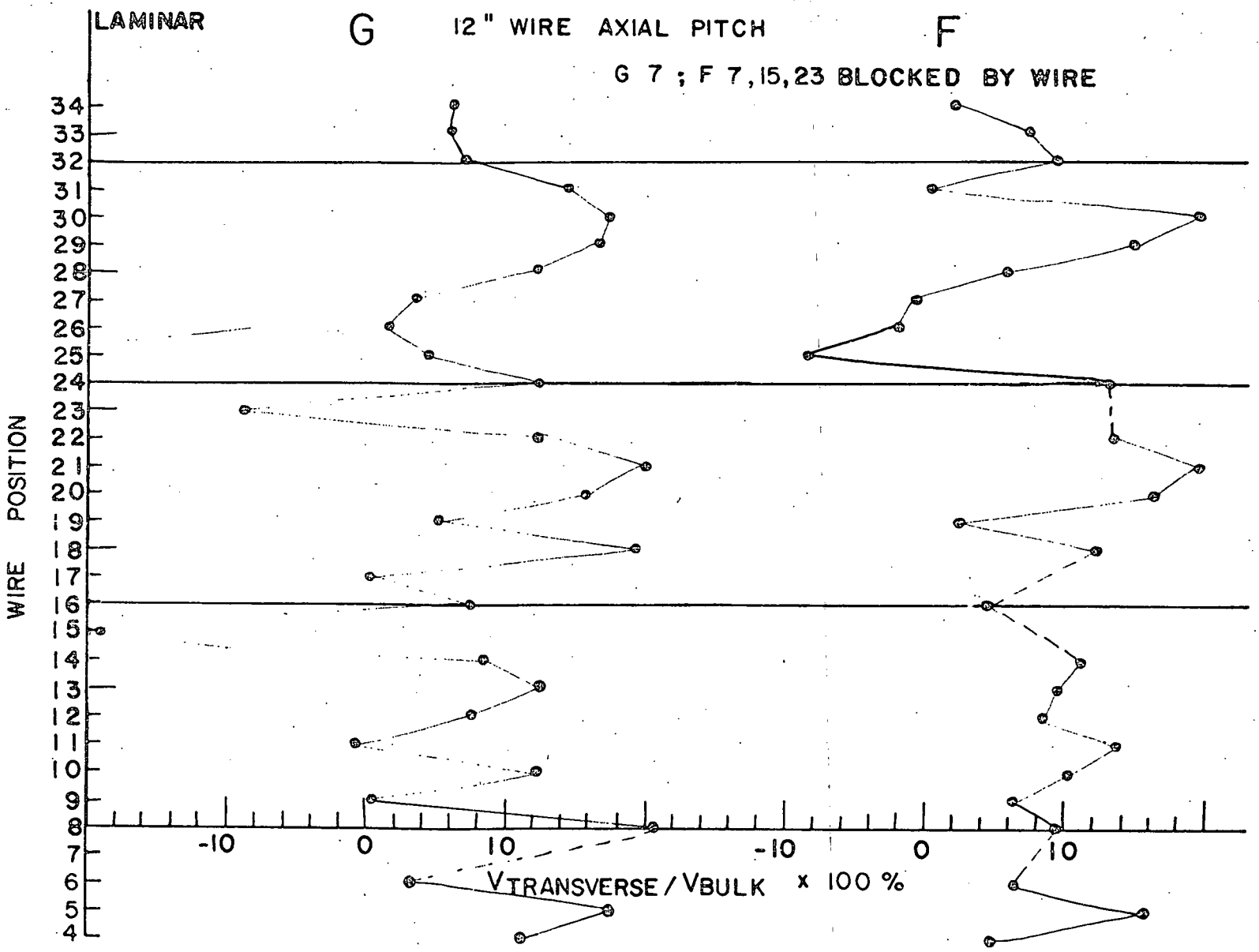
LAMINAR
G
12" WIRE AXIAL PITCH
F
G 7 ; F 7,15,23 BLOCKED BY WIRE
WIRE POSITION
34
33
32
31
30
29
28
27
26
25
24
23
22
21
20
19
18
17
16
15
14
13
12
11
10
9
8
7
6
5
4
-10
0
10
-10
0
10
VTRANSVERSE / VBULK x 100 %

FIGURE 4.10

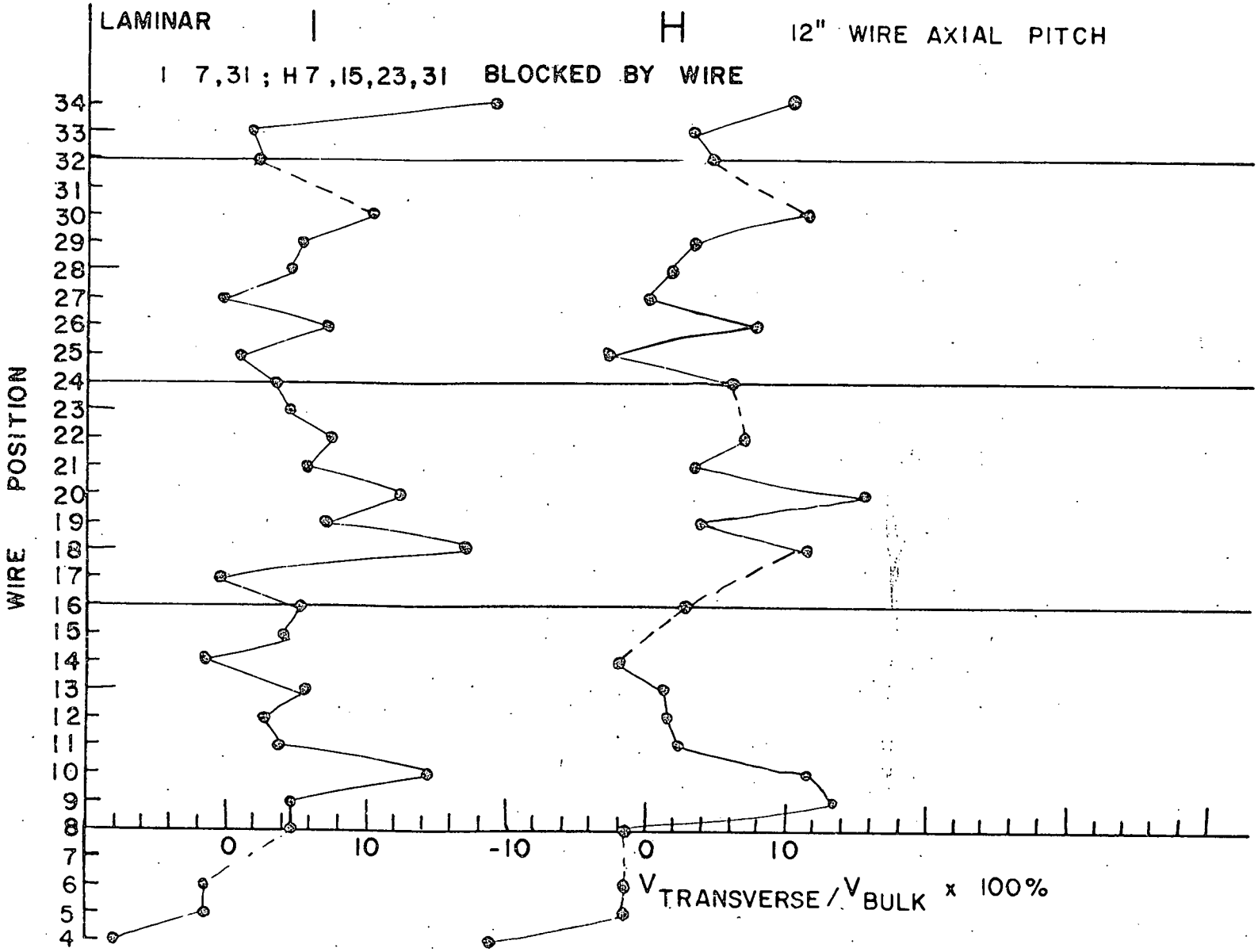
LAMINAR
I
H
12" WIRE AXIAL PITCH
I 7,31 ; H 7,15,23,31 BLOCKED BY WIRE
WIRE POSITION
34
33
32
31
30
29
28
27
26
25
24
23
22
21
20
19
18
17
16
15
14
13
12
11
10
9
8
7
6
5
4
0
10
-10
0
10
V TRANSVERSE / V BULK x 100%

FIGURE 4.11

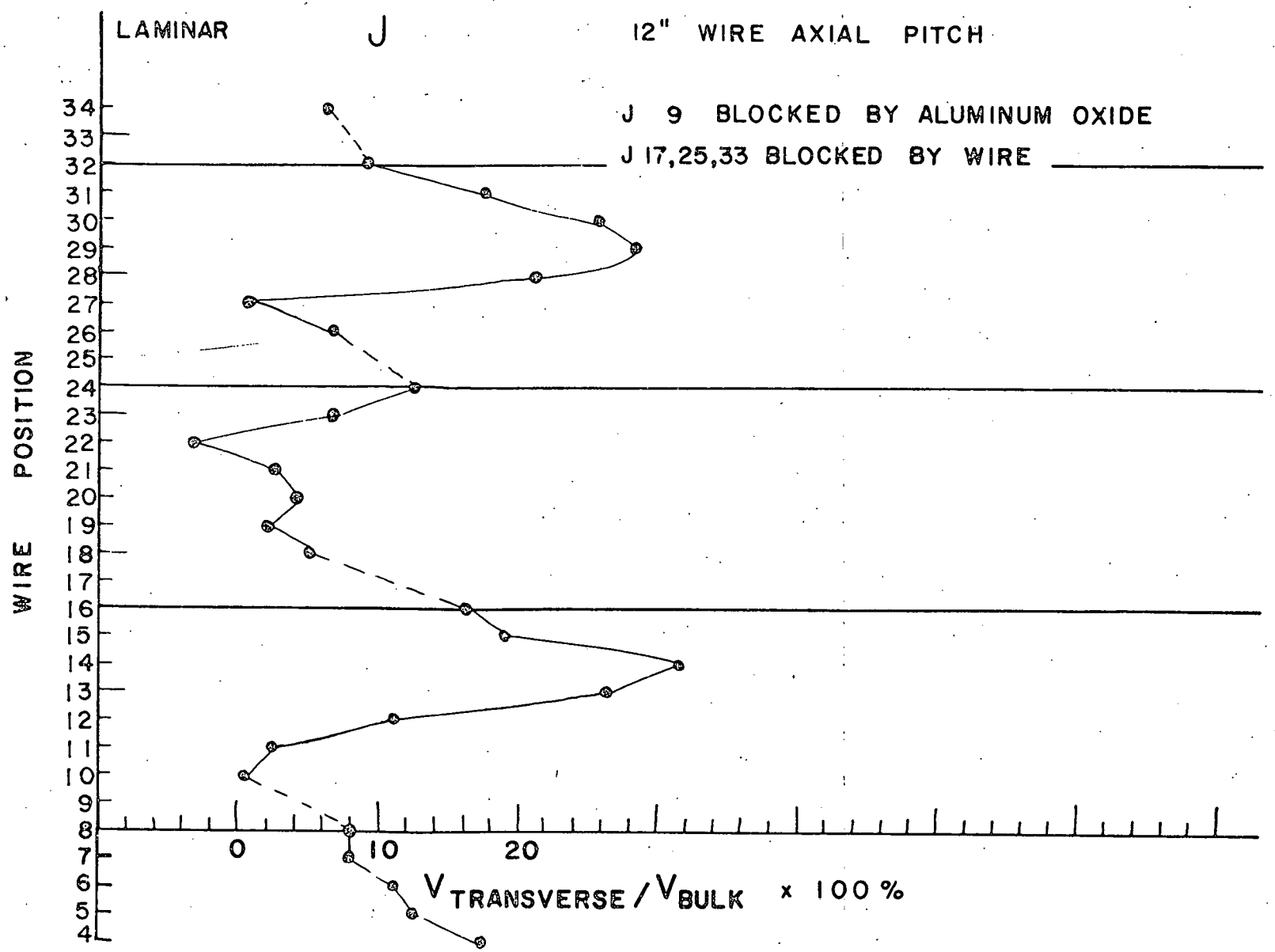
LAMINAR
J
12" WIRE AXIAL PITCH
J 9 BLOCKED BY ALUMINUM OXIDE
J 17,25,33 BLOCKED BY WIRE
WIRE POSITION
34
33
32
31
30
29
28
27
26
25
24
23
22
21
20
19
18
17
16
15
14
13
12
11
10
9
8
7
6
5
4
0
10
20
V TRANSVERSE / V BULK x 100 %

FIGURE 4.12

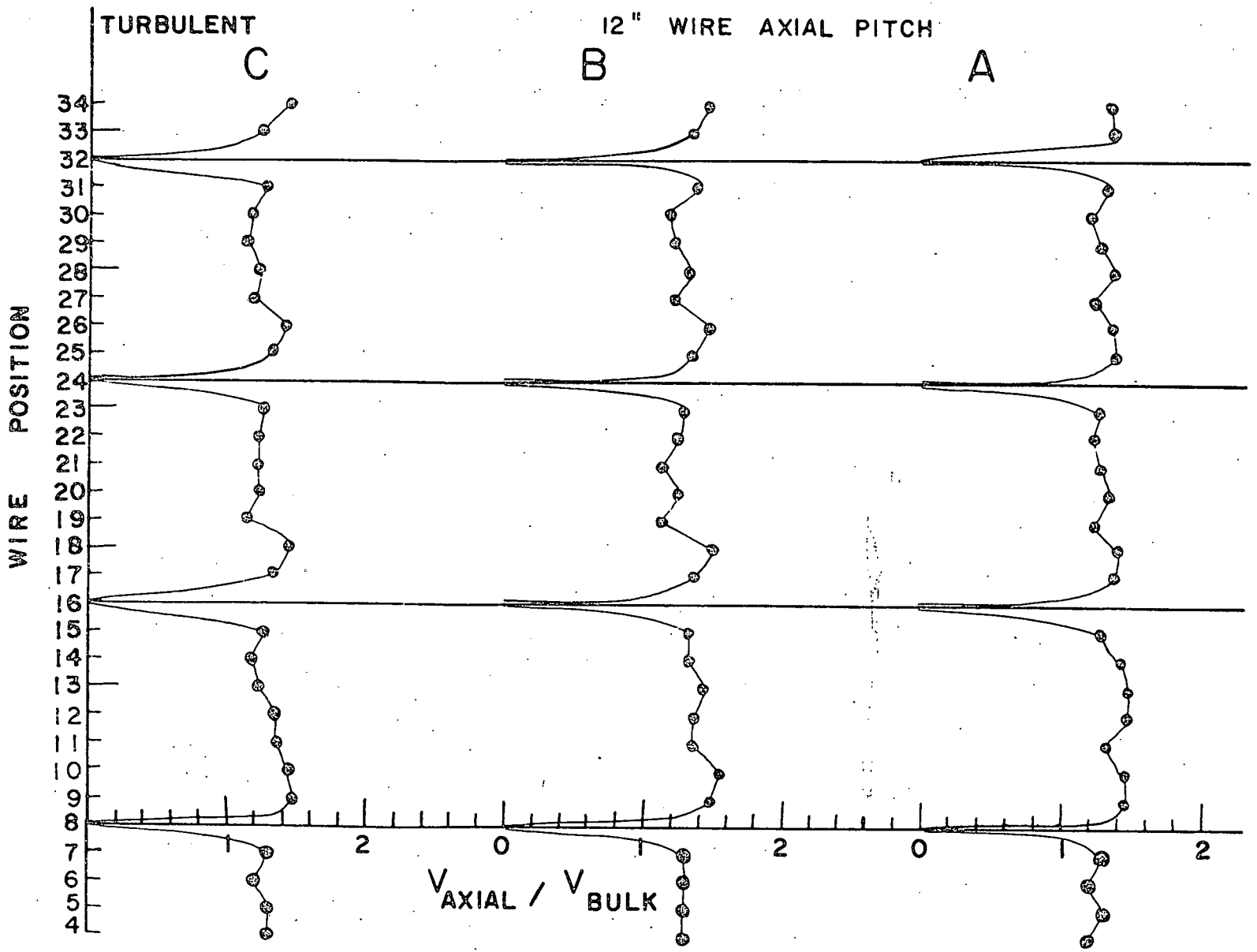
TURBULENT
12" WIRE AXIAL PITCH
C
B
A
WIRE POSITION
34
33
32
31
30
29
28
27
26
25
24
23
22
21
20
19
18
17
16
15
14
13
12
11
10
9
8
7
6
5
4
2
0
2
0
2
V AXIAL / V BULK

FIGURE 4.13

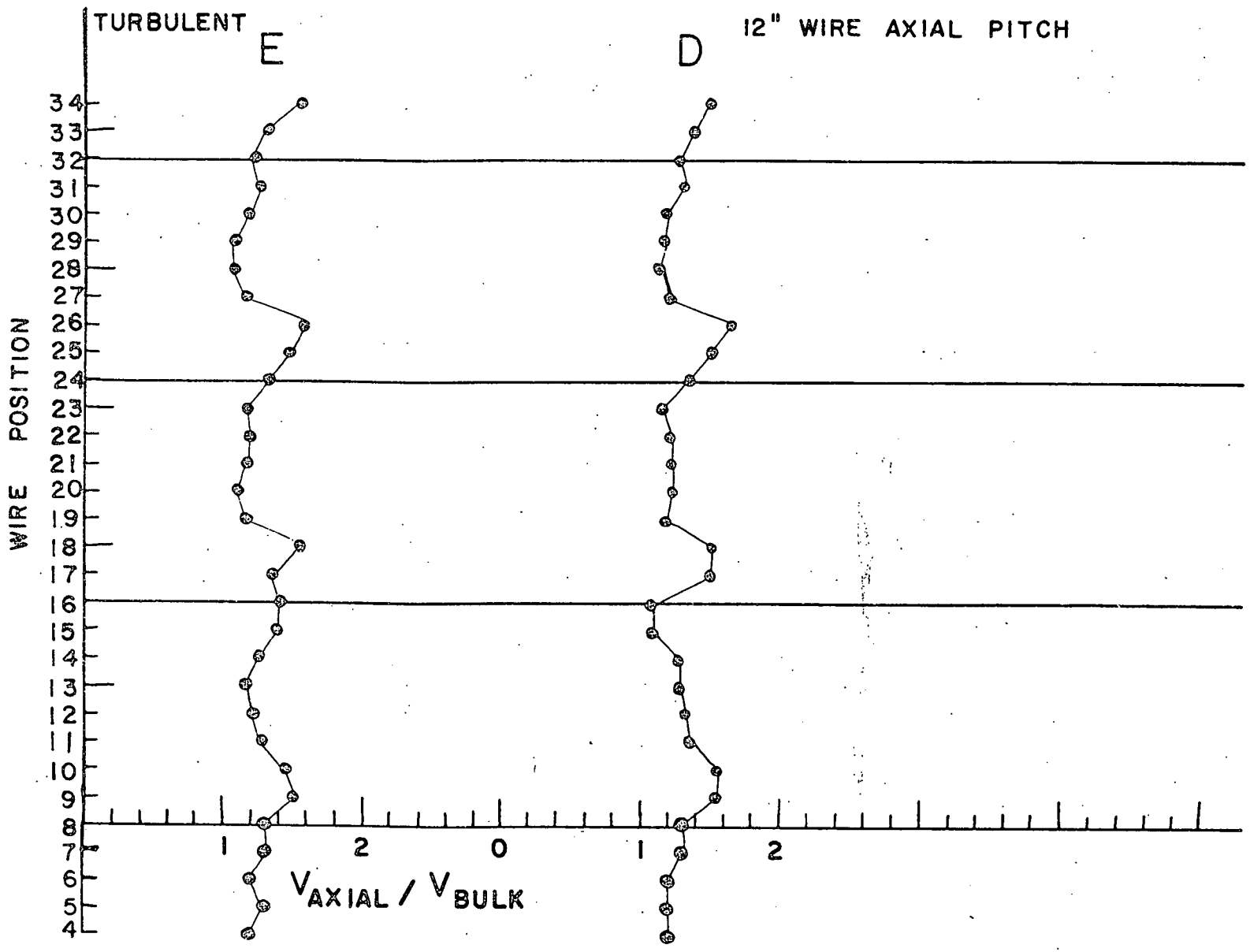
TURBULENT
E
D
12" WIRE AXIAL PITCH
WIRE POSITION
34
33
32
31
30
29
28
27
26
25
24
23
22
21
20
19
18
17
16
15
14
13
12
11
10
9
8
7
6
5
4
1
2
0
1
2
VAXIAL / VBULK

FIGURE 4.14

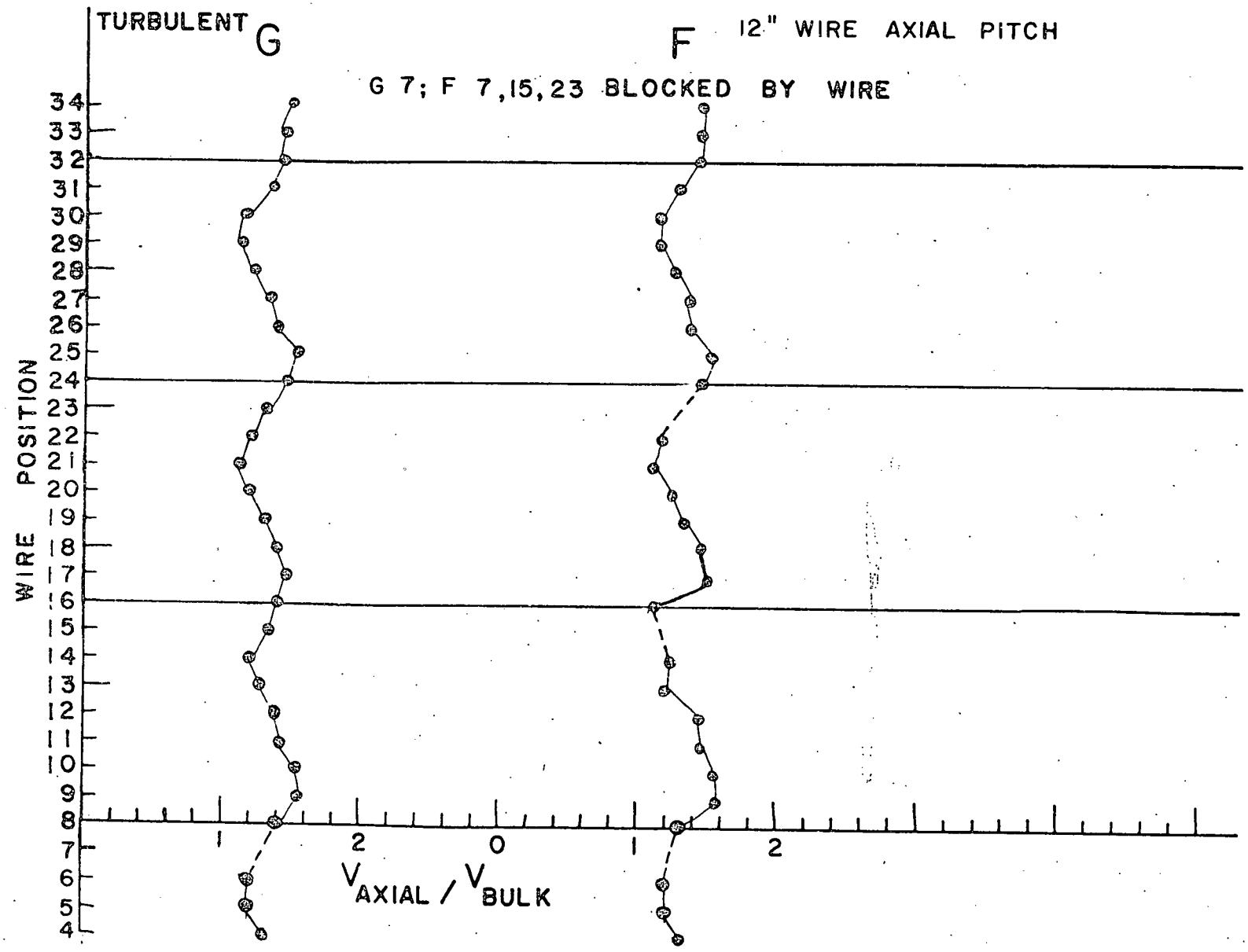
TURBULENT
G
F
12" WIRE AXIAL PITCH
G 7; F 7,15,23 BLOCKED BY WIRE
WIRE POSITION
34
33
32
31
30
29
28
27
26
25
24
23
22
21
20
19
18
17
16
15
14
13
12
11
10
9
8
7
6
5
4
1
2
0
1
2
V_{AXIAL} / V_{BULK}

FIGURE 4.15

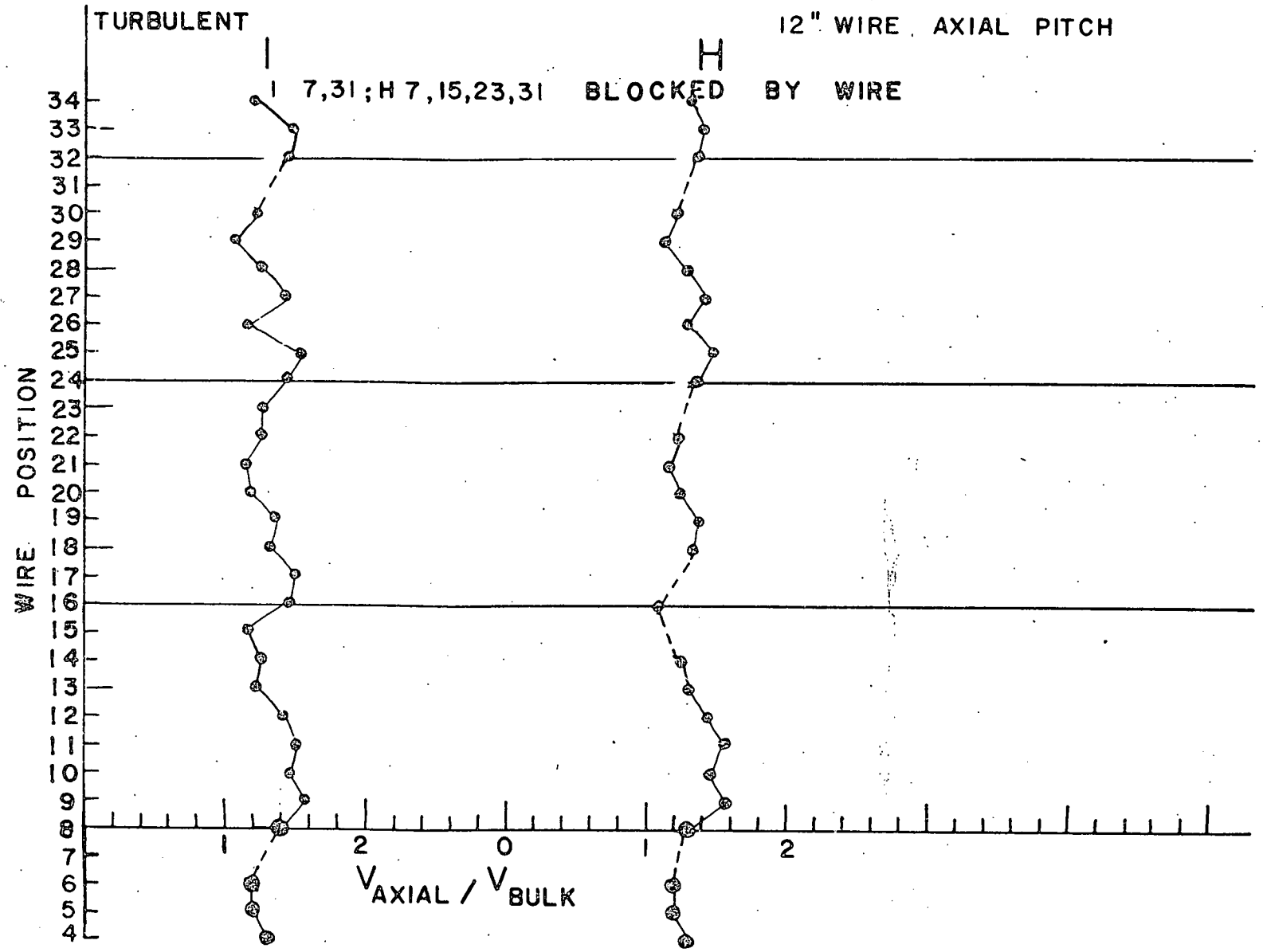
TURBULENT
12" WIRE AXIAL PITCH
I
H
I 7,31 ; H 7,15,23,31 BLOCKED BY WIRE
WIRE POSITION
34
33
32
31
30
29
28
27
26
25
24
23
22
21
20
19
18
17
16
15
14
13
12
11
10
9
8
7
6
5
4
1
2
0
1
2
V_{AXIAL} / V_{BULK}

FIGURE 4.16

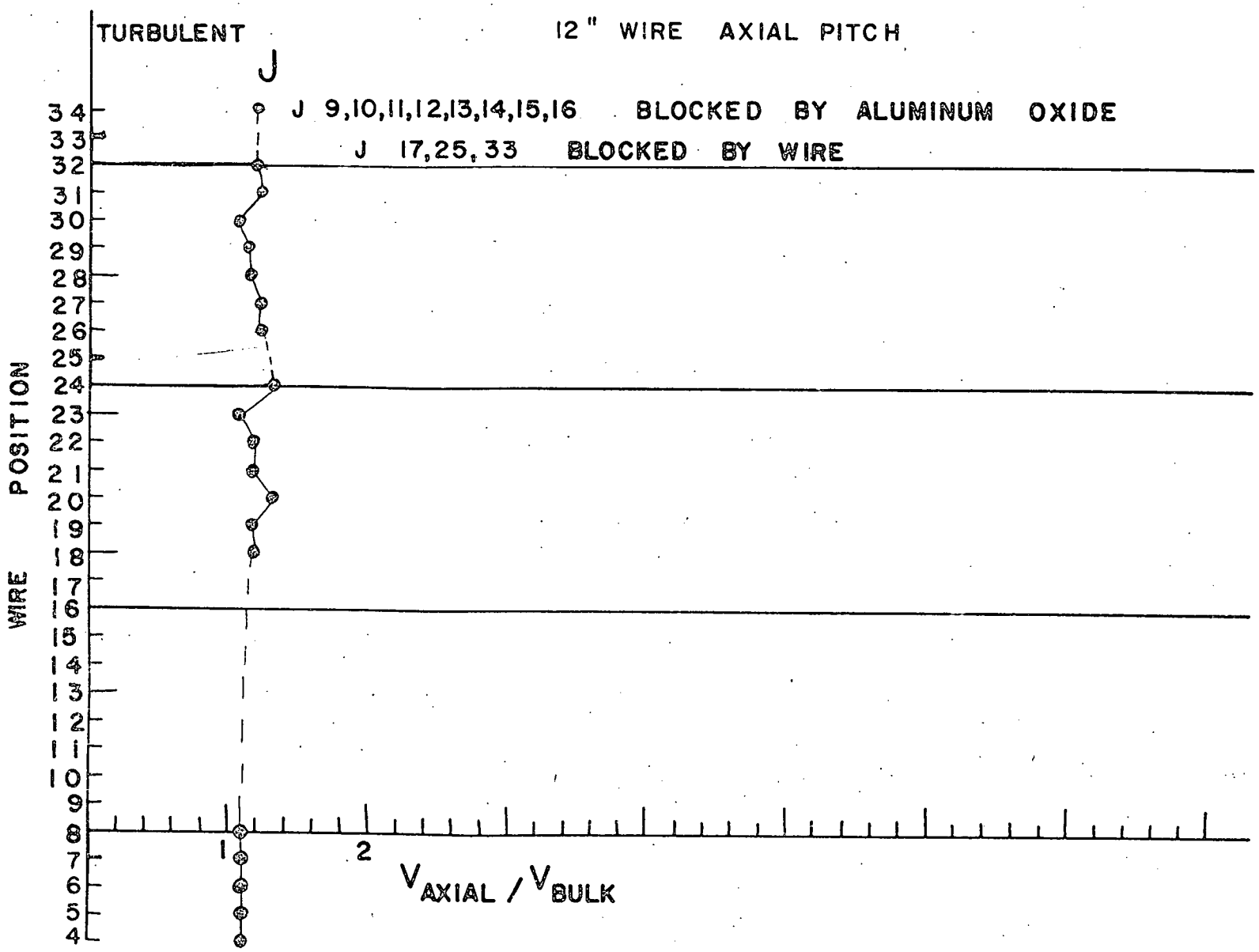
TURBULENT
12" WIRE AXIAL PITCH
J
J 9,10,11,12,13,14,15,16 BLOCKED BY ALUMINUM OXIDE
J 17,25,33 BLOCKED BY WIRE
WIRE POSITION
34
33
32
31
30
29
28
27
26
25
24
23
22
21
20
19
18
17
16
15
14
13
12
11
10
9
8
7
6
5
4
1
2
VAXIAL / VBULK

FIGURE 4.17

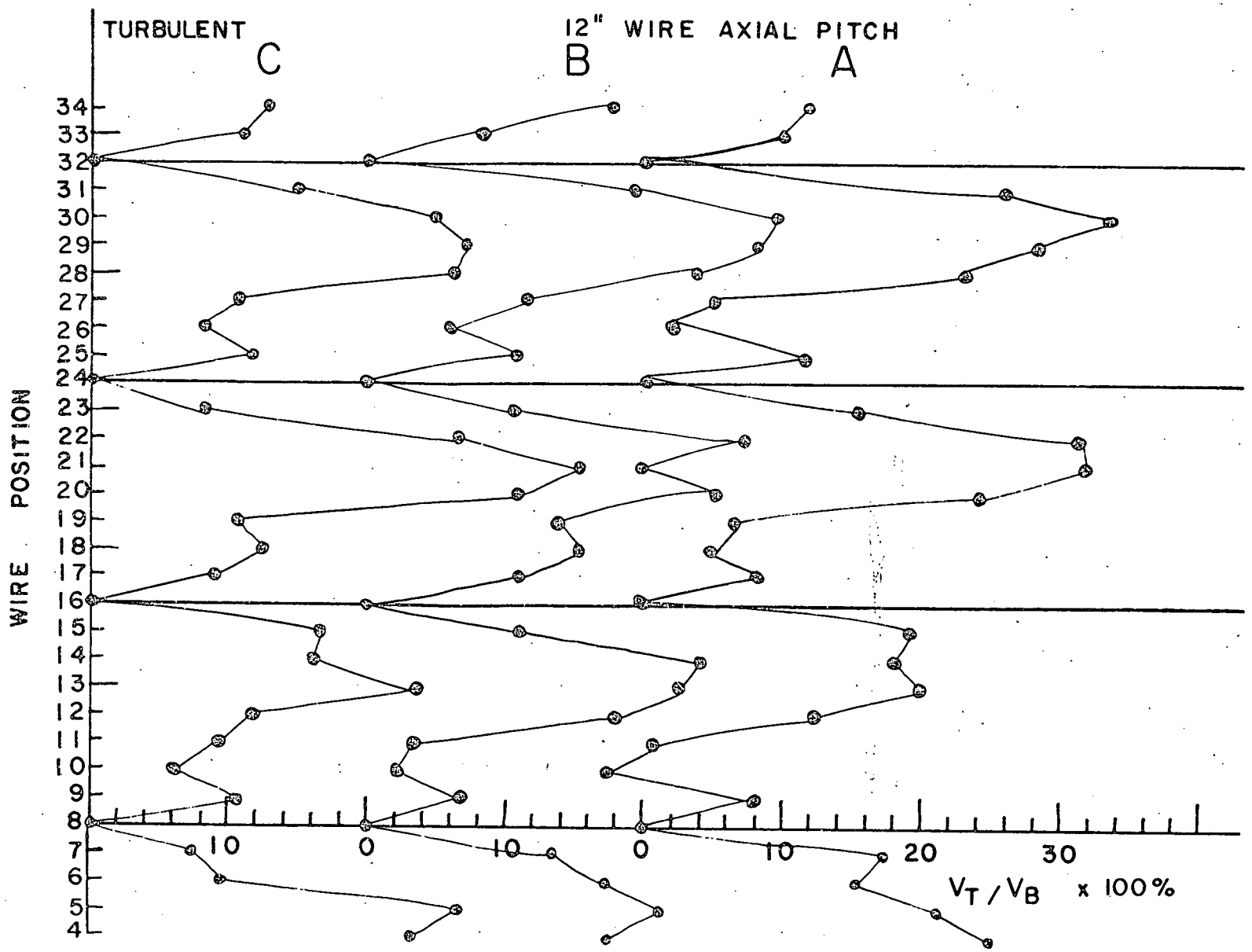
TURBULENT
12" WIRE AXIAL PITCH
C
B
A
WIRE POSITION
34
33
32
31
30
29
28
27
26
25
24
23
22
21
20
19
18
17
16
15
14
13
12
11
10
9
8
7
6
5
4
10
0
10
0
10
20
30
V_T / V_B x 100%

FIGURE 4.18

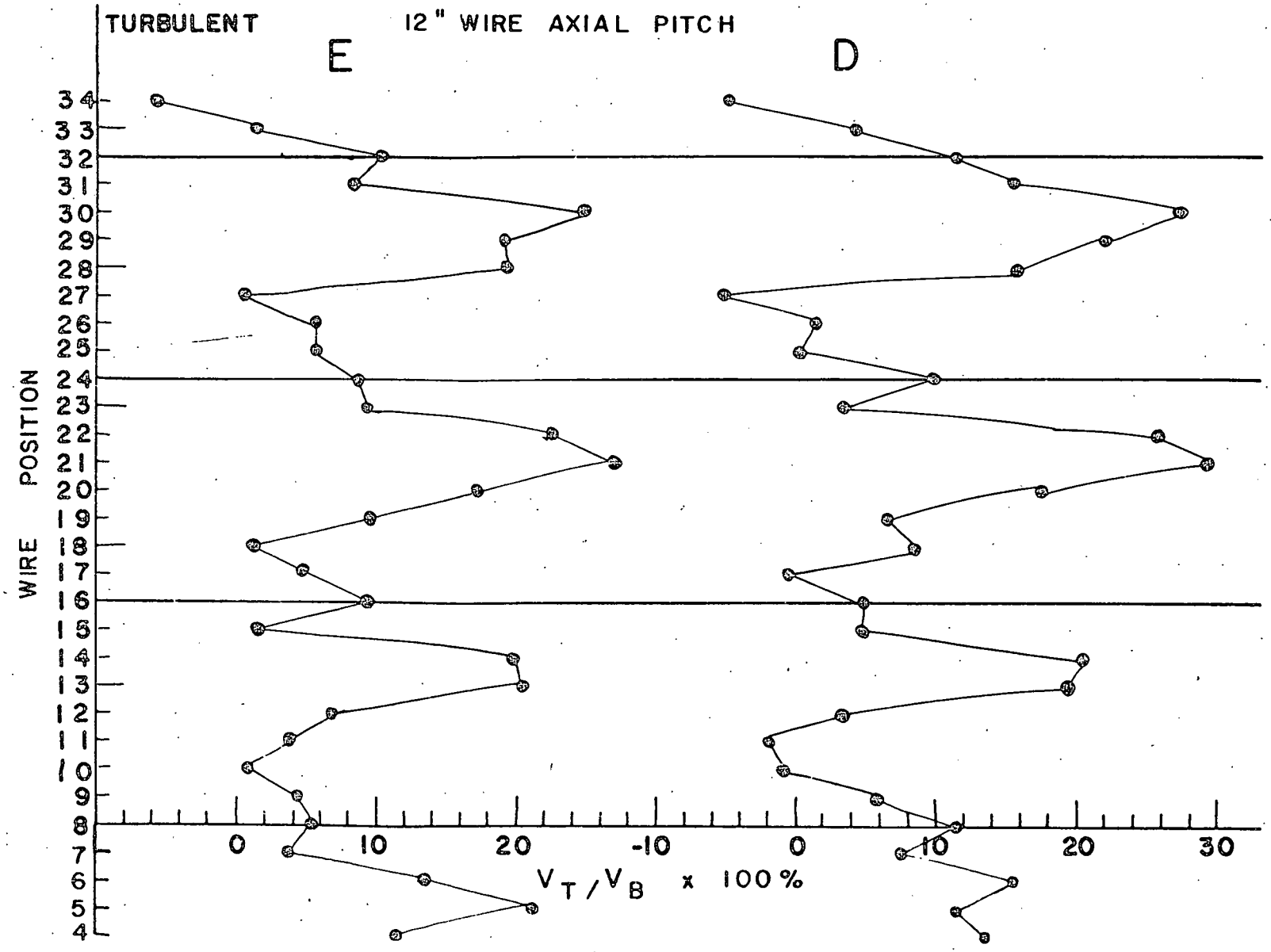
TURBULENT
12" WIRE AXIAL PITCH
E
D
WIRE POSITION
34
33
32
31
30
29
28
27
26
25
24
23
22
21
20
19
18
17
16
15
14
13
12
11
10
9
8
7
6
5
4
0
10
20
-10
0
10
20
30
V_T / V_B x 100%

FIGURE 4.19

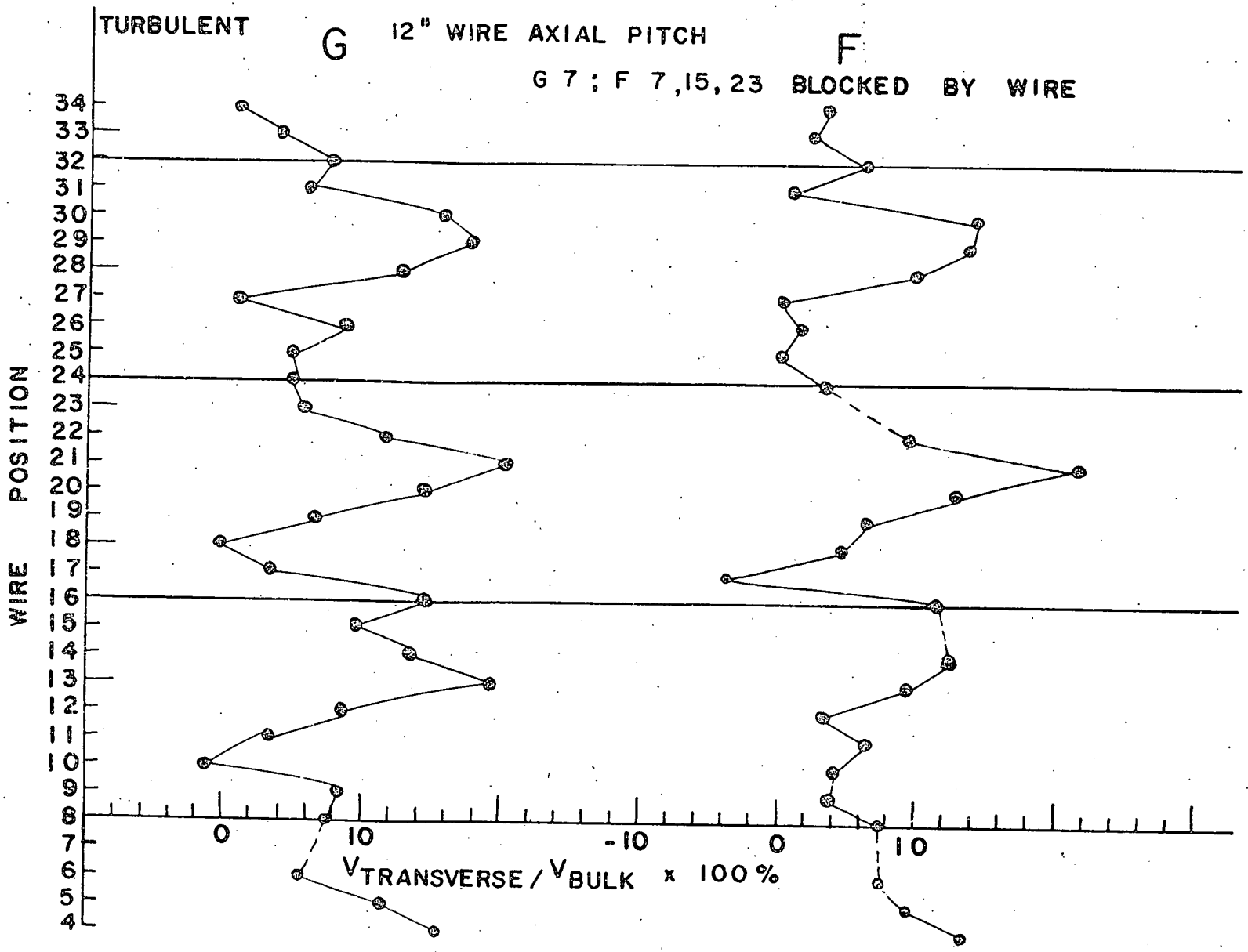
TURBULENT
G
12" WIRE AXIAL PITCH
F
G 7 ; F 7,15,23 BLOCKED BY WIRE
WIRE POSITION
34
33
32
31
30
29
28
27
26
25
24
23
22
21
20
19
18
17
16
15
14
13
12
11
10
9
8
7
6
5
4
0
10
-10
0
10
VTRANSVERSE / VBULK x 100 %

FIGURE 4.20

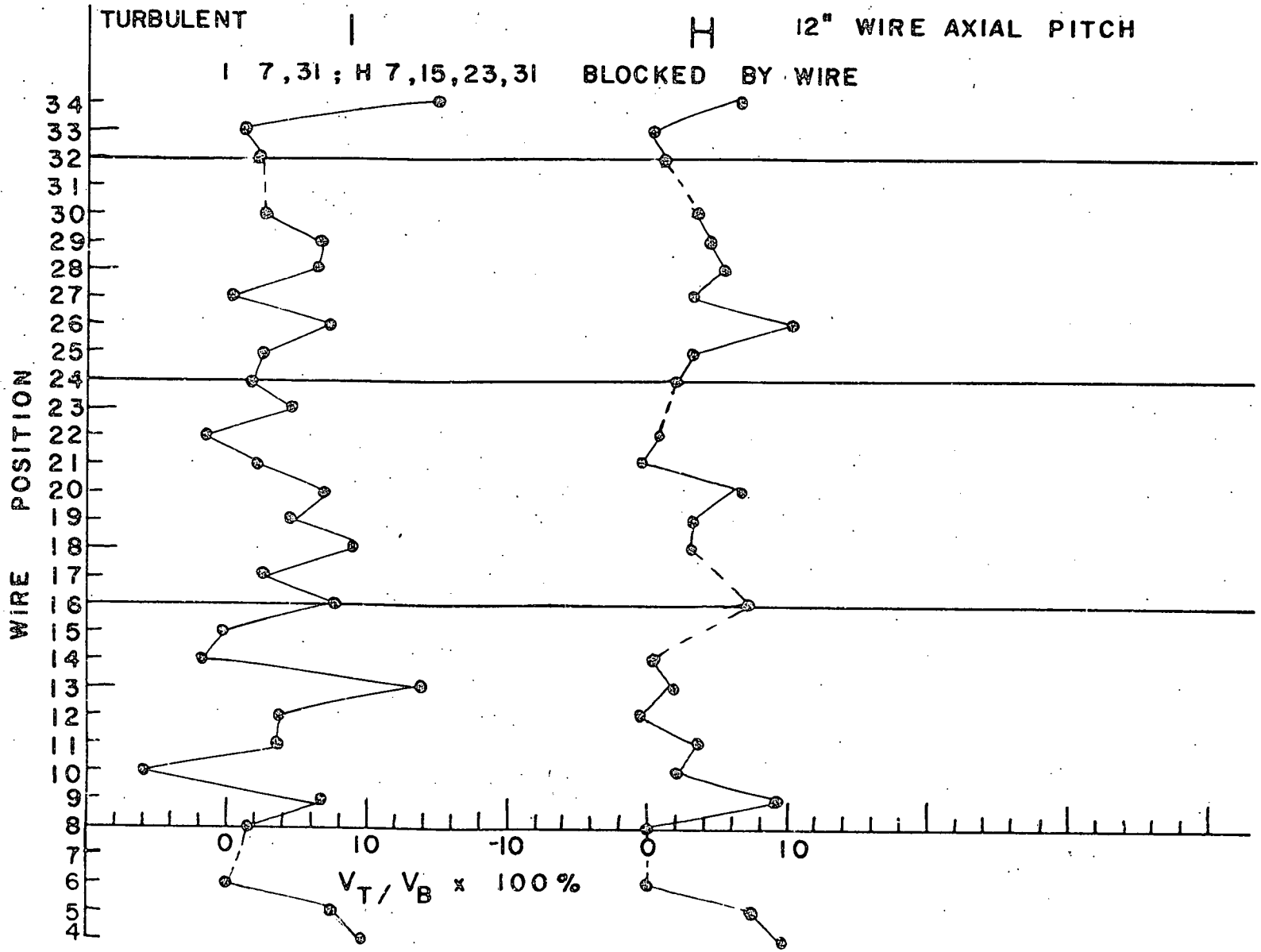
TURBULENT
I
H
12" WIRE AXIAL PITCH
I 7,31 ; H 7,15,23,31 BLOCKED BY WIRE
WIRE POSITION
34
33
32
31
30
29
28
27
26
25
24
23
22
21
20
19
18
17
16
15
14
13
12
11
10
9
8
7
6
5
4
0
10
-10
0
10
V_T / V_B x 100 %

FIGURE 4.21

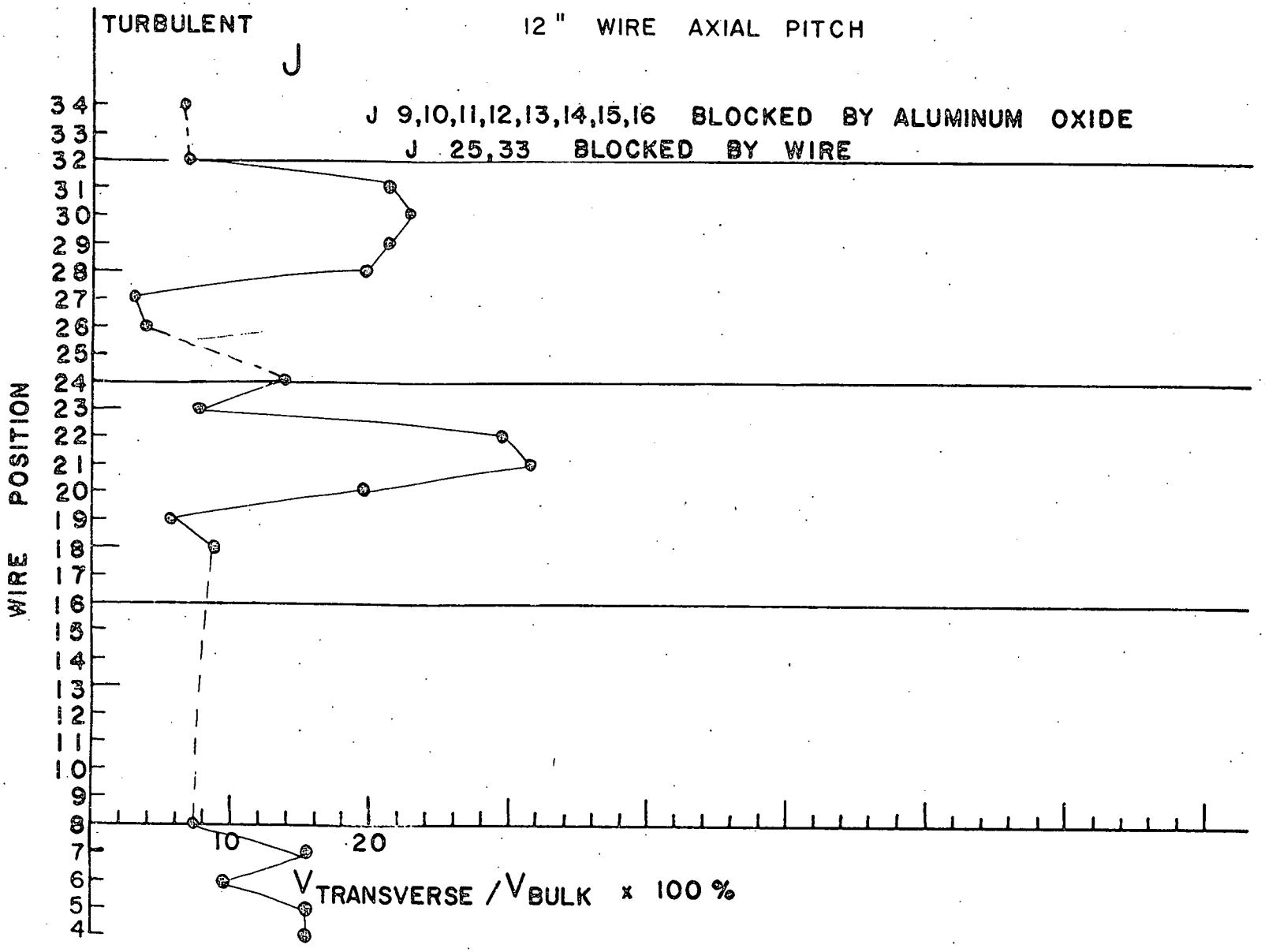
TURBULENT
12 " WIRE AXIAL PITCH
J
J 9,10,11,12,13,14,15,16 BLOCKED BY ALUMINUM OXIDE
J 25,33 BLOCKED BY WIRE
WIRE POSITION
34
33
32
31
30
29
28
27
26
25
24
23
22
21
20
19
18
17
16
15
14
13
12
11
10
9
8
7
6
5
4
10
20
V TRANSVERSE / V BULK x 100 %

FIGURE 4.22

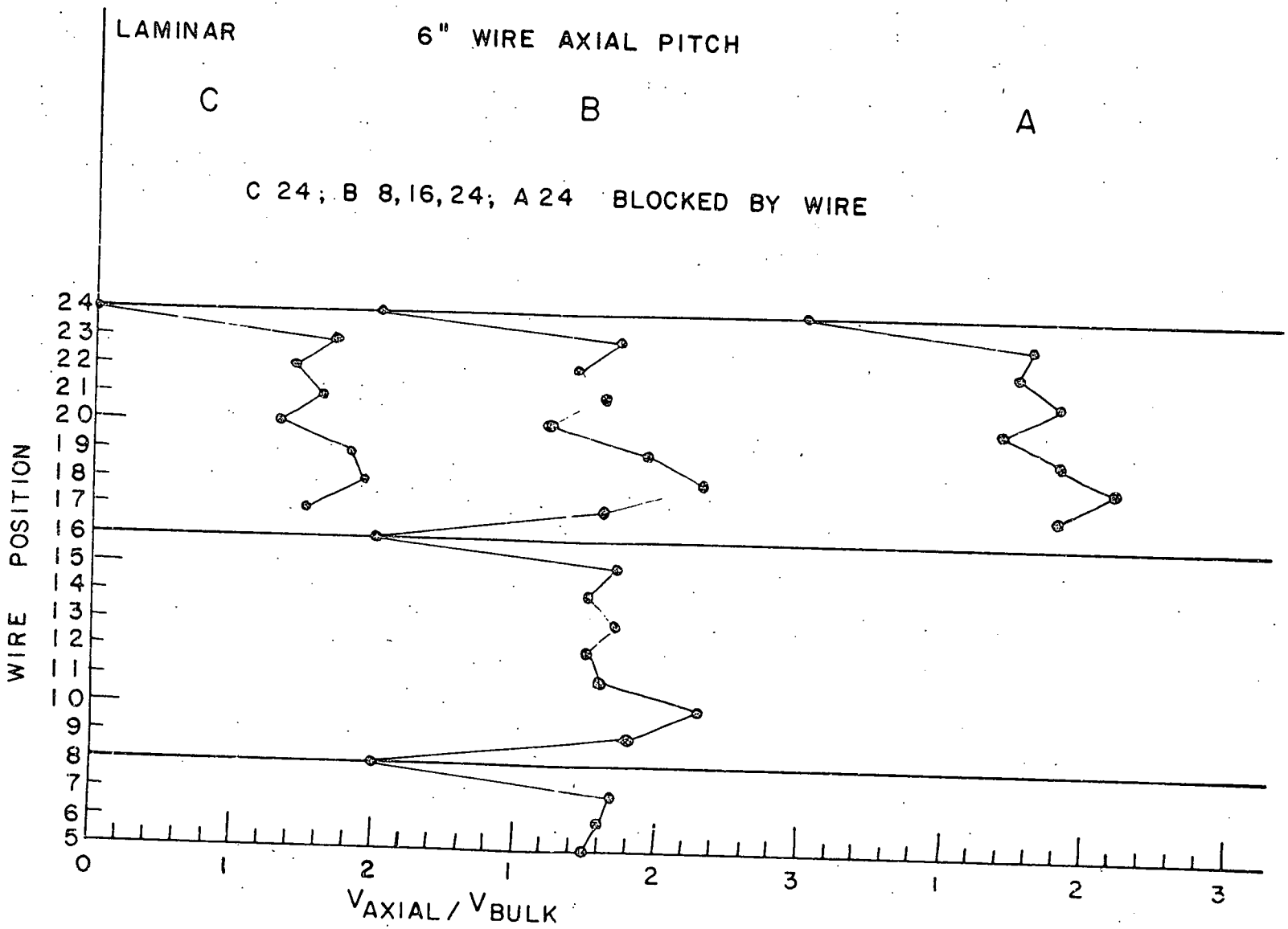
LAMINAR
6" WIRE AXIAL PITCH
C
B
A
C 24; B 8, 16, 24; A 24 BLOCKED BY WIRE
WIRE POSITION
24
23
22
21
20
19
18
17
16
15
14
13
12
11
10
9
8
7
6
5
0
1
2
1
2
3
1
2
3
VAXIAL / VBULK

FIGURE 4.23

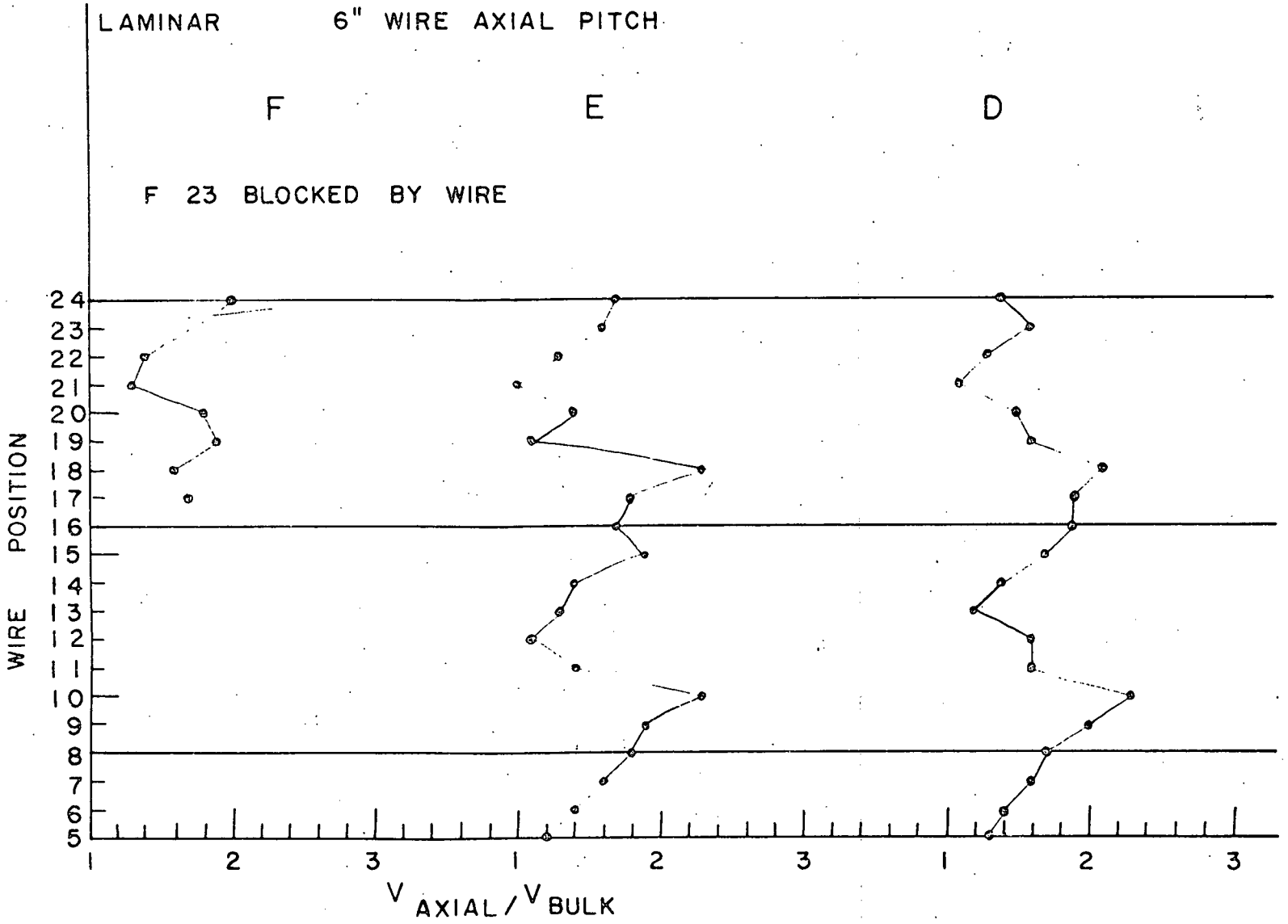
LAMINAR
6" WIRE AXIAL PITCH
F
E
D
F 23 BLOCKED BY WIRE
WIRE POSITION
24
23
22
21
20
19
18
17
16
15
14
13
12
11
10
9
8
7
6
5
1
2
3
1
2
3
1
2
3
V AXIAL / V BULK

FIGURE 4.24

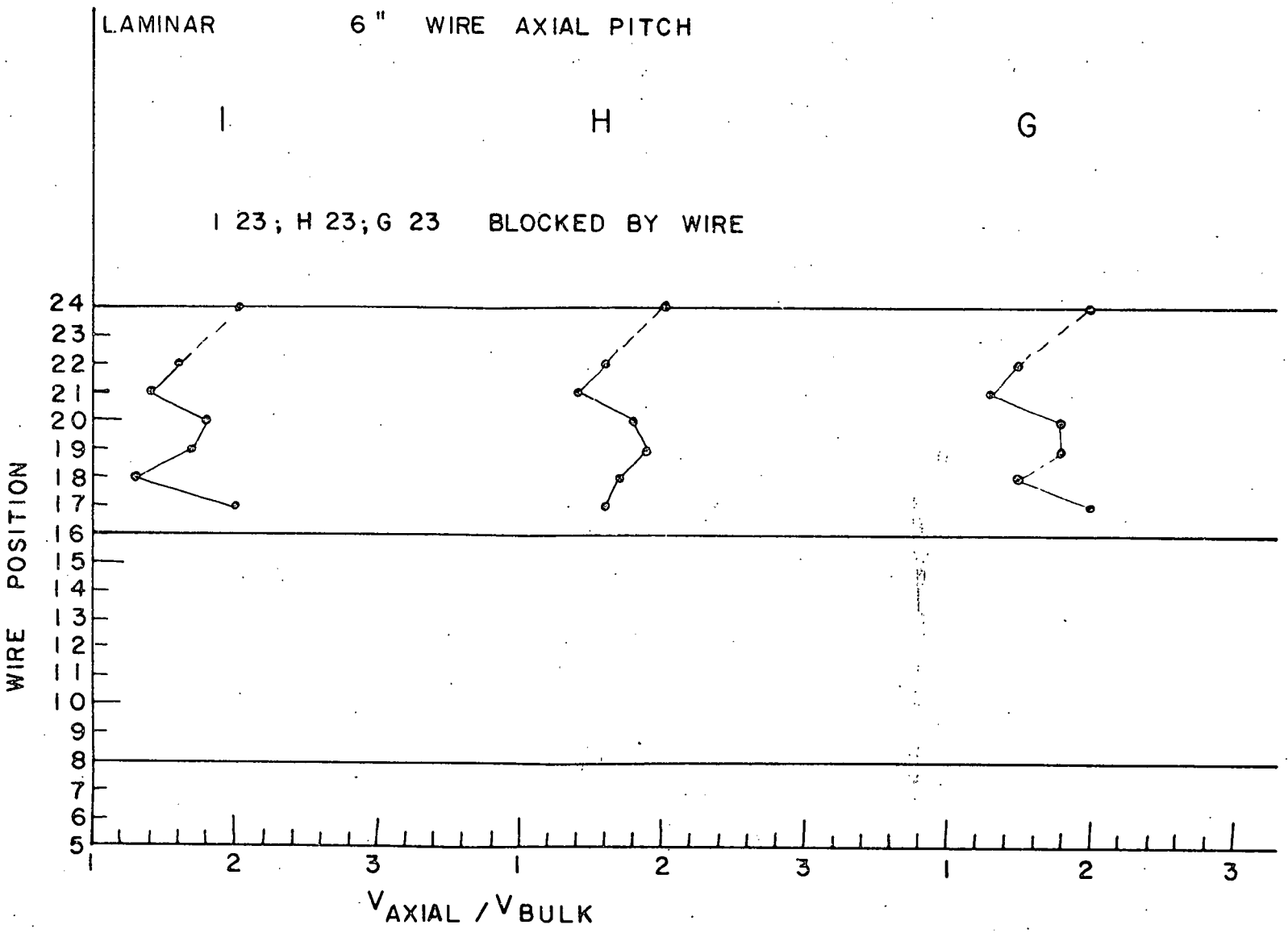
LAMINAR
6" WIRE AXIAL PITCH
I
H
G
I 23; H 23; G 23 BLOCKED BY WIRE
WIRE POSITION
24
23
22
21
20
19
18
17
16
15
14
13
12
11
10
9
8
7
6
5
1
2
3
1
2
3
1
2
3
VAXIAL / VBULK

FIGURE 4.25

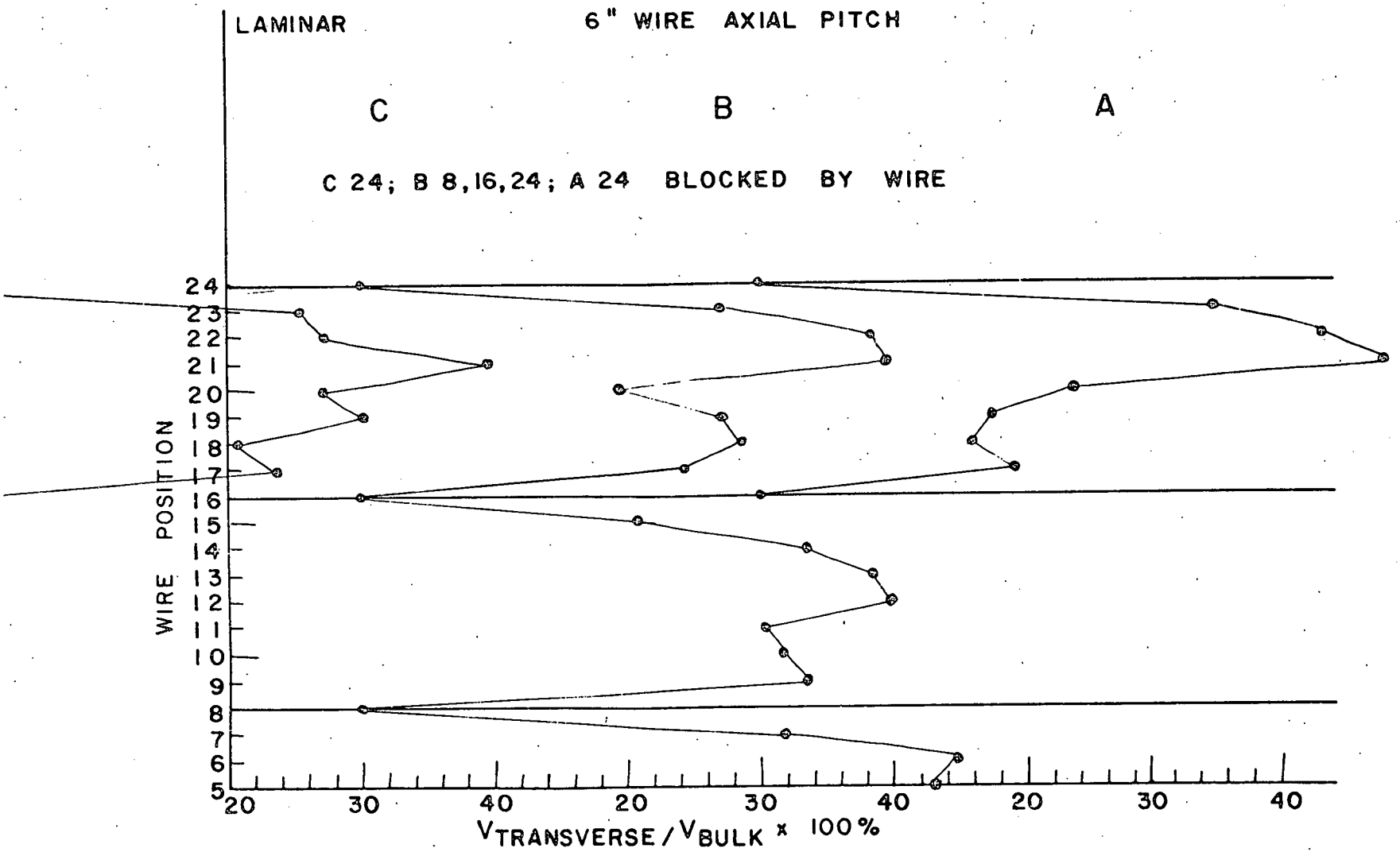
LAMINAR
6" WIRE AXIAL PITCH
C
B
A
C 24; B 8,16,24; A 24 BLOCKED BY WIRE
WIRE POSITION
24
23
22
21
20
19
18
17
16
15
14
13
12
11
10
9
8
7
6
5
20
30
40
20
30
40
20
30
40
VTRANSVERSE / VBULK x 100%

FIGURE 4.26

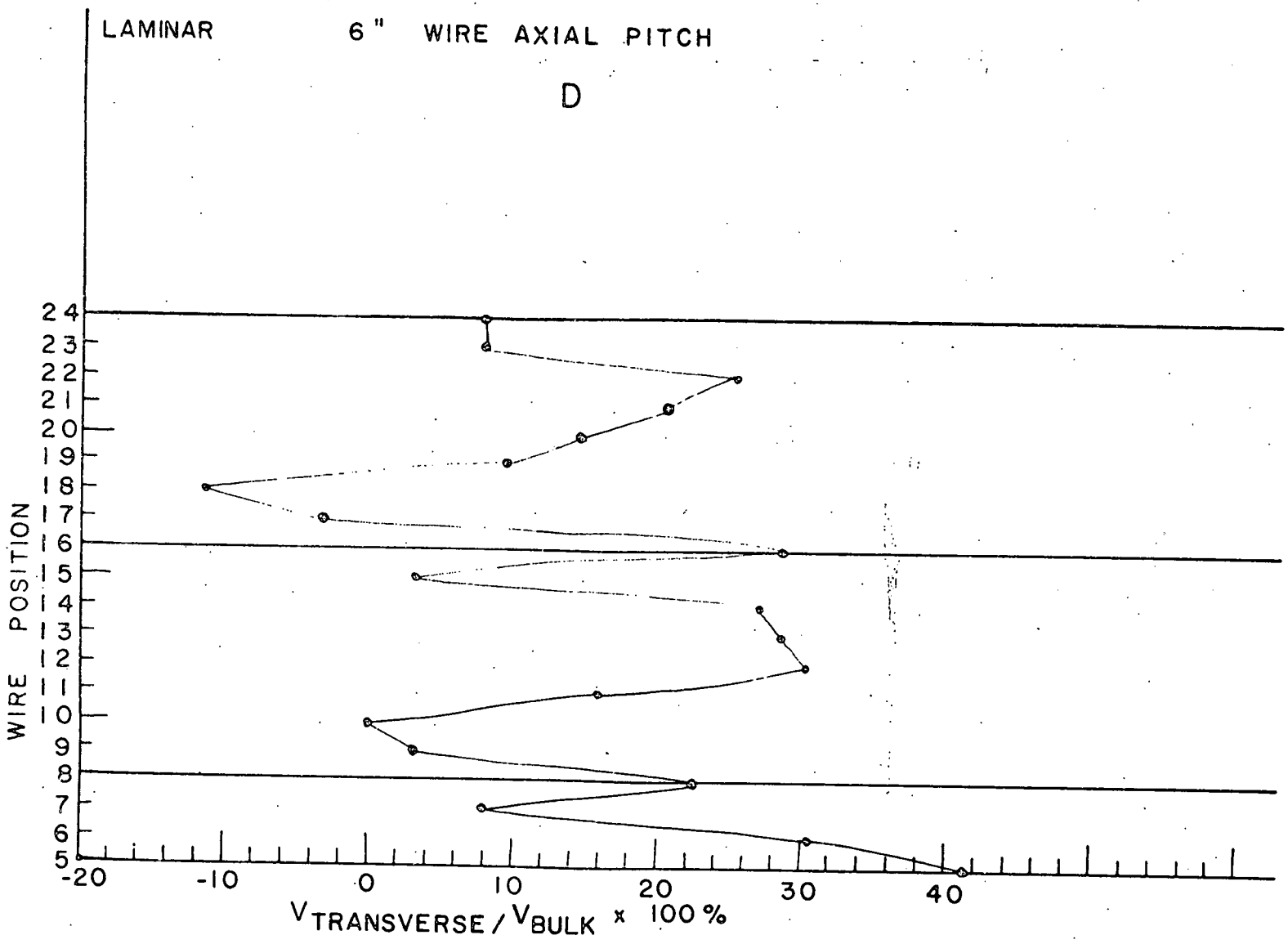
LAMINAR
6" WIRE AXIAL PITCH
D
WIRE POSITION
24
23
22
21
20
19
18
17
16
15
14
13
12
11
10
9
8
7
6
5
-20
-10
0
10
20
30
40
VTRANSVERSE / VBULK x 100 %

FIGURE 4.27

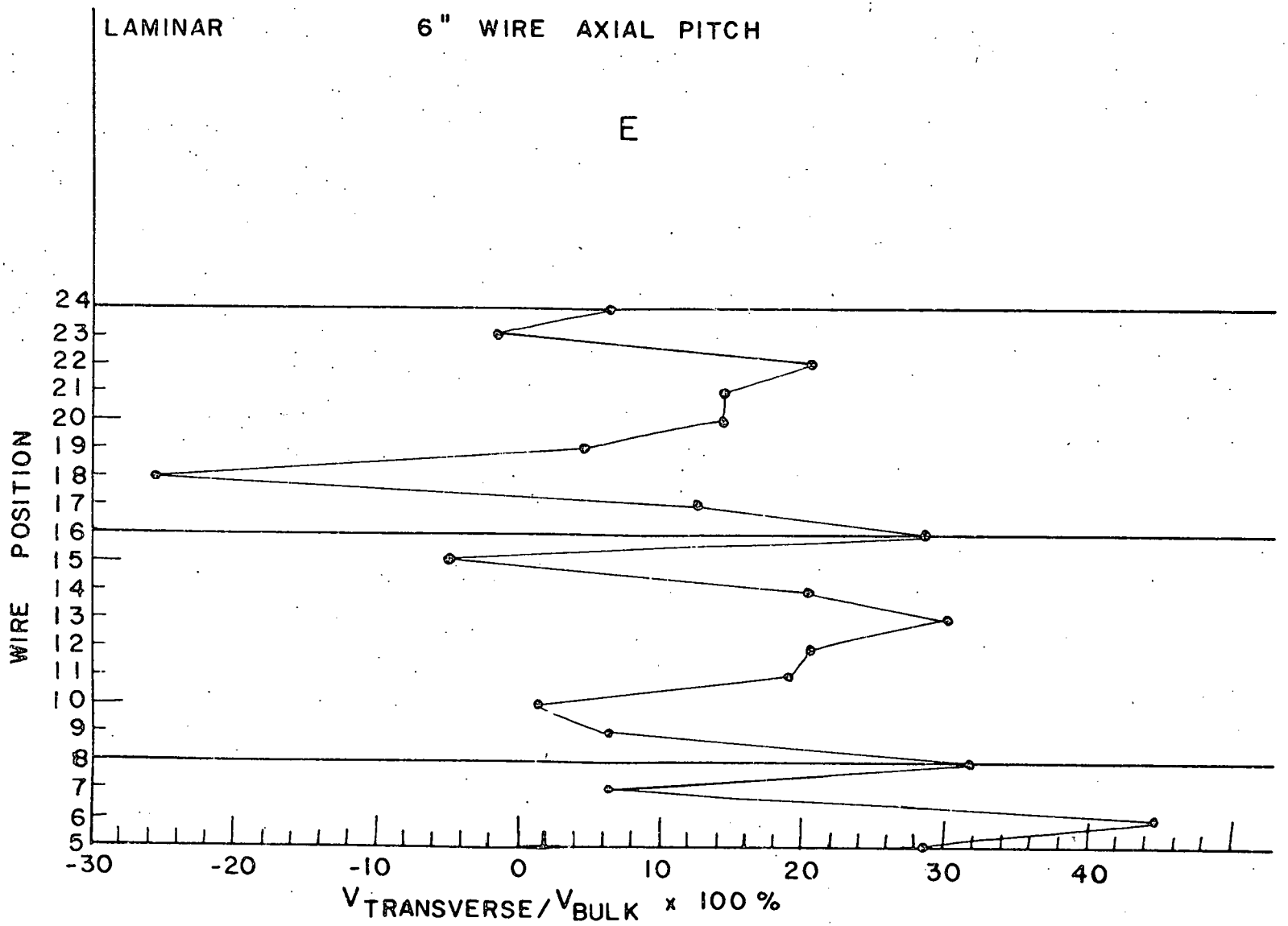
LAMINAR
6" WIRE AXIAL PITCH
E
WIRE POSITION
24
23
22
21
20
19
18
17
16
15
14
13
12
11
10
9
8
7
6
5
-30
-20
-10
0
10
20
30
40
V TRANSVERSE / V BULK x 100 %

FIGURE 4.28

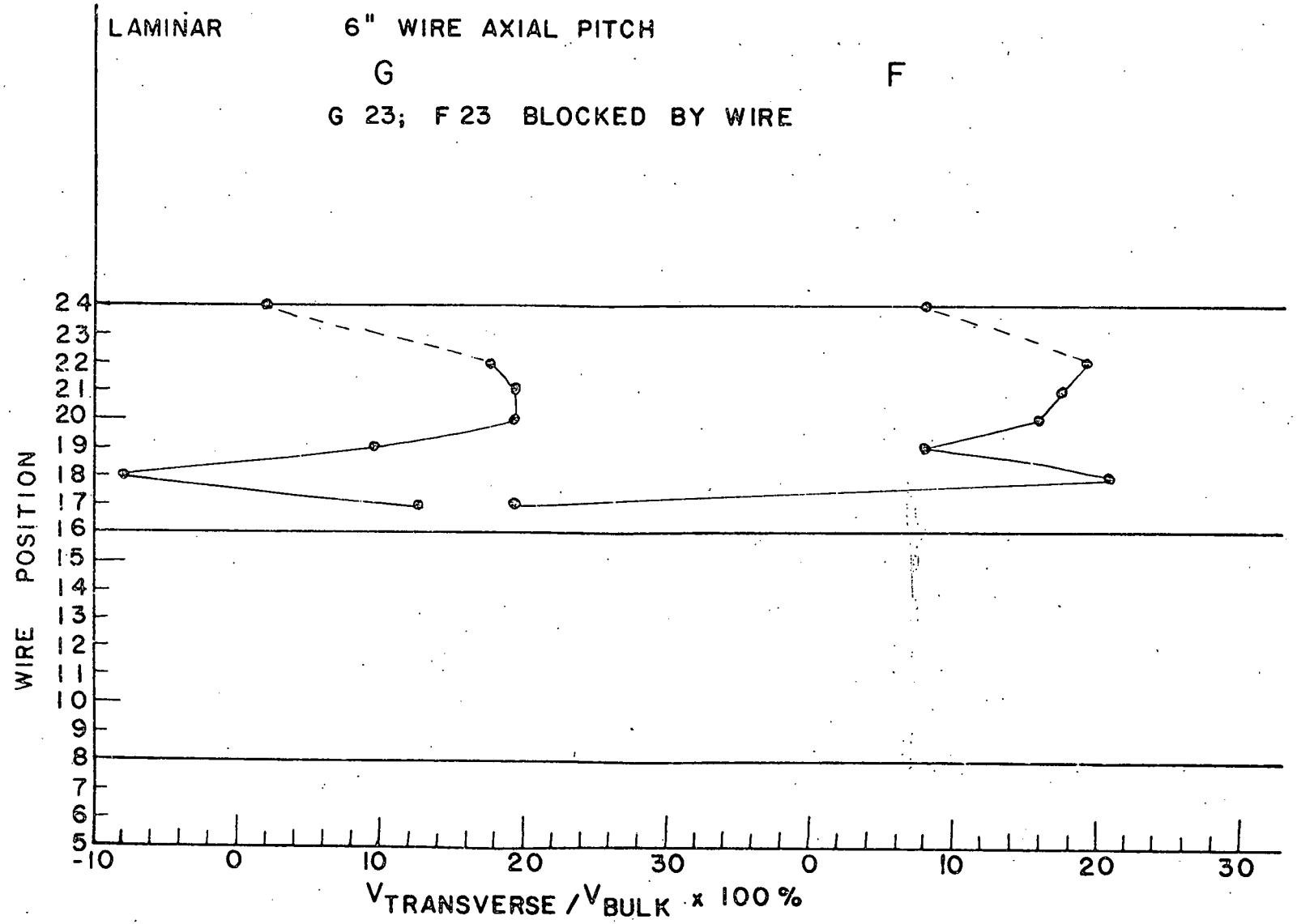
LAMINAR
6" WIRE AXIAL PITCH
G
F
G 23; F 23 BLOCKED BY WIRE
WIRE POSITION
24
23
22
21
20
19
18
17
16
15
14
13
12
11
10
9
8
7
6
5
-10
0
10
20
30
0
10
20
30
V TRANSVERSE / V BULK x 100 %

FIGURE 4.29

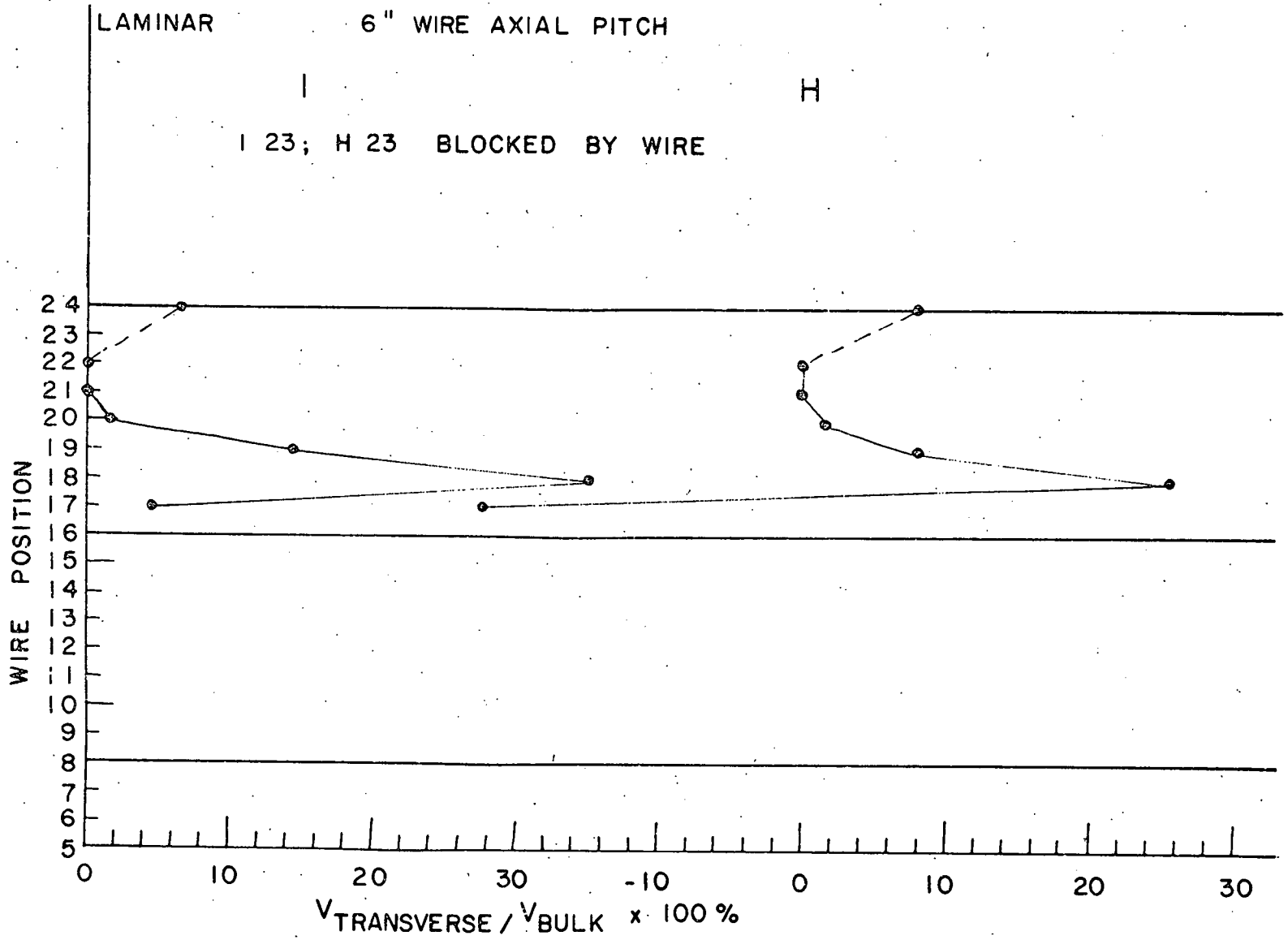
LAMINAR
6" WIRE AXIAL PITCH
I
H
I 23; H 23 BLOCKED BY WIRE
WIRE POSITION
24
23
22
21
20
19
18
17
16
15
14
13
12
11
10
9
8
7
6
5
0
10
20
30
-10
0
10
20
30
V TRANSVERSE / V BULK x 100 %

FIGURE 4.30

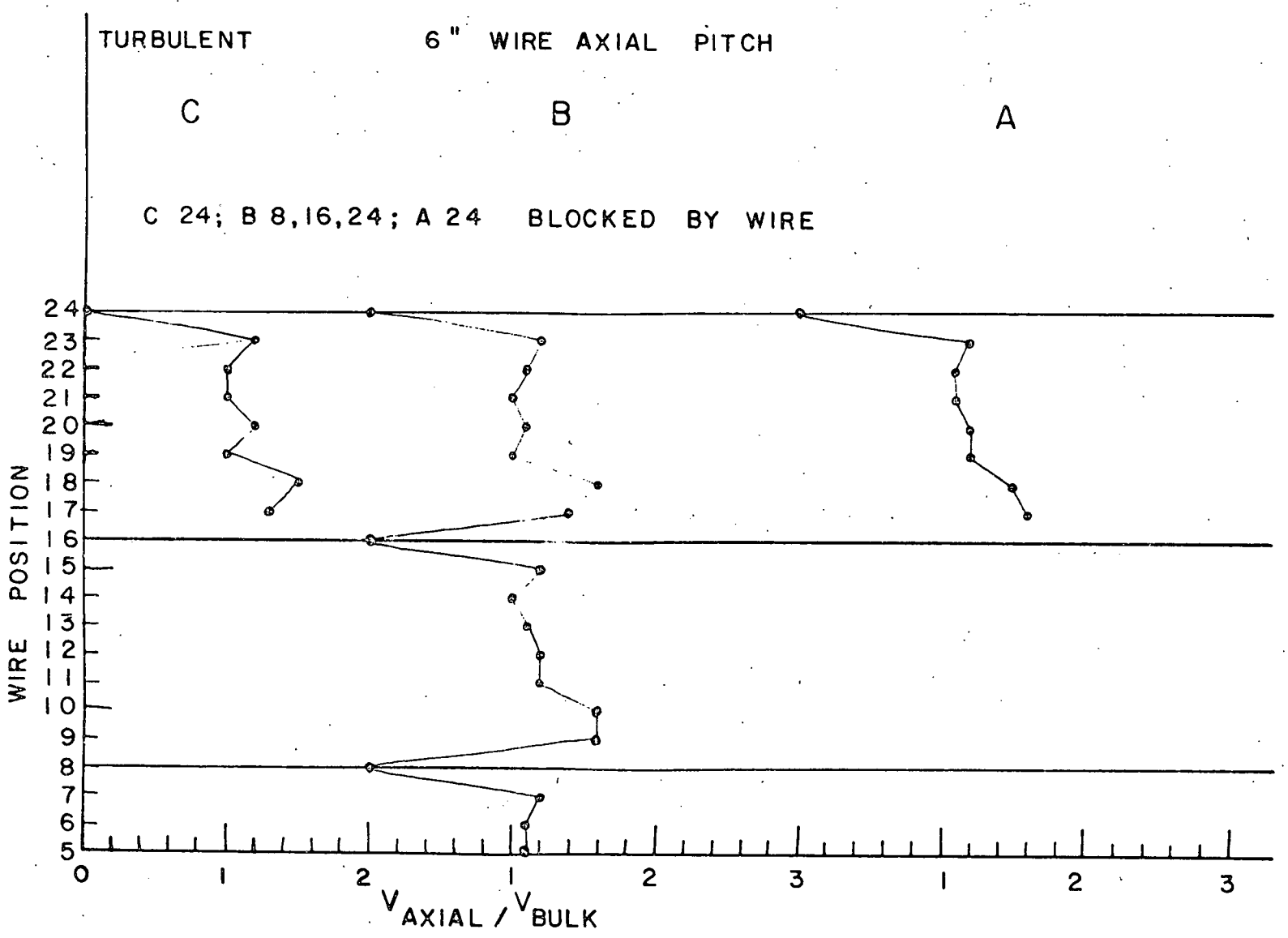
TURBULENT
6" WIRE AXIAL PITCH
C
B
A
C 24; B 8,16,24; A 24 BLOCKED BY WIRE
WIRE POSITION
24
23
22
21
20
19
18
17
16
15
14
13
12
11
10
9
8
7
6
5
0
1
2
1
2
3
1
2
3
V AXIAL / V BULK

FIGURE 4.31

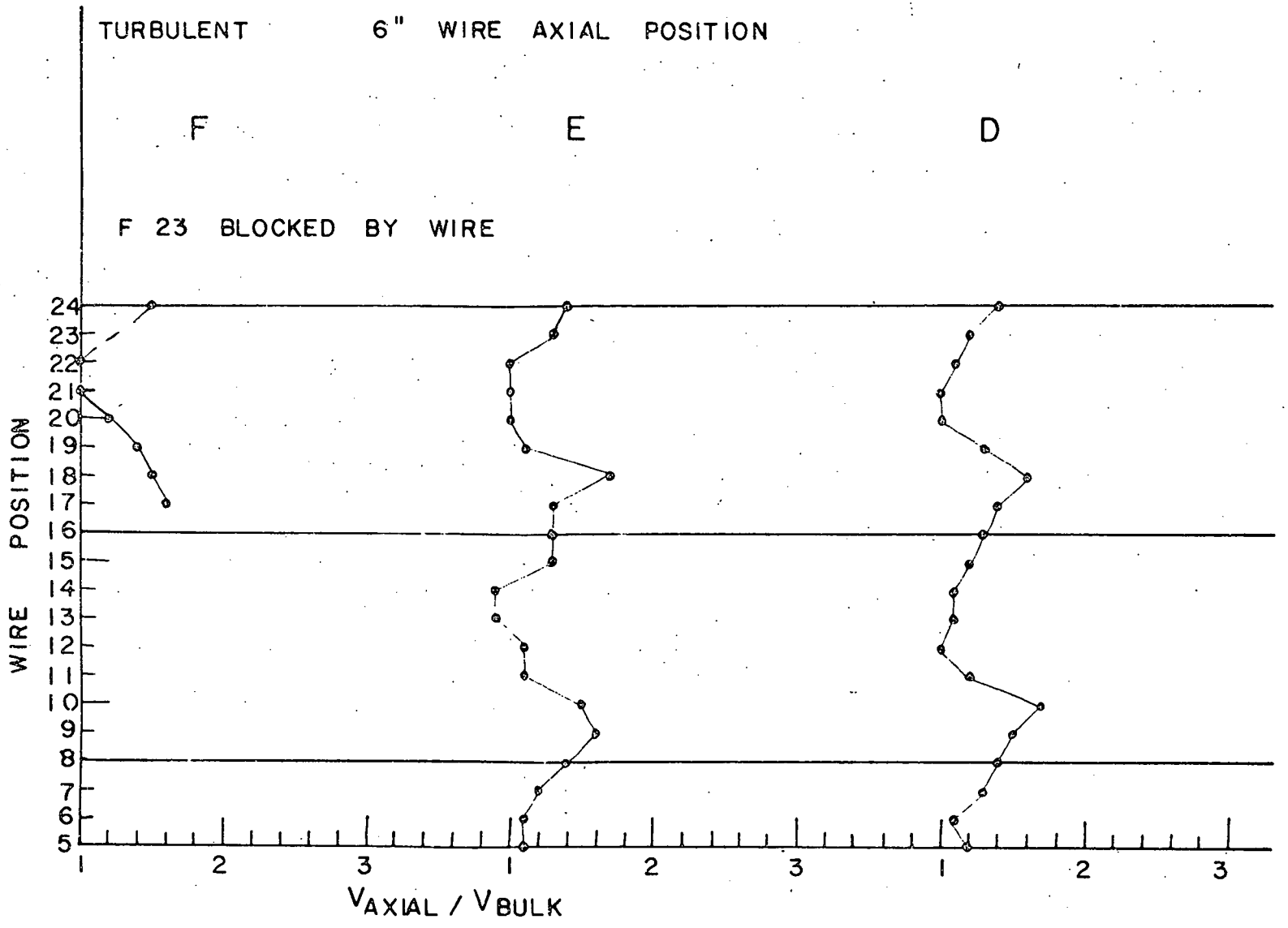
TURBULENT
6" WIRE AXIAL POSITION
F
E
D
F 23 BLOCKED BY WIRE
WIRE POSITION
24
23
22
21
20
19
18
17
16
15
14
13
12
11
10
9
8
7
6
5
1
2
3
1
2
3
1
2
3
VAXIAL / VBULK

FIGURE 4.32

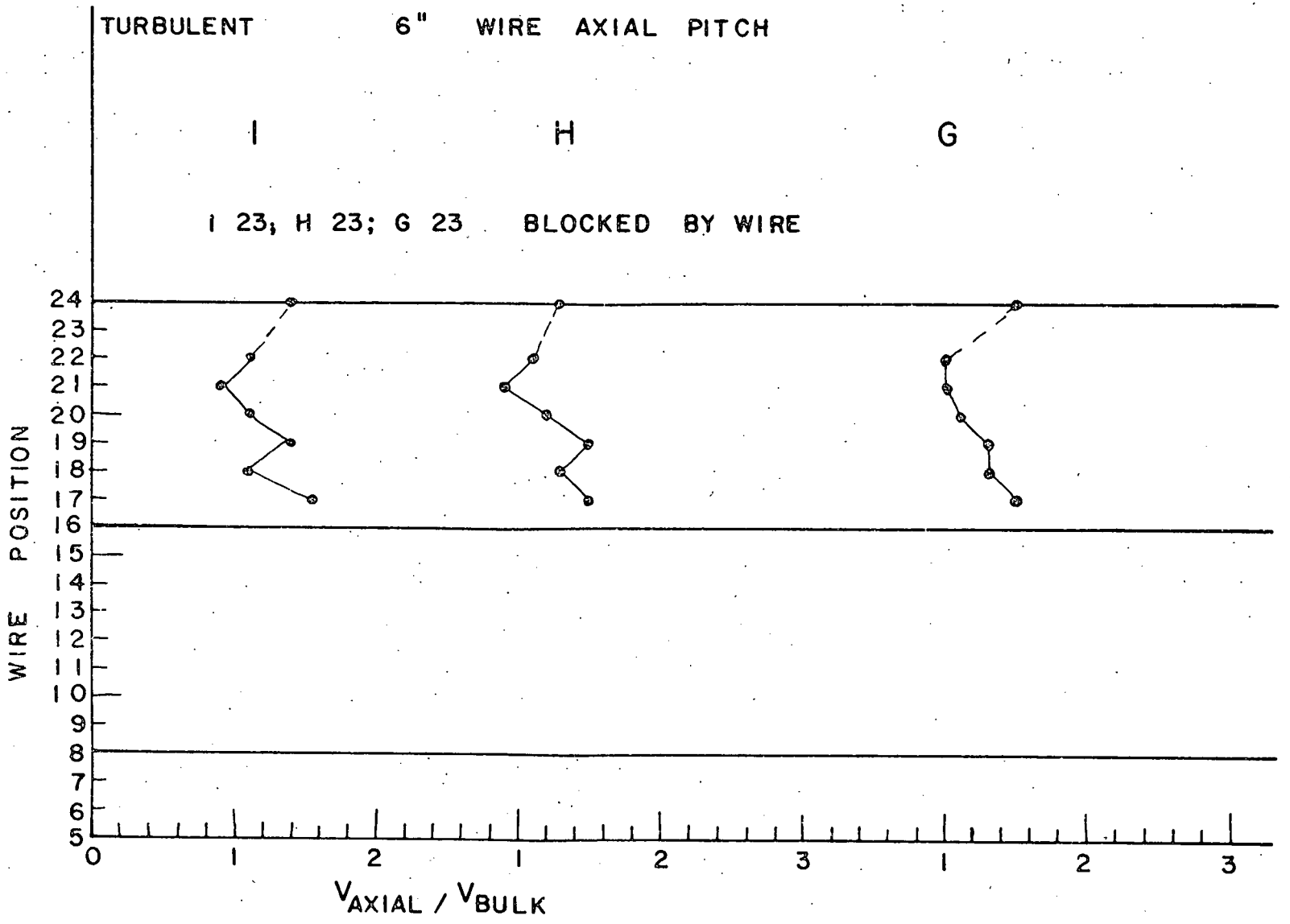
TURBULENT 6" WIRE AXIAL PITCH
I
H
G
I 23; H 23; G 23 BLOCKED BY WIRE
WIRE POSITION
24
23
22
21
20
19
18
17
16
15
14
13
12
11
10
9
8
7
6
5
0
1
2
1
2
3
1
2
3
VAXIAL / VBULK

FIGURE 4.33

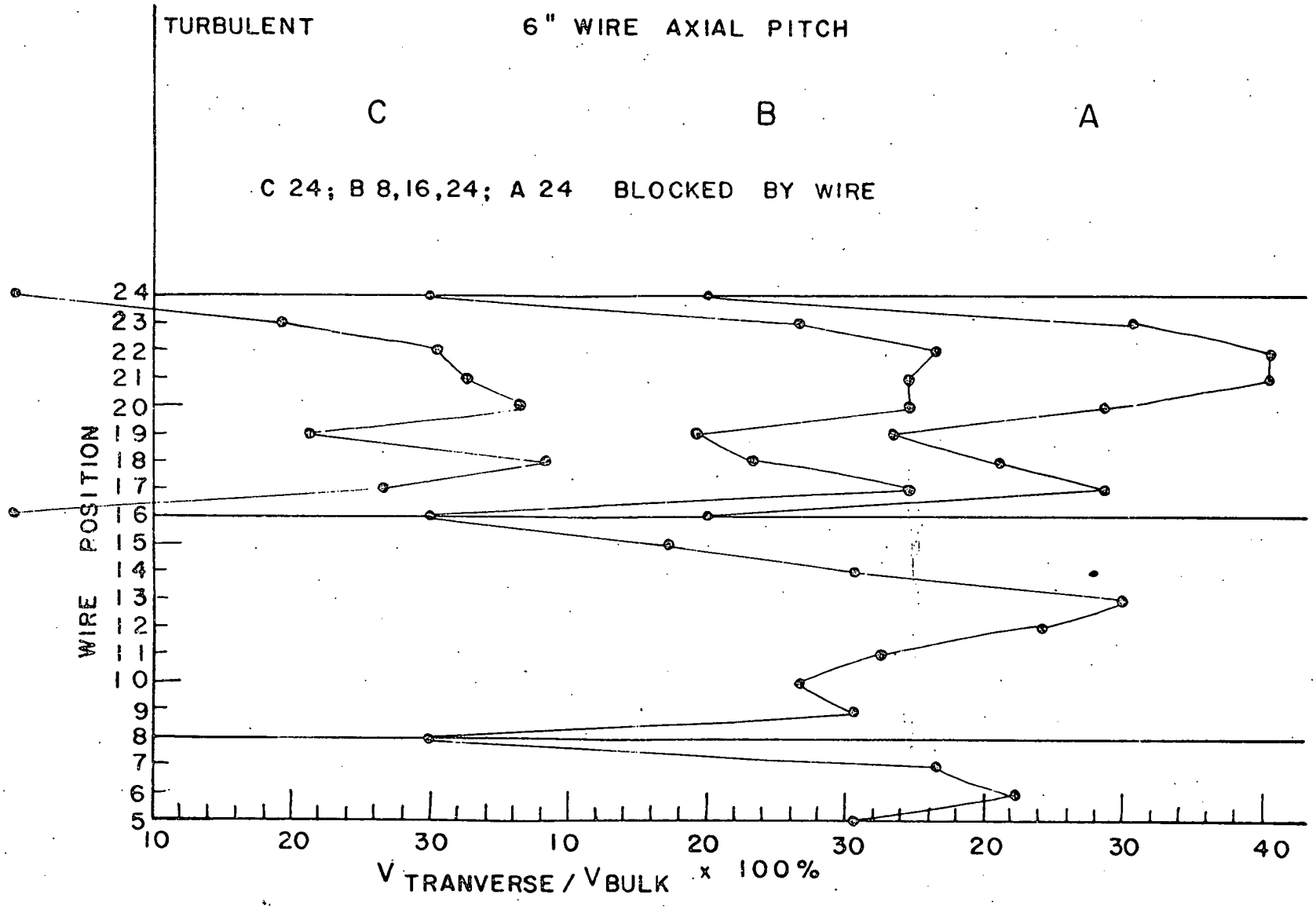
TURBULENT
6" WIRE AXIAL PITCH
C
B
A
C 24; B 8,16,24; A 24 BLOCKED BY WIRE
WIRE POSITION
24
23
22
21
20
19
18
17
16
15
14
13
12
11
10
9
8
7
6
5
10
20
30
10
20
30
20
30
40
V TRANVERSE / V BULK x 100%

FIGURE 4.34

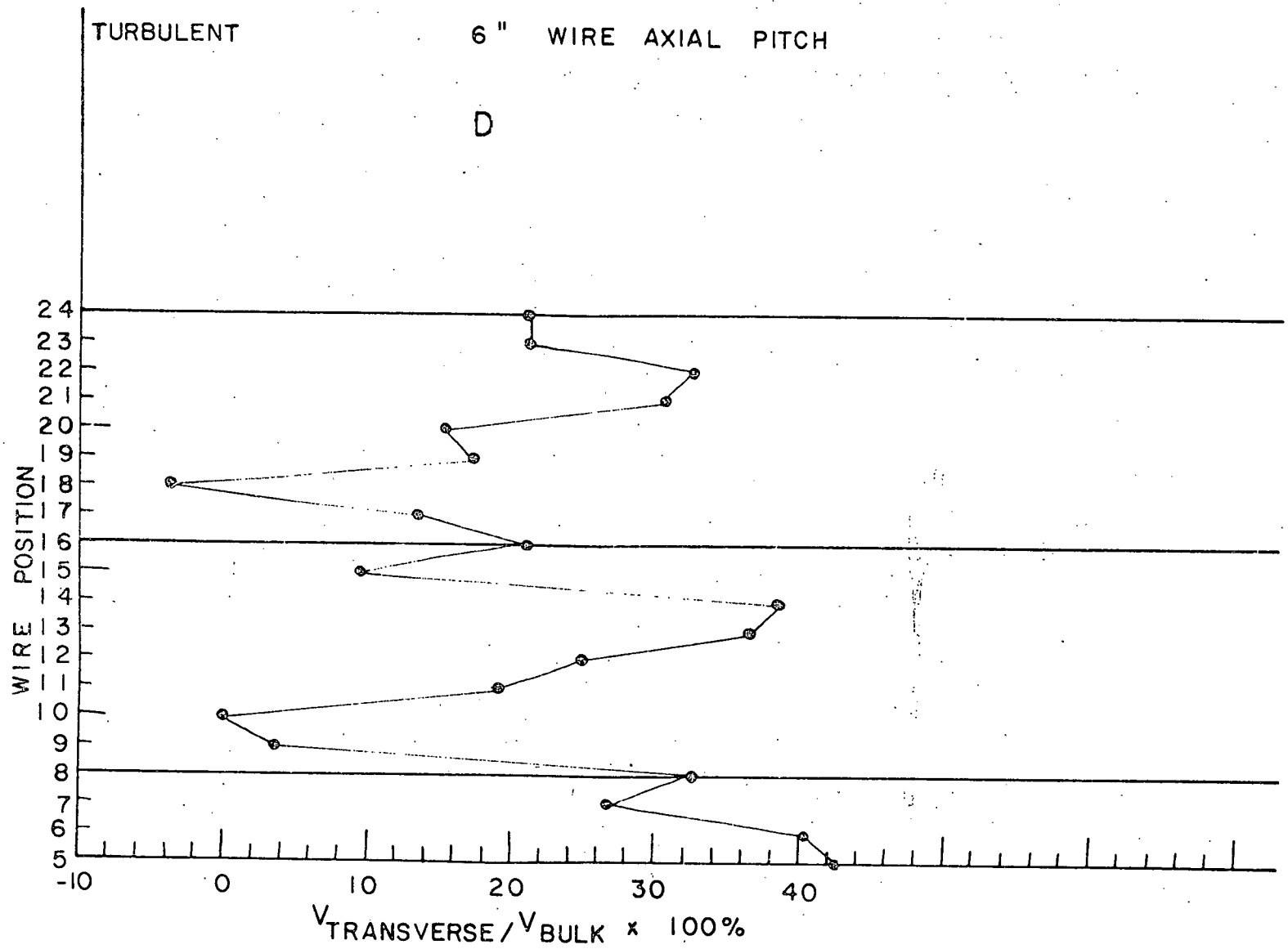
TURBULENT
6" WIRE AXIAL PITCH
D
WIRE POSITION
24
23
22
21
20
19
18
17
16
15
14
13
12
11
10
9
8
7
6
5
-10
0
10
20
30
40
$V_{TRANSVERSE}/V_{BULK} \times 100\%$

FIGURE 4.35

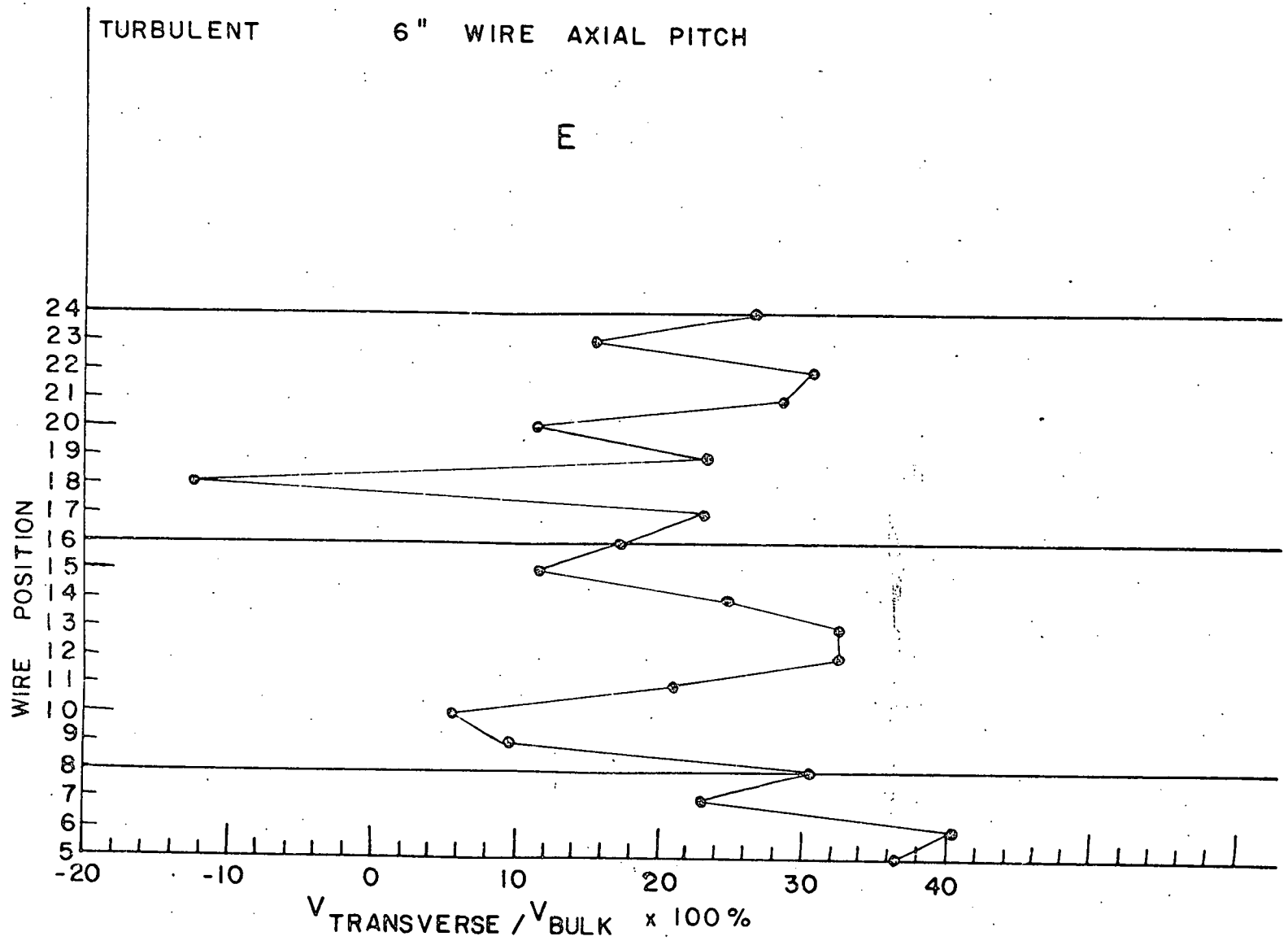
TURBULENT
6" WIRE AXIAL PITCH
E
WIRE POSITION
24
23
22
21
20
19
18
17
16
15
14
13
12
11
10
9
8
7
6
5
-20
-10
0
10
20
30
40
V TRANSVERSE / V BULK x 100 %

FIGURE 4.36

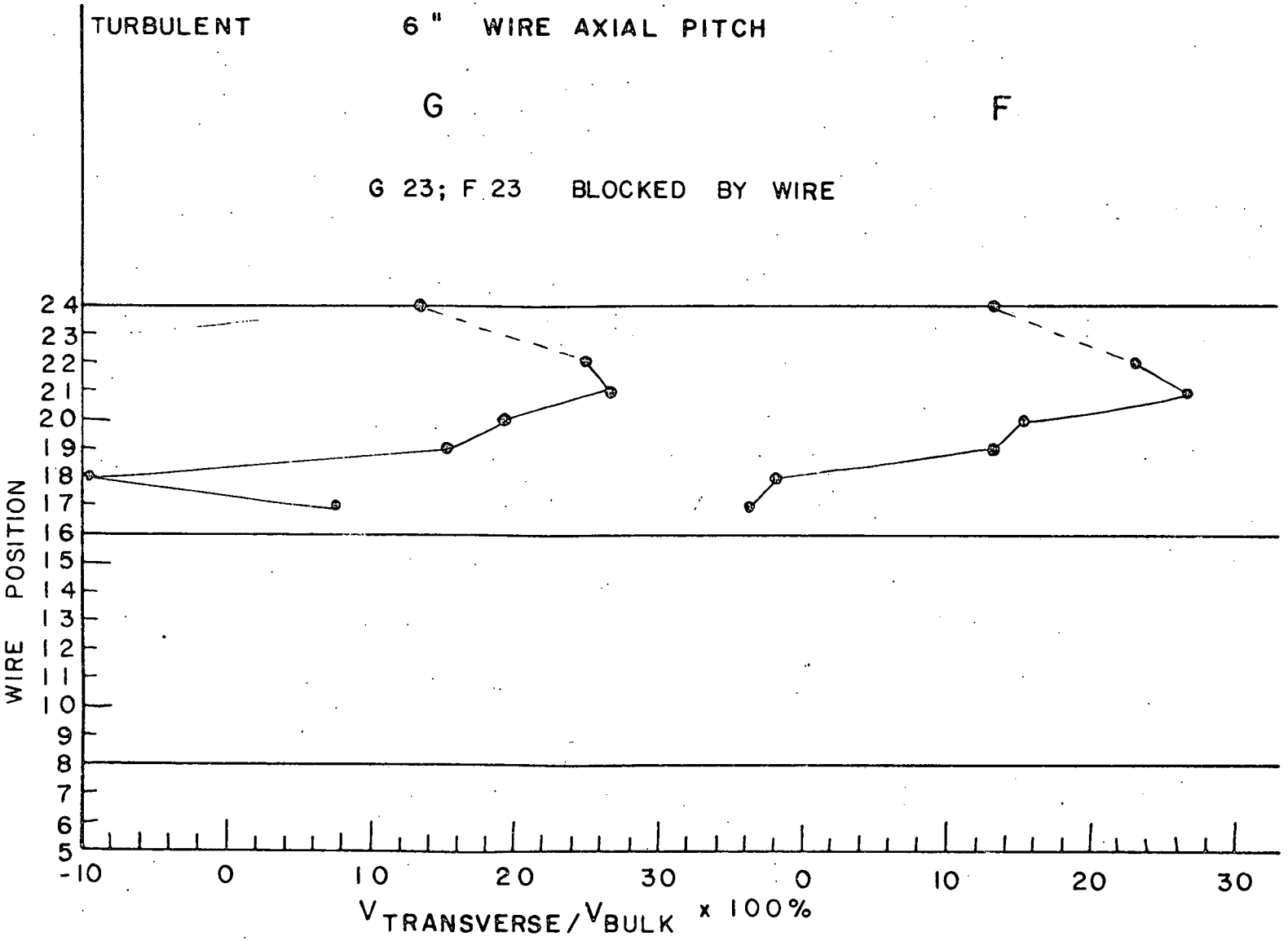
TURBULENT
6" WIRE AXIAL PITCH
G
F
G 23; F 23 BLOCKED BY WIRE
WIRE POSITION
24
23
22
21
20
19
18
17
16
15
14
13
12
11
10
9
8
7
6
5
-10
0
10
20
30
0
10
20
30
V TRANSVERSE / V BULK x 100%

FIGURE 4.37

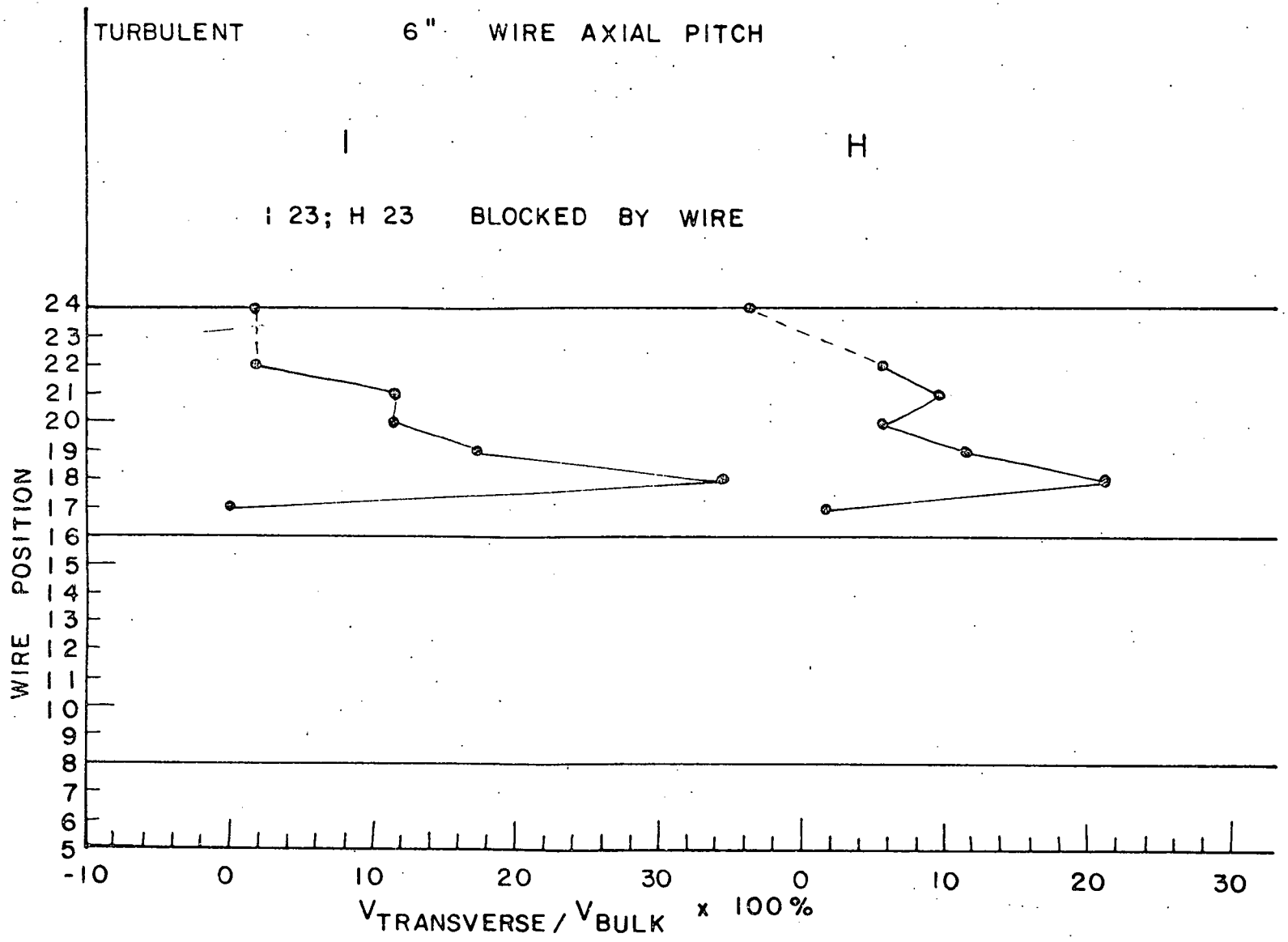
TURBULENT
6" WIRE AXIAL PITCH
I
H
I 23; H 23 BLOCKED BY WIRE
WIRE POSITION
24
23
22
21
20
19
18
17
16
15
14
13
12
11
10
9
8
7
6
5
-10
0
10
20
30
0
10
20
30
V TRANSVERSE / V BULK x 100%

FIGURE 4.38

OPERATING CONDITIONS

DATE: 6/11/74

FLOW RATE: 15 % S

REYNOLDS NUMBER: 640

T: 70 ° F

LASER POWER: 50 mWatts

FREQUENCY: 150 K

GEOMETRY

WIRE AXIAL PITCH: 12"

PLANE 10, 3 O'CLOCK

RESULT:

$$\frac{\bar{V}_{AXIAL\ sc}}{\bar{V}_{BUNDLE}} = 1.25$$

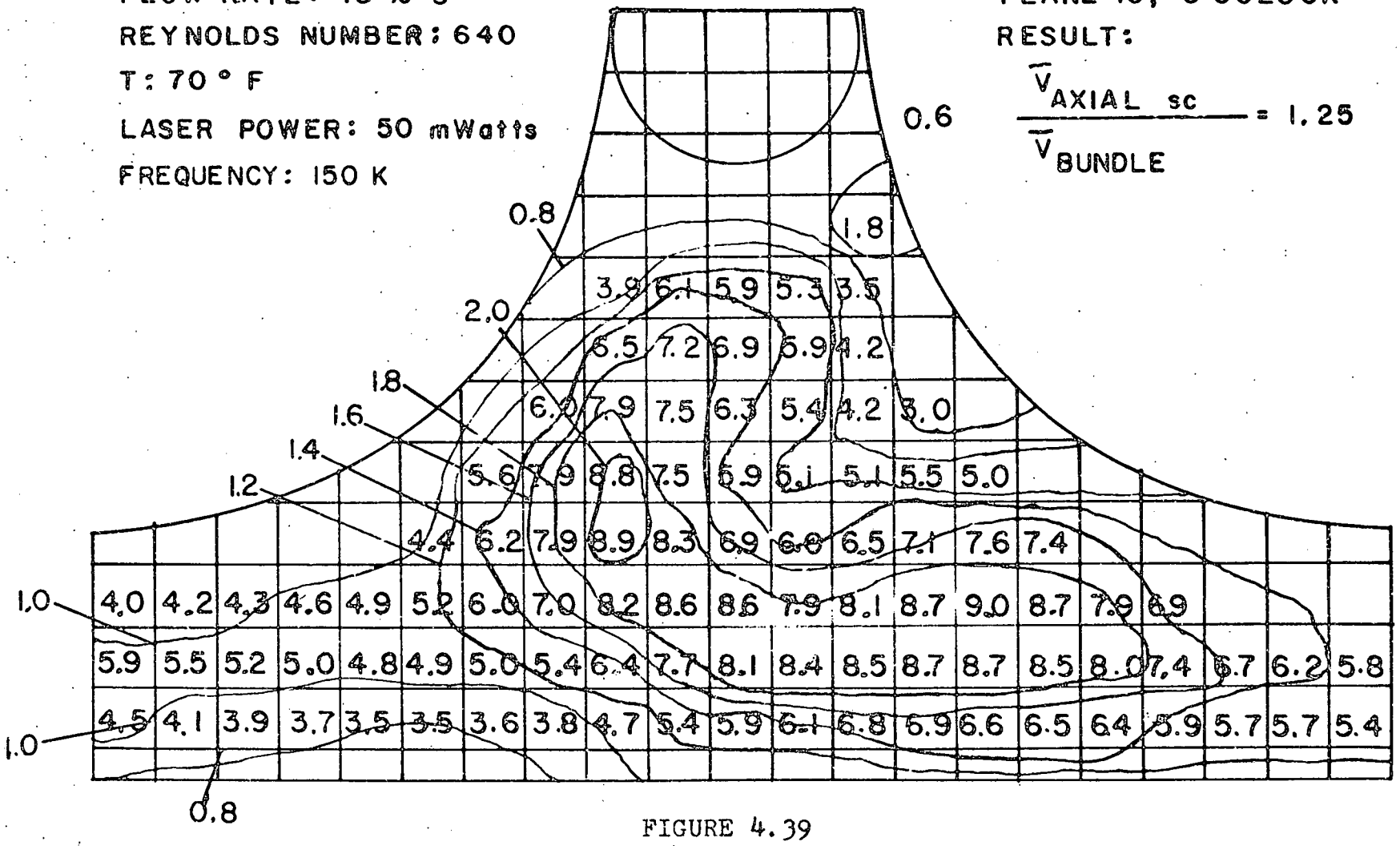

FIGURE 4.39

OPERATING CONDITIONS

DATE : 6/10/74

FLOW RATE: 15 % S

REYNOLDS NUMBER: 640

T: 70° F

LASER POWER: 50 mWatts

FREQUENCY: 150 K

GEOMETRY

WIRE AXIAL PITCH: 12"

PLANE 11, 1:30 O'CLOCK

RESULT:

$$\frac{\overline{V}_{AXIAL\ sc}}{\overline{V}_{BUNDLE}} = 1.26$$

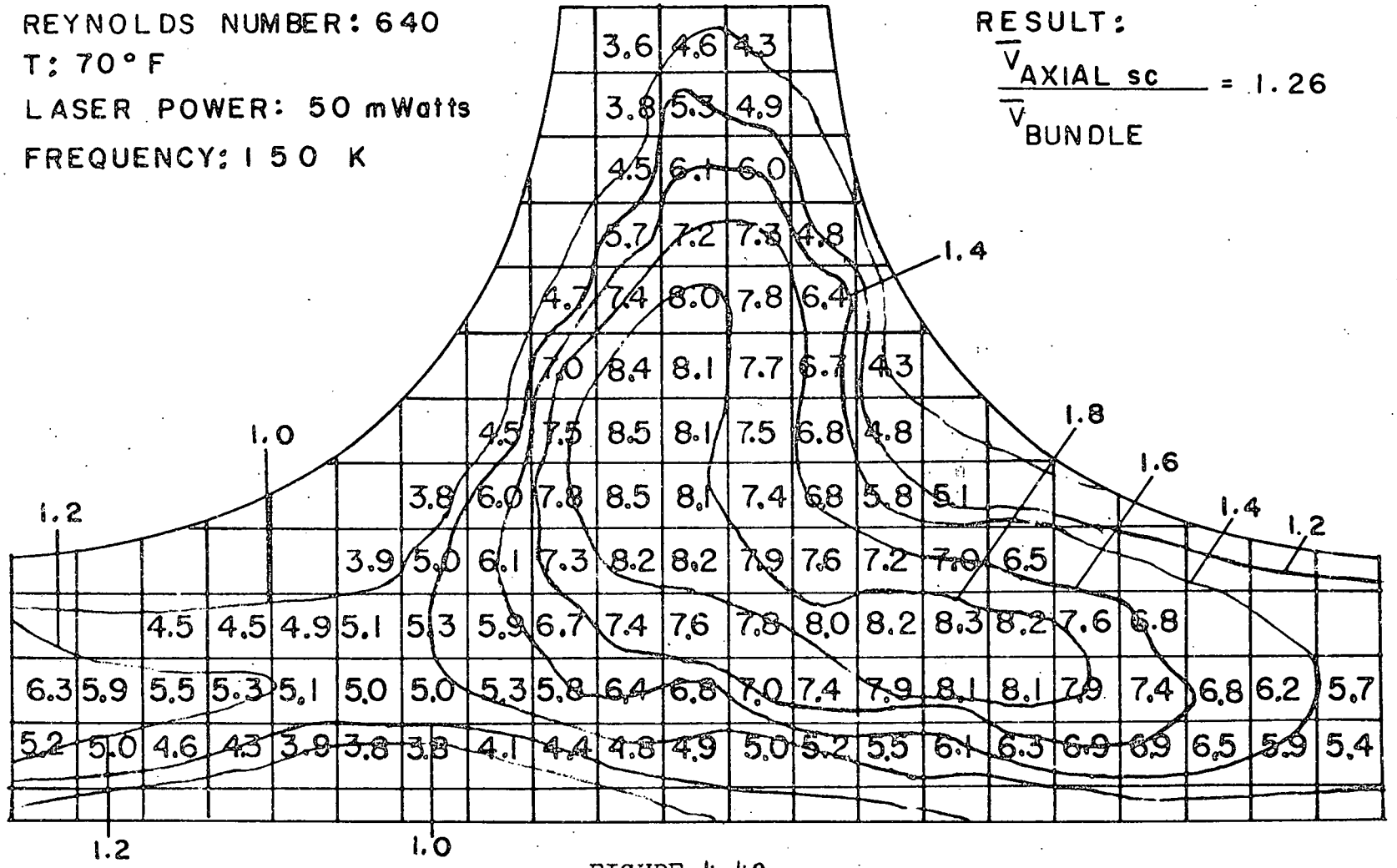

FIGURE 4.40

OPERATING CONDITIONS

DATE: 6/10/74
FLOW RATE: 15 % S
REYNOLDS NUMBER: 640
T: 70° F
LASER POWER: 50 mWatts
FREQUENCY: 150 K

GEOMETRY

WIRE AXIAL PITCH: 12 "
PLANE 12, 12 O'CLOCK
RESULT:

$$\frac{\overline{V}_{AXIAL\ SC}}{\overline{V}_{BUNDLE}} = 1.18$$

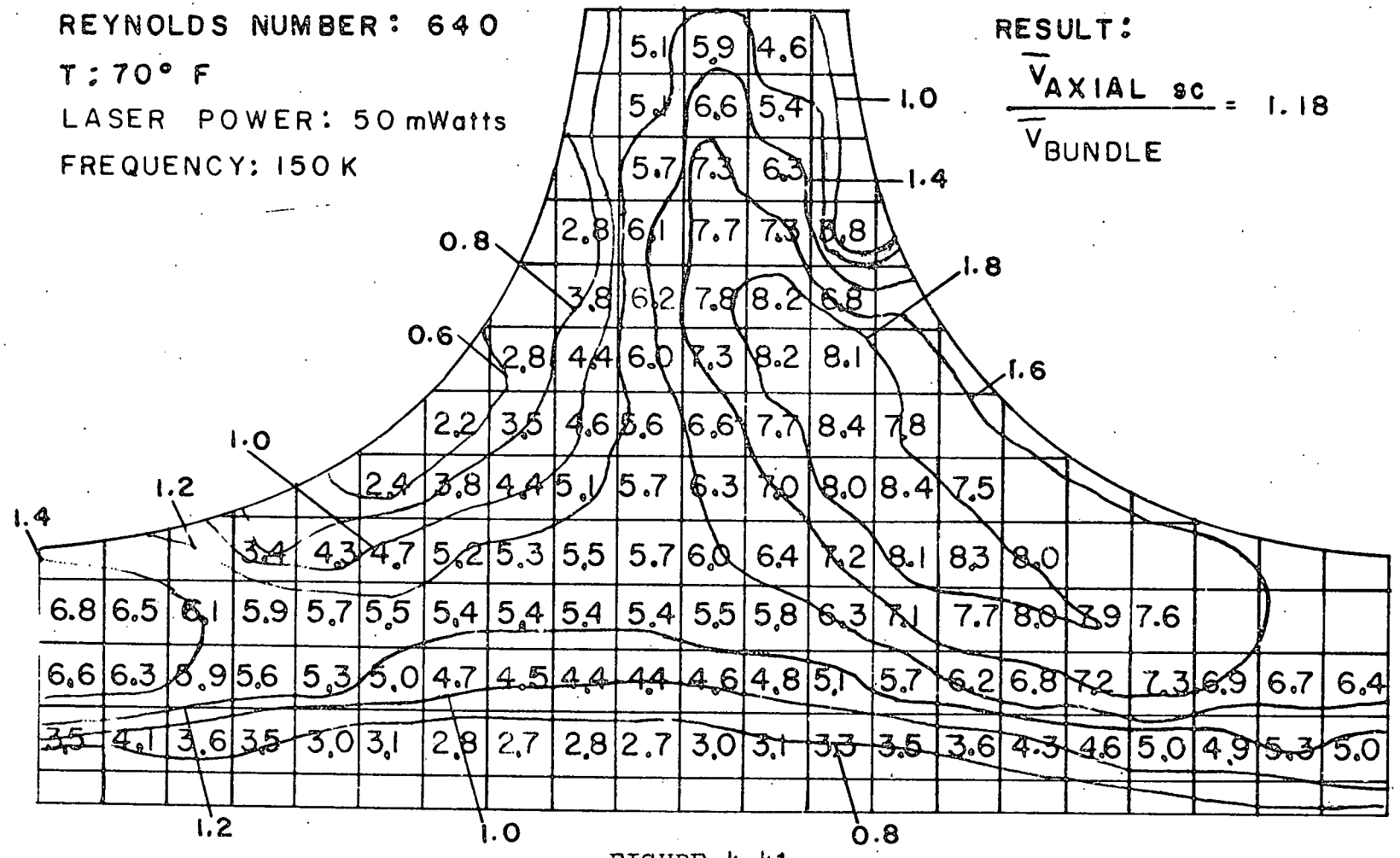

FIGURE 4.41

OPERATING CONDITIONS

DATE: 6/10/74
FLOW RATE: 15 % S
REYNOLDS NUMBER: 640
T: 70° F
LASER POWER: 50 mWatts
FREQUENCY: 150K

GEOMETRY

WIRE AXIAL PITCH: 12"
PLANE 13, 10:30 O'CLOCK
RESULT:

$$\frac{\bar{V}_{AXIAL\ sc}}{\bar{V}_{BUNDLE}} = 1.11$$

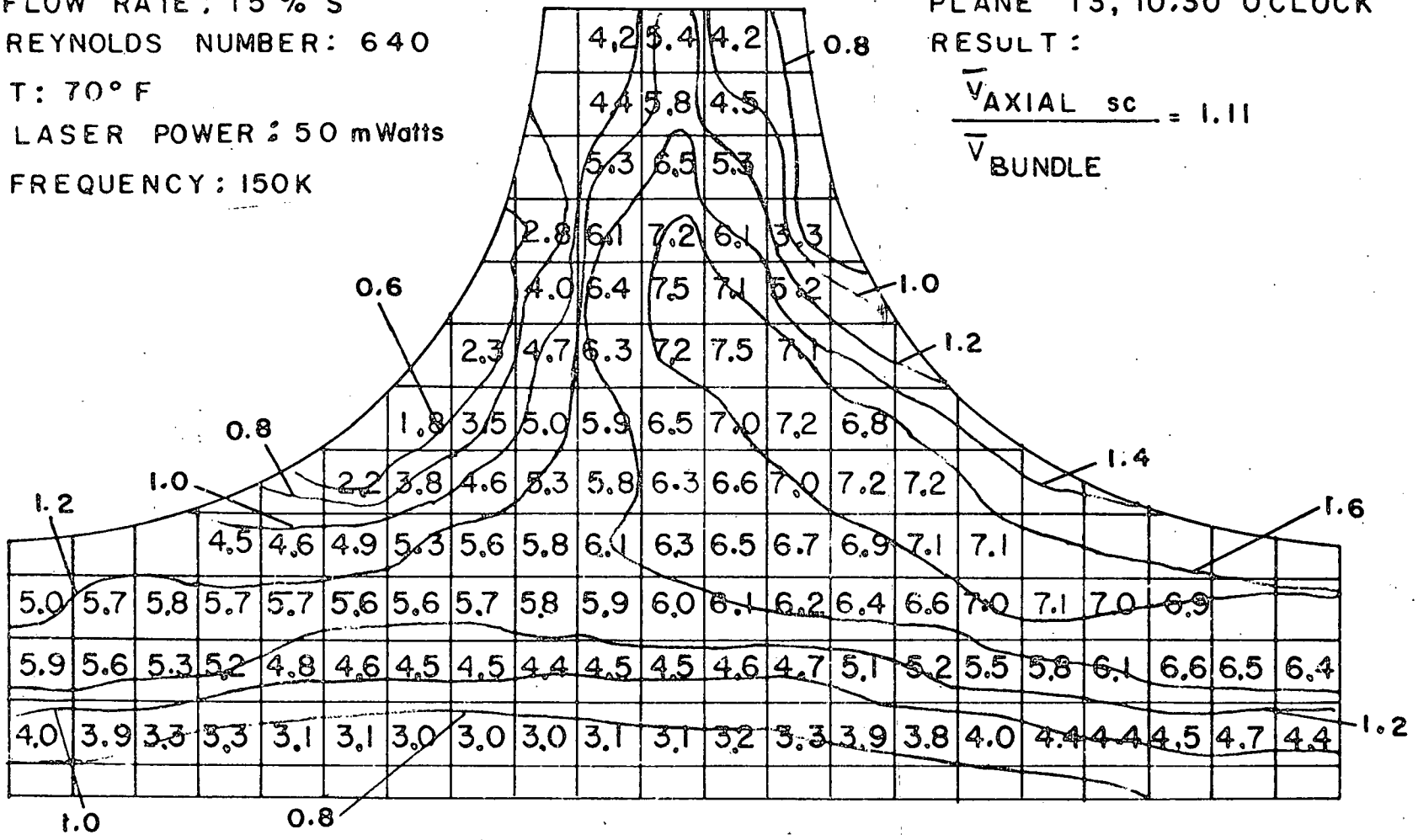

FIGURE 4.42

OPERATING CONDITIONS

DATE: 6/11/74

FLOW RATE: 15% S

REYNOLDS NUMBER: 640

T: 70° F

LASER POWER: 50 mWatts

FREQUENCY: 150 K

GEOMETRY

WIRE AXIAL PITCH: 12"

PLANE 14, 9 O'CLOCK

RESULT:

$$\frac{\overline{V}_{AXIAL\ sc}}{\overline{V}_{BUNDLE}} = 1.13$$

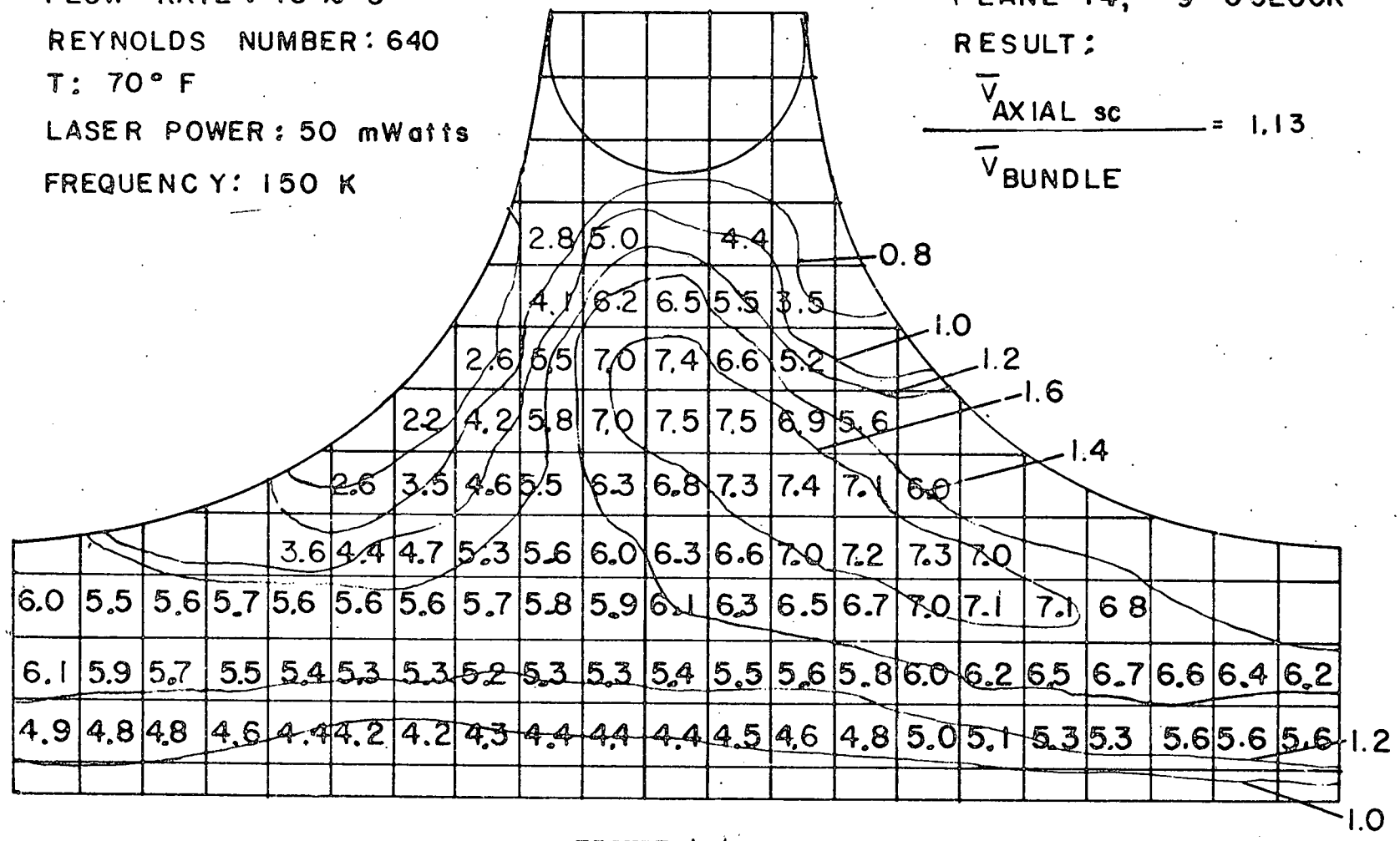

FIGURE 4.43

OPERATING CONDITIONS

DATE: 6/9/74
FLOW RATE: 15% S
REYNOLDS NUMBER: 640
T: 70° F
LASER POWER: 55 mWatts
FREQUENCY: 150 K

GEOMETRY

WIRE AXIAL PITCH: 12"
PLANE 15, 7:30 O'CLOCK
RESULT

$$\frac{\bar{V}_{AXIAL\ sc}}{\bar{V}_{BUNDLE}} = 1.17$$

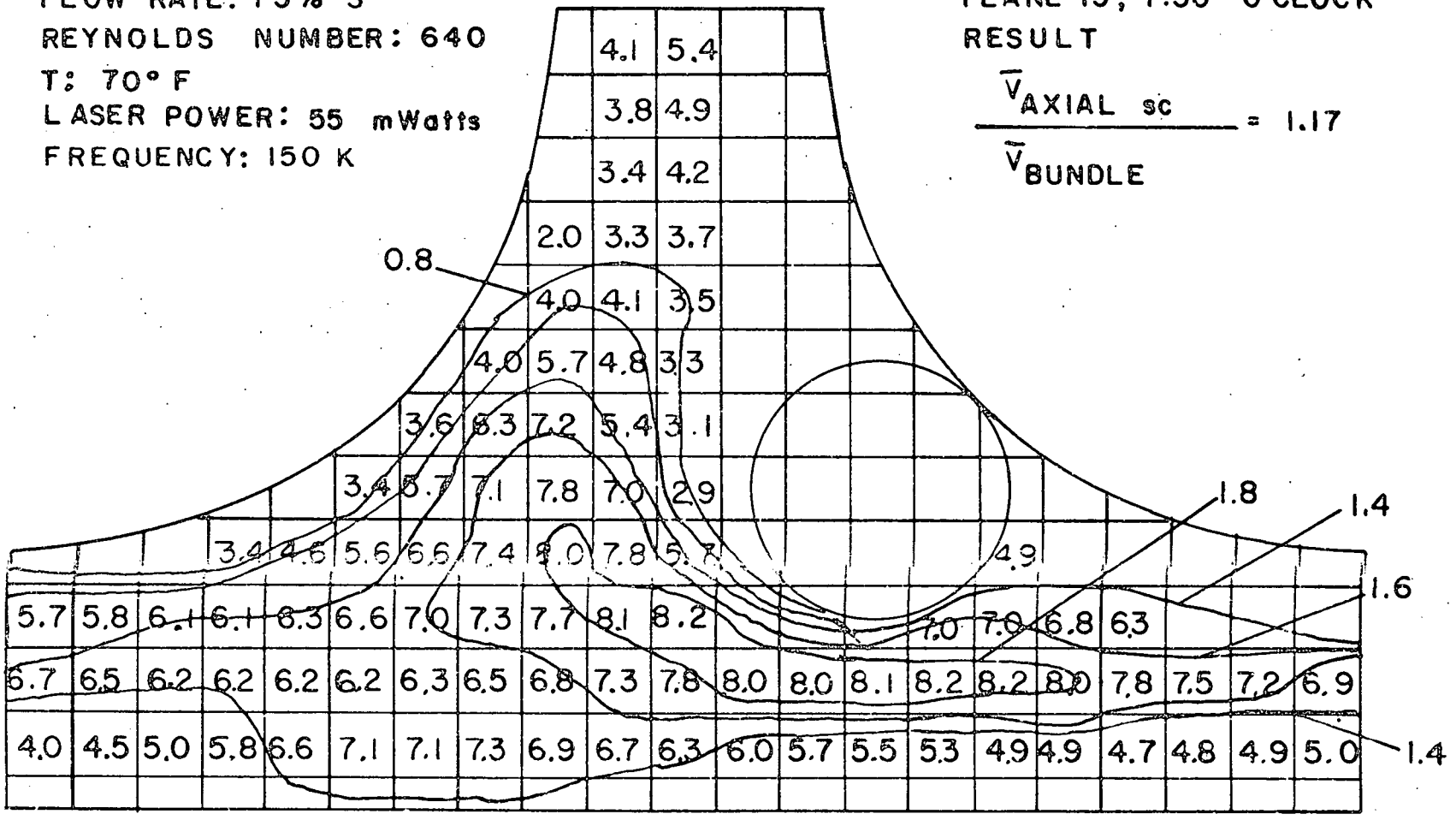

FIGURE 4.44

OPERATING CONDITIONS

DATE: 6/9/74
FLOW RATE: 15 % S
REYNOLDS NUMBER: 640
T: 70° F
LASER POWER: 55 mWatts
FREQUENCY: 150 K

GEOMETRY

WIRE AXIAL PITCH: 12"
PLANE 16, 6 O'CLOCK
RESULT:

$$\frac{\bar{V}_{AXIAL\ sc}}{\bar{V}_{BUNDLE}} = 1.18$$

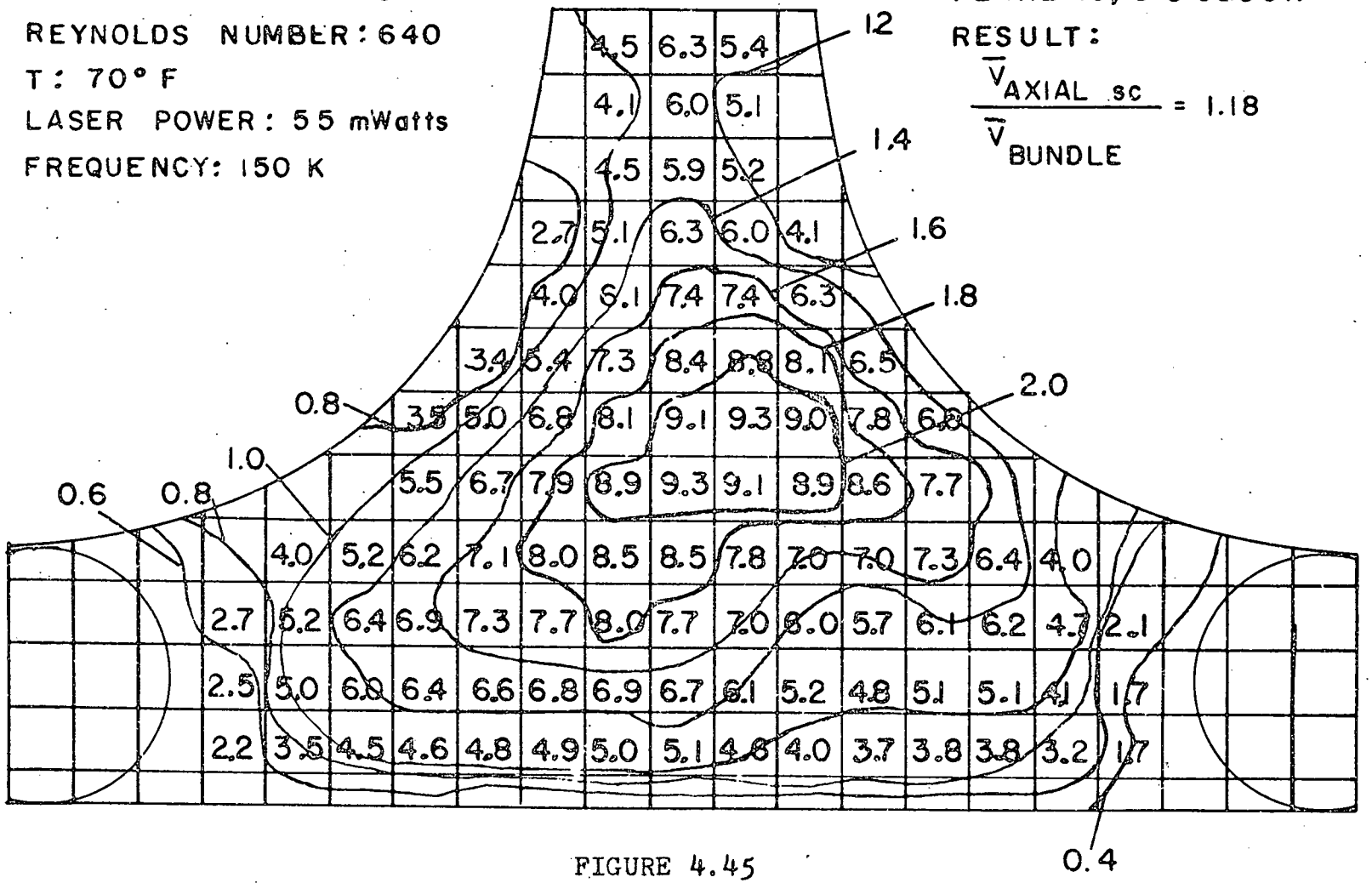

FIGURE 4.45

OPERATING CONDITIONS

DATE : 6/11/74
FLOW RATE: 15 % S
REYNOLDS NUMBER: 640
T: 70 ° F
LASER POWER: 50 mWatts
FREQUENCY: 150 K

GEOMETRY

WIRE AXIAL PITCH: 12"
PLANE 17, 4:30 O'CLOCK
RESULT:

$$\frac{\overline{V}_{AXIAL\ sc}}{\overline{V}_{BUNDLE}} = 1.20$$

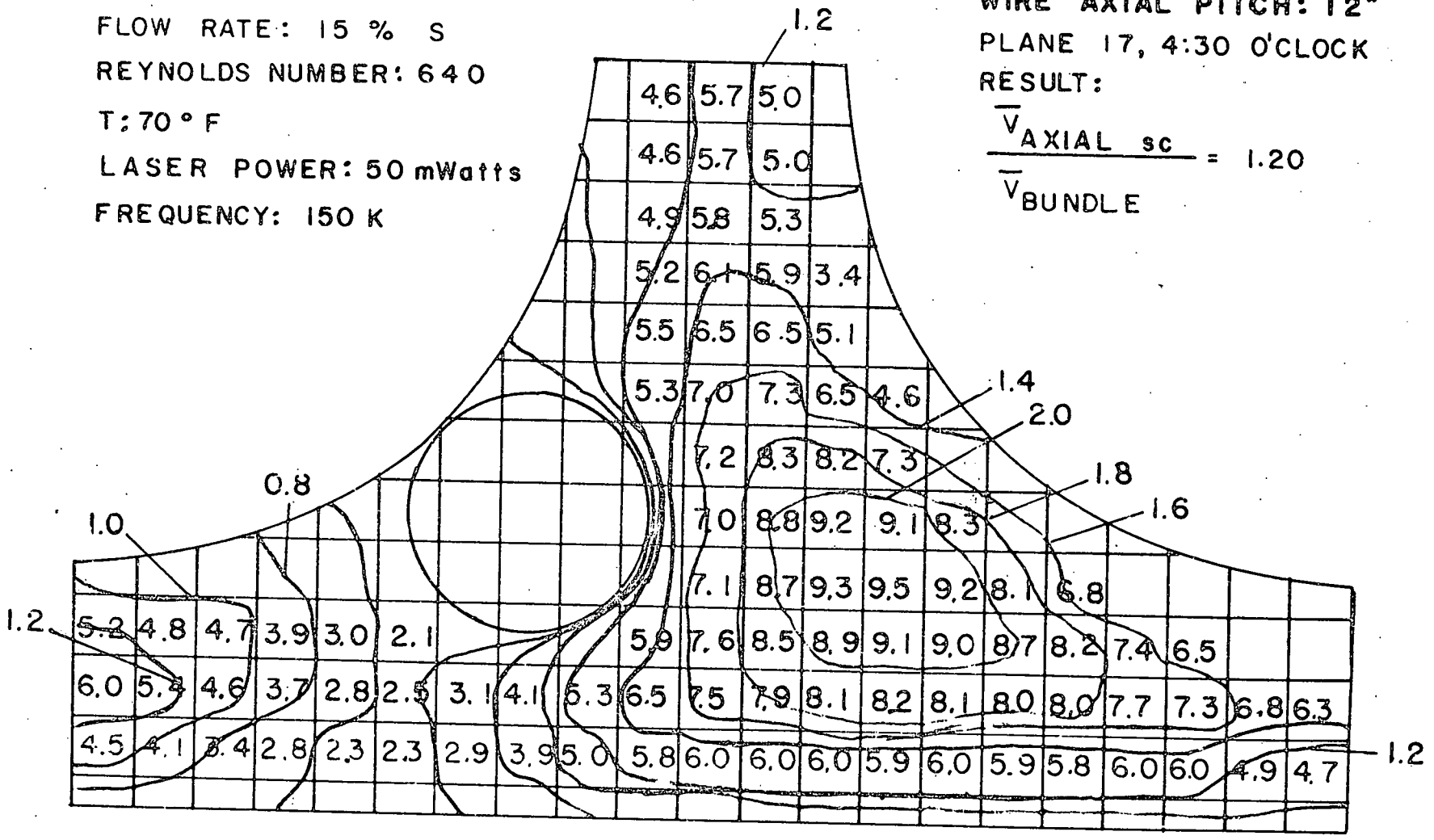

FIGURE 4.46

OPERATING CONDITIONS

DATE: 6/11/74
FLOW RATE: 65 % L
REYNOLDS NUMBER: 4500
T: 70° F
LASER POWER: 50 mWatts
FREQUENCY: 1.5 M

GEOMETRY

WIRE AXIAL PITCH: 12"
PLANE 10, 3 O'CLOCK
RESULT:

$$\frac{\bar{V}_{AXIAL\ sc}}{\bar{V}_{BUNDLE}} = 1.10$$

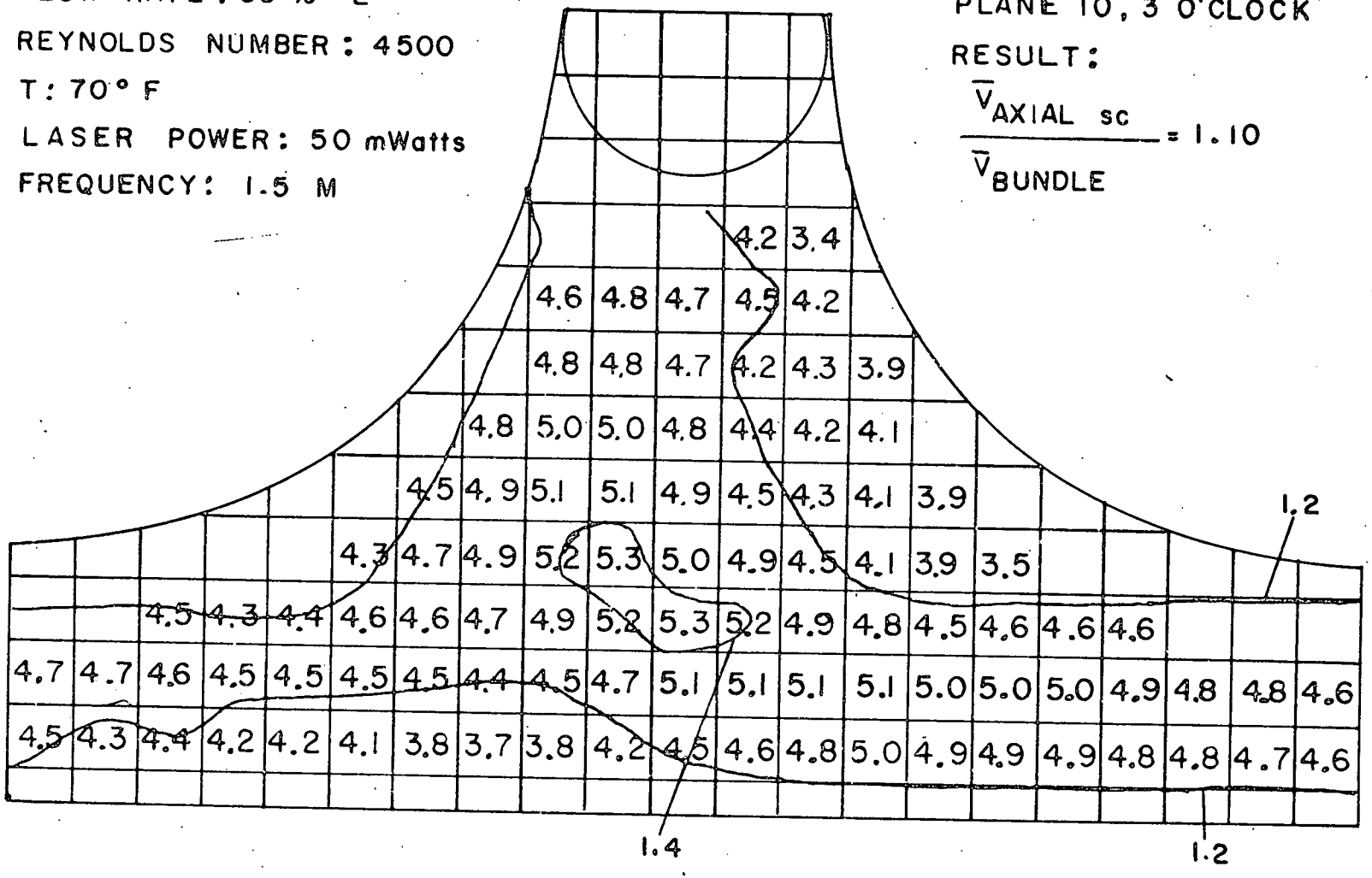

FIGURE 4.47

OPERATING CONDITIONS

DATE : 6/10/74
FLOW RATE : 65 % L
REYNOLDS NUMBER : 4500
T : 70 °F
LASER POWER : 50 mWdtts
FREQUENCY : 1.5 M

GEOMETRY

WIRE AXIAL PITCH : 12"
PLANE II , 1: 30 O'CLOCK
RESULT :

$$\frac{\overline{V}_{AXIAL\ sc}}{\overline{V}_{BUNDLE}} = 1.05$$

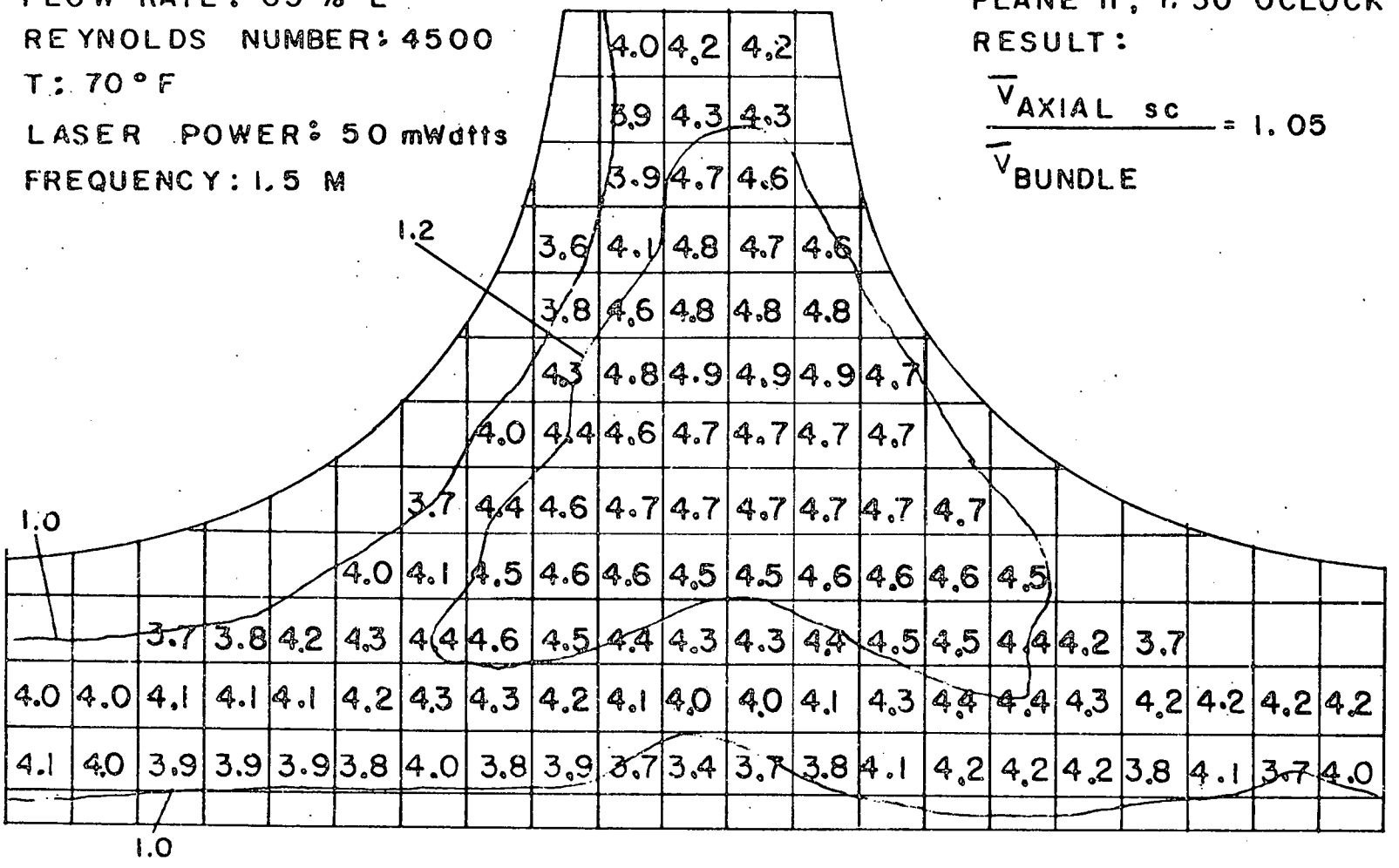

FIGURE 4.48

OPERATING CONDITIONS

DATE : 6/10/74
FLOW RATE : 65% L
REYNOLDS NUMBER : 4500
T : 70° F
LASER POWER : 50 mWatts
FREQUENCY : 1.5 M

GEOMETRY

WIRE AXIAL PITCH : 12"
PLANE 12, 12 O'CLOCK
RESULT :

$$\frac{\bar{V}_{AXIAL\ sc}}{\bar{V}_{BUNDLE}} = 1.02$$

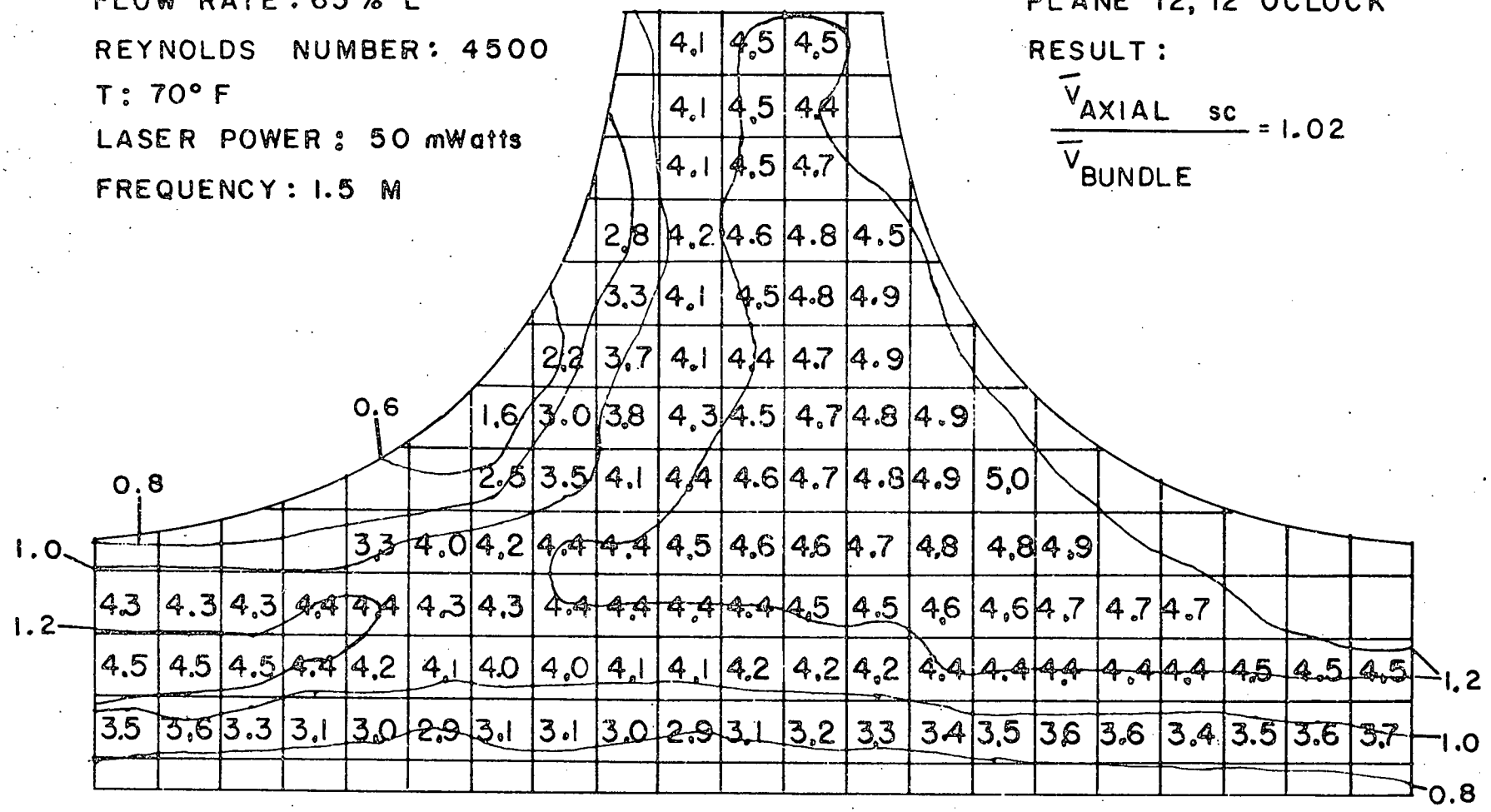

FIGURE 4.49

OPERATING CONDITIONS

DATE: 6/10/74
FLOW RATE : 65 % L
REYNOLDS NUMBER: 4500
T: 70° F
LASER POWER: 50 mWatts
FREQUENCY: 1.5 M

GEOMETRY

WIRE AXIAL PITCH: 12"
PLANE 13, 10:30 O'CLOCK
RESULT:

$$\frac{\bar{V}_{AXIAL\ sc}}{\bar{V}_{BUNDLE}} = 0.99$$

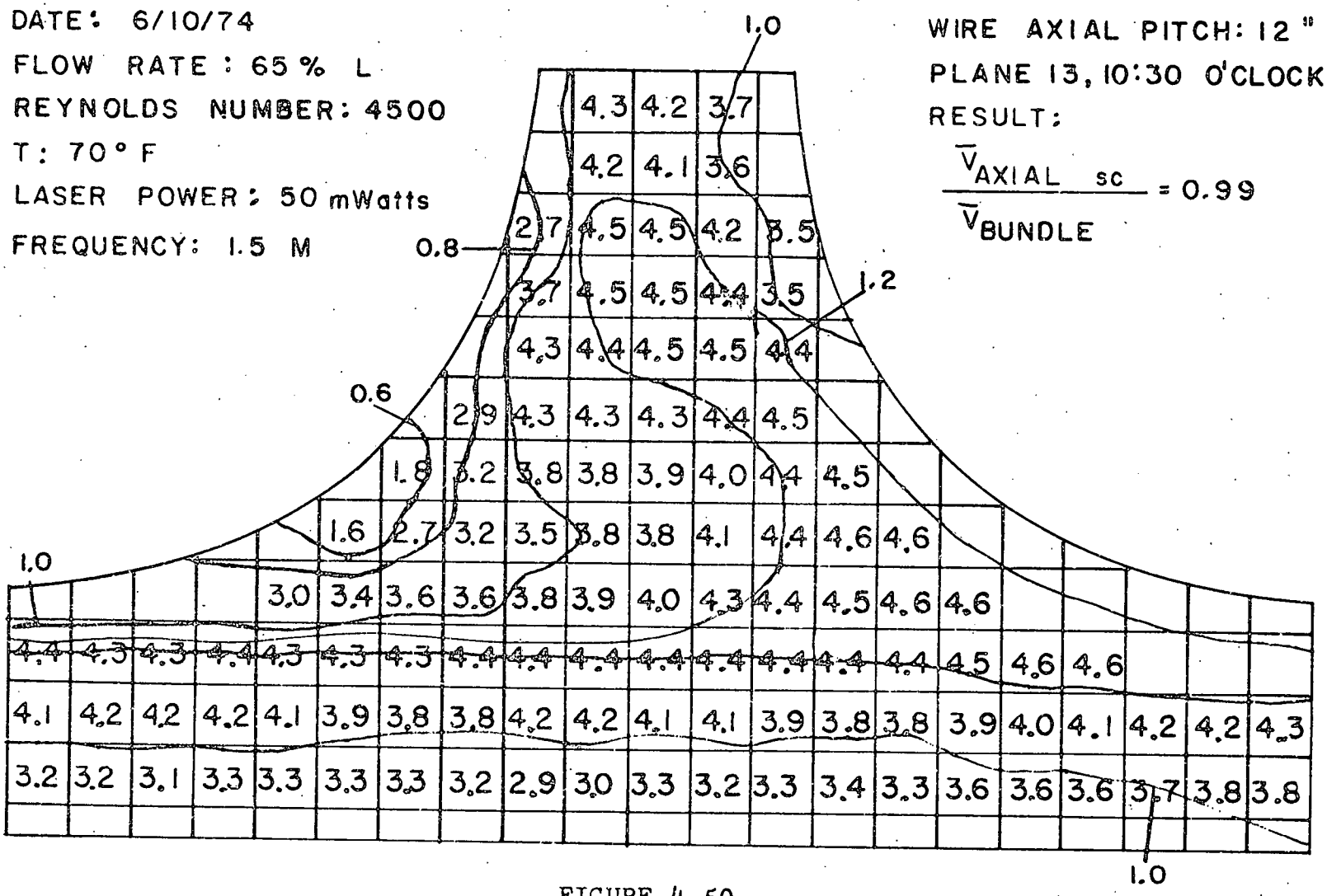

FIGURE 4.50

OPERATING CONDITIONS

DATE: 6/11/74

FLOW RATE: 65% L

REYNOLDS NUMBER: 4500

T: 70° F

LASER POWER: 50 mWatts

FREQUENCY: 1.5 M

GEOMETRY

WIRE AXIAL PITCH: 12"

PLANE 14, 9 O'CLOCK

RESULT:

$$\frac{\bar{V}_{AXIAL\ sc}}{\bar{V}_{BUNDLE}} = 0.97$$

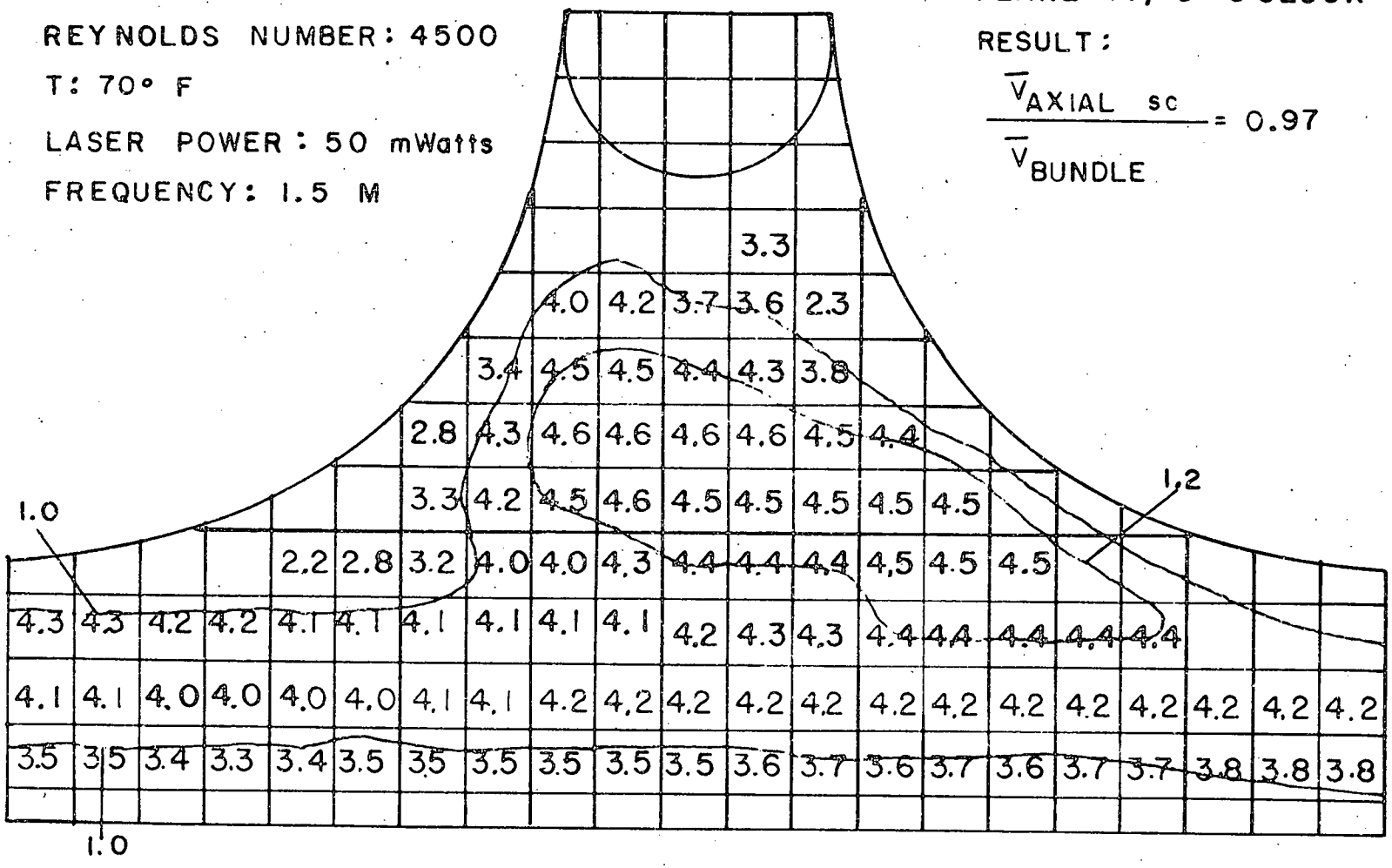

FIGURE 4.51

OPERATING CONDITIONS

DATE : 6/9/74

FLOW RATE : 65% L

REYNOLDS NUMBER: 4500

T: 70° F

LASER POWER : 55 mWatts

FREQUENCY: 1.5 M

GEOMETRY

WIRE AXIAL PITCH: 12"

PLANE 15, 7:30 O'CLOCK

RESULT:

$$\frac{\overline{V}_{AXIAL\ sc}}{\overline{V}_{BUNDLE}} = 1.02$$

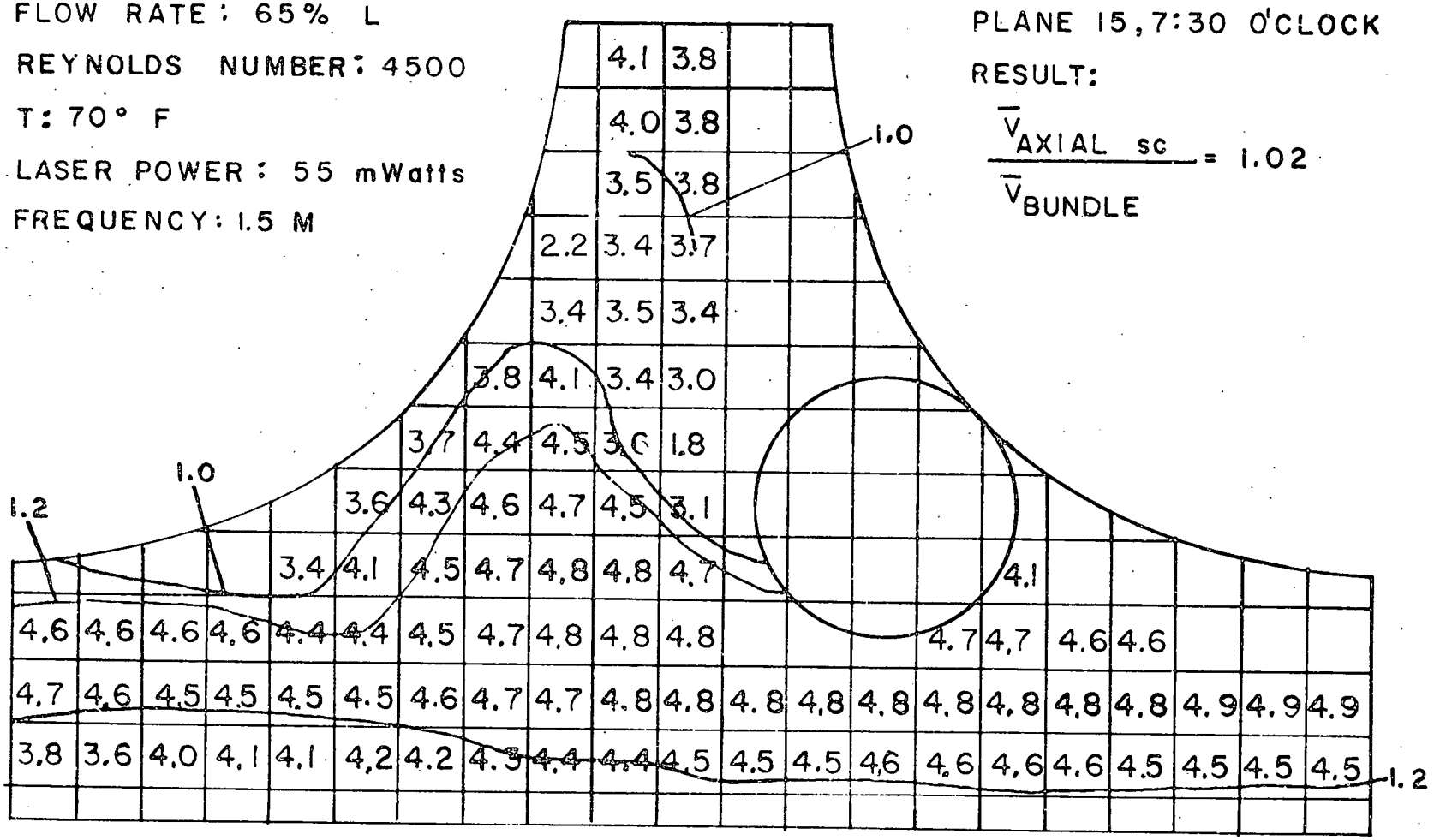

FIGURE 4.52

OPERATING CONDITIONS

DATE: 6/9/74
FLOW RATE: 65% L
REYNOLDS NUMBER: 4500
T: 70° F
LASER POWER: 55 mWatts
FREQUENCY: 1.5 M

GEOMETRY

WIRE AXIAL PITCH: 12"
PLANE 16, 6 O'CLOCK
RESULT:

$$\frac{\overline{V}_{AXIAL\ sc}}{\overline{V}_{BUNDLE}} = 1.07$$

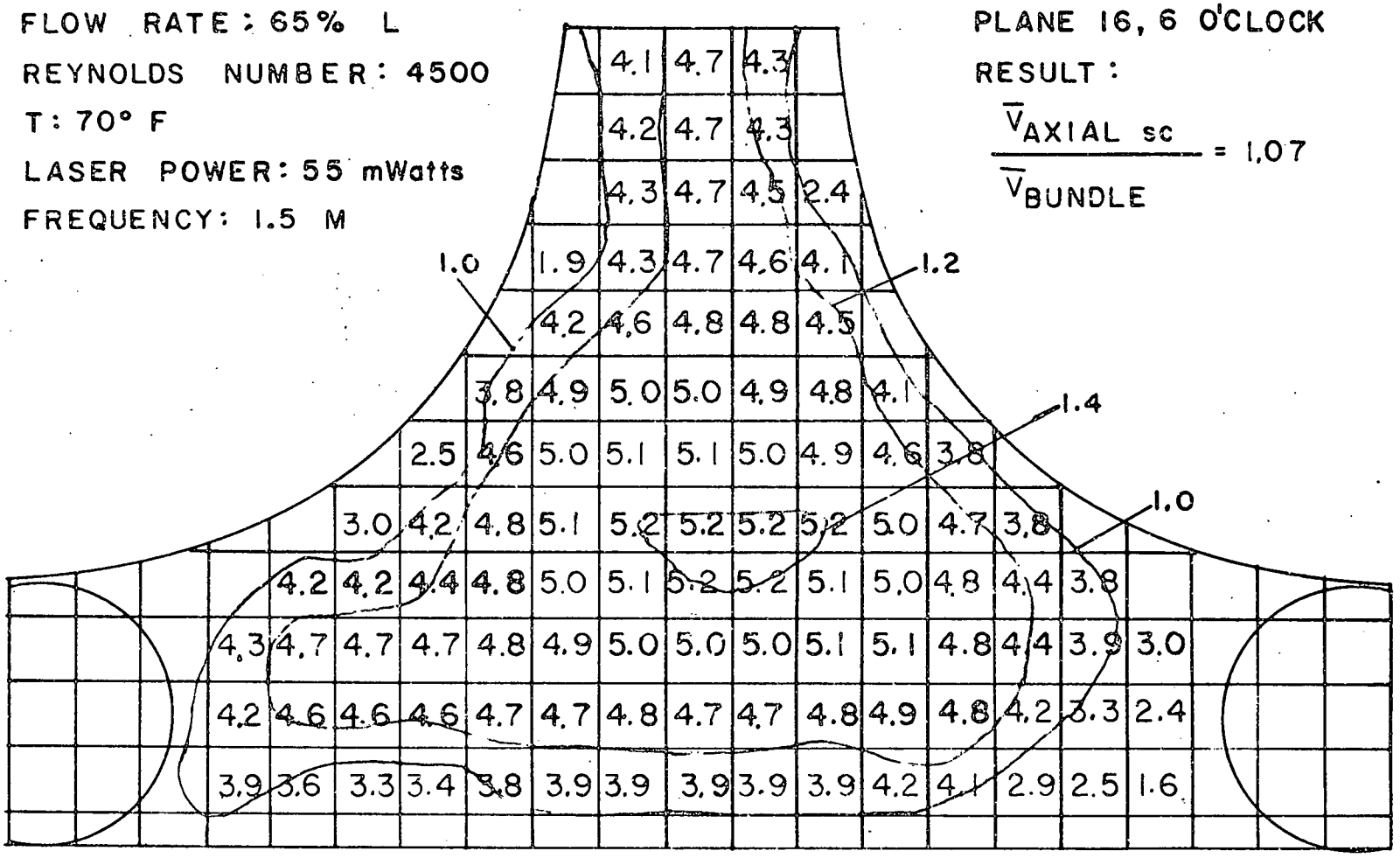

FIGURE 4.53

OPERATING CONDITIONS

DATE: 6/11/74
FLOW RATE: 65 % L
REYNOLDS NUMBER: 4500
T: 70° F
LASER POWER: 50 mWatts
FREQUENCY: 1.5 M

GEOMETRY

WIRE AXIAL PITCH: 12"
PLANE 17, 4:30 O'CLOCK
RESULT:

$$\frac{\bar{V}_{AXIAL\ sc}}{\bar{V}_{BUNDLE}} = 1.12$$

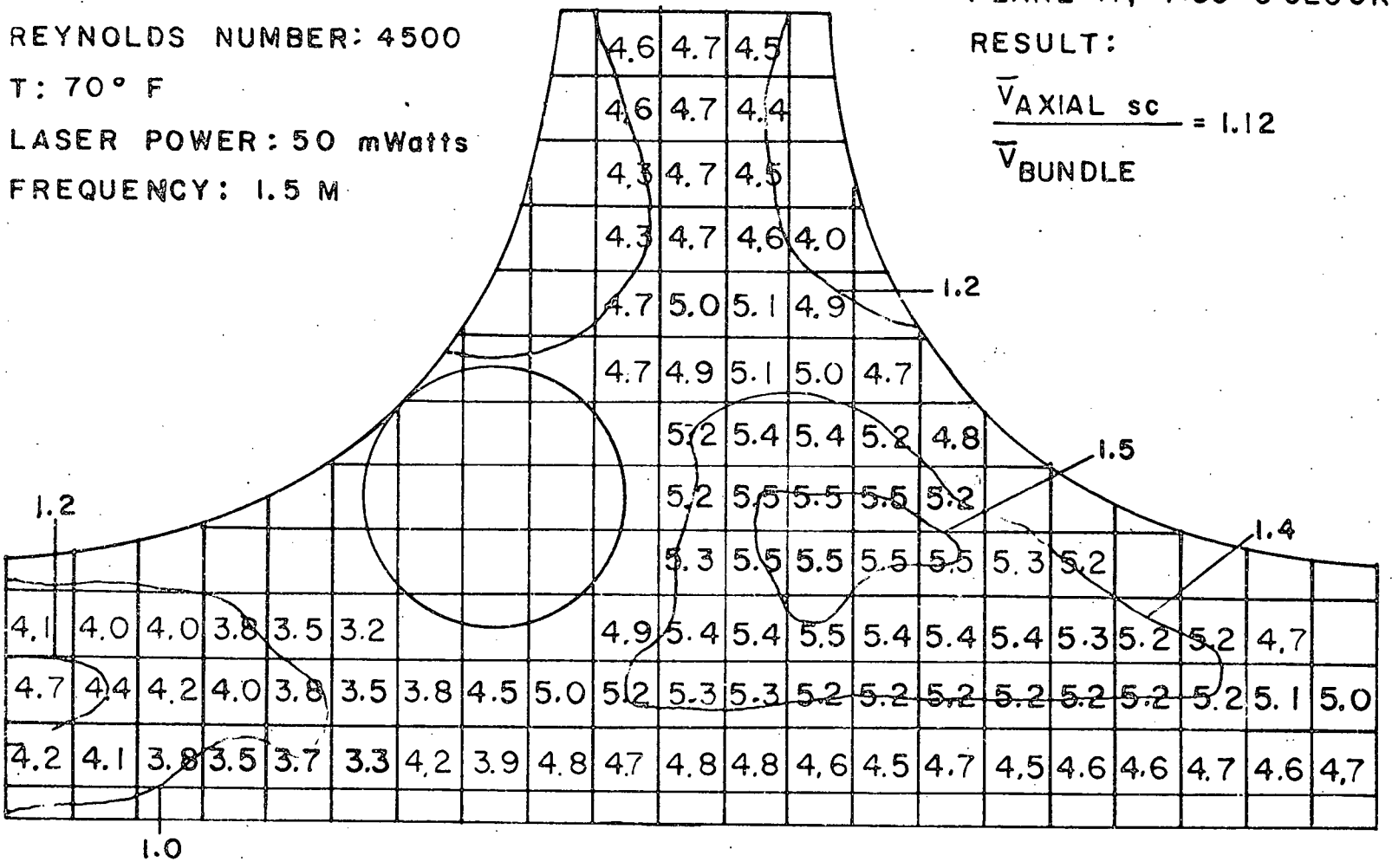

FIGURE 4.54

OPERATING CONDITIONS

DATE: 5/28/74
FLOW RATE: 15% S
REYNOLDS NUMBER: 640
T: 70° F
LASER POWER: 55 mWatts
FREQUENCY: 150 K

GEOMETRY

WIRE AXIAL PITCH: 6"
PLANE 16, 6 O'CLOCK
RESULT:

$$\frac{\overline{V}_{AXIAL\ sc}}{\overline{V}_{BUNDLE}} = 1.36$$

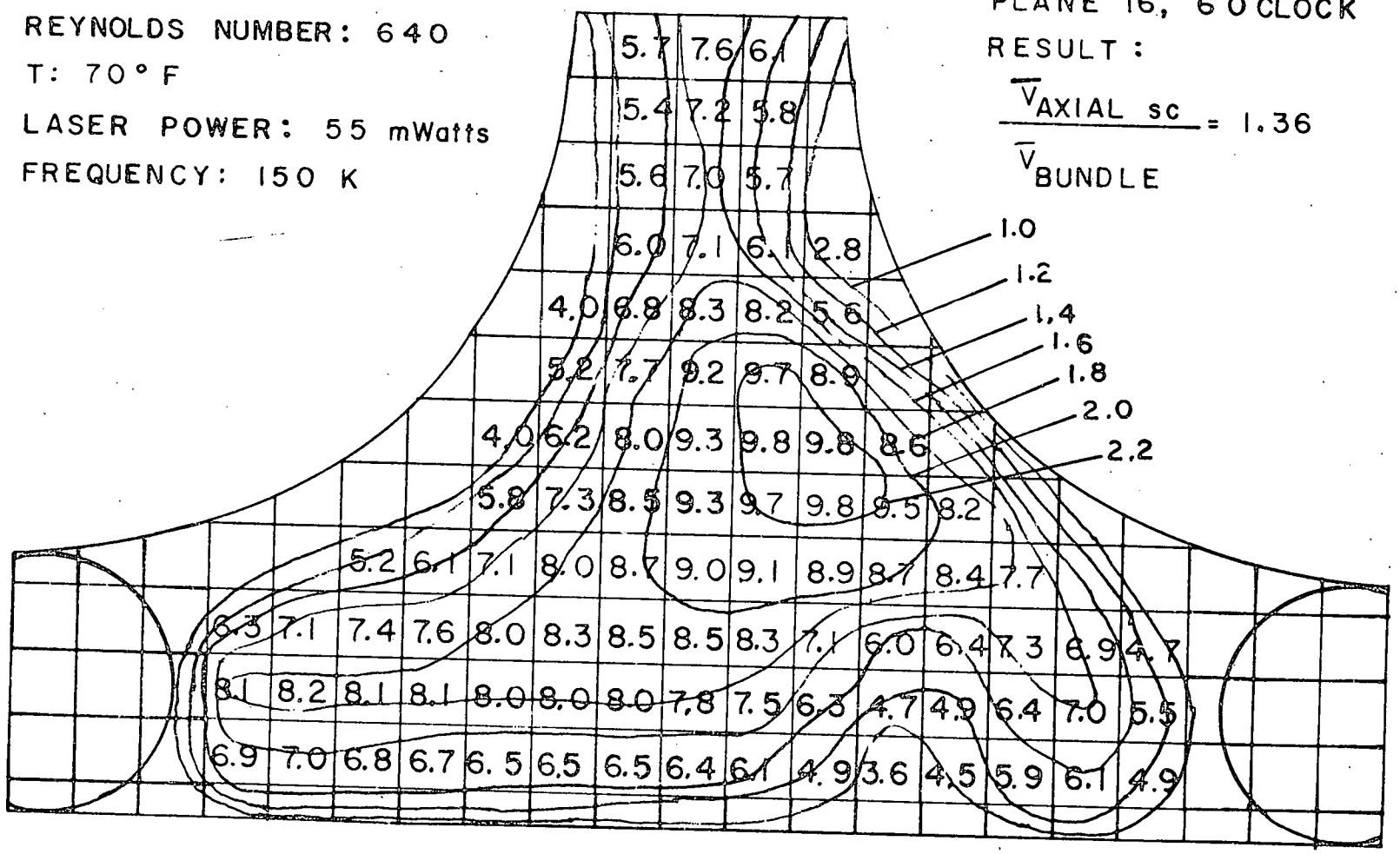

FIGURE 4.55

OPERATING CONDITIONS

DATE: 5/26/74
FLOW RATE : 15 % S
REYNOLDS NUMBER : 640
T : 70° F
LASER POWER: 55 mWatts
FREQUENCY : 1.5 M

GEOMETRY

WIRE AXIAL PITCH : 6"
PLANE 17, 5 O'CLOCK
RESULT:

$$\frac{\overline{V}_{AXIAL\ sc}}{\overline{V}_{BUNDLE}} = 1.36$$

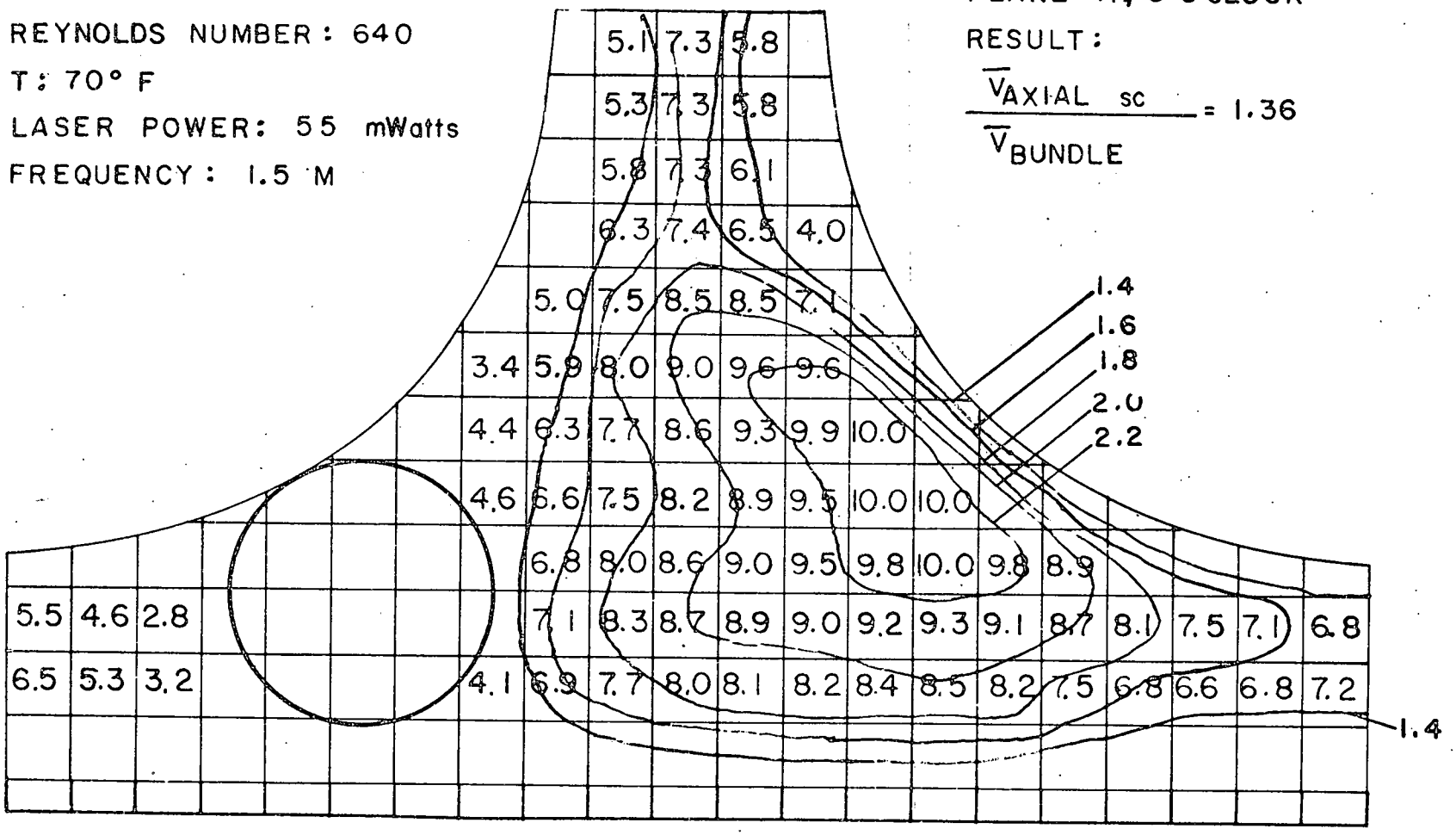

FIGURE 4.56

OPERATING CONDITIONS

DATE: 5/29/74
FLOW RATE: 15% S
REYNOLDS NUMBER: 640
T: 70° F
LASER POWER: 55 mWatts
FREQUENCY: 150 K

GEOMETRY

WIRE AXIAL PITCH: 6"
PLANE 18, 3 O'CLOCK
RESULT:

$$\frac{\overline{V}_{AXIAL\ sc}}{\overline{V}_{BUNDLE}} = 1.35$$

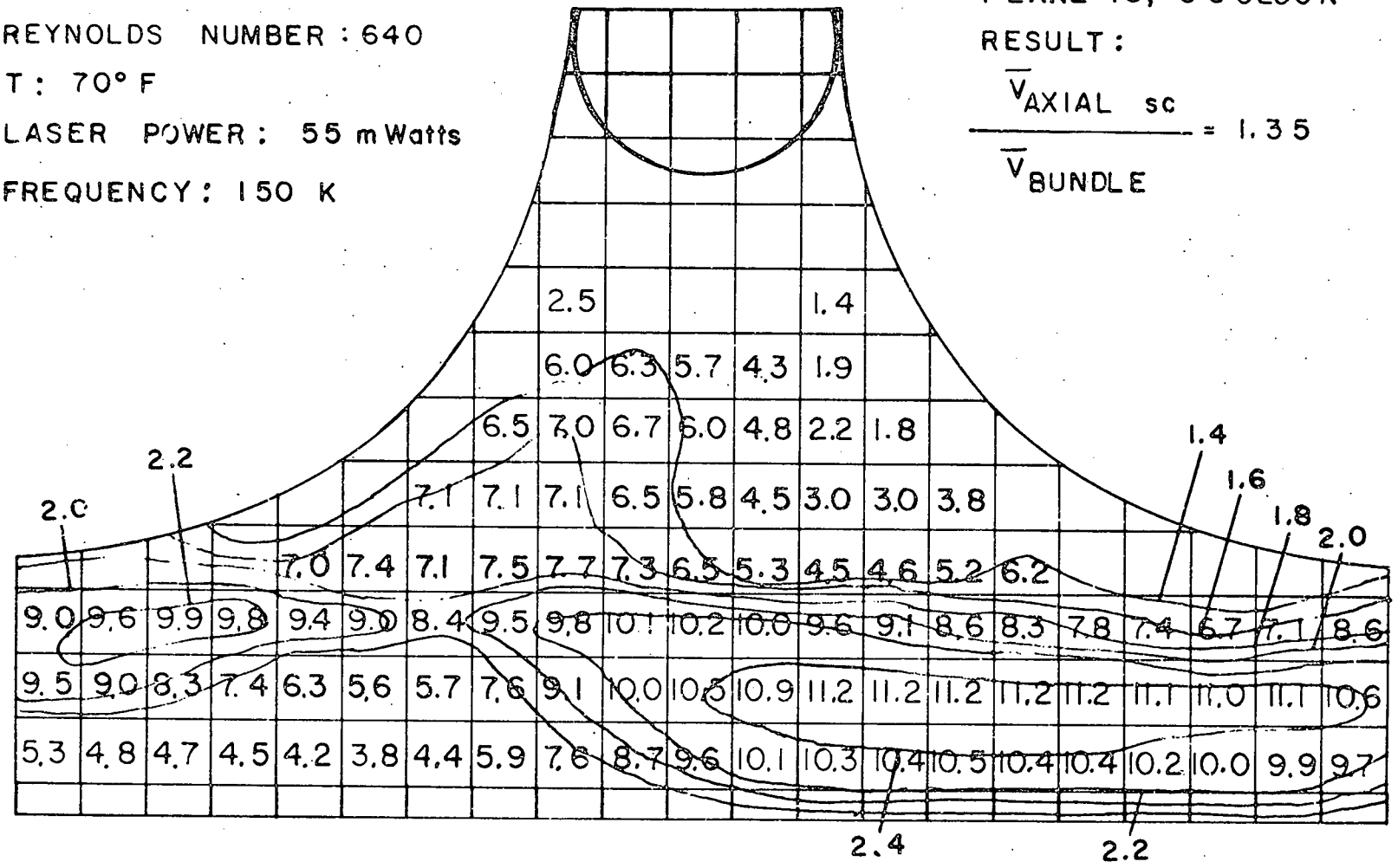

FIGURE 4.57

OPERATING CONDITIONS

DATE : 5/30/74
FLOW RATE : 15% S
REYNOLDS NUMBER: 640
T: 70° F
LASER POWER: 55 mWatts
FREQUENCY: 150 K

GEOMETRY

WIRE AXIAL PITCH: 6"
PLANE 19, 1:30 O'CLOCK
RESULT:

$$\frac{\overline{V}_{AXIAL\ sc}}{\overline{V}_{BUNDLE}} = 1.26$$

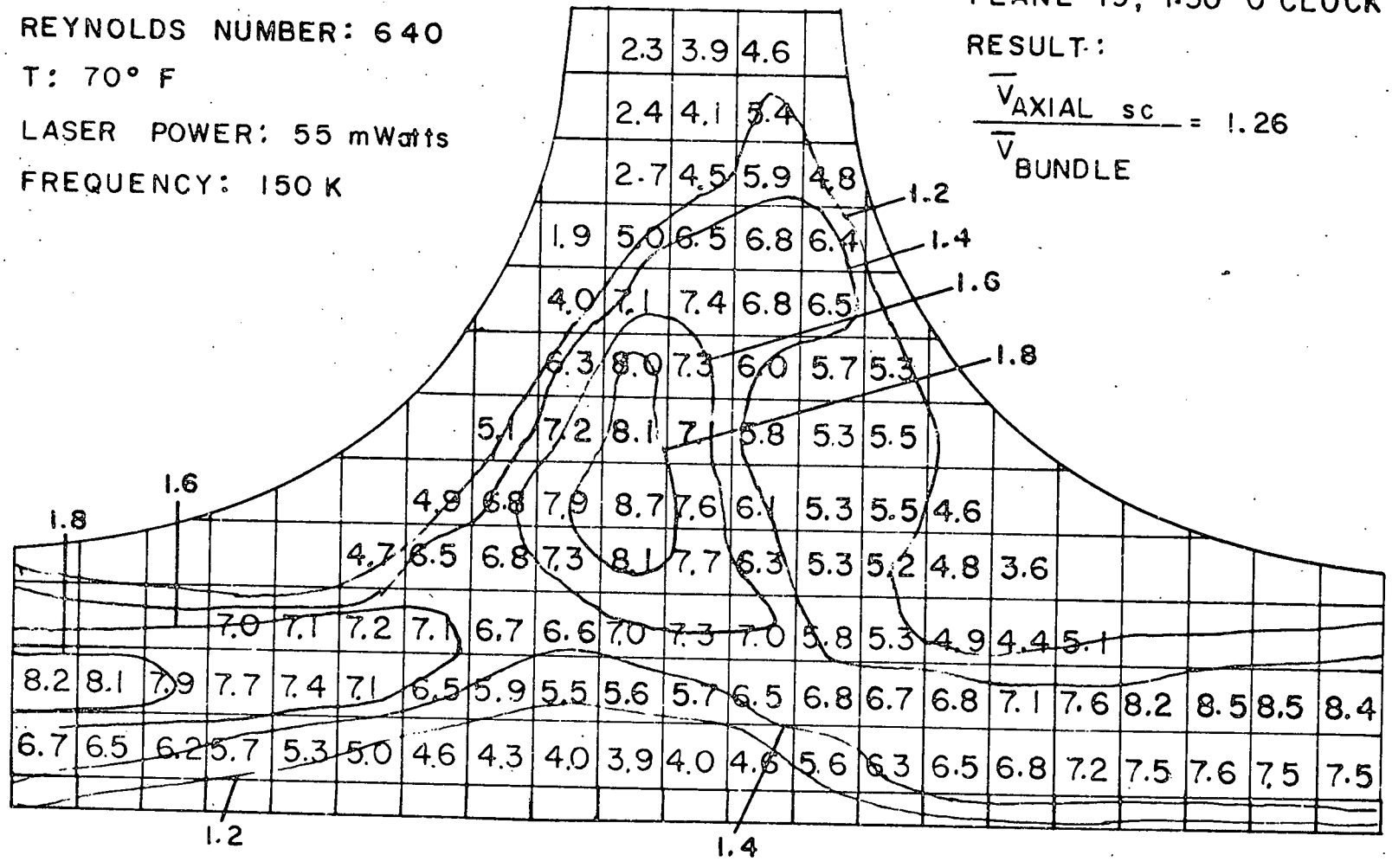

FIGURE 4.58

OPERATING CONDITIONS

DATE: 5/24/74

FLOW RATE: 15% S

REYNOLDS NUMBER: 640

T: 70° F

LASER POWER: 55 mWatts

FREQUENCY: 150K

GEOMETRY

WIRE AXIAL PITCH: 6"

PLANE 20, 12 O'CLOCK

RESULT:

$$\frac{\overline{V}_{AXIAL\ sc}}{\overline{V}_{BUNDLE}} = 1.21$$

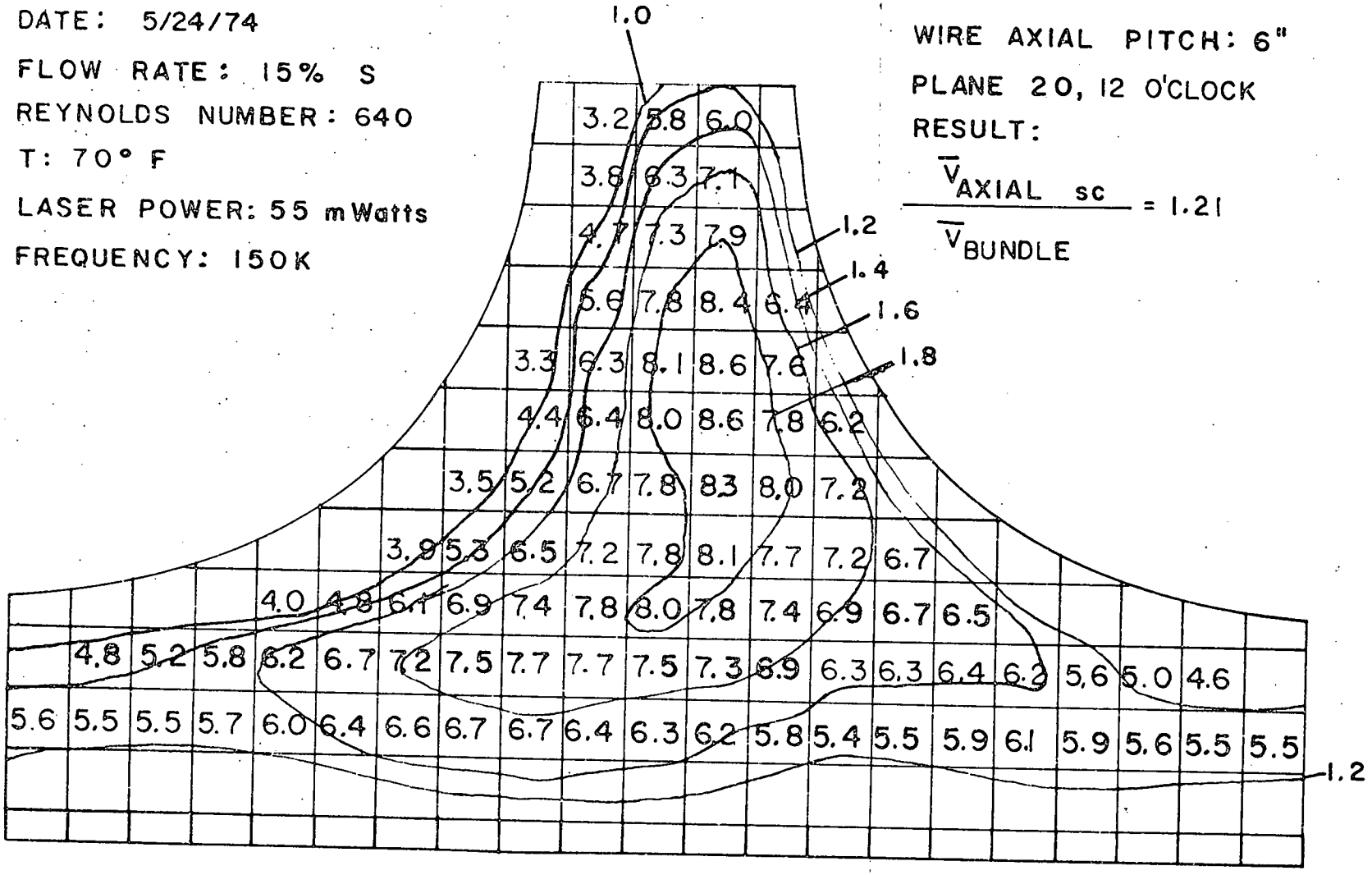

FIGURE 4.59

OPERATING CONDITIONS

DATE : 5/30/74
FLOW RATE : 15 % S
REYNOLDS NUMBER : 640
T : 70° F
LASER POWER : 55 mWatts
FREQUENCY : 150 K

GEOMETRY

WIRE AXIAL PITCH : 6"
PLANE 21, 10:30 dCLOCK
RESULT :

$$\frac{\overline{V}_{AXIAL\ sc}}{\overline{V}_{BUNDLE}} = 1.20$$

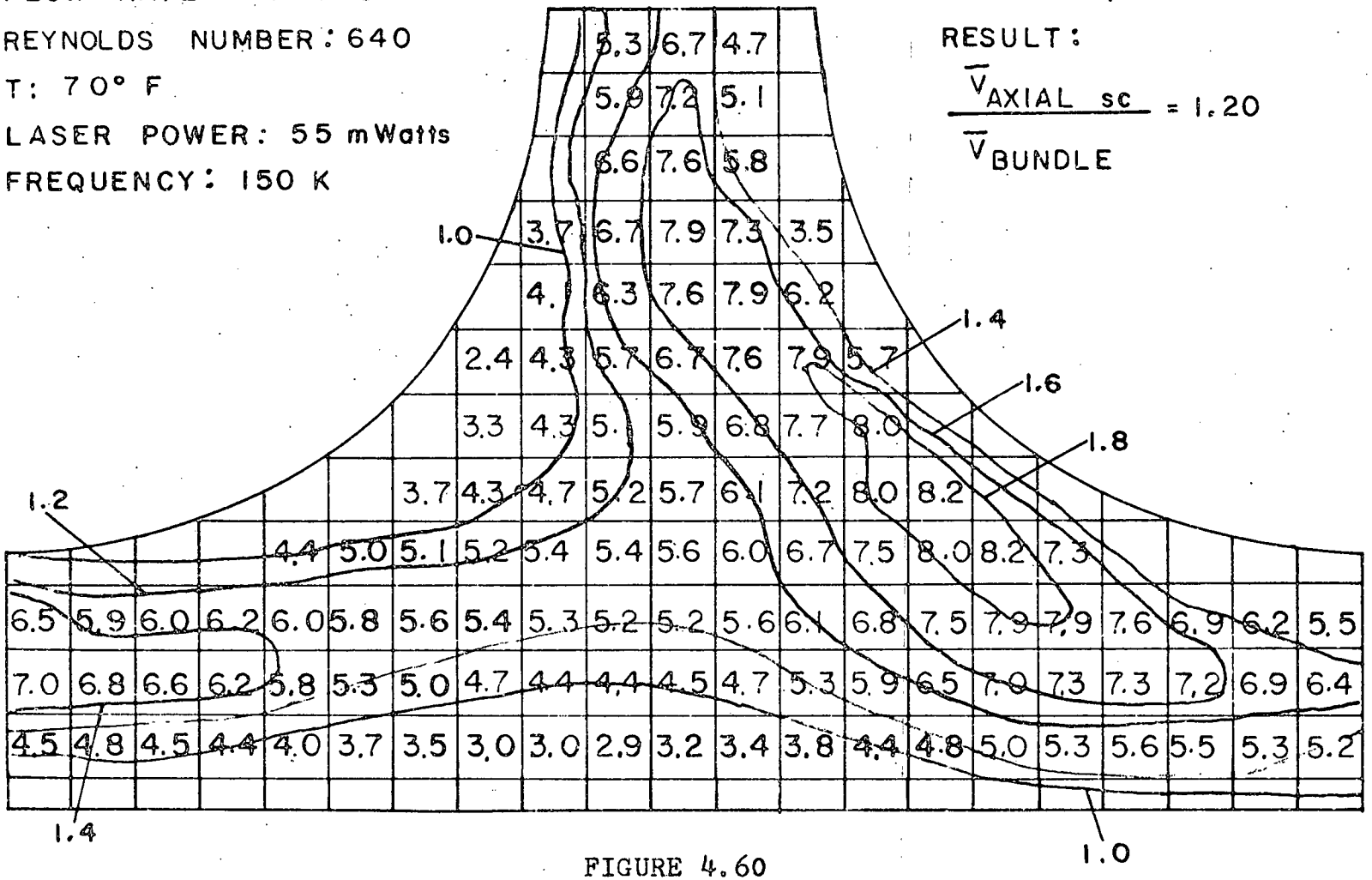

FIGURE 4.60

OPERATING CONDITIONS

DATE: 6/1/74

FLOW RATE: 15 % S

REYNOLDS NUMBER: 640

T: 70° F

LASER POWER: 55 mWatts

FREQUENCY: 150 K

GEOMETRY

WIRE AXIAL PITCH: 6"

PLANE 22, 9 O'CLOCK

RESULT:

$$\frac{\bar{V}_{AXIAL\ sc}}{\bar{V}_{BUNDLE}} = 1.07$$

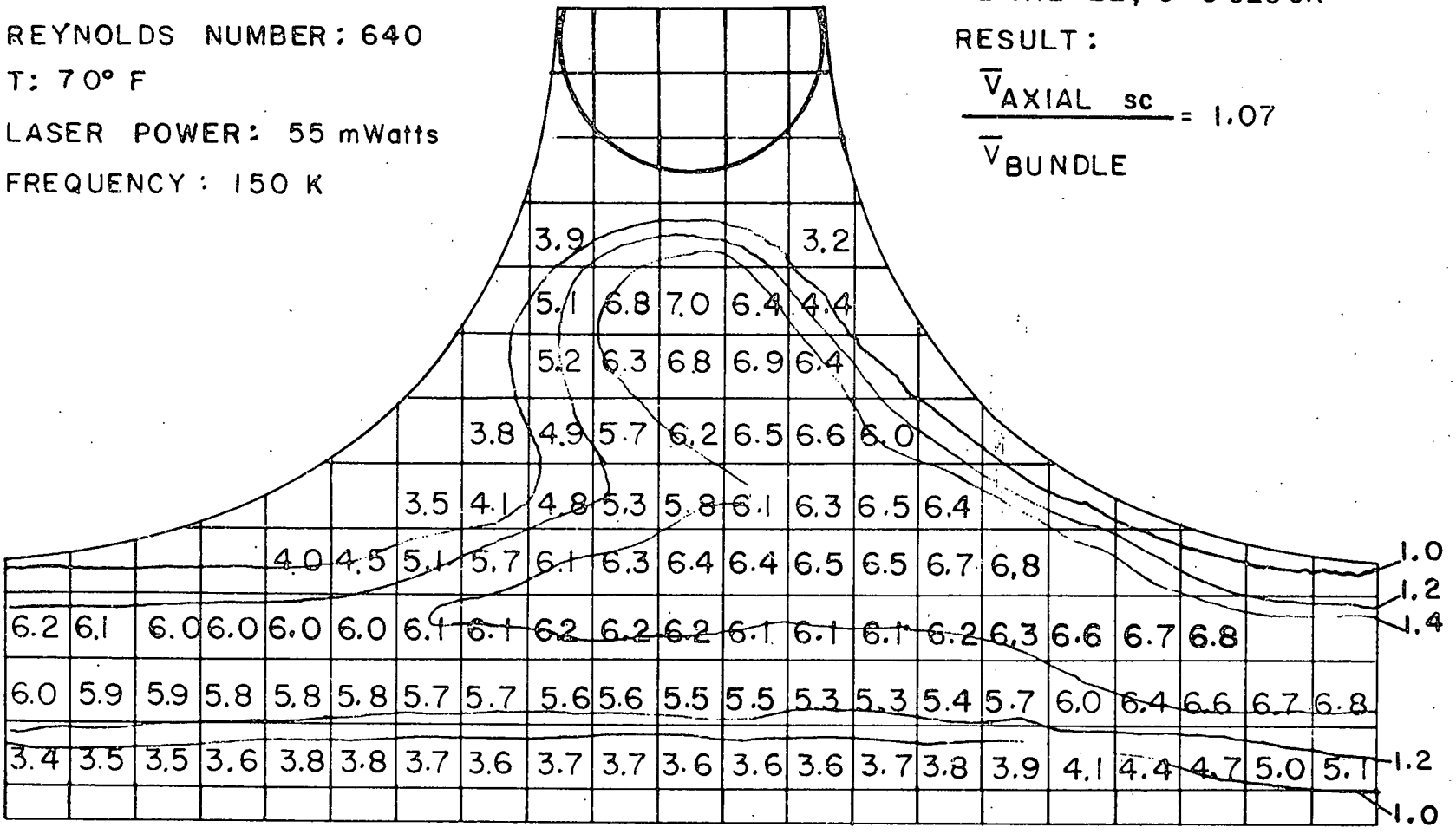

FIGURE 4.61

OPERATING CONDITIONS

DATE: 6/1/74
FLOW RATE: 15% S
REYNOLDS NUMBER: 640
T: 70° F
LASER POWER: 55 mWatts
FREQUENCY: 150 K

GEOMETRY

WIRE AXIAL PITCH: 6"
PLANE 23, 7:30 d'CLOCK
RESULT:

$$\frac{\overline{V}_{AXIAL\ sc}}{\overline{V}_{BUNDLE}} = 1.15$$

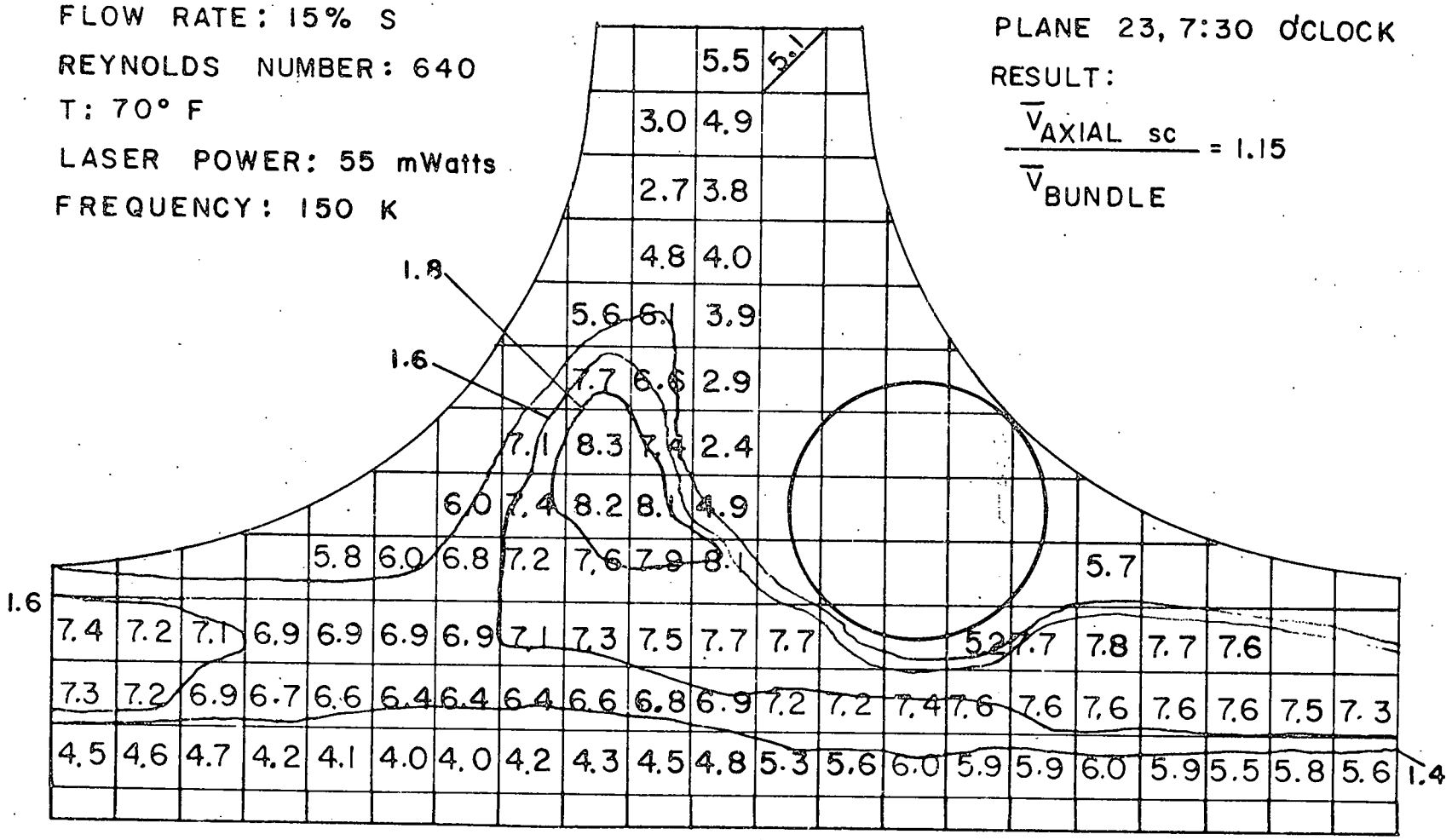

FIGURE 4.62

OPERATING CONDITIONS

DATE: 5/28/74
FLOW RATE: 65% L
REYNOLDS NUMBER: 4500
T: 70° F
LASER POWER: 55 mWatts
FREQUENCY: 1.5 M

GEOMETRY

WIRE AXIAL PITCH: 6"
PLANE 16, 6 O'CLOCK
RESULT:

$$\frac{\overline{V}_{AXIAL\ sc}}{\overline{V}_{BUNDLE}} = 1.17$$

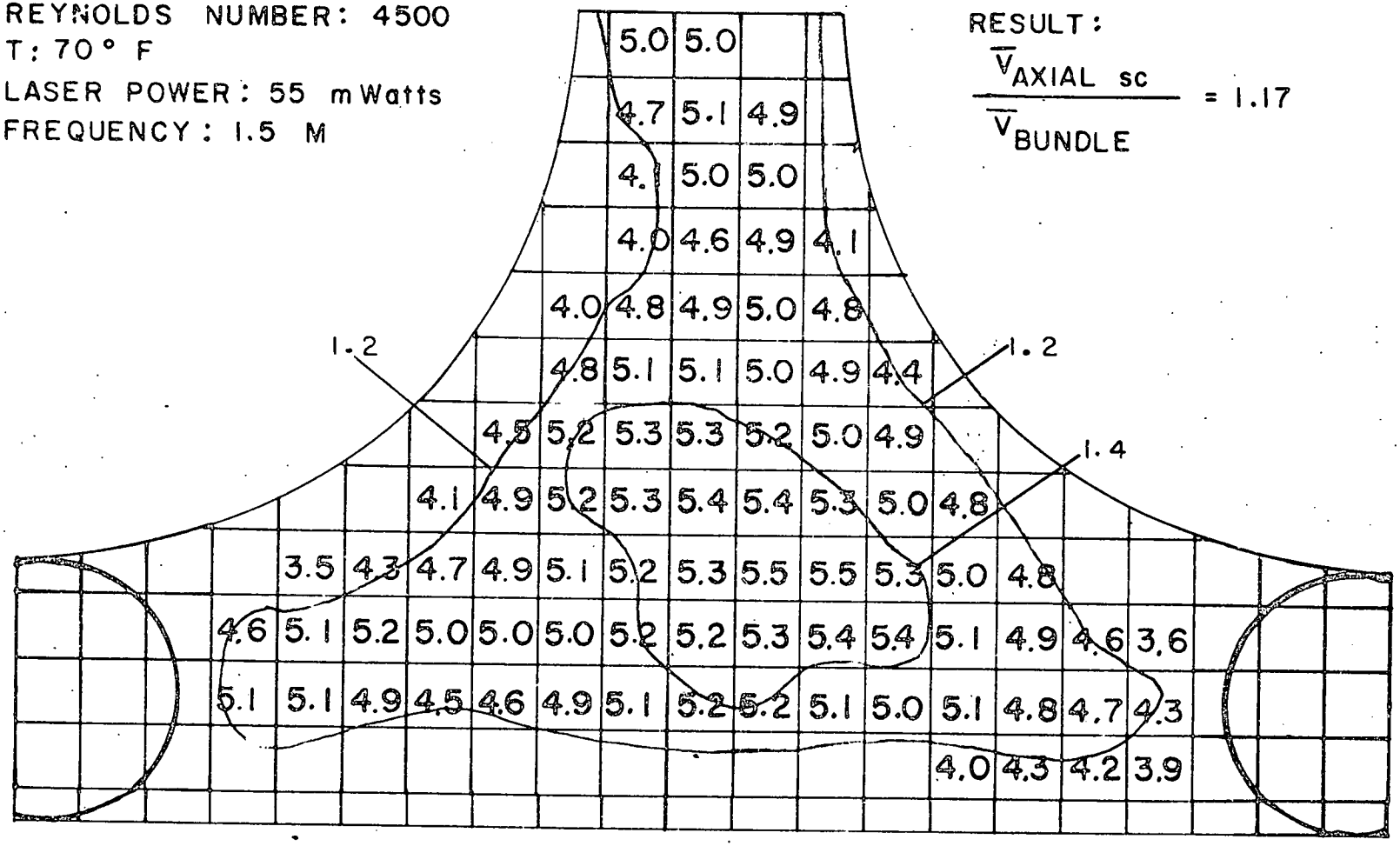

FIGURE 4.63

OPERATING CONDITIONS

DATE: 5/26/74

FLOW RATE: 65 % L

REYNOLDS NUMBER: 4500

T: 70° F

LASER POWER: 55 mWatts

FREQUENCY: 150 K

GEOMETRY

WIRE AXIAL PITCH : 6"

PLANE 17, 5 O'CLOCK

RESULT:

$$\frac{\overline{V}_{AXIAL\ sc}}{\overline{V}_{BUNDLE}} = 1.18$$

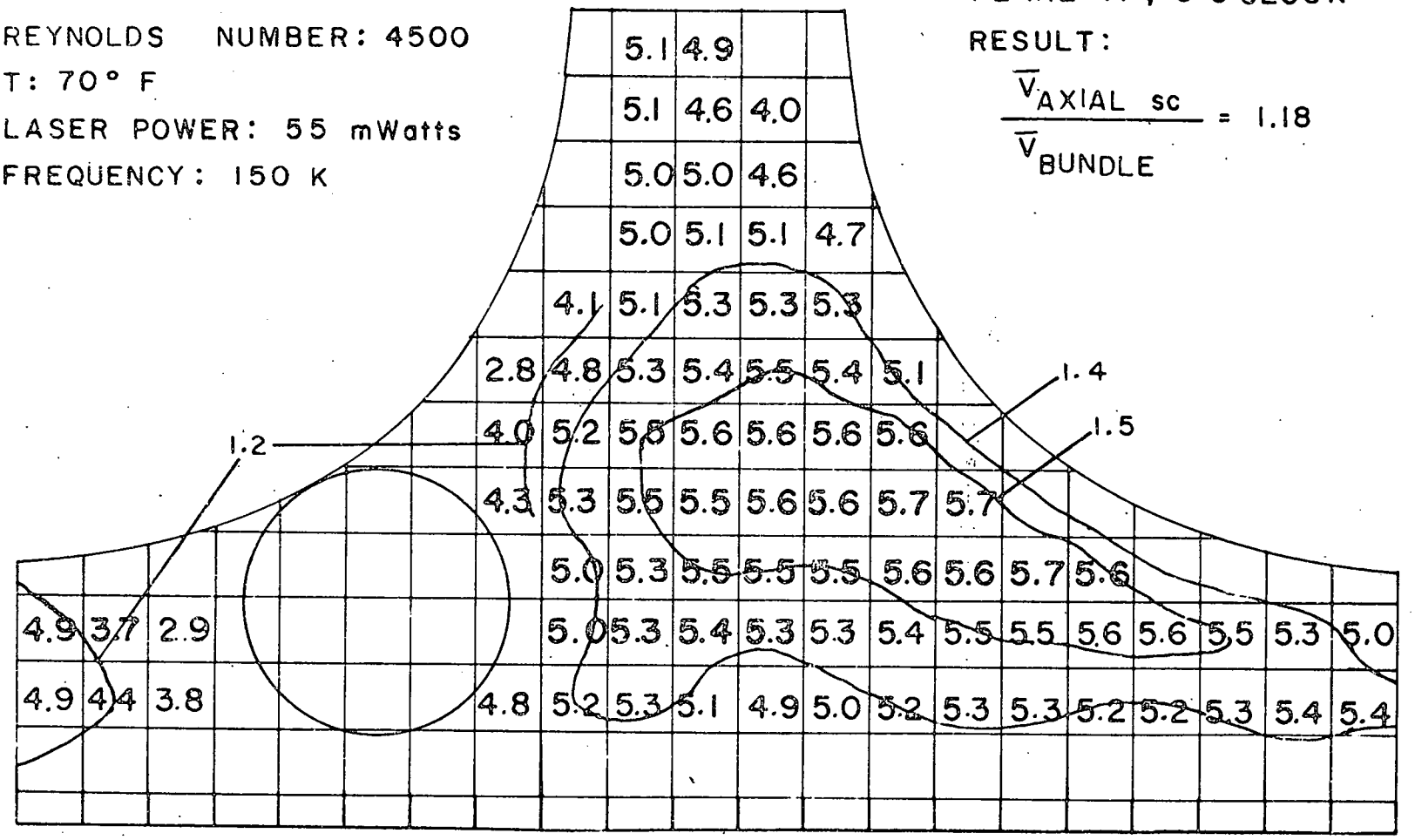

FIGURE 4.64

OPERATING CONDITIONS

DATE: 5/29/74
FLOW RATE: 65 % L
REYNOLDS NUMBER: 4500
T: 70 ° F
LASER POWER: 55 mWatts
FREQUENCY: 1.5 M

GEOMETRY

WIRE AXIAL PITCH: 6"
PLANE 18, 3 O'CLOCK
RESULT:

$$\frac{\overline{V}_{AXIAL\ sc}}{\overline{V}_{BUNDLE}} = 1.21$$

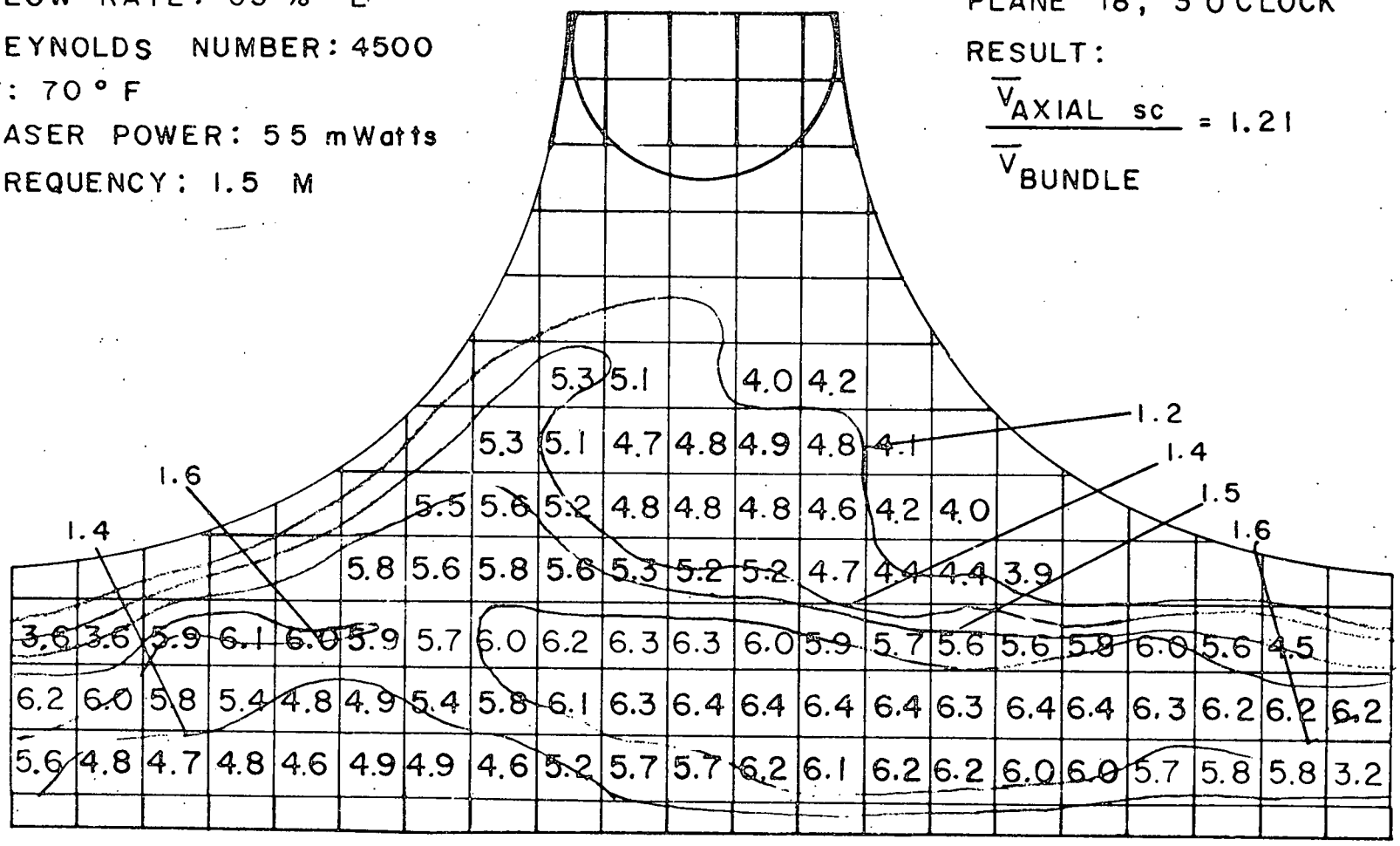

FIGURE 4.65

OPERATING CONDITIONS

DATE: 5/30/74
FLOW RATE: 65 % L
REYNOLDS NUMBER: 4500
T: 70 ° F
LASER POWER: 55 mWatts
FREQUENCY: 1.5 M

GEOMETRY

WIRE AXIAL PITCH: 6"
PLANE 19, 1:30 O'CLOCK
RESULT:

$$\frac{\overline{V}_{AXIAL\ sc}}{V_{BUNDLE}} = 1.0$$

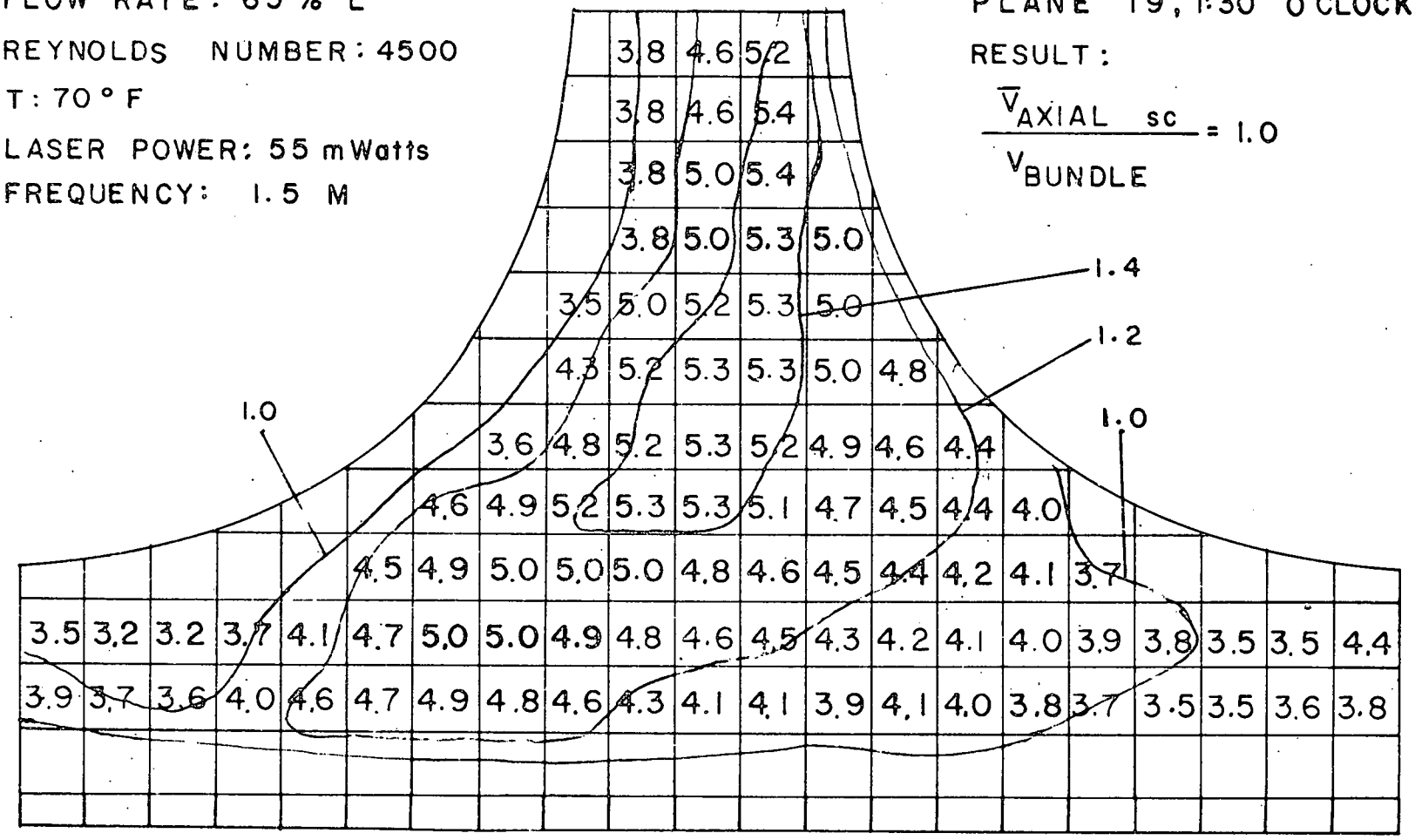

FIGURE 4.66

OPERATING CONDITIONS

DATE: 5/26/74

FLOW RATE: 65% L

REYNOLDS NUMBER: 4500

T: 70° F

LASER POWER: 55 mWatts

FREQUENCY: 1.5 M

GEOMETRY

WIRE AXIAL PITCH: 6"

PLANE 20, 12 O'CLOCK

RESULT:

$$\frac{\overline{V}_{AXIAL\ sc}}{\overline{V}_{BUNDLE}} = 0.98$$

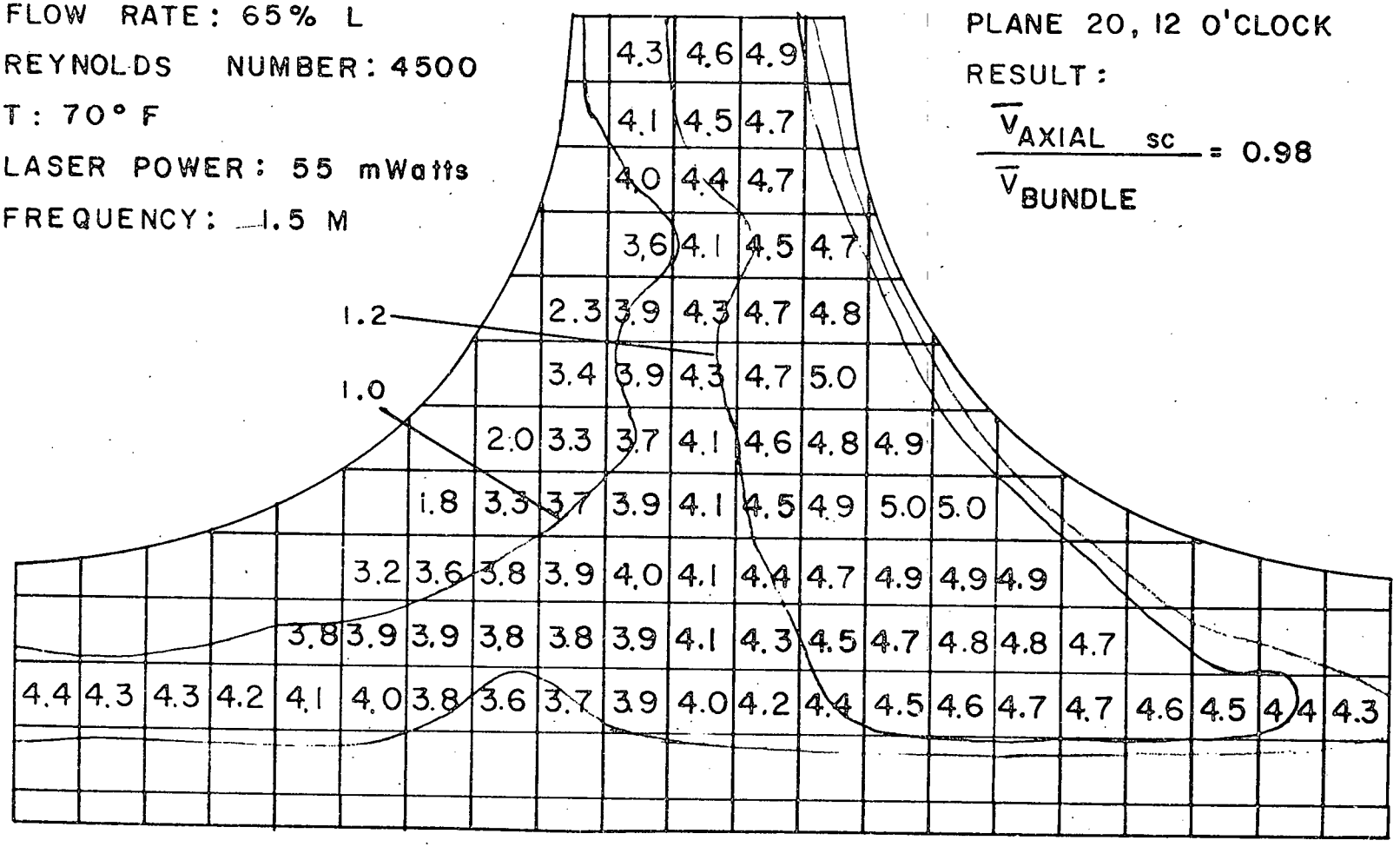

FIGURE 4.67

OPERATING CONDITIONS

DATE: 5/30/74

FLOW RATE: 65% L

REYNOLDS NUMBER: 4500

T: 70° F

LASER POWER: 55 mWatts

FREQUENCY: 1.5 M

GEOMETRY

WIRE AXIAL PITCH: 6"

PLANE 21, 10:30 O'CLOCK

RESULT:

$$\frac{\overline{V}_{AXIAL\ sc}}{\overline{V}_{BUNDLE}} = 0.80$$

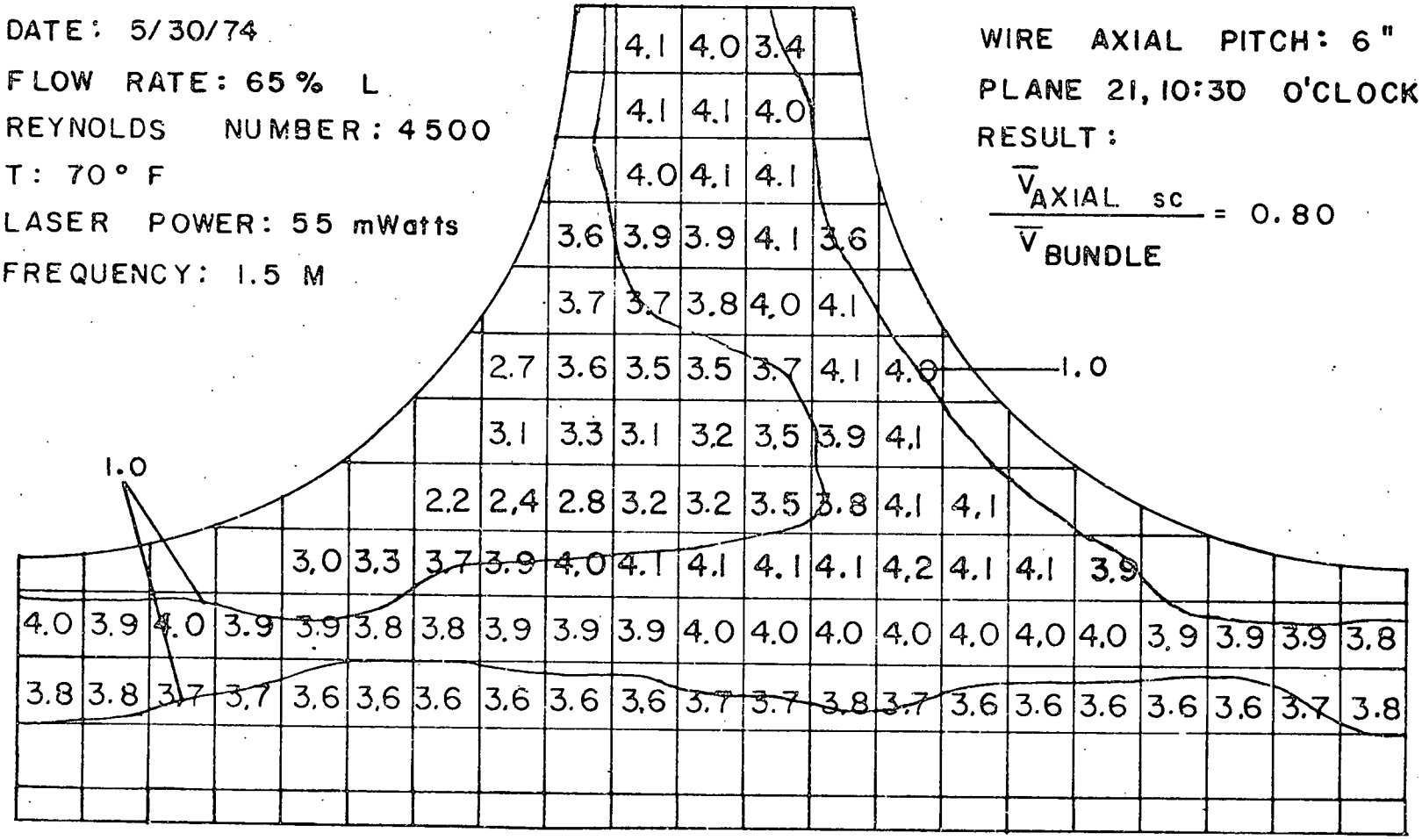

FIGURE 4.68

OPERATING CONDITIONS

DATE: 6/1/74

FLOW RATE: 65% L

REYNOLDS NUMBER: 4500

T: 70° F

LASER POWER: 55 mWatts

FREQUENCY: 1.5 M

GEOMETRY

WIRE AXIAL PITCH: 6"

PLANE 22, 9 O'CLOCK

RESULT:

$$\frac{\bar{V}_{AXIAL\ sc}}{\bar{V}_{BUNDLE}} = 0.92$$

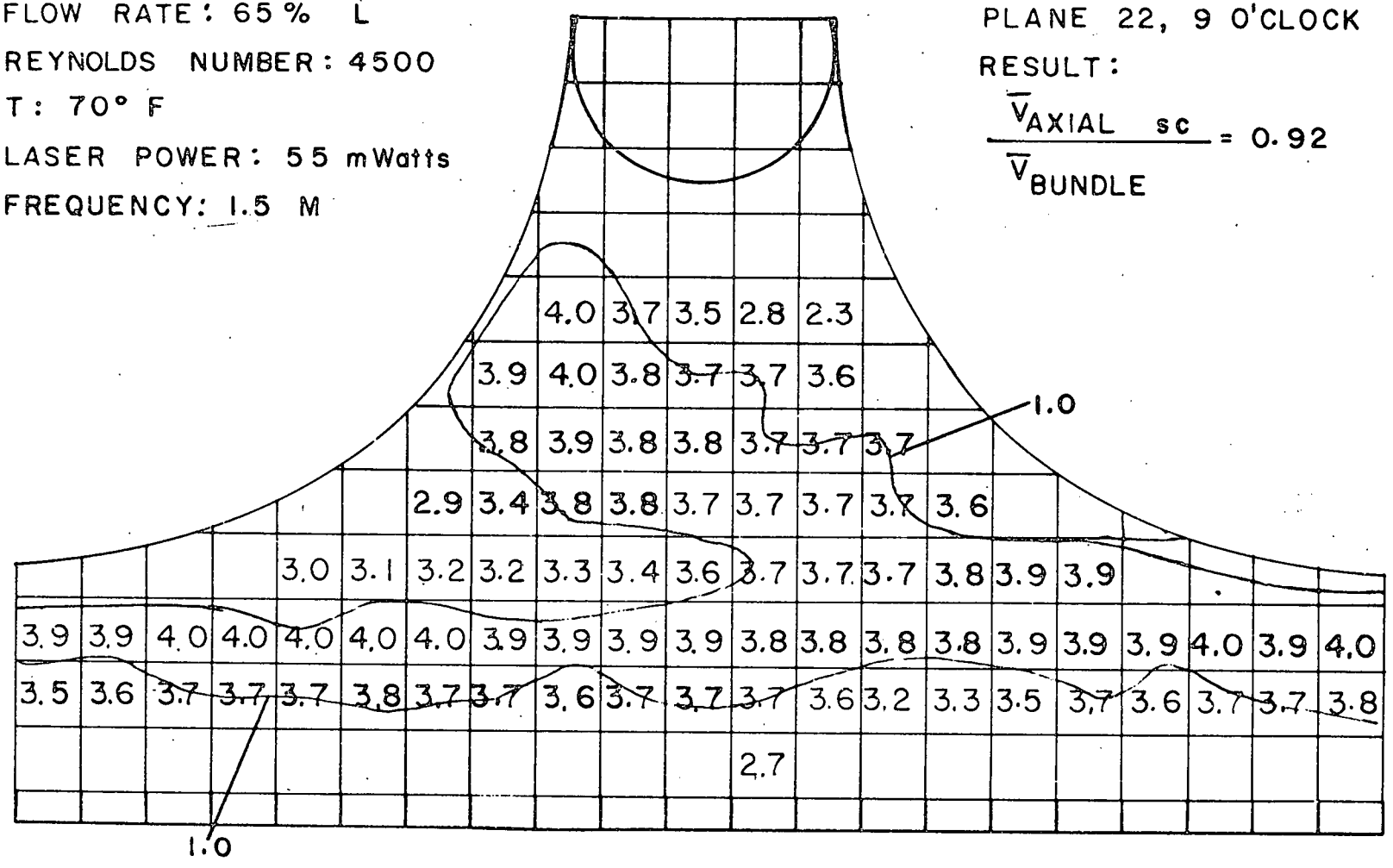

FIGURE4.69

OPERATING CONDITIONS

DATE: 6/1/74
FLOW RATE: 65% L
REYNOLDS NUMBER: 4500
T: 70° F
LASER POWER: 55 mWatts
FREQUENCY: 1.5 M

GEOMETRY

WIRE AXIAL PITCH: 6"
PLANE 23, 7:30 O'CLOCK
RESULT:

$$\frac{\bar{V}_{AXIAL\ sc}}{\bar{V}_{BUNDLE}} = 0.94$$

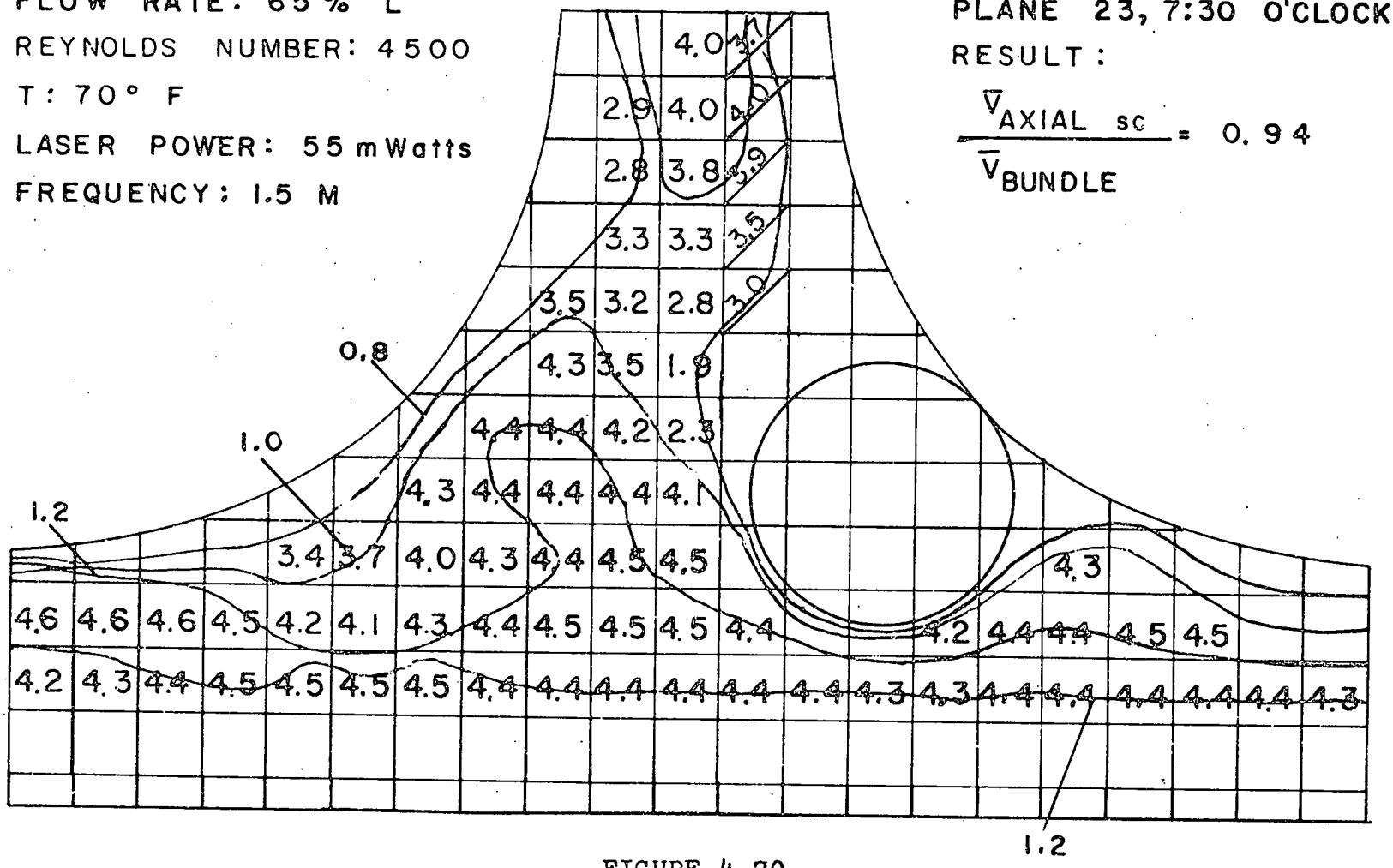

FIGURE 4.70

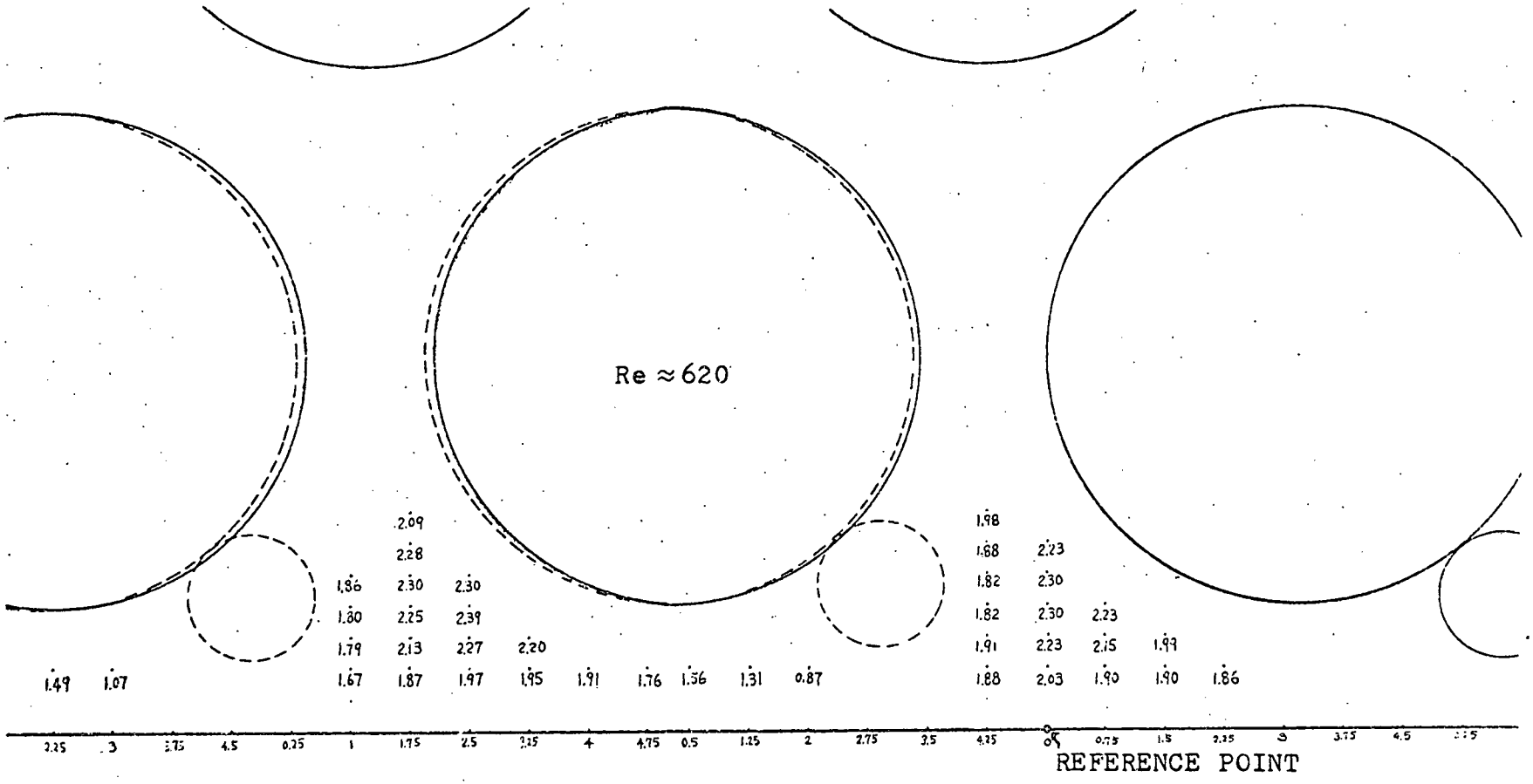

Note: 1. The horizontal and vertical distance between each point are 0.75 mm and 0.40 mm respectively. The first row of measuring points is 0.80 mm from the plexiglas wall.

2. "-----" means real locations of wires or pins relative to the reference point
"——————" means ideal locations of wires or pins relative to the reference point

3. The numbers shown in the figure are the ratio of axial to bulk velocity

FIGURE 4.71 AXIAL VELOCITY DISTRIBUTION IN PLANE 9

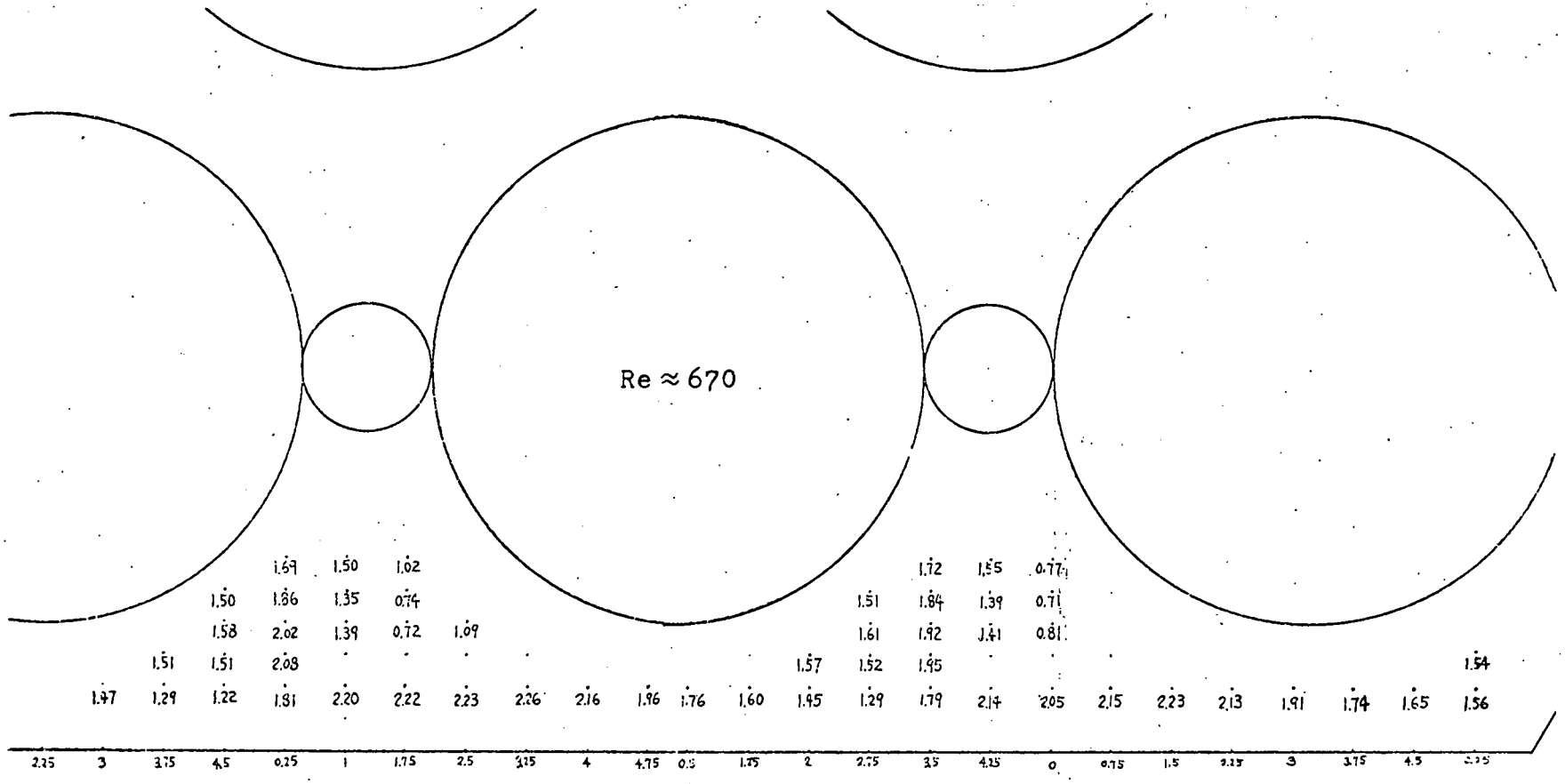

FIGURE 4.72 AXIAL VELOCITY DISTRIBUTION IN PLANE 10

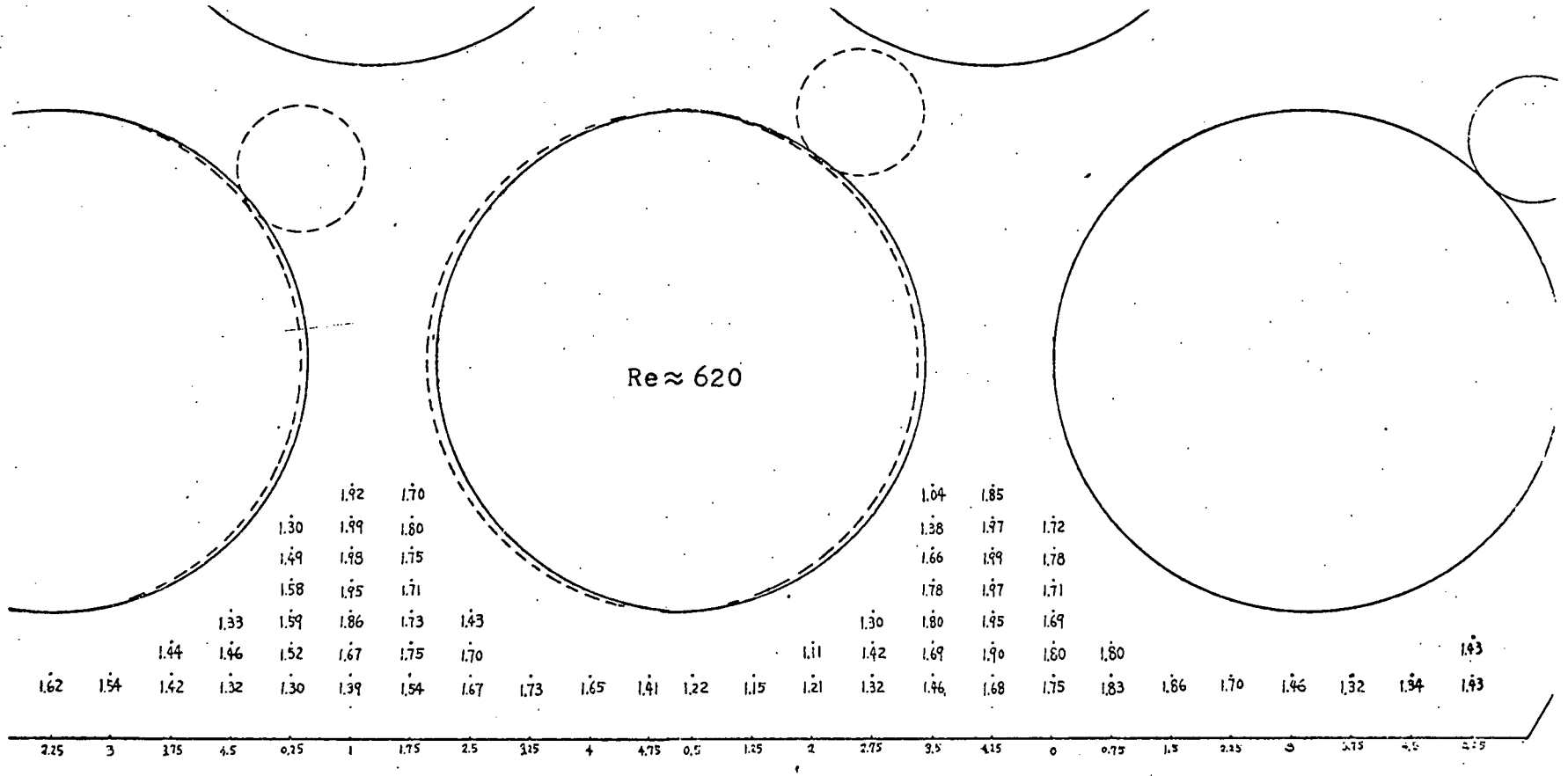

FIGURE 4.73 AXIAL VELOCITY DISTRIBUTION IN PLANE 11

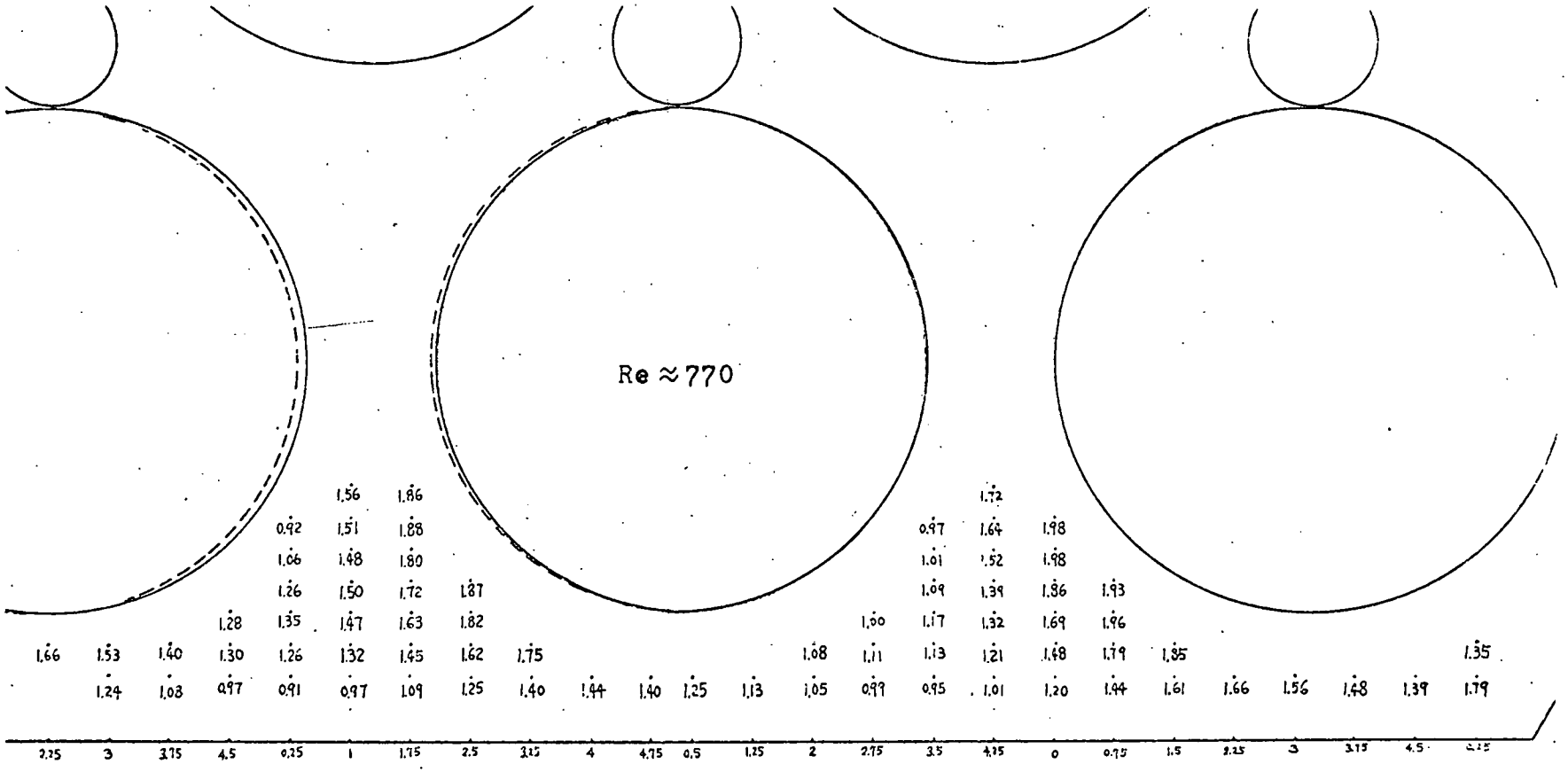

FIGURE 4.74 AXIAL VELOCITY DISTRIBUTION IN PLANE 12

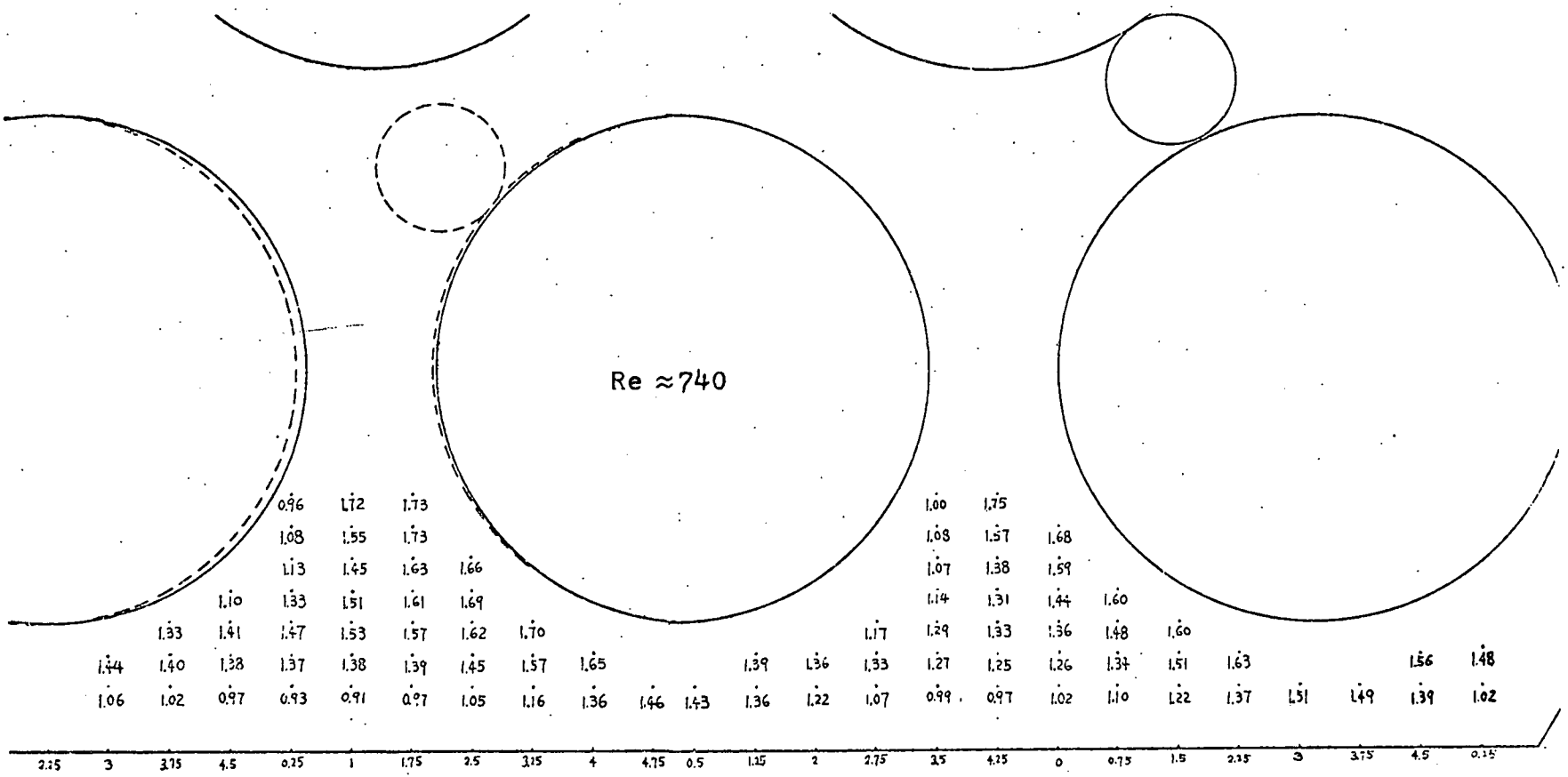

FIGURE 4.75 AXIAL VELOCITY DISTRIBUTION IN PLANE 13

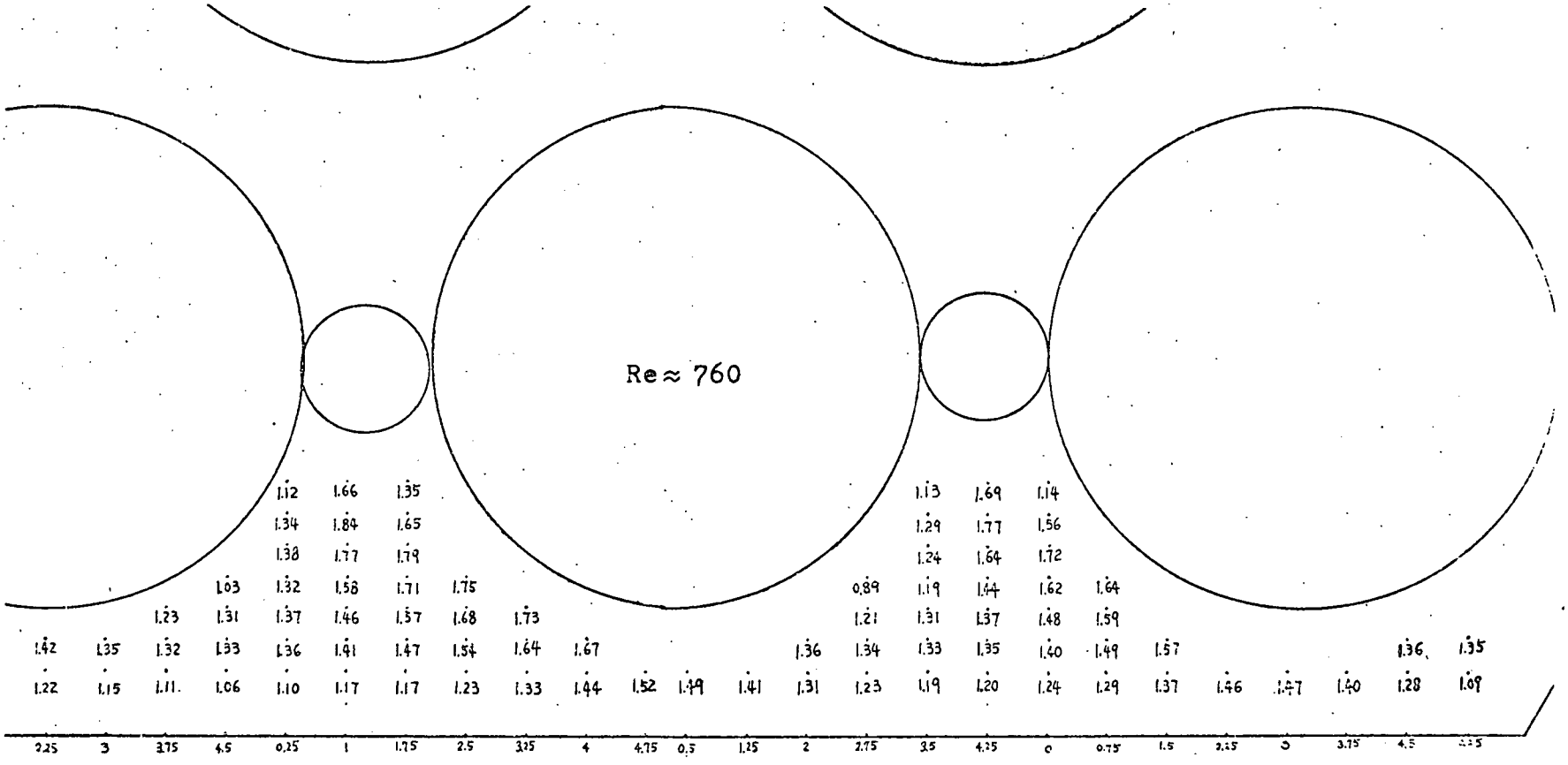

FIGURE 4.76 AXIAL VELOCITY DISTRIBUTION IN PLANE 14

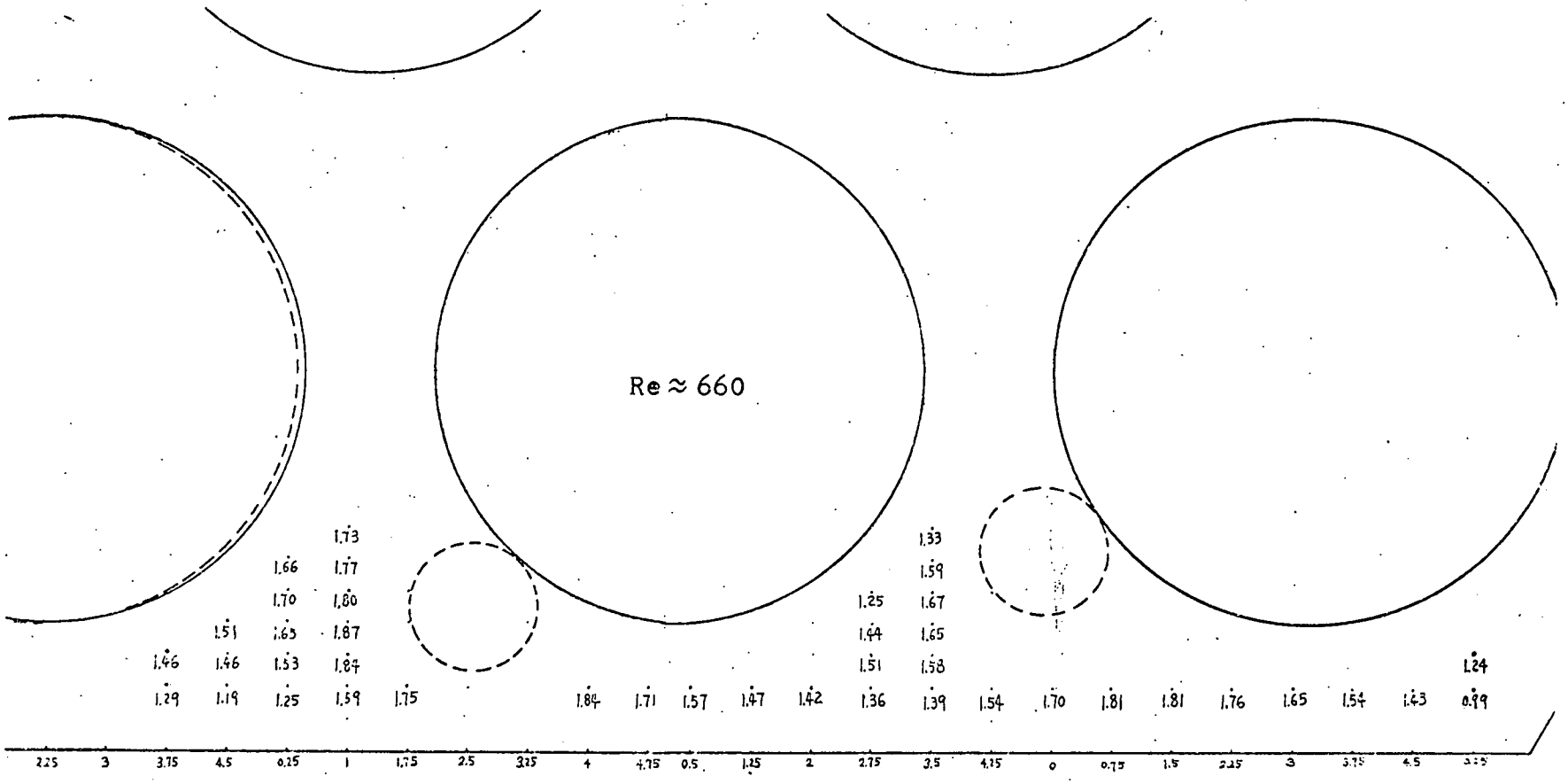

FIGURE 4.77 AXIAL VELOCITY DISTRIBUTION IN PLANE 15

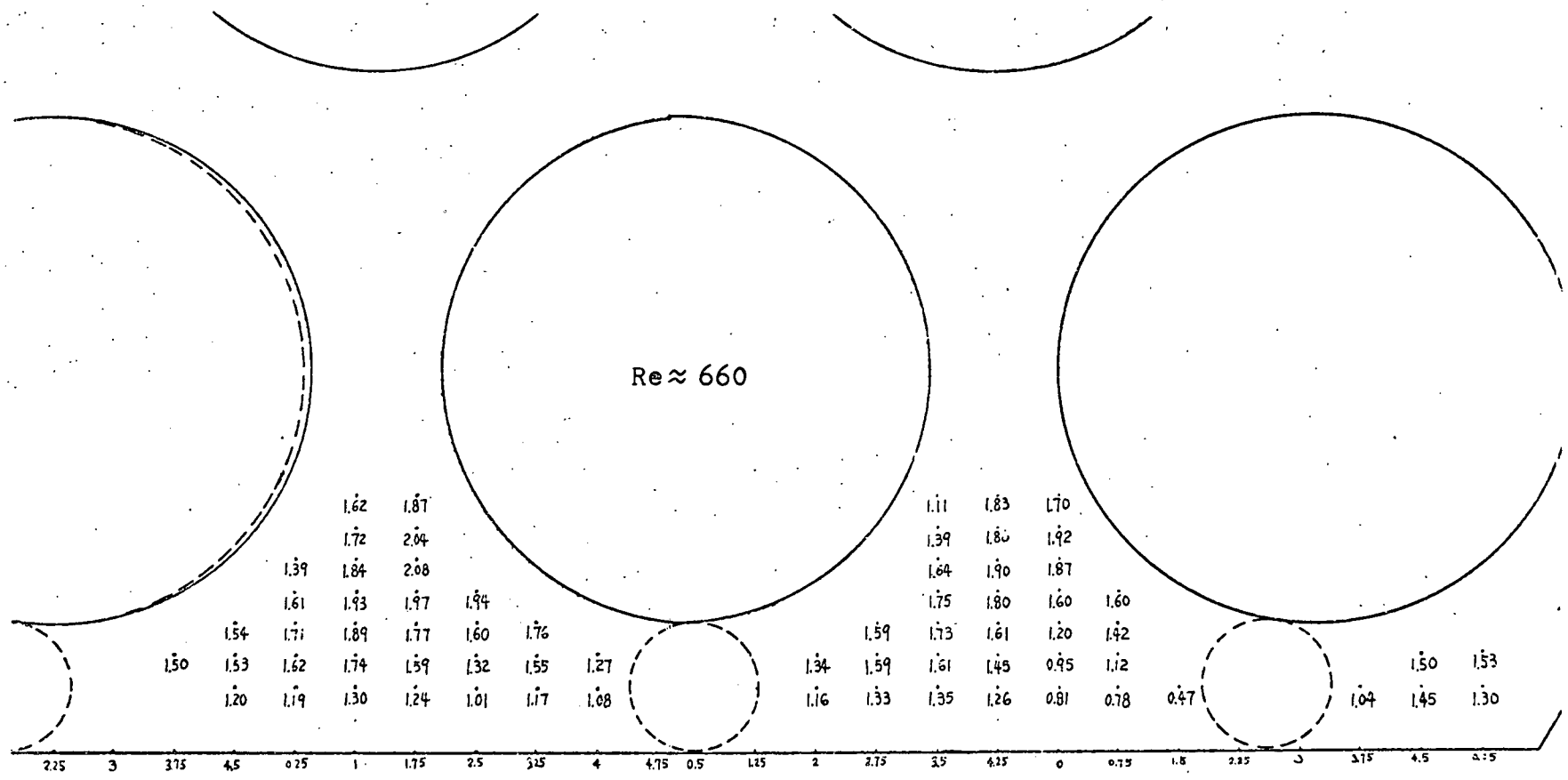

FIGURE 4.78 AXIAL VELOCITY DISTRIBUTION IN PLANE 16

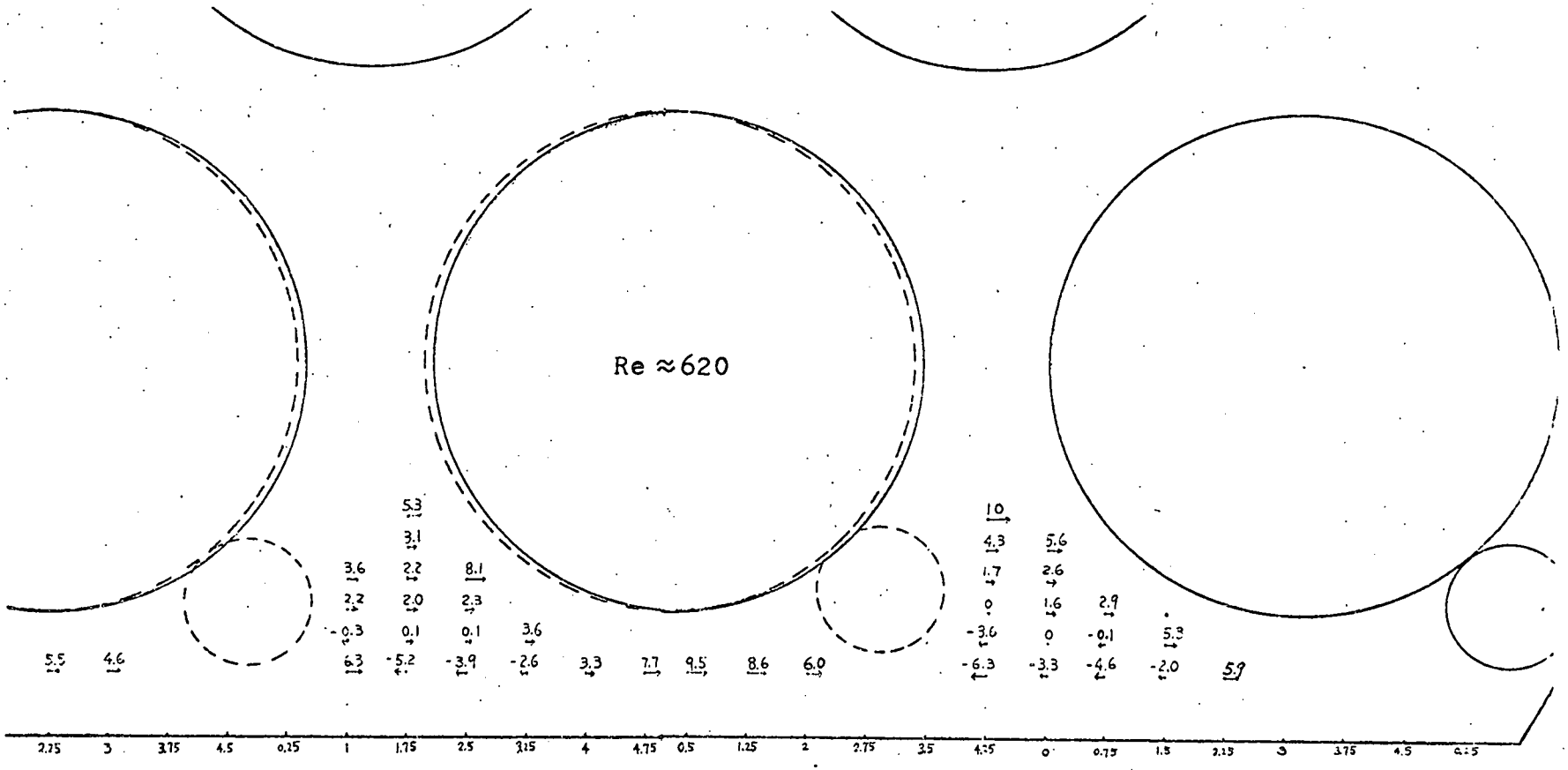

Note: The numbers shown in the figure are the ratio of transverse to bulk velocity in percent.

FIGURE 4.79 TRANSVERSE VELOCITY DISTRIBUTION IN PLANE 9

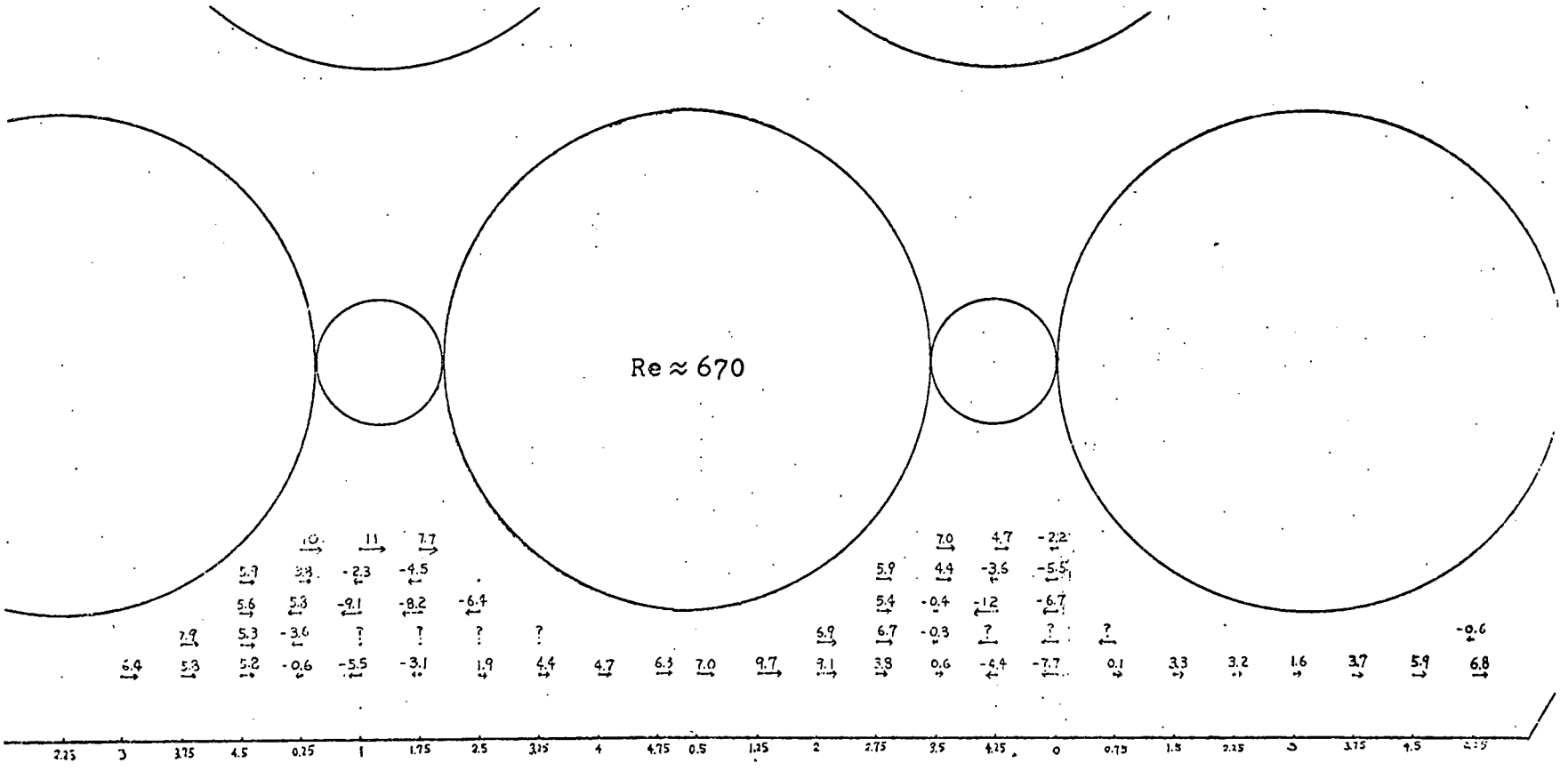

FIGURE 4.80 TRANSVERSE VELOCITY DISTRIBUTION IN PLANE 10

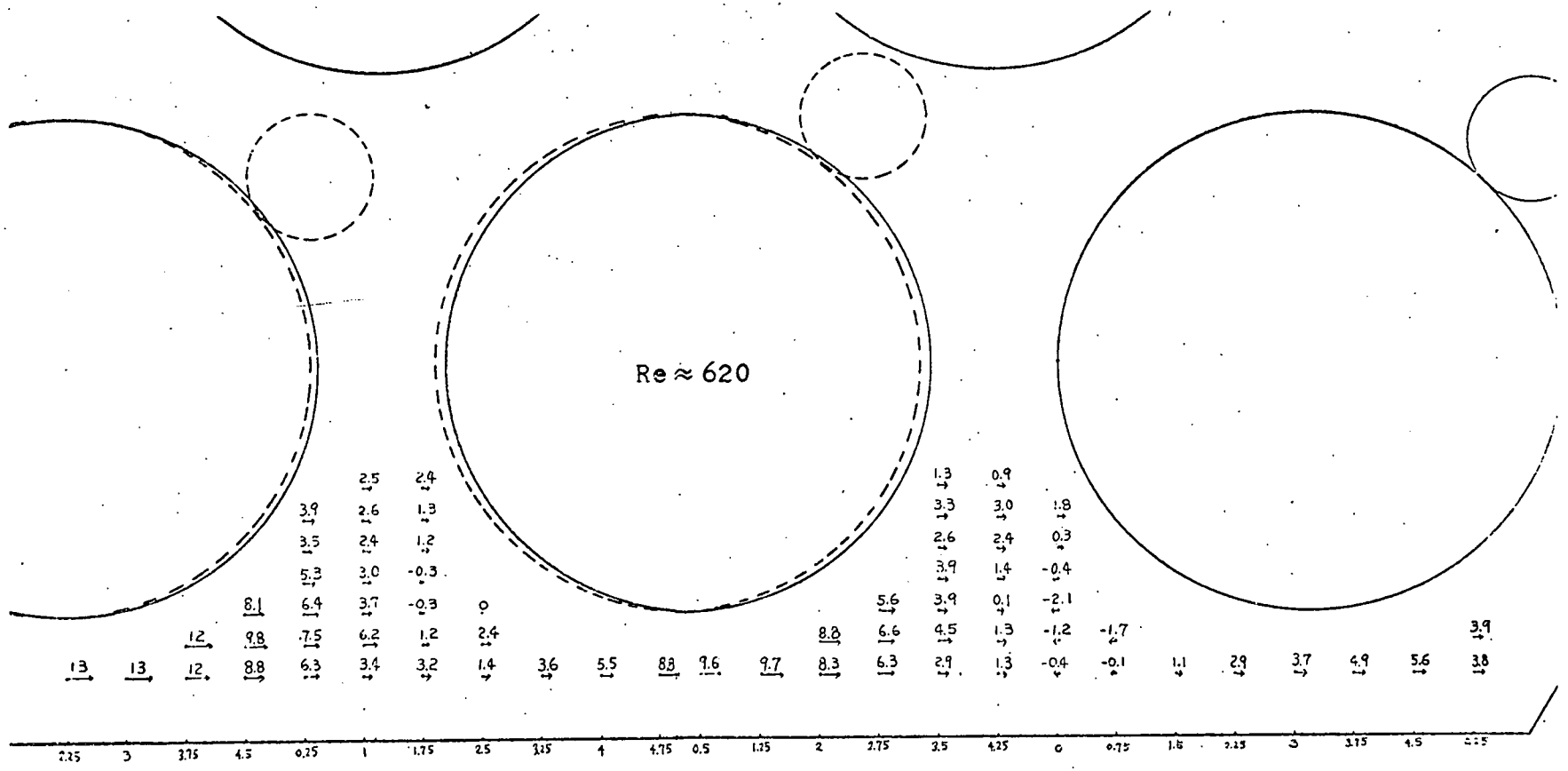

FIGURE 4.81 TRANSVERSE VELOCITY DISTRIBUTION IN PLANE 11

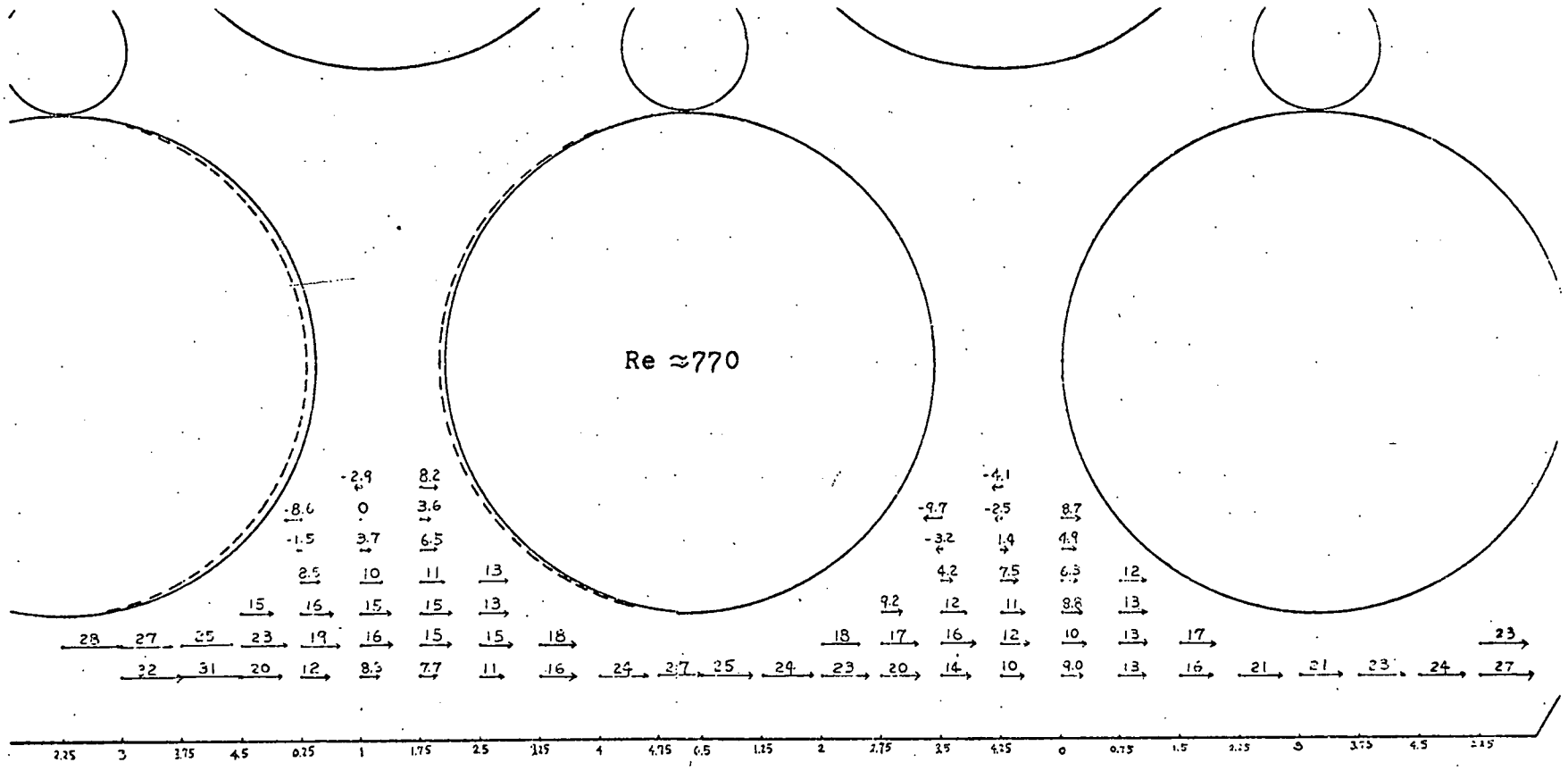

FIGURE 4.82 TRANSVERSE VELOCITY DISTRIBUTION IN PLANE 12

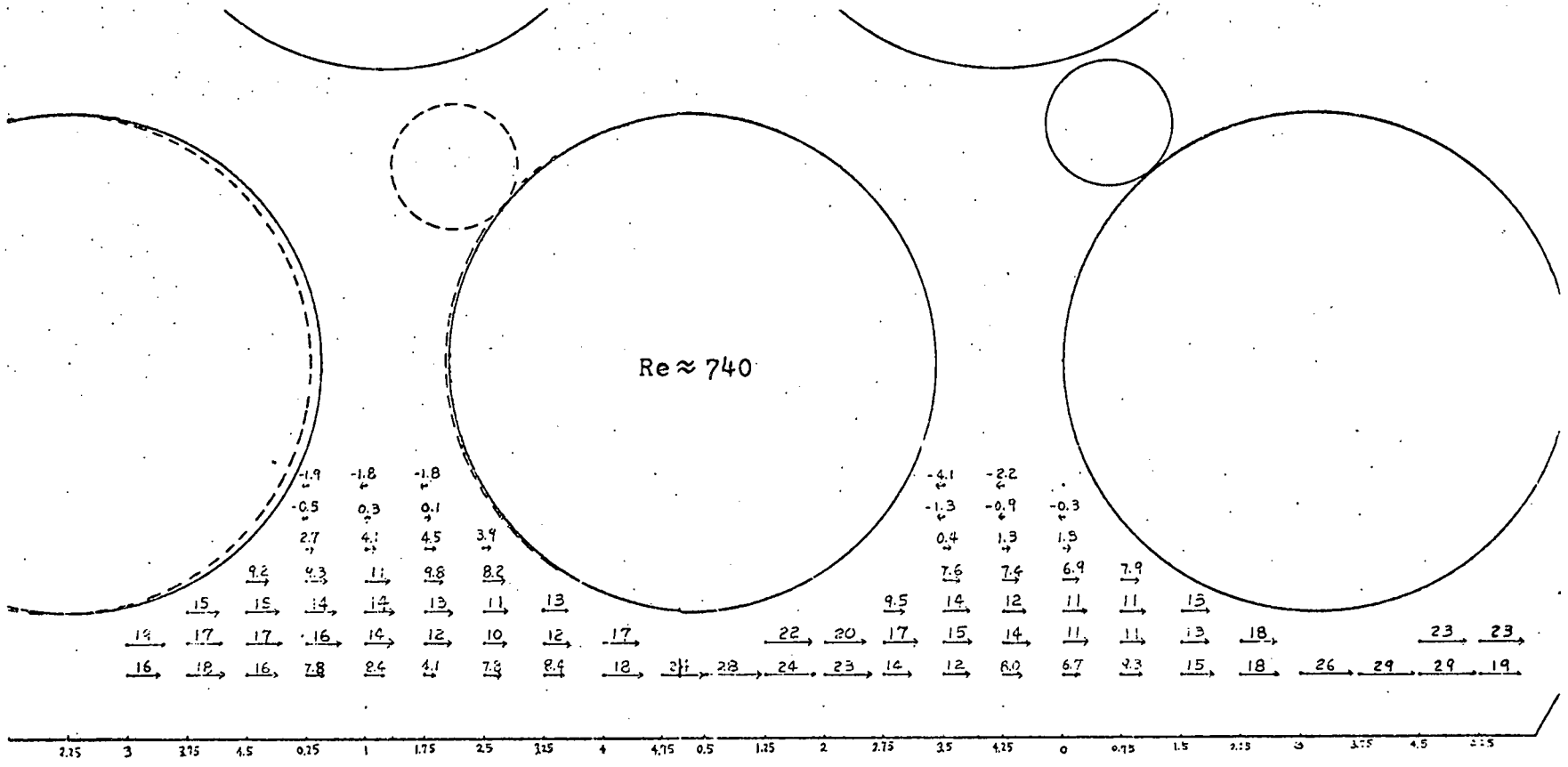

FIGURE 4.83 TRANSVERSE VELOCITY DISTRIBUTION IN PLANE 13

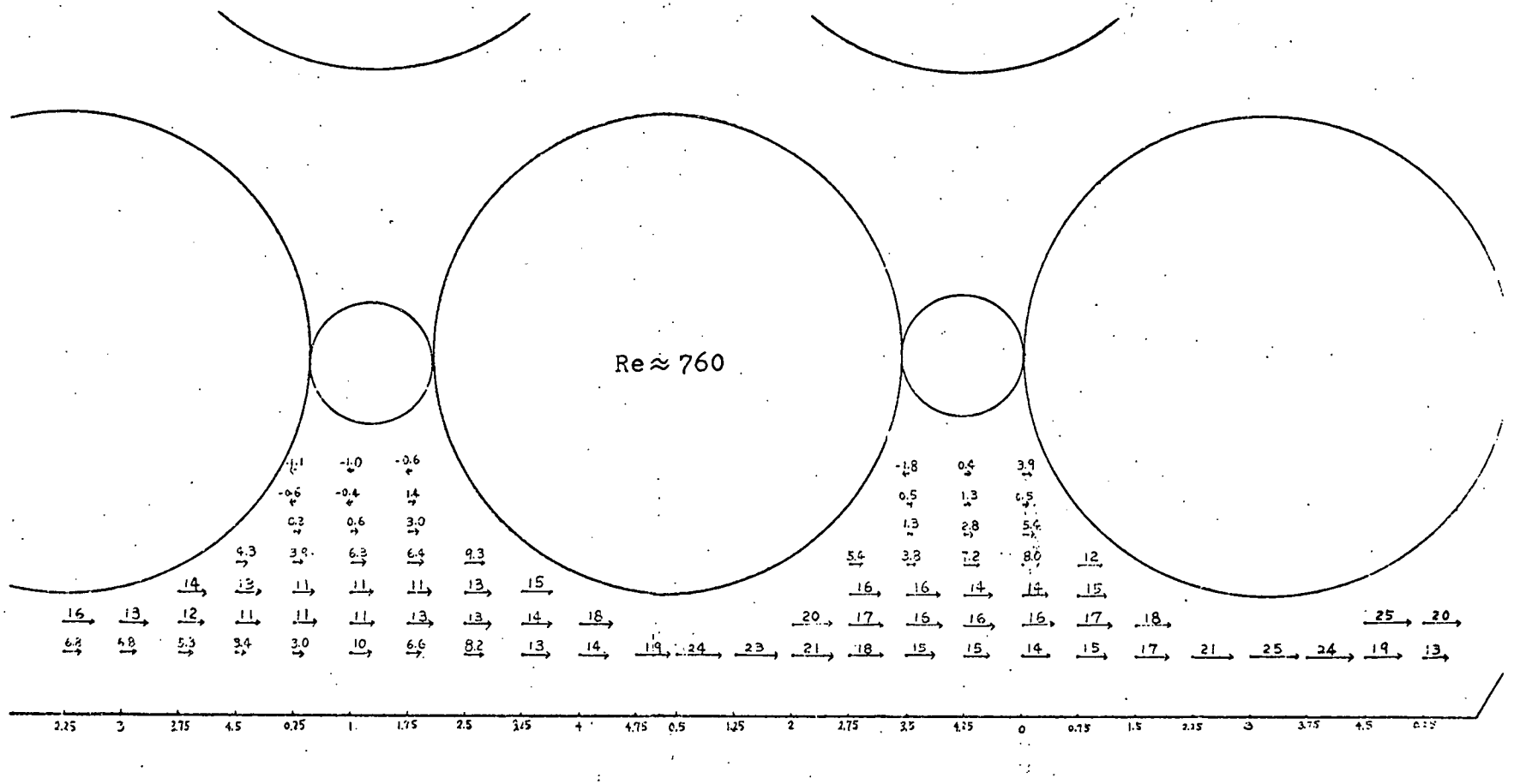

FIGURE 4.84 TRANSVERSE VELOCITY DISTRIBUTION IN PLANE 14

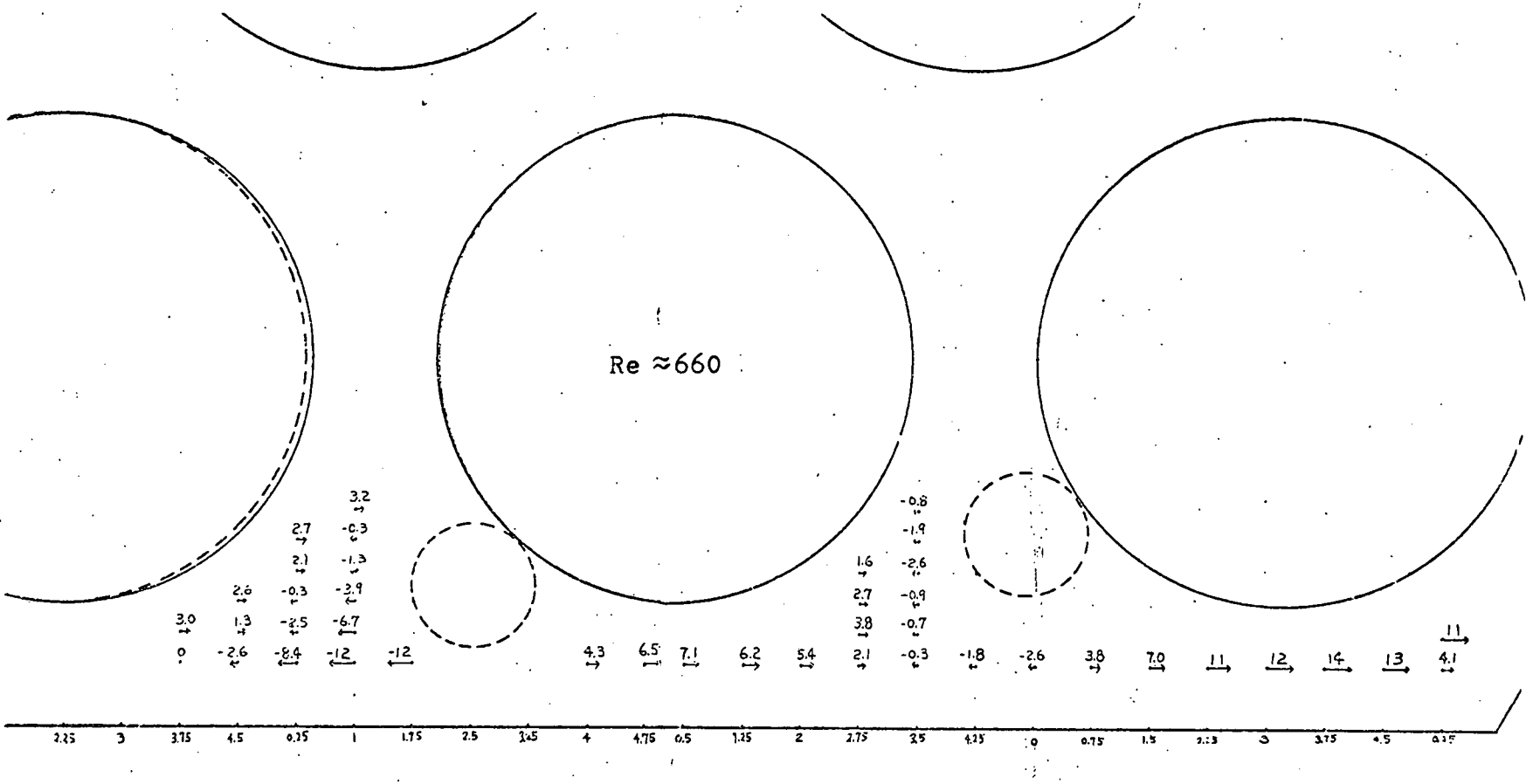

FIGURE 4.85 TRANSVERSE VELOCITY DISTRIBUTION IN PLANE 15

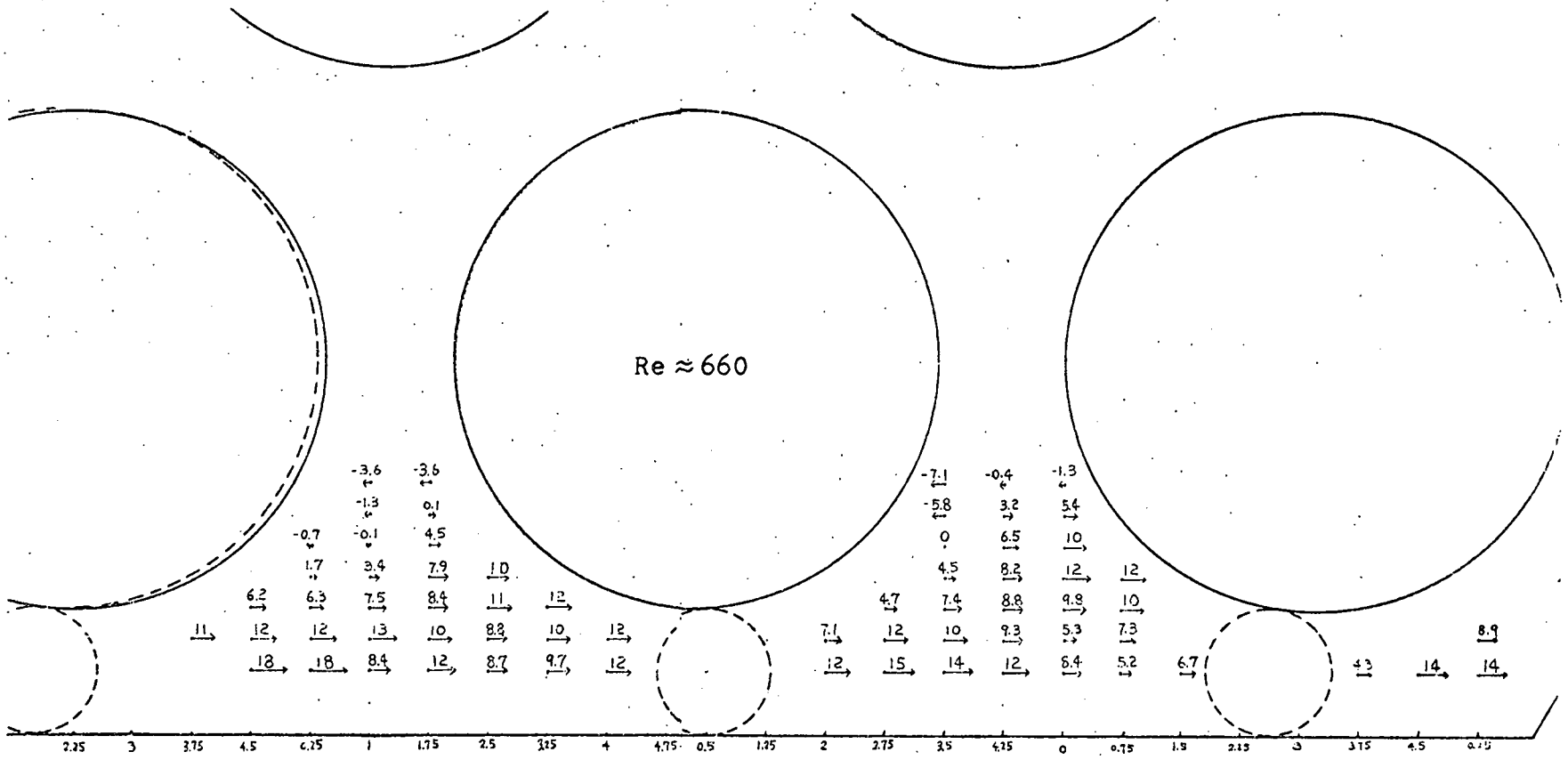

FIGURE 4.86 TRANSVERSE VELOCITY DISTRIBUTION IN PLANE 16

CHAPTER 5

INTERPRETATION OF RESULTS

5.1 Turbulent Intensity Measurement

From Fig. 4.1 the transition Reynolds number was determined to be 1500. Compared to the result of the rectangular test section (see Appendix I), the small transition Reynolds number is probably due to the wire effect. For high Reynolds numbers (or flow rate), the tracker could not follow the signal. The reason is explained in detail in Appendix A. Briefly for high flow rate a high power laser is needed to keep a sufficiently good signal to noise ratio. For our 50 mw laser, the best operating fluid velocity is less than 1 m/sec or about 4600 Reynolds number (assume uniform edge subchannel velocity at $T = 70^{o}F$). However it is hard to estimate how the accuracy of experimental results will be affected by insufficient laser power.

5.2 Axial and Transverse Velocity vs. Axial Position

5.2.1 12-inch Wire Axial Pitch Bundle

5.2.1.1 Laminar

From the plots presented in Figures 4.3 to 4.12,

a. The axial flow seems to have fully developed in the 2nd axial pitch, while the transverse flow looks like it is still developing in the 2nd axial pitch.

b. The maximum transverse gap velocity is about 30% of the bundle average velocity. It occurs when the wire position is at 10 o'clock (see Figure 4.2).

c. The value of $\overline{V_T(\text{center of gap})}/V_B$ is evaluated, where "$\overline{\qquad\qquad}$" indicates axially average over an axial pitch. The values are listed in Tables 5.1 The values of $\overline{V_T(\text{center of gap})}/V_B$ in the 4th pitch are plotted in Figure 5.1.

5.2.1.2 Turbulent

From the plots presented in Figures 4.13 to 4.22,

a. The axial flow seems to have fully developed in the 2nd axial pitch, while the transverse flow looks like it is still developing in the 2nd axial pitch.

b. The maximum transverse gap velocity is about 28% of the bundle average velocity. It also occurs when the wire position is at 10 o'clock.

c. The value of $\overline{V_T(\text{center of gap})}/V_B$ are listed in Table 5.1 and plotted in Fig. 5.1.

The measuring point which was in the middle of the gap is that location which has the maximum gap velocity and the length of measuring volume is 15 mil (1/4 of the gap). Thus the average transverse

gap velocity would probably be 20% and 40% less than the mean value for turbulent and laminar flow cases respectively. Khan, et al[6] using the Argonne and Oak Ridge data in the code ENERGY arrived at an estimate of 12 to 14% for the turbulent flow. In Fig. 5.1 the values of $\overline{V_T(\text{center of gap})}/V_B$ remain about the same from C to B to A towards the corner. This set of data disagrees with the prediction by Pederson, et al[2] for turbulent flow that the value increases by a very large amount as it approached the corner. They used hot water tracer injection method on a 91-element bundle.

5.2.2 6-inch Wire Axial Pitch Bundle

In this experiment, due to mistakes in constructing the wire starting position, the maximum error in the nominal wire starting position is as much as 1/8 inch. The wire geometry was adjusted so that any error was confined to the first pitch only. Consequently data were taken at the 3rd pitch which is believed far enough (40 edge subchannel hydraulic diameter) from the poor geometry area to yield reliable results. The values of $\overline{V_T(\text{center of gap})}/V_B$ are given in Table 5.1 and plotted in Fig. 5.1. The average gap transverse velocities are about 21% and 16% for turbulent and laminar flow cases respectively.

5.2.3 Both 12-inch and 6-inch Axial Pitch Bundles

For both set ups, the maximum transverse gap velocities occur when the wire was at about the 10 o'clock position, while the minimum occur at about 3 o'clock. This is close to the results obtained by Lorenz, et al[1] who used salt injection analysis in a 91-pin bundle of 12-inch axial pitch.

5.3 Flow Split

5.3.1 Nonsymmetry

For bare pin bundle, the velocity profile in the edge subchannel is quite symmetric. (see Ref. 7). Due to the introduction of the wire, the velocity profile is nonsymmetric as shown in Figures 4.39 to 4.70.

5.3.2 Average Edge Subchannel Velocity

The average edge subchannel velocity over the bundle average velocity at each plane has been calculated. (See Chapter 6 for method of data reduction.) The results are presented in Fig. 5.2. In all four cases, the minimum ocuur at about 10 o'clock; and the maximum occur at about 4 o'clock except for the 12-inch laminar case which occurs at about 2 o'clock. Pedersen, et al[2] reported that the maximum velocity occurs when the wire is at the 5 o'clock position; they used time-of-flight analysis of slug-dye injection and slug hot-water injection in a 91 pin bundle.

The pitch average velocity, $\bar{V}_A/V_B$, is calculated by averaging V_A'/V_B over 8 planes, (one axial pitch distance) and the results are shown in Table 5.2. These experimentally determined edge subchannel velocities are closer to the nominal bundle velocity than those predicted by the hydraulic diameter flow split concept. (See appendix J for details.)

Such a deviation was first anticipated by Graves and Catton[8] on their interpretation of 217 pin bundle salt conductivity results. It was further demonstrated by Pederson et al[2]. They used slug-thermal tracer injection and time-of-flight analysis in turbulent regime and obtained a value of 1.03. Lorenz, et al.[1] obtained a value of 0.99 in their salt injection experiment. Fig. 5.3[9] summarizes these data and shows the difference between theoretical predictions and available experimental data. Note particularly however that there are bounds as discussed in Appendix J on the theoretical flow split due to various possible distribution of as-built tolerances. These bounds are shown for the MIT bundle.

5.4 Detailed Axial and Transverse Velocity Distribution in Edge Subchannels - Laminar Flow

From Figures 4.71 to 4.86 we also can predict the magnitude and location of maximum transverse gap velocity, the location of maximum axial velocity, and nonsymmetry in axial velocity distribution. The results agree with the conclusion in Section 5.2 and 5.3. But several additional conclusions on the transverse velocity behavior can be made.

1. For different wire positions the spatial location of the maximum axial velocity within the edge subchannel is different. From comparison of axial and

transverse velocity distributions, one might conclude that the shift of maximum axial velocity is related to the transverse velocity in the edge subchannel. For example, when wire is in 10 position (3 o'clock) the maximum velocity is shifted to left and when wire is in 12 position (12 o'clock) the maximum velocity is shifted to right.

2. Reverse flow was observed at some positions in all eight planes. This is probably due to the vortex in the edge subchannel or pressure difference between edge and interior subchannels.

3. The transverse velocity was observed to decrease as the measuring point was moved toward the interior subchannel. Therefore, we might expect that the transverse velocity in the interior subchannel is very low (at least less than 5%.) However, large transverse velocity (>5% in interior subchannel was observed in 7 pin bundle[3]. This is probably due to the bundle size effect, i.e. for small bundles (less than 19 pins) the transverse velocity in the interior subchannels is still significant.

These measurements cover axial velocity determinations at approximately same positions as measurements of Section 4.3.1.1. These measurements however are made at $\pm 45°$ from axial axis and hence yield both axial and transverse velocities whereas the measurements of Section 4.3.1.1 were made as direct axial velocity measurements to gain improved accuracy.

Figure 5.4 provides a typical comparison of the results of these two measurements. Note that most of the values for the indirect method were obtained by interpolation method. As seen from the figure the shape of the velocity within the subchannel are similar although the magnitudes are different. This difference may be due to the interpolation method and the wall roughness due to corrosion which existed during these (Section 4.4) measurements. However this effect did not exert a consistent effect on velocity as shown in Table 5.3. Finally the reproducibility of the data of Sections 4.3.1.1 was specifically confirmed as discussed in Section 6.3.2. Because the data of Sections 4.2 and 4.3 was obtained after that of Section 4.4, they are considered more reliable and should be used for numerical analysis. The data of Section 4.4 should be viewed as a qualitative representation of the flow field.

5.5 Velocity Vectors in the Edge Subchannels

From the experimental results in Section 4.2 we plotted the velocity vectors in the 4th and 3rd axial pitch for 12 inch and 6 inch bundle respectively. These are shown in Figures 5.5 to Fig. 5.8. Figure 5.9 is presented to facilitate the interpretation of the above mentioned figures. We have examined the velocity vector orientation as a function of axial position within an axial pitch. At the axial positions, where the wire is in the gap the velocity is zero since the wire occupies the measuring volume. Moving axially we observe that the velocity vector in gap positions rotates from axial achieving a maximum angle with respect to vertical (angle tilt) at approximately 10 o'clock. After the wire passes the 9 o'clock position, the tilt starts to decrease. This phenomenon is somewhat contrary to our intuitive thinking that the velocity vectors should have the largest tilt, although not the largest magnitude, within the axial pitch just downstream of the position where the wire is in the gap.

Although the normalized transverse velocity (V_T/V_B) is quite large in certain points, the ratio of local transverse and axial velocity is relatively small. due to the large local axial velocity. This is probably the reason why the dye injection method shows small swirl flow in the wire wrapped bundle.

5.6 Transverse Velocity versus Surface Roughness

At the same axial pitch the maximum and average transverse gap velocity are shown in Table 5.3 for different surface conditions. There seems to be no special relationship between the transverse velocity and surface roughness.

TABLE 5.1 $\overline{V_T(\text{center of gap})}/V_B$ AT MEASURING POINTS A,B,C

BUNDLE	FLOW REGIME	REGION	C	B	A
12-INCH	LAMINAR	2nd AXIAL PITCH	8.3	12.0	11.2
		3rd AXIAL PITCH	15.3	15.3	14.4
		4th AXIAL PITCH	16.0	16.4	18.5
	TURBULENT	2nd AXIAL PITCH	12.0	12.0	10.2
		3rd AXIAL PITCH	16.1	13.7	15.0
		4th AXIAL PITCH	15.3	16.0	16.0
6-INCH	LAMINAR	3rd AXIAL PITCH	24.1	27.7	25.6
	TURBULENT	3rd AXIAL PITCH	25.7	26.8	25.1

TABLE 5.2 $\overline{V_A}/V_B$ AT THE EDGE SUBCHANNELS 2

BUNDLE	FLOW REGIME	HYDRAULIC DIAMETER FLOW SPLIT PREDICTION*	THIS EXPERIMENT	ANL EXPERIMENT	AI EXPERIMENT
12-INCH	LAMINAR	1.25-1.41	1.19		
	TURBULENT	1.09-1.14	1.04	1.03[2] 0.99[1]	1.00[8]
6-INCH	LAMINAR	1.25-1.41	1.24		
	TURBULENT	1.09-1.14	1.02		

* see Appendix J

TABLE 5.3 TRANSVERSE VELOCITY VERSUS SURFACE ROUGHNESS

EXPERIMENTER	CHEN[11]		IP[10]	
LOCATION (WIRE, MEASURING POINT)	(13,B)	(14,B)	(13,B)	(14,B)
FLOW REGIME	LAMINAR	LAMINAR	LAMINAR	TURBULENT
SURFACE CONDITION	SLIGHTLY ROUGH	ROUGH	SMOOTH	SMOOTH
MAXIMUM TRANSVERSE GAP VELOCITY (V_T/V_B)	28%	22%	24%	24%
AVERAGE TRANSVERSE GAP VELOCITY (V_T/V_B)	14%	12%	12%	12%

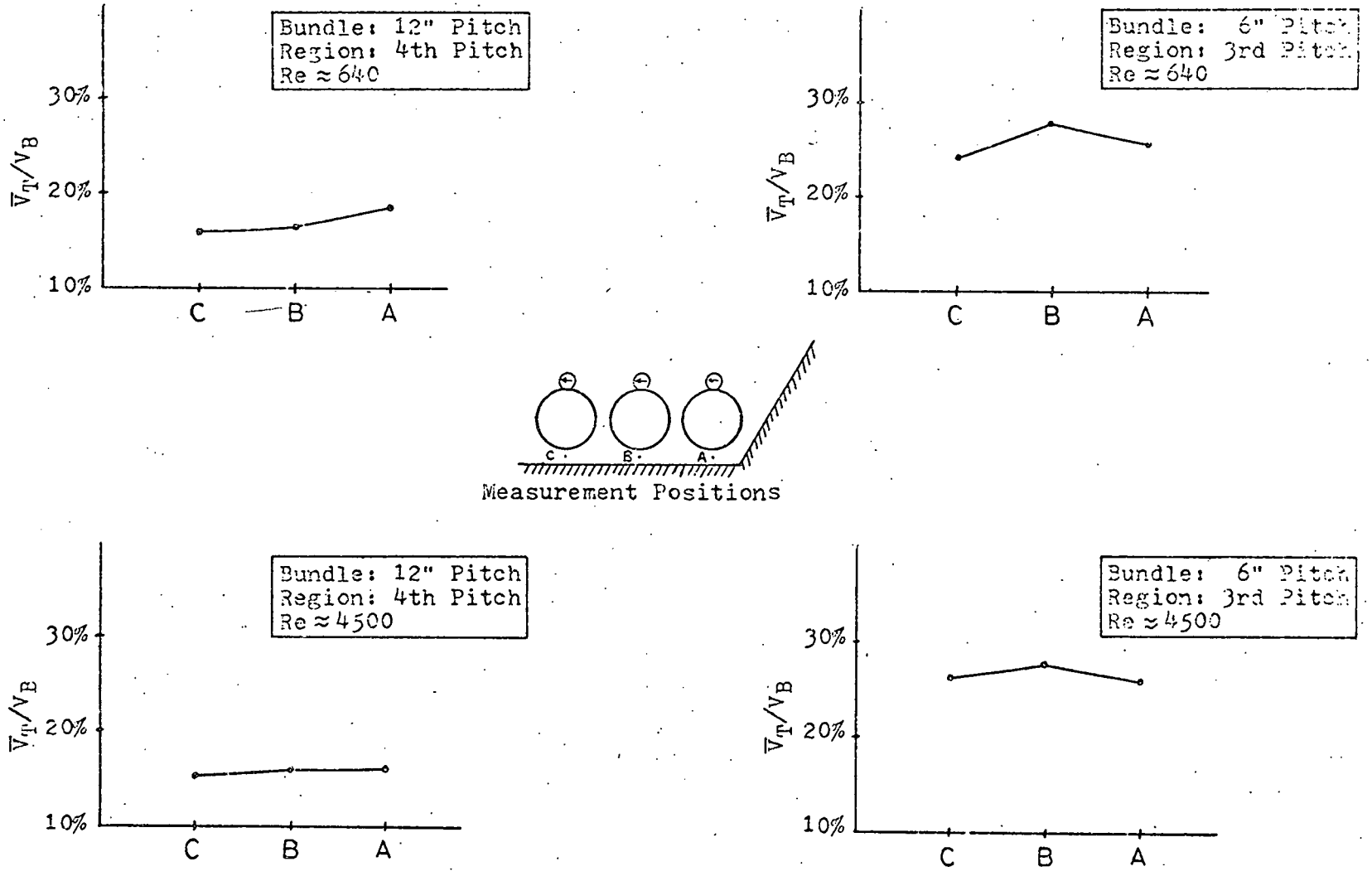

FIGURE 5.1 AXIALLY AVERAGED TRANSVERSE GAP VELOCITY MEASUREMENT

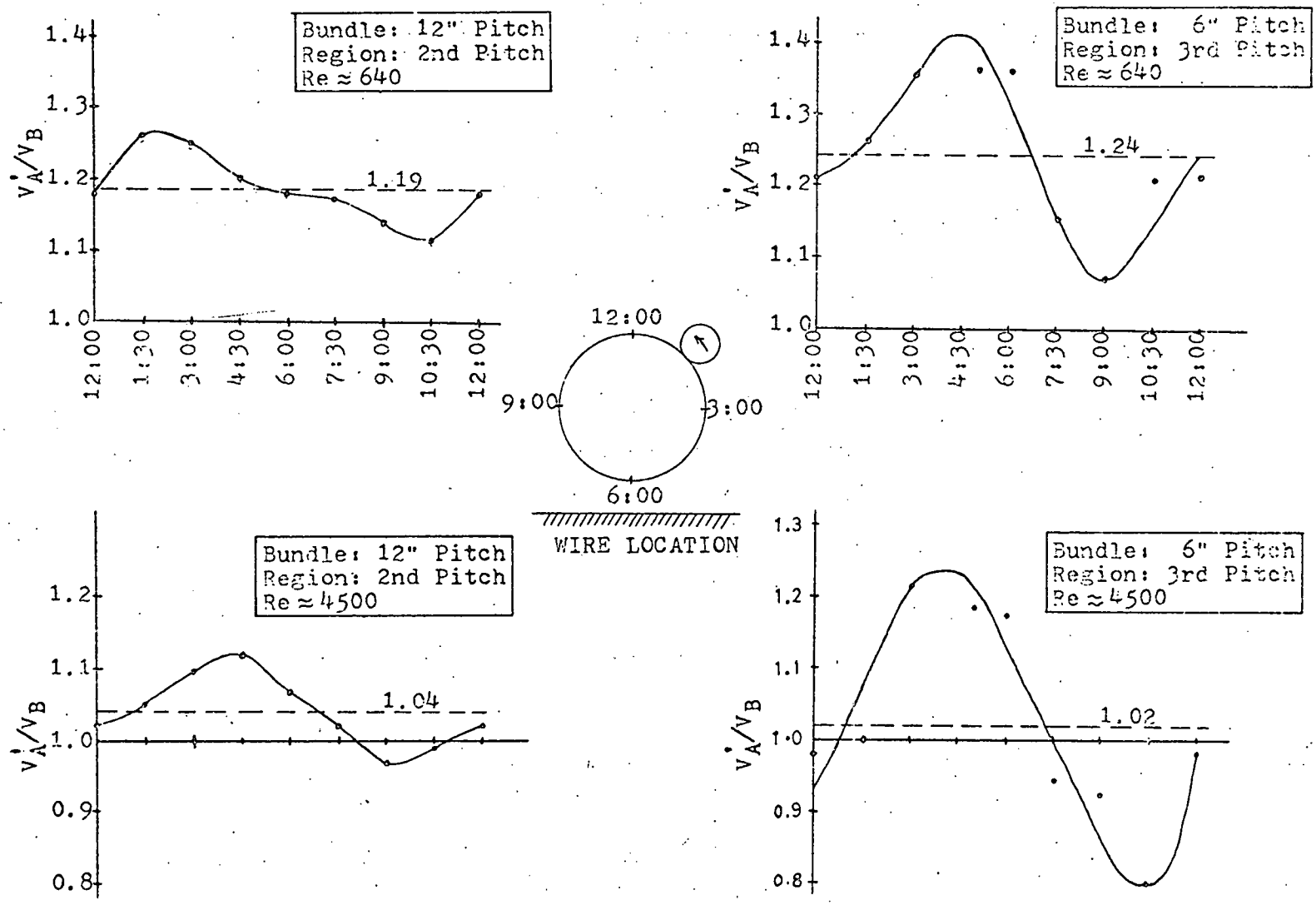

FIGURE 5.2 SUBCHANNEL AVERAGED AXIAL VELOCITY MEASUREMENT

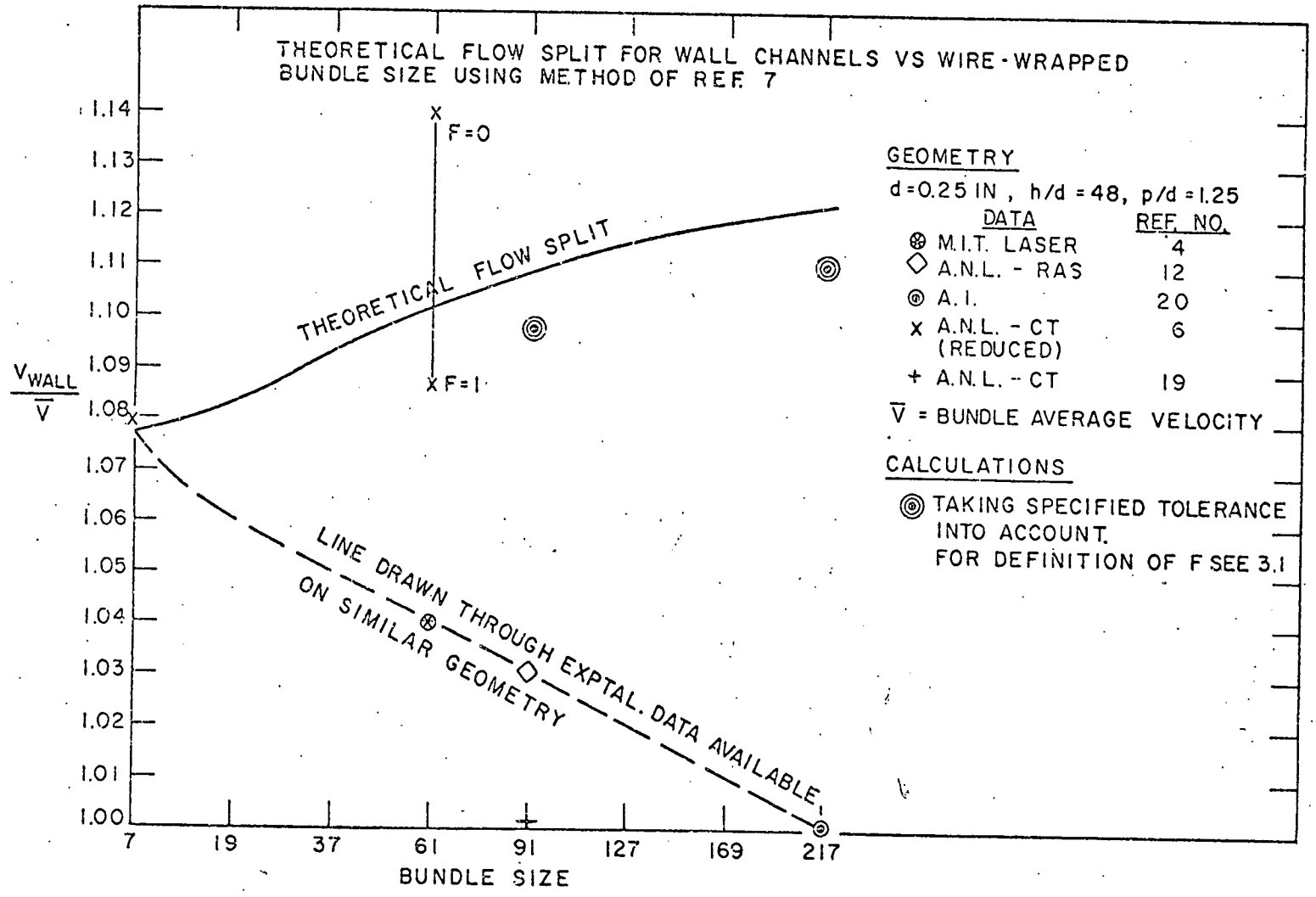

Fig. 5.3 Theoretical versus Experimental Flow Split [9]

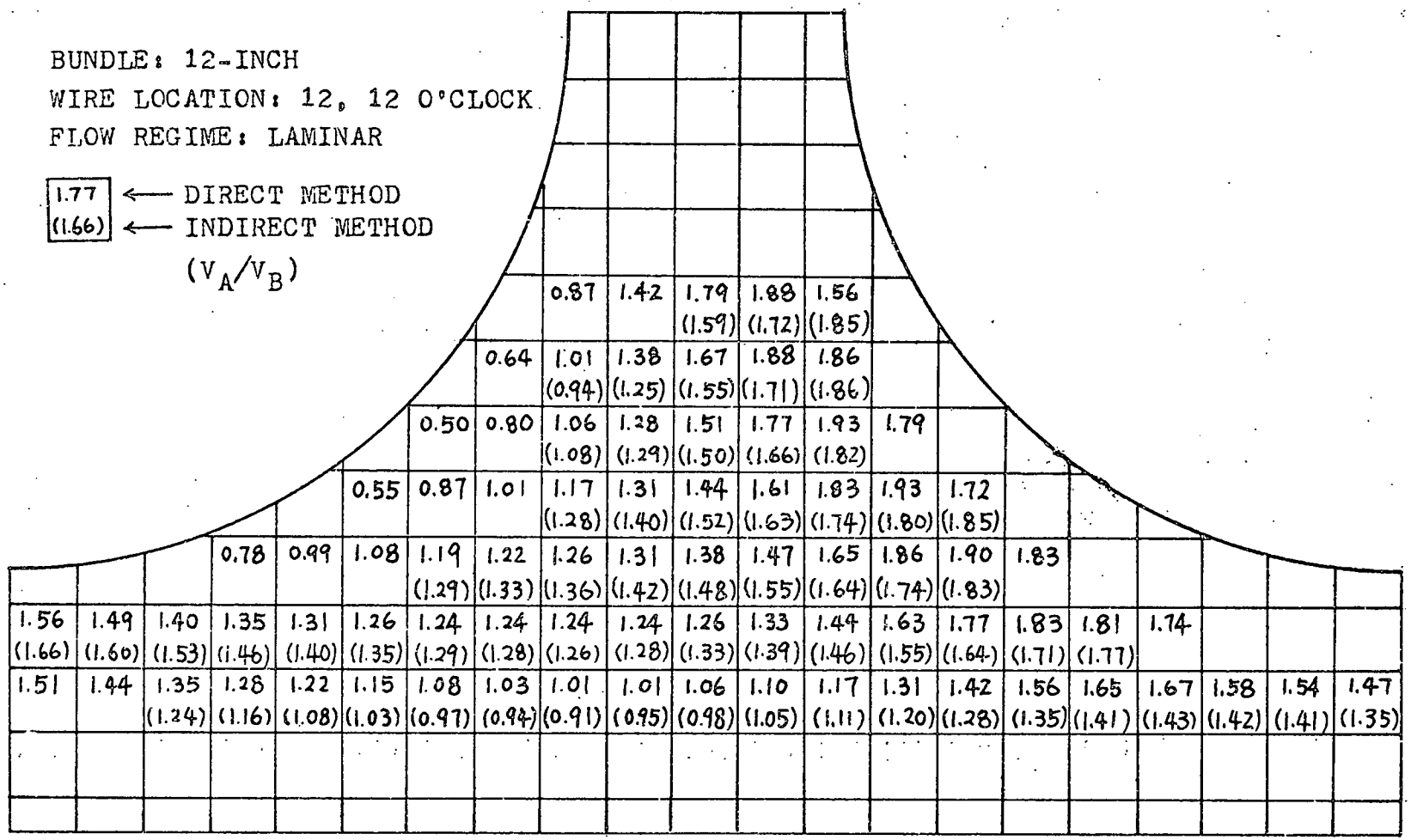

FIGURE 5.4 COMPARISON OF DIRECT AND INDIRECT METHODS FOR AXIAL VELOCITY MEASUREMENT

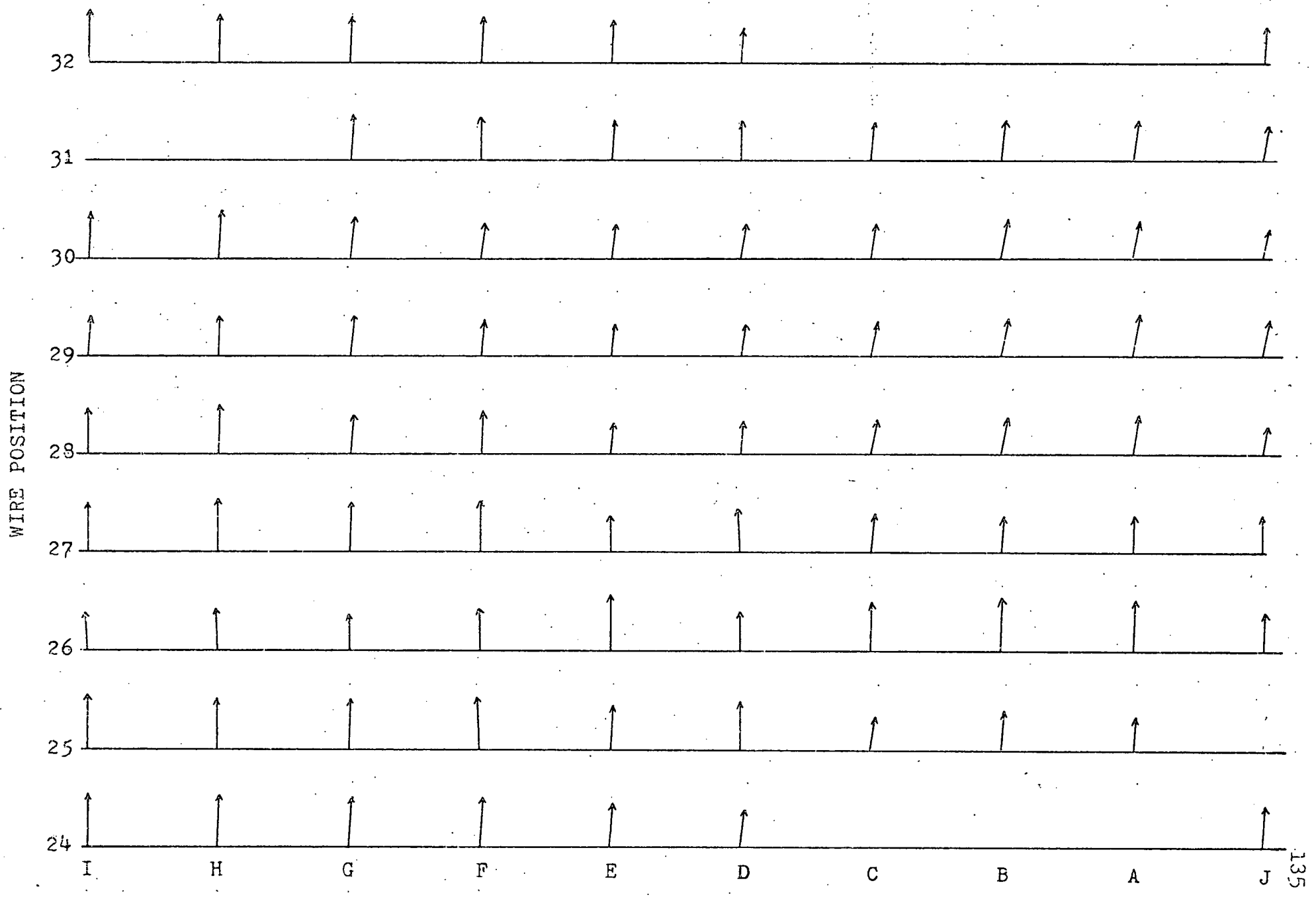

FIGURE 5.5 VELOCITY VECTORS, 12-INCH, LAMINAR

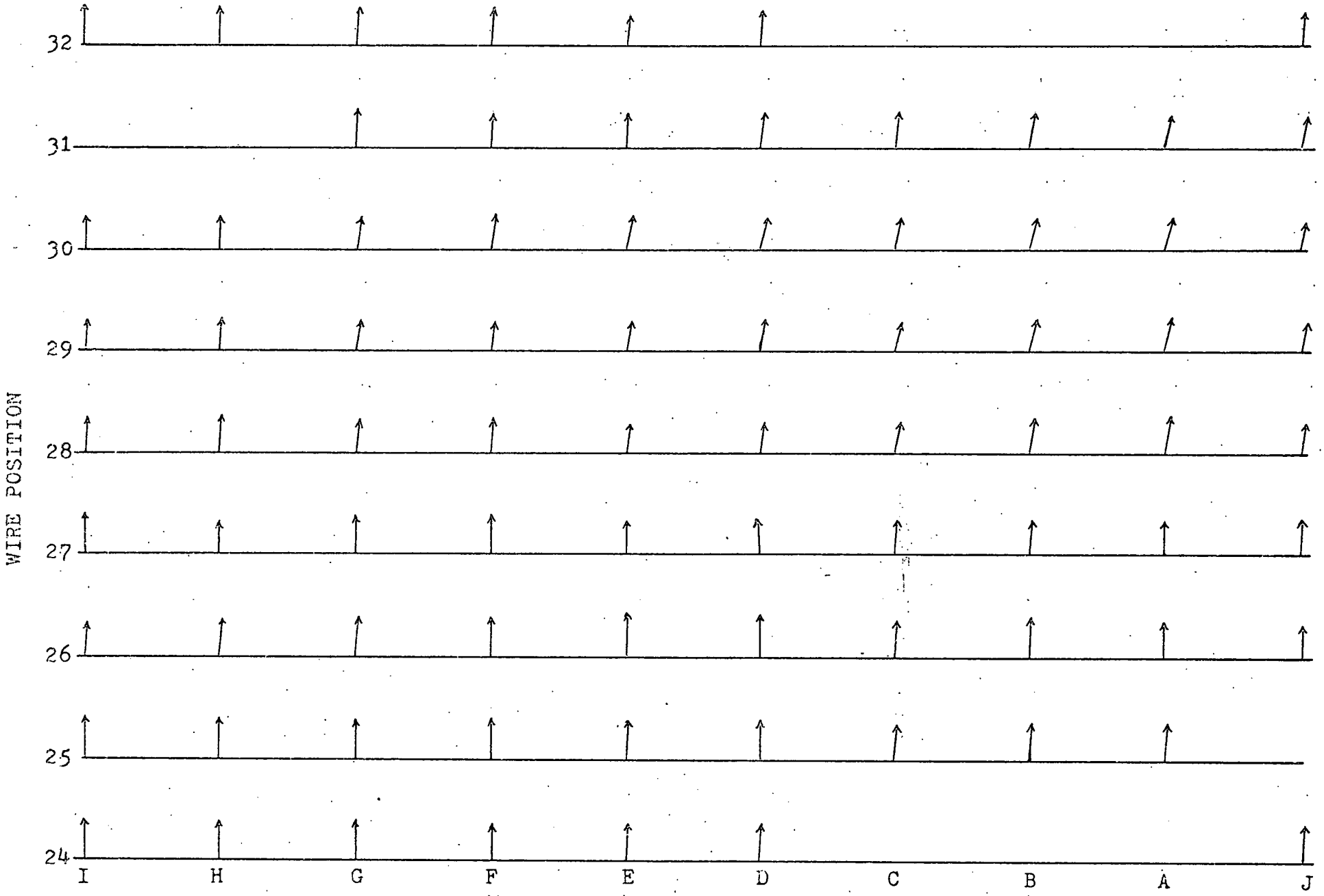

FIGURE 5.6 VELOCITY VECTORS, 12-INCH, TURBULENT

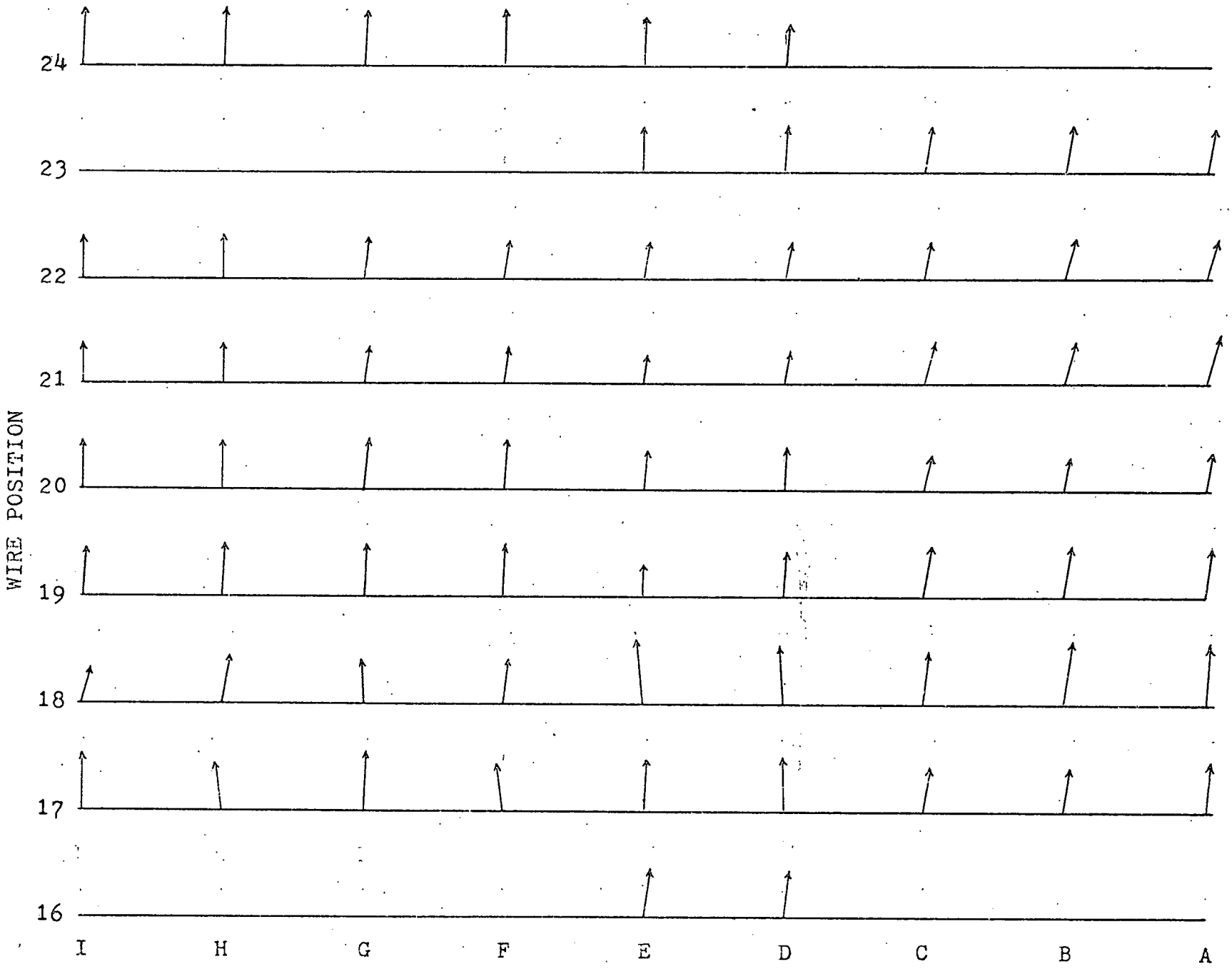

FIGURE 5.7 VELOCITY VECTORS, 6-INCH, LAMINAR

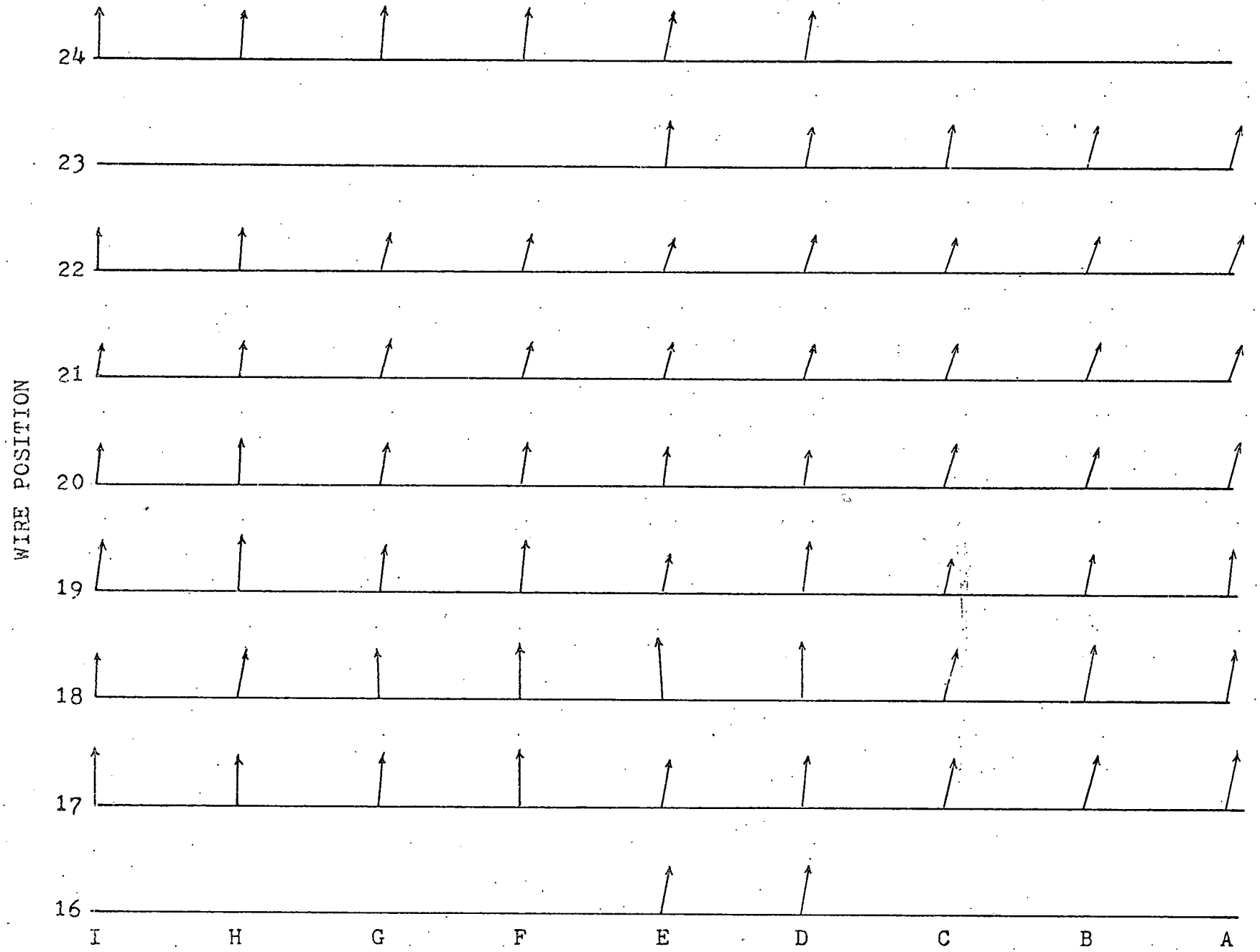

FIGURE 5.8 VELOCITY VECTORS, 6-INCH, TURBULENT

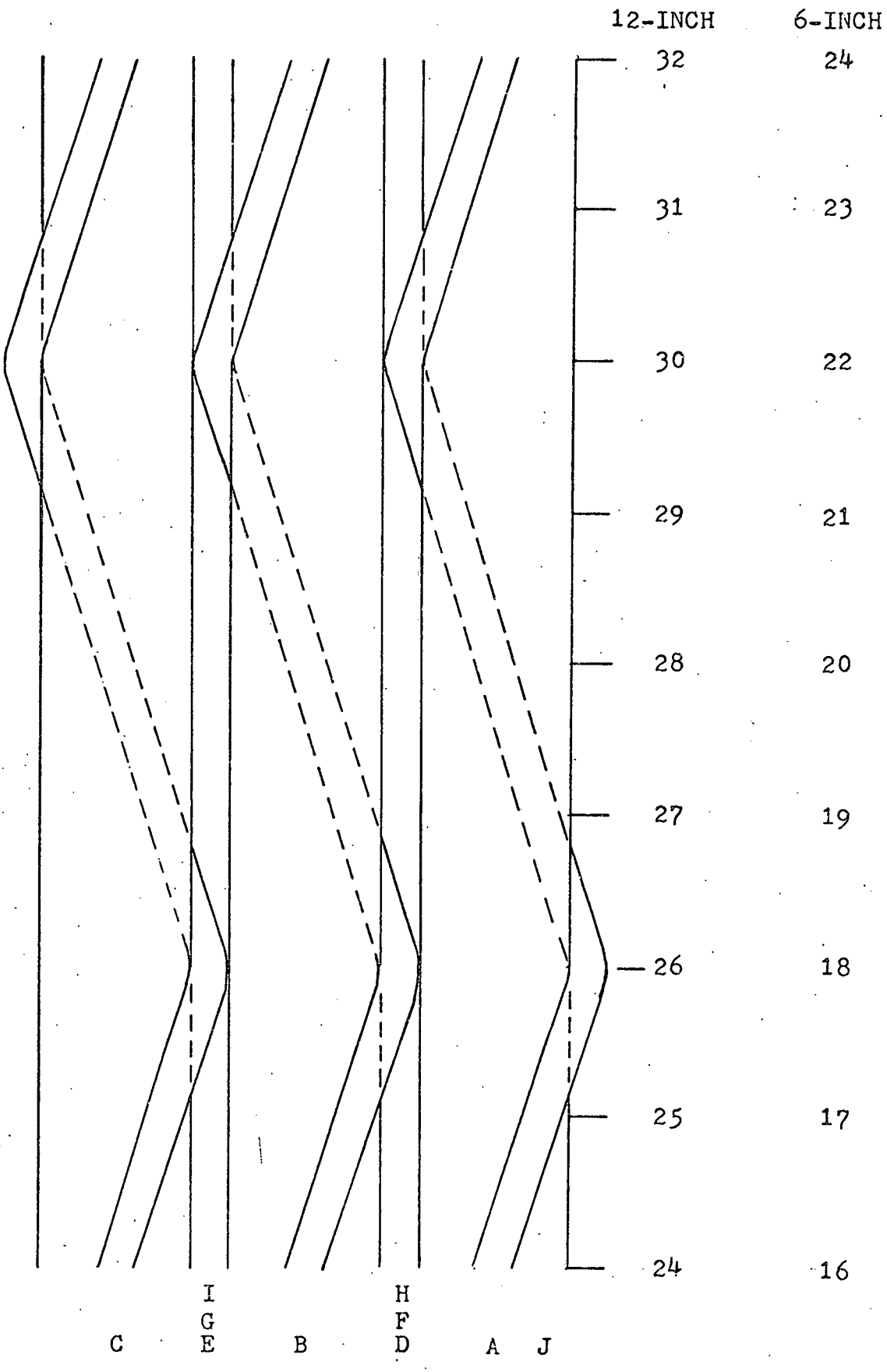

FIGURE 5.9 LOCATIONS OF MEASURING POINTS PRESENTED IN FIGURES 5.5 to 5.8 (NOT TO SCALE)

CHAPTER 6

DATA ANALYSIS

This chapter discusses the method of data acquisition, data reduction, and accuracy of experimental results.

6.1 Acquisition

The experimental procedures are discussed in Chapter 3 and Appendix H. Since the loop had a very stable flow, pressure, and temperature, no minor adjustment was necessary during data acquisition.

Data were taken by hand from the readings of the digital voltmeter and RMS voltmeter. No on-line storage or processing machine was used.

One output socket of the frequency tracker was first connected to a RC-integrating circuit with several different time constants, then fed to the digital voltmeter. This arrangement can smooth the signal and improve the readability of digital voltmeter. In order to save data acquisition time, a one second time constant was used in this experiment. The reading of the digital voltmeter corresponds to the mean velocity of the flow.

Another output socket of the tracker was connected to the RMS voltmeter. Since RMS voltmeter already has a built-in integrating circuit, the time average RMS value can easily be obtained. All the data presented in Section 4.2 and 4.3 are tabulated in Ref. 8. Data in Section 4.4 are tabulated in Ref. 9.

6.2 Reduction

6.2.1 Axial and Transverse Velocity Measurement

The calculation of axial and transverse velocity is simple and straightforward. Since velocity was measured at +45° and -45° from the axial axis, the axial and transverse velocity is simply

$$V_A = \frac{V_1 + V_2}{\sqrt{2}} \tag{6.1}$$

$$V_T = \frac{V_1 - V_2}{\sqrt{2}} \tag{6.2}$$

where

$$V_1 = \frac{\lambda f_1}{2 \sin \theta/2} \, , \; V_2 = \frac{\lambda f_2}{2 \sin \theta/2} \tag{6.3}$$

Based on the geometry of the bundle and optical unit setup, a data reduction procedure is given in Appendix C. A data reduction program for WANG Model 360K Programmable Calculator was written to reduce the recorded data. The program is listed in Appendix C. The reduced

data for Section 4.2 and 4.4 are tabulated in Ref. 8 and 9 respectively.

6.2.2 Flow Split Measurement

Since in the flow split measurement the squares are very small (only 15.6 mils square) the average velocity of the whole area inside a square is assumed to be equal to that measured at the center. Then the average edge subchannel velocity is calculated by integrating over all the flow area in the subchannel.

No data was obtained near the wall surfaces because the laser reflection from the wall was too great to make data acquisition possible. The velocities in these empty squares near the walls are estimated as follows.

In the laminar flow, the velocity was simply determined by extrapolating the velocity to zero at the wall surface.

In the turbulent flow it was estimated that the laminar boundary layer was about 5 to 10 mils thick. Within this layer, the velocity drops linearly to zero at the wall surface. The velocities are extrapolated accordingly. For example in Fig. 4.53 (12-inch, turbulent, at 6 o'clock) in the middle column near the flat wall, the velocities of the four and a half squares vary from 5.2 to 5.0 to 4.7 to 3.9. The velocity at the center

point of the last half grid was estimated by extrapolation as in the following sketch.

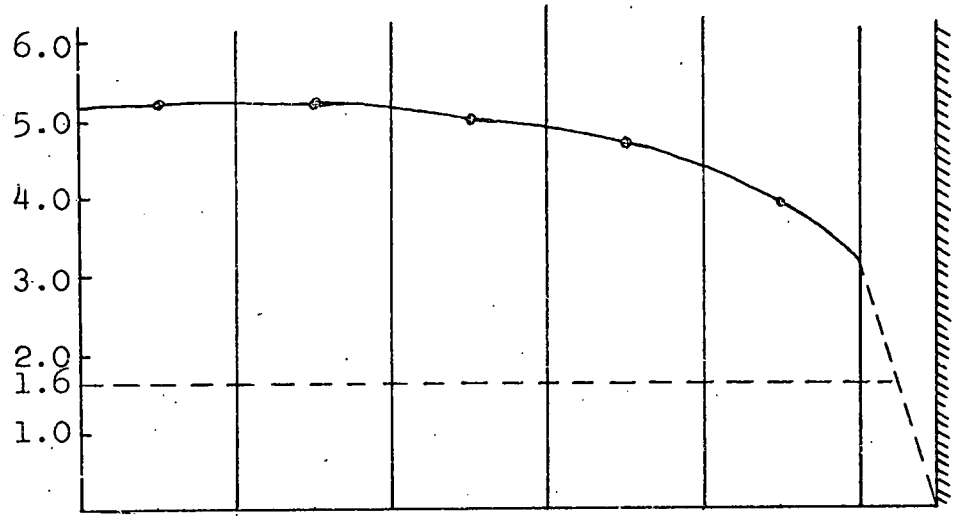

First the velocity was extrapolated using the measured velocities up to about 8 mils from the wall (solid line). From there to the wall the velocity was extrapolated linearly to zero (dashed line). By this method the voltage equivalent to the velocity at center point of the last half grid was estimated to be 1.6.

The reduced data for flow split measurement are presented in Ref. 8.

6.3 Errors

This section discusses the accuracy of the experimental results as affected by the LDA measurement technique and accuracy of the instrument.

6.3.1 Axial and Transverse Velocity Measurement

Errors in both measurement position and velocity determination exist.

The error in measurement position comes from two sources. First the gearing involved in carriage motion which positions the intersecting laser beams at the selected test region. This error was estimated by repeated positioning the beams at the reference position (see below) and noting the variation in dial indicator readings. Figure 6.1 shows the results that the intersection region lies in a region 19 mils by 3.5 mils. Second all positioning was referenced from a position on the inside surface of the duct wall laterally at the 9 o'clock position of the corner pin (see Figure 4.2). All data representations locate the rods at their theoretical locations within the bundle. It should be recognized that the pins may be moved from these locations.

The error in velocity determination comes from the following sources:

1. Uncertainty in the measurement angle.
2. Accuracy of the frequency tracker.
3. Signal broadening
4. Uncertainty of the measurement position

5. Uncertainty in the bundle flow area.

6. Uncertainty in the flowmeter reading.

Factor one, the uncertainty of angle, was determined to be $\pm 0.5^{\circ}$ by repeatedly rotating the optical unit to 45°.

Factor two, the overall accuracy of the tracker, is specified by the manufacturer to be about 1%.

Factor three, signal broadening, is discussed in detail in Appendix A. Since the average velocity was obtained by taking the time average of the Doppler signal, the value should be quite accurate. But this time average value was not constant in turbulent flow, thus, a visual average method was used. To account for the possible error, a 1% error is assumed for this factor.

Factor four is somewhat difficult to predict. Since V_1 and V_2 were not measured simultaneously, the two measuring points probably were not at the same location. If position 1 is the point we measured for V_1, the measuring volume 2 for V_2 will be within a 19 mil long by 3-1/2 mil wide area about position 1. Since the velocity gradient is small within that region, it is reasonable to assume 1% error for both V_1 and V_2.

Total errors due to these four factors are discussed in Appendix D. For the axial velocity the total errors is about 1.4%. For the transverse velocity the magnitude of error depends largely on the relative magnitude of the transverse and axial velocity. Typical values are shown below for different V_T/V_A ratio.

	Accuracy	
V_T/V_A	Transverse	Axial
0.01	± 140%	± 1.4%
0.1	± 14%	± 1.4%
0.2	± 7%	± 1.4%
0.3	± 5%	± 1.4%

The last two factors affected only the average bundle velocity. the ratio of axial or transverse velocity to bulk bundle velocity (V_A/V_B, V_T/V_B) will have errors due to these two factors. The uncertainty in the bundle flow area was estimated to be 2% (see Appendix G). The uncertainty of the flow meter reading is specified by the manufacturer to be 2%.

The total error for V_T/V_B and V_A/V_B is shown below:

	Accuracy	
$V_T/V_B(=p)$	V_T/V_B	V_A/V_B
0.01	± 140%	± 3.1%
0.1	± 14%	± 3.1%
0.2	± 7.5%	± 3.2%
0.3	± 5.5%	± 3.2%

The above values are derived in Appendix D.

Since in laminar flow the signal broadening is very small, the above estimated accuracy is very conservative. For turbulent flow the above estimation is probably quite good.

6.3.2 Flow Split Measurement

In the flow split experiment, the errors are estimated as follows:

1. Acquisition of axial velocity
   a. Tracker ± 1%
   b. Signal broadening ± 1%
   c. Measurement angle ± 0.3%
2. Variation in the ratio of axial to bulk velocity
   a. Bundle flow area ± 2%
   b. Flowmeter reading ± 2%
3. Determination of average normalized velocity
   a. Data reduction procedure ± 2%

The errors in tracker, signal broadening, bundle flow area, and flowmeter reading have been previously described.

The error in measurement angle is different than discussed earlier since here a direct measurement of axial velocity is made. As shown in Fig. 6.2:

$$V_A = V \cos \phi$$

When measurement axis has a small deviation $d\phi$ from the axial axis then the measured axial velocity also has a small variation dV_A about nominal value

$$dV_A = -V \sin \phi \, d\phi$$

The percentage of axial velocity change is

$$\frac{dV_A}{V_A} = -\tan \phi \, d\phi$$

In this experiment the maximum tan ϕ is 0.3. (in 6-inch axial pitch bundle) and $d\phi$ is estimated about $\pm$ 0.5° (0.00873 radian). Thus the error in measurement angle is calculated to be about $\pm$ 0.3%.

In data reduction, since velocity values near the wall surfaces are lacking, there is an uncertainty in the velocity extrapolation. A conservative estimate for this error is 2%.

Using the approach in Appendix D, the total error in the flow split results is equal to

$$\sqrt{1^2 + 1^2 + (0.3)^2 + 2^2 + 2^2 + 2^2} \approx 4\%$$

One more possible error is the error in edge subchannel measurement region. As discussed in Appendix J, the real geometry of the edge subchannel is different from the ideal geometry due to the various possible distribution of the as-built tolerances. Figure 6.3 shows the two extreme cases (F = 0 and F = 1). The shaded regions represent the actual measurement regions. Although we did not know the exact magnitude of the error, but it was judged to be small compared to the total error.

During the experiment, corrosion occurred at the corners of the aluminum housing. In the 12-inch set up the aluminum oxide formation at any position was estimated to be about 4 mils diameter sphere. About 10% of the burdle length at the corners was corroded. In the 6-inch set up, the oxide was about 8 mils diameter and covered about 20% of bundle length. Our measurement points are reasonably far from the corners, we believe the corrosion products had little effect, if any, on our results. This corrosion decreased the bundle flow area. However this decrease is very small compared to the variation possible in bundle flow area due to tolerances on pins, wire and flow channel fit up. The net effect of these uncertainties is well covered within the large, 2%, uncertainty assumed above in bundle flow area.

Some data were repeated in this experiment to test the reproducibility. These data are plotted in Figures 4.5 and 4.10 in small crosses.

6.3.3 Average Transverse Gap Velocity

6.3.3.1 Axially Averaged Transverse Gap Velocity (center of gap)

The axially average transverse velocity was obtained by dividing the area under the curve (for example, figure 4.8) by the length over one axial

pitch. The error for this value was determined by the same way. First we calculate the ratio of transverse to axial velocity at every point and then estimate the errors from Figure D.2. Plot a point with maximum uncertainty for every point then draw a dashed line to connect all these uncertainty points (See Figure 6.4). We can estimate the axially averaged velocity for the dashed line. The error is then the percentage change of the axially averaged transverse gap velocity. The typical values are shown in Table 6.1.

6.3.3.2 Average Transverse Gap Velocity

When we estimate the average transverse gap velocity, we assume that the average value is 20% or 40% less than the value measured in the center of gap for the turbulent and laminar cases respectively. In the turbulent flow it is known that the ratio of average to maximum velocity is approximately 80%. In the laminar flow the corresponding value is 60%. (This value is between 66% and 50% for parallel plate and circular tube respectively). Since we don't know the exact velocity profile, the estimated average transverse gap velocity will have some uncertainties.

TABLE 6.1 TYPICAL ERRORS FOR TABLE 5.1

BUNDLE	12-INCH		6-INCH	
MEASUREMENT REGION	4th AXIAL PITCH		3rd AXIAL PITCH	
MEASURING POINT	B		B	
FLOW REGIME	LAMINAR	TURBULENT	LAMINAR	TURBULENT
$\bar{V}_T/V_B$ x 100%	16.4	16.0	27.7	26.8
ERROR	12%	11%	10%	7.5%

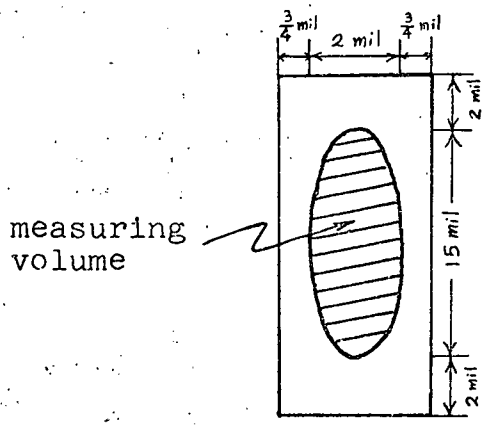

FIGURE 6.1 THE INTERSECTION REGION LIES WITHIN THE SQUARE AREA

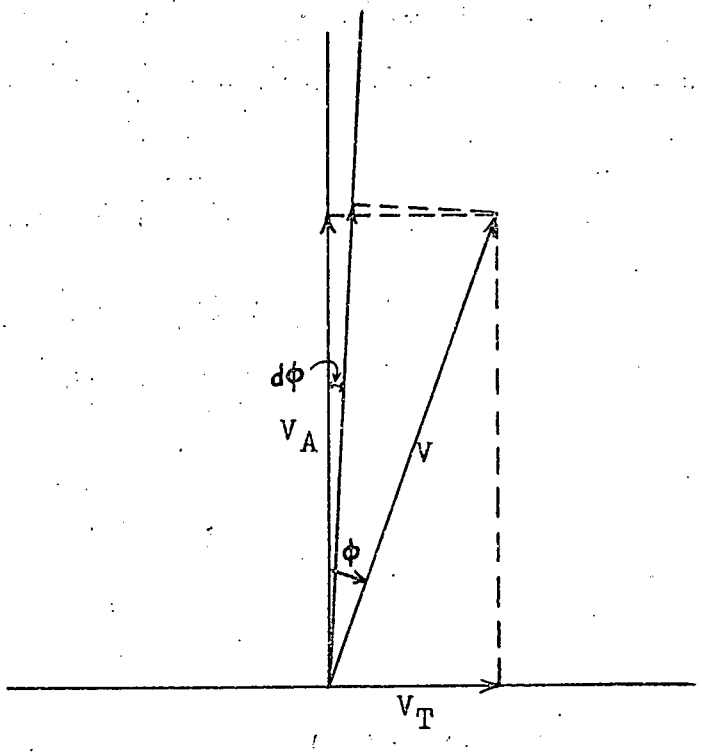

FIGURE 6.2 ERROR IN MEASUREMENT ANGLE

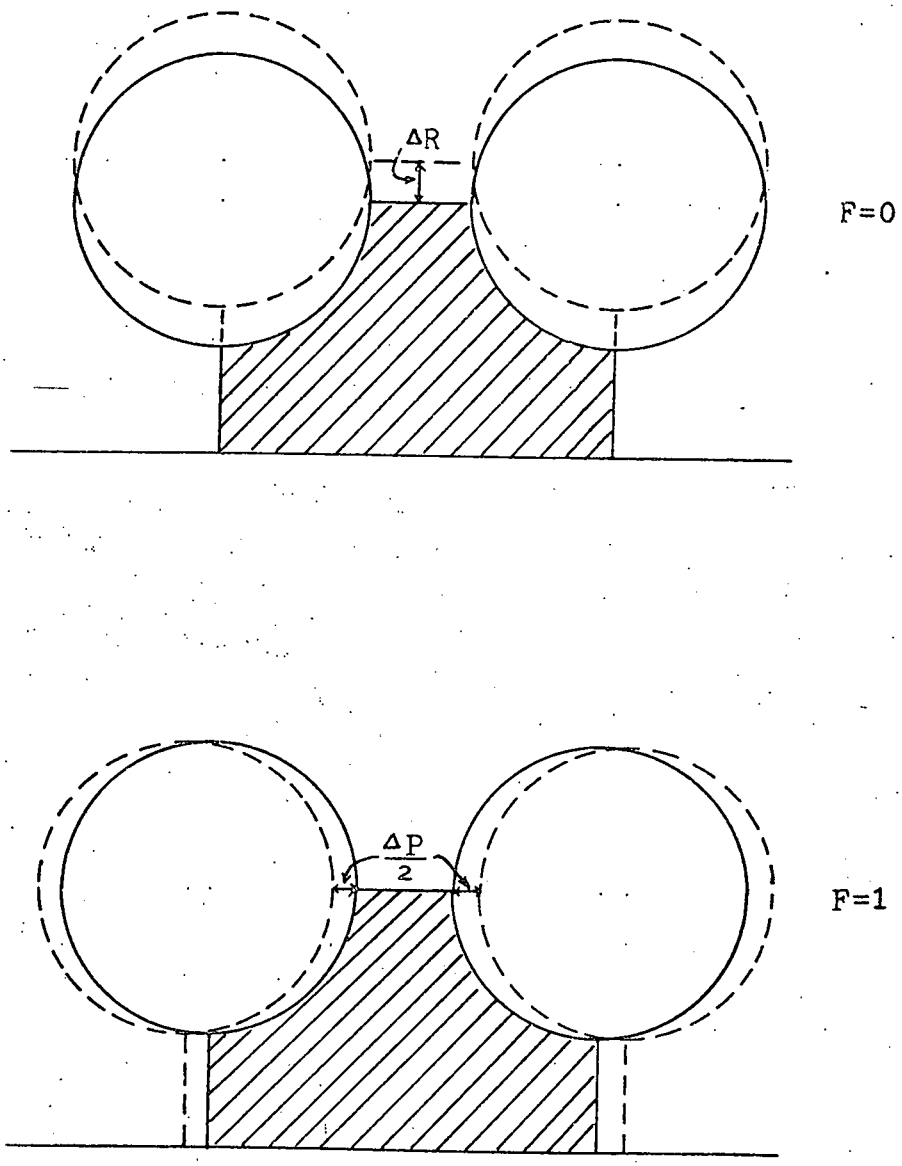

FIGURE 6.3 ERROR IN EDGE SUBCHANNEL MEASUREMENT REGION (NOT TO SCALE)

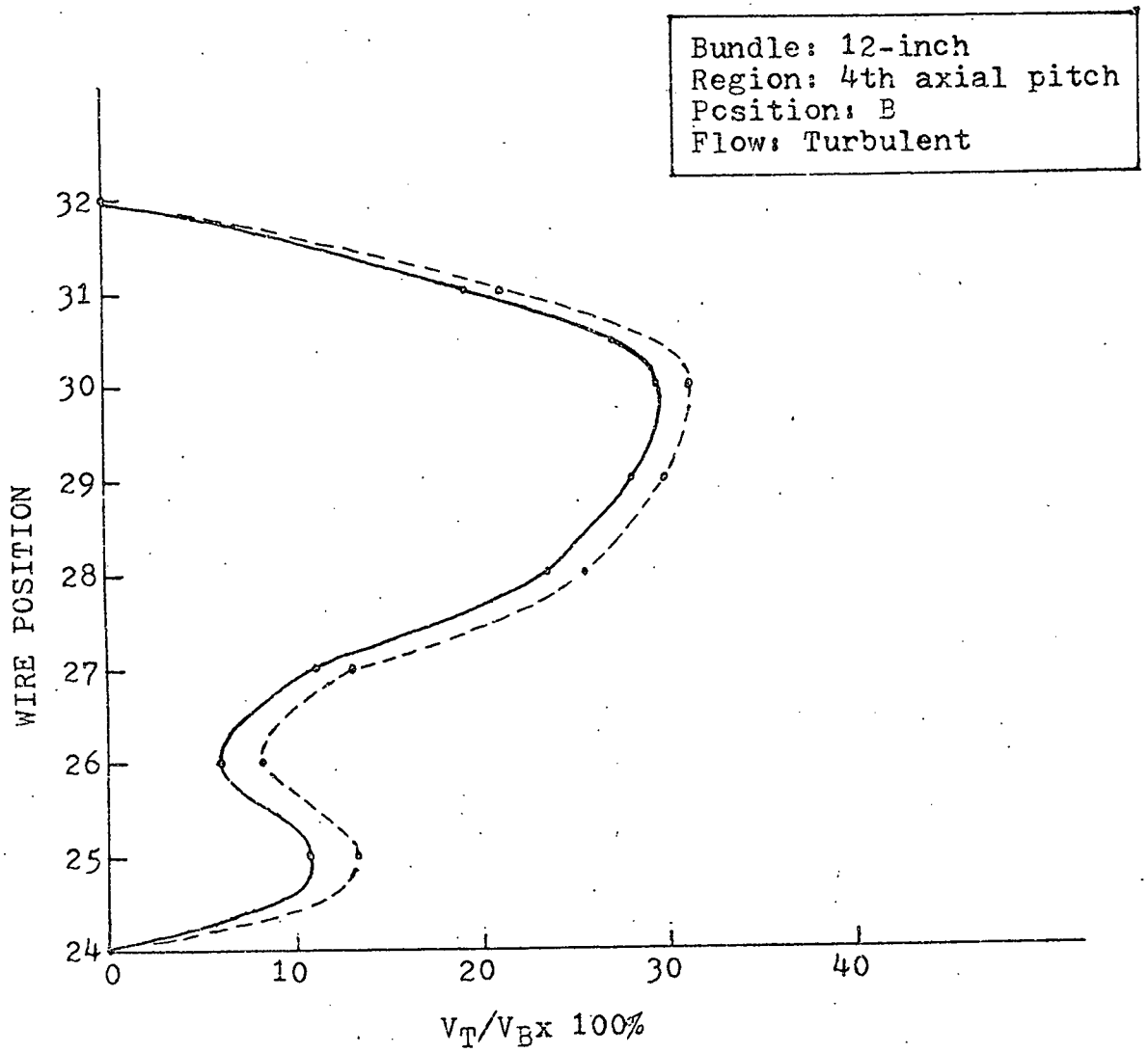

FIGURE 6.4 ESTIMATION OF ERRORS FOR AXIALLY AVERAGED TRANSVERSE GAP VELOCITY

CHAPTER 7

CONCLUSIONS AND RECOMMENDATIONS

The present experimental study has provided new and useful information about the axial and transverse velocity distribution and flow split phenomenon in the edge subchannels of wire wrapped bundle. The LDA also was proved to be a very useful technique to measure the local velocity in the bundle.

7.1 Conclusions

By using wire spacers, transverse velocity is generated which makes the velocity profile nonsymmetric. The ratio of average transverse gap velocity to bundle average velocity is found to be about twice the slope of the wire. And this average transverse gap velocity remains at about the same value along the flat wall of the bundle.

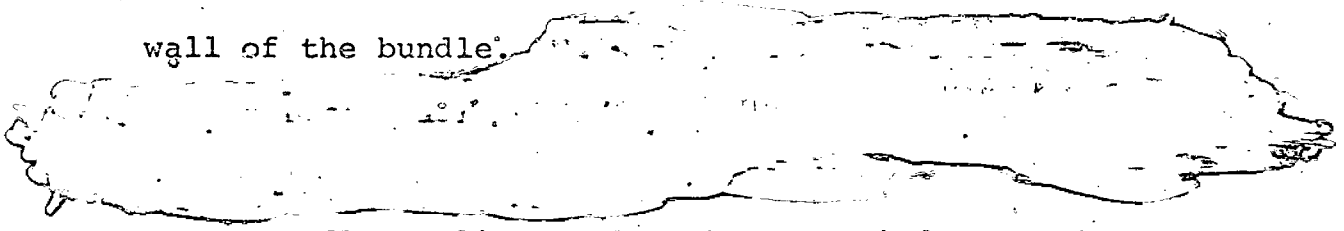

The flow split results show a much lower value at the edge subchannel than that predicted by the hydraulic diameter flow split prediction. When taken together with the flow split experimental results by other investigators, these results indicate that it might be necessary to refine the hydraulic diameter flow split theory for wire wrapped bundles.

7.2 Recommendations

1. Since backward scattered mode must be used in this experiment, a high power laser (probably 2W Argon laser) is needed for high velocity flow measurement.

2. In order to improve the accuracy of the results, direct velocity measurement is needed instead of indirect method used in the present experiment. For the direct method a frequency shifter is required to measure the small or reverse flow.

3. Transverse velocity profile in the gap is recommended to be measured in order to get accurate average transverse velocity.

4. Since LDA is a new technique to measure the fluid velocity, the signal processing system (or tracker) is still under development by many investigators. Future work should be performed with improved tracking systems.

5. Due to the serious corrosion in the aluminum hexagonal housing future test sections should be made of stainless steel, or care should be taken in assembling bundles to insure that galvanic action is precluded by elminating all conduction between stainless steel pins and aluminum housing.

6. A thin plexiglas faceplate is needed to replace the present 7/8 inch thick faceplate. The reason is given in Appendix A. But this thin faceplate should be still strong enough to hold the fluid pressure under any operating condition.

REFERENCES

1. Lorenz, J.J., T. Ginsberg, R.A. Morris, "Experimental Mixing Studies and Velocity Measurements With a Simulated 91-Element LMFBR Fuel Assembly," ANL-CT-74-09, March 1974.

2. Pedersen, D.R., Argonne National Laboratory, personal communication between Todreas, N.E. and Pedersen, D.R. in July 1974.

3. Wheeler, C.L., D.S. Rowe, J.D. Smith, "An Experimental Study of Axial and Crossflow Velocity in a 7-pin Wire Wrapped Bundle," BNWL-1804, February 1974.

4. DISA Type 55L Laser Doppler Anemometer Instruction Manual.

5. Deighton, M.O., E.A. Sayle, "An Electronic Tracker for the Continuous Measurement of Doppler Frequency From a Laser Anemometer," DISA Information , No. 12, 5, 1971.

6. Khan, E.U., N.E. Todreas, "Coolant Mixing in LMFBR Rod Bundles," Quarterly Progress Report, COO-2245-8, March 1974.

7. Rowe, D.S., "Measurement of Turbulent Velocity, Intensity and Scale in Rod Bundle Flow Channels," BNWL-1736, May 1973.

8. Graves, A.W., Catton, I., "A Numerical Model of Heat Transfer in a Rod Bundle With Helical Wire Wrap Spacer," ASME-72-HT-55, 1972.

9. Khan, E.U., N.E. Todreas, W. Rohsenow, A. Sonin, "Analysis of Mixing Data Relevant to LMFBR Wire Wrapped Fuel Assembly Thermal-Hydraulic Design," COO-2245-12TR, August 1974.

10. Ip, Ka-Lam, "Velocity Measurement in Edge Channel of Wire Wrapped Fuel Assembly by the Laser Doppler Method," S.M. Thesis, Dept. of Nuclear Engineering, MIT, June 1974.

11. Chen, Yi Bin, "Preliminary Velocity Measurement in Edge Subchannels of Wire Wrapped Bundle by the Laser Doppler Anemometer, S.M. Thesis, Dept. of Nuclear Engineering, MIT, September 1974.

12. Yeh, Y., Cummins, H., "Localized Fluid Flow Measurement with a He-Ne Laser Spectrometer," App. Phys. Letters, 4, 176, 1964.

13. Goldstein, R.J., D.K. Kreid, "Measurement of Laminar Flow Development in a Square Duct Using a Laser-Doppler Flowmeter," J. Apl. Mech., 34-E, 813, 1967.

14. Goldstein, R.J., D.K. Kreid, "Fluid Velocity Measurement from the Doppler Shift of Scattered Laser Radiation," University of Minnesota Heat Transfer Laboratory Technical Report No. 85, 1968.

15. George, W.K., J.L. Lumley, "The Laser-Doppler Velocimeter and Its Application to the Measurement of Turbulence," J. Fluid Mech., 60, 321, 1973.

16. Durst, F., Whitelaw, J.H., "Light Source and Geometrical Requirements for the Optimization of Optical Anemometry Signals," Opto-electronics, 5, 137, 1973.

17. Notes Purdue University International Short Course and Workshop on Laser Velocimetry, March 25-29, 1974.

18. Foreman, J.W., Jr., "Optical Path-Length Difference Effect in Photomixing With Multimode Gas Laser Radiation," Applied Optics, 6:5, 821, 1967.

19. Wilson, E.B., Jr., "An Introduction to Scientific Research," McGraw-Hill, New York, 1952.

20. Sangster, W.A., "Calculation of Rod Bundle Pressure Loss," ASME-68-WA/HT-35, 1968.

21. Novendstern, E.H., "Turbulent Flow Pressure Drop Model for Fuel Rod Assemblies Utilizing a Helical Wire Wrap Spacer System," Nucl. Eng. and Des., 22-1, August 1972.

APPENDIX A

LASER DOPPLER ANEMOMETER (LDA)

This section is included to give a brief explanation of the theory and application of the LDA system used in this investigation.

1. Introduction

Local fluid velocity can be measured from the Doppler shift of the laser radiation scattered by small particles which are moving with fluid. This technique was first demonstrated by Yeh and Cummins[12] in 1964. Since then, many investigators have attempted to develop this new technique.

The major advantages of LDA over conventional hot wire or hot film anemometer methods are:

1. Measurement is performed with laser beams, so no probes disturb the flow.

2. Measuring (or scattering) volume is very small, which gives high spatial resolution.

3. No calibration is required.

4. Fluid velocity is linearly proportional to the Doppler shift.

5. Direction sensitivity is ideal for two-dimensional measurements

2. Principles of Laser Doppler Anemometer

If a source of sound or electromagnetic waves of constant frequency is put into motion, a fixed observer will receive a different frequency. This is the well-known Doppler shift. A similar phenomenon is also observed when the source is fixed but the wave is scattered by the moving body before reaching a fixed observer. The Doppler shift of electromagnetic waves is usually very small relative to the source frequency and very difficult to detect. Conventional light sources usually have a bandwidth larger than the Doppler shift and this change in frequency cannot be detected from the broad signal. It is the introduction of the laser that permits the measurement of Doppler shift at optical frequencies. The laser is a source of monochromatic beam of light with a very small bandwidth. A single axial mode of the He-Ne laser operating at 6328 $\mathring{A}$ ($f \sim 10^{14}$ Hz) has a bandwidth of 10 Hz. The Doppler shift is usually larger than a kilo-Hertz. Although this is still small compared to source frequency, it is large compared to the source bandwidth and is thus detectable by heterodyne technique.

In Figure A.1 the scattered radiation from beam 1 to the fixed observer is[13]

$$f_{s1} = f_i \frac{1 - \frac{\vec{V} \cdot \hat{n}_1}{c}}{1 - \frac{\vec{V} \cdot \hat{n}_{sc}}{c}}$$

Similarly,

$$f_{s2} = f_i \frac{1 - \frac{\vec{V} \cdot \hat{n}_2}{c}}{1 - \frac{\vec{V} \cdot \hat{n}_{sc}}{c}}$$

The Doppler shift f_D is

$$f_D = f_{s1} - f_{s2} = f_i \frac{\frac{\vec{V}}{c} \cdot (\hat{n}_2 - \hat{n}_1)}{1 - \frac{\vec{V} \cdot \hat{n}_{sc}}{c}}$$

Since $|\vec{V}| << c$

$$f_D \approx \frac{n}{\lambda_o} \vec{V} \cdot (\hat{n}_2 - \hat{n}_1) \qquad \text{(A.1)}$$

where λ_o is the vacuum wavelength of the laser beam and n is the index of refraction of the fluid.

Note:

1. If the direction of two incoming light beams is fixed, the Doppler shift gives the component of velocity in a given direction ($\vec{V} \cdot (\hat{n}_2 - \hat{n}_1)$). This result permits us to measure components of velocity in any direction.

2. LDA has 180° ambiguity of the velocity direction, i.e. for the velocity $\vec{V}$ and $-\vec{V}$ the Doppler shift is the same (see Equation (A.1)). Unless a frequency shift device is used, the LDA will give an erroneous result for small and possible reverse flow.

A photomultiplier is used to receive the scattered light. The probability for the emission of electrons from the photocathode is proportional to the intensity of the light incident upon it. However, the intensity of light is proportional to the square of electric field intensity. Consider two monochromatic light beams of slightly different frequency incident upon the surface of photocathode. The two light beams may be represented by:

$$E_1 = E_{10} \sin 2\pi f_o t$$

$$E_2 = E_{20} \sin 2\pi (f_o + f_D) t$$

The output current i_D is proportional to the square of the total electric field intensity incident on it

$$i_D \propto (E_1 + E_2)^2 = E_{10}^2 \sin^2 2\pi f_o t + E_{20}^2 \sin^2 2\pi (f_o + f_D) t + E_{10} E_{20} [\cos 2\pi f_D t - \cos 2\pi (2 f_o + f_D) t]$$

Since the photomultiplier cannot follow frequencies greater than several hundred MHz, terms in the expansion involving f_o, $f_o + f_D$, and $2f_o + f_D$ will give rise only to a D.C. current proportional to the time average of those terms. If, however, f_D is below 100 MHz, there will be an A.C. signal of frequency,

$$i_D \propto \frac{E_{10}^2 + D_{20}^2}{2} + E_{10} E_{20} \cos 2\pi f_D t \qquad (A.2)$$

The first term is the D.C. current and the second term is the A.C. or Doppler current. To determine the velocity, the spectrum of the photomultiplier current is analyzed and the resulting Doppler frequency is used in Equation A.1 to compute $\vec{V}$.

The above derivation is based on a rigorous mathematical approach. However, an explanation that is generally easier to visualize is available for the differential beam mode. When the two coherence

monochromatic light beams cross each other they interfere in a way to establish a "fringe pattern" or regions of alternating high and low light intensity as in Figure A.2.

As a particle passes through this fringe area, the intensity of the scattered light from the particle will vary as it passes through regions of low intensity to regions of high intensity. When this scattered light is collected by the photomultiplier it is converted to an electrical signal with frequency proportional to the rate the particle is crossing the interference fringes. A typical photomultiplier output is shown in Fig. A.3.

The distance between fringes depends only on the wavelength of laser in the fluid and the intersection angle of the beams. It is derived in Figure A.2. Multiplying this distance by the output frequency f_D (number of fringes transversed per unit time) gives the particle velocity V.

$$F = f_D d = \frac{f_D \lambda}{2 \sin \theta/2}$$

A very important point is shown in Figure A.4. When three particles pass the fringe with different directions only the X-component of velocity is detected. This result agrees with equation (A.1)

Since interference fringes are formed only at the beams crossing points, this defines the maximum measuring volume of the system. The equations for the measuring volume are shown in Appendix E.

3. Modes of Operation

There are several ways to operate the LDA system. Three basic schemes are discussed here.

3.1 Reference Beam Mode

In the reference beam mode laser light is split into two beams before passing the focal lens. Then the two beams intersect within the fluid to form the measuring volume. (See Figure A.5). A neutral density filter is used to reduce the intensity of the reference beam to optimize the Doppler signal. This mode is preferred for measurements in flows with high scattering particle concentration.

3.2 Differential Doppler Mode

In the differential Doppler mode two equal intensity beams intersect to form the fringe pattern (see Figure A.6). Since the Doppler shift is independent of the direction of detection, scattered

light can be picked up at every angle. Therefore this mode is very useful if the scattered intensity is low since scattered light over a large solid angle can be collected and processed. This mode requires low scattering particle concentration for good signal to noise ratio.

3.3 Dual Beam Mode

In the dual beam mode the laser beam is focused on the measuring point. An aperture disk with two small holes mounted over the lens of the optical unit allows the two scattered beams to pass through the lens. The beams are then combined into one beam by the beam splitter (See Figure A.7). Since the LDA system is directionally sensitive, this mode can be used for two dimensional velocity measurements, although the scattered beams alignment is very difficult because they are of very low intensity.

4. Characteristics of Signals

The Laser Doppler anemometer provides absolute measurements of velocity and does not require any calibration. Its frequency and spatial resolution are excellent. This technique also allows the scattering volume to be positioned easily in the flow channel by transversing only the optical components.

In spite of these advantages over other anemometers, LDA still has many limitations. A major one is the Doppler ambiguity causing signal broadening due to the finite transit time of particles through the scattering volume, turbulent velocity fluctuations across the scattering volume, mean velocity gradient, and electronic noise. In order to improve the signal, optimization of optical components is required. We shall discuss the signal broadening first.

4.1 Signal Broadening [7] [14] [15]

Fig. A.8 shows the typical signal observed in the spectrum analyzer. The reason for the broadening is discussed in the following sections.

4.1.1 Transit Time Broadening

The finite transit time of particles through the scattering volume causes a broadening of the signal. This broadening is inversely proportional to the number of fringes in the measuring volume and can be expressed as

$$\frac{\Delta f}{f} \propto \frac{1}{n_{fringe}}$$

Usually $n_{fringe} \geq 100$ is recommended to reduce the signal broadening.

4.1.2 Velocity Gradient Broadening

Velocity gradient across the small scattering volume also causes signal broadening. This can be expressed as

$$\frac{\Delta f}{f} = \frac{1}{u}\left[\frac{\partial u}{\partial x}\right] \Delta X$$

Where X(=2C) is the dimension of the scattering volume perpendicular to the direction of velocity gradient measured. If a steep velocity gradient is present, this represents the major cause of signal broadening. For slow varying or uniform flows gradient broadening may be neglected.

4.1.3 Temporal Turbulence Broadening

Temporal broadening is caused by the time variation of the Doppler frequency (or velocity). Therefore, this can be expressed as

$$\frac{\Delta f}{f} = \frac{u'}{u}$$

This quantity is called turbulent intensity and is very important for the studies of turbulent flows.

4.1.4 Spatial Turbulence Broadening

Spatial broadening is caused by variation of the turbelence intensities of the velocity across the finite scattering volume. This broadening is related to the scattering volume size, turbulent intensity and turbulent microscale.

4.2 Optimization of the Doppler Signal [14],[16],[17]

Some optimization procedures are usually needed to improve the signal, decrease the noise, and increase the accuracy of the measurement.

4.2.1 Laser Power

When light strikes a particle, it will be scattered in every direction. The typical spatial scattering intensity distribution is shown in Figure A.9. In fact, this distribution depends on several factors such as properties of light (wavelength), scattering particles (shape, size, refractive index). As seen in the Figure A.9, the intensity of light radiated backward is very much lower (about 3 orders of magnitude) than the intensity of the light scattered forward.

Since only part of the total light power scattered by a particle is collected by the photomultiplier and several photons per unit time are required to get good exit signal the laser power required varies with scattering direction. For the forward scattering the suggested laser power[18] is $p_\ell > 0.05$ mW/(m/s). For the backward scattering the required laser power is $p_\ell > 50$ mW/(m/s).

4.2.2 Signal to Noise Ratio (SNR)

The major source of noise in the photomultiplier is shot noise which is proportional to the current level or equivalently, the light intensity incident upon the surface of photocathode. An additional noise source may come from the noise in the laser. But if the path length of two beams are the same, the laser noise may not be significant. Since the SNR is proportional to the scattering beam intensity, the requirement for small scattering angle (relative to the incident beam) is very important. Using the reference beam mode the SNR is maximum when the reference beam is about ten times as intense as the scattered beam.

4.2.3 Effect of Optical Path-Length Difference [18]:

It is known that when a multi-mode gas laser is employed in photomixing experiments, the amplitude of heterodyne signal depends on the optical path length difference between the paths traversed by the two light beams. The requirement is that the optical path length difference of two beams should be the same or differ by integral multiple of 2L where L is the laser resonator cavity length. However, the allowable path difference varies inversely with the number of oscillating axial modes (or laser cavity length L) in the laser output. For a 180 cm long laser with 21 axial modes, a path length difference of 5 centimeters results in signal intensity loss of 10%. In practice therefore using a differential beam mode, the beam separation distance in the optical unit represents the path length difference which should be less than 5 cm if signal intensity loss less than 10% is desired.

4.2.4 Measuring Volume

The formula for measuring volume is given in Appendix E. As discussed in Section 4.1 a small scattering volume is desirable for high spatial resolution and to minimize broadening due to velocity gradient

and spatial turbulence. But small scattering volume can cause large transit time broadening. So there exists an optimum size for minimum broadening. However, it is somewhat difficult to choose it before actually performing the experiment.

4.2.5 Scattering Particles

Since the scattered light comes from interaction of the laser beams with the particles suspended on the fluid, it is very important to choose them properly to get accurate results.

a. Relative Density of Particle and Fluid

In the LDA system we, in fact, measure particle velocity in the fluid instead of fluid velocity itself. It is very important to know whether the particles suspended in the fluid will follow the fluid. It has been shown[17] that particles with density close to that of the fluid follow the fluid within a broad velocity range.

b. Particle Concentration

When several particles are simultaneously passing through the measuring volume, the scattered signal from each particle will mix together. As shown in Fig. A.10 for fringe operation mode the mixed signal

will cause some difficulties in processing the signal. Thus the best concentration is that which results in only one particle being within the measuring volume at any time. This condition can be obtained by properly seeding the fluid and adjusting the size of measuring volume. The reference beam mode usually requires large seeding particle concentration.

c. Particle Size

As shown in Figure A.11, if the size of particle is larger than the fringe spacing, no signal can be detected. So the size of particles should be smaller than a 1/4 of a fringe spacing (i.e. $D \leq 1/4\ d$) in order to yield a good signal. But the particle size should not be too small because the scattering intensity decreases with the size of the particles.

4.2.6 Size of Aperture in Front of Photomultiplier

As shown in Figure A.12 the aperture in front of the photomultiplier, is chosen according to the equation

$$D_{ph} \leq \left(\frac{4 \lambda F}{\pi D \cos \frac{\theta}{2}} \right) M$$

where $M = \frac{f_b}{f_a}$, $\frac{4 \lambda F}{\pi D \cos \frac{\theta}{2}} = 2A$ (see Appendix E)

which allows only light scattered from the measuring volume to be directed onto the photomultiplier. This selection of aperture size will increase the signal to noise ratio.

4.2.7 Thickness of the Wall

The thickness of the wall also has some effect on the quality of the signal. For the thick wall some of the following effects probably will arise:

1. Due to the different index of refraction between fluid, air, and wall, the two laser beams may not intersect at their waists. If this happens the fringe pattern in the measuring point will be distorted and signal broadening will be produced.

2. Scattered light intensity will be attenuated by the thick wall.

Thus thin wall is preferred as long as it can hold the loop pressure.

5. Signal Processing System

Several methods can be used to process the Doppler frequency signal as detected by the photomultiplier. We do not intend to explain the detail structure of various electronic instruments. Only the major functions of each instrument are discussed here.

The simplest way is to determine the Doppler frequency from the oscilloscope screen if the velocity is steady or slowly varying. However,the accuracy of this approach is limited. The oscilloscope is also used to help in optical alignment to optimize the signal and to monitor the turbulent signal while measurements are made whith other suitable instrument. The most common method is to measure frequency spectrum of the Doppler signal with a spectrum analyzer. The peak of the spectrum corresponds to the mean velocity and the width of the spectral peak is related to the turbulent intensity. The disadvantage of this method is that spectrum analysis does not give real time record of instantaneous velocity, thus several turbulent parameters cannot be obtained and processing of spectra is slow and tedious. Another method is that of continuous frequency demodulation, in which the Doppler frequency is converted to an analog voltage which is proportional to the instantaneous velocity.

Using this method, data can be collected more rapidly and conveniently than with a spectrum analyzer.

6. Special Application to our Experiments

Some points are important in our experiments and are discussed in the following sections.

6.1 Wall Signal

When the measuring point is very near the wall, the photomultiplier may collect the light scattered from the wall. The result is that a wall signal will appear simultaneously with flow signal because of the superposition of the scattered light from the measuring point and wall. Although the frequency of the wall signal is usually only half of that of the flow signal, special attention still should be made to avoid tracking the wall signal.

6.2 Painting

Operating the LDA on backward-scattered mode a special attention must be made to avoid collecting reflected light from any sources, for instance, rods, walls, and lenses. The strong reflected light may represent noise for the photomultiplier which makes the velocity measurement impossible. In our experiment, the first two rows of rods adjacent to the plexiglas

faceplates were painted to black in order to eliminate the problem of laser light reflection from the shiny surface of stainless steel rods.

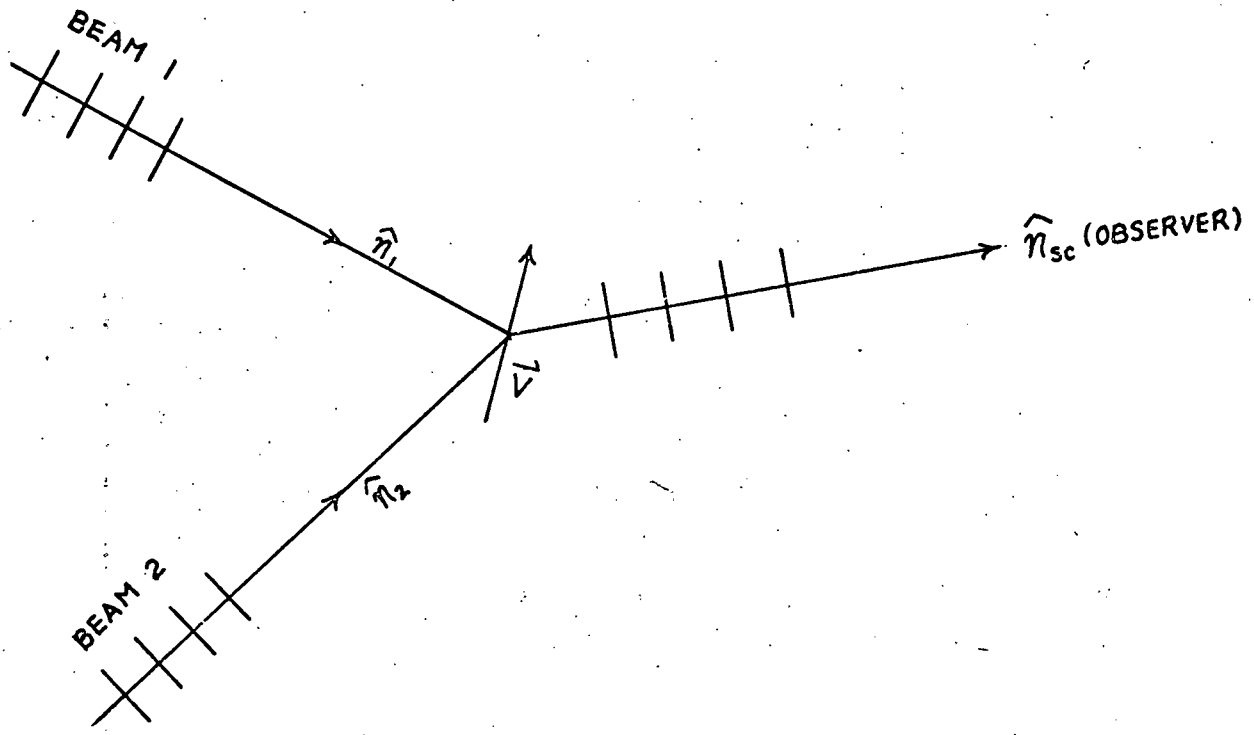

FIGURE A.1 FREQUENCY SHIFT FOR LIGHT SCATTERED FROM A MOVING PARTICLE

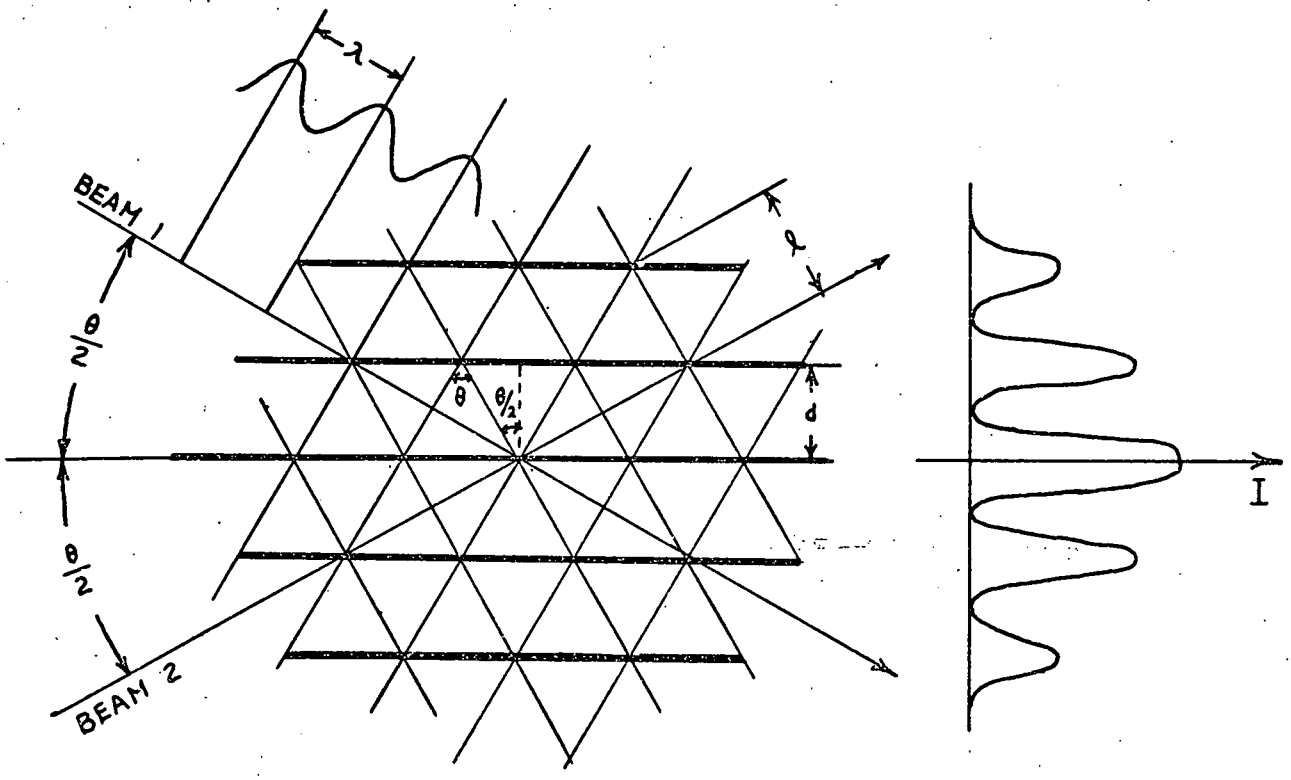

From figure above we can get the following expressions

$$\ell = \frac{\lambda}{\sin\theta} \quad , \quad d = \ell \cos\theta/2$$

Thus the distance between fringes is

$$d = \frac{\lambda \cos\theta/2}{\sin\theta} = \frac{\lambda}{2\sin\theta/2}$$

Where λ = wavelength of incident light

d = distance between fringes

θ = angle of the beam intersection

f_D = frequency detected at photomultiplier

V = velocity of flow perpendicular to fringes

FIGURE A.2 FRINGE PATTERN AT BEAM CROSSING POINT

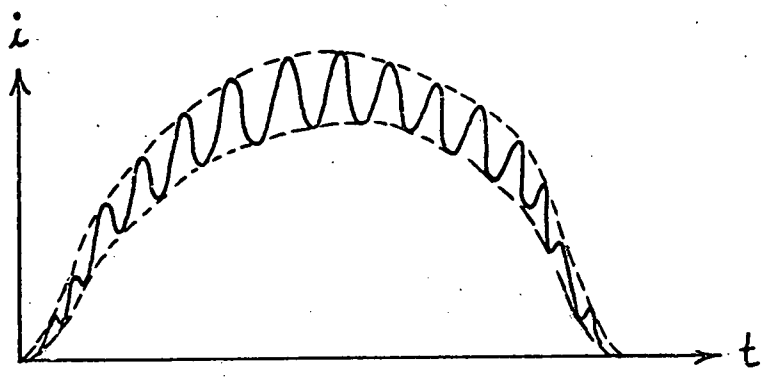

FIGURE A.3 TYPICAL DOPPLER SIGNAL FROM PHOTOMULTIPLIER

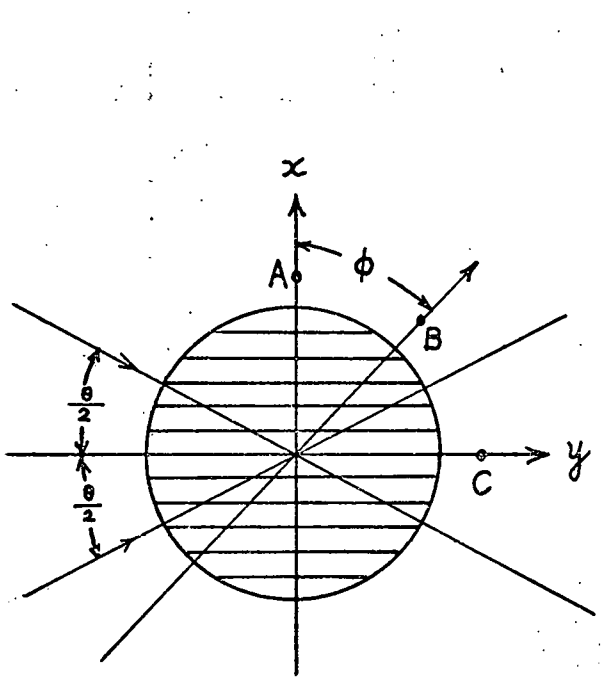

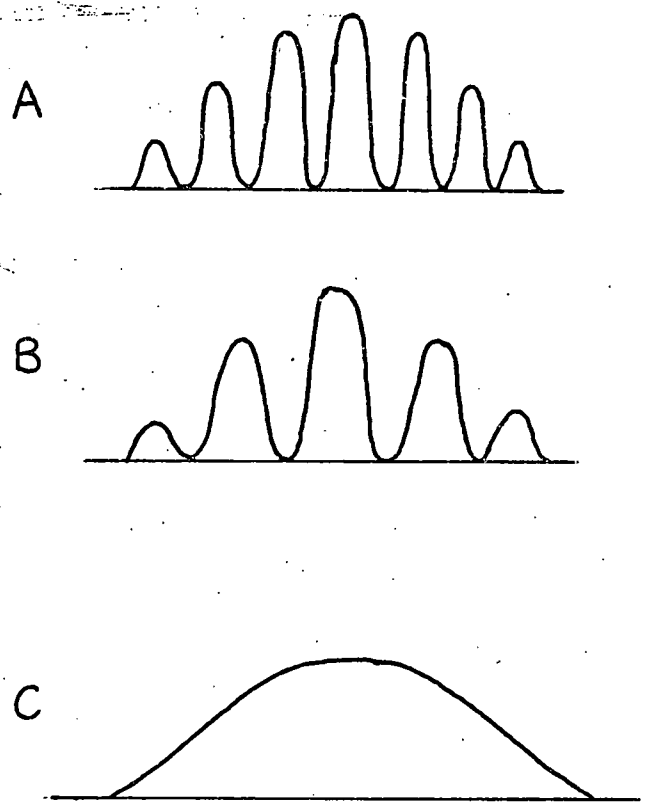

Where $V_A = V_B = V_C = V$

$$f = \frac{2V \sin\theta/2}{\lambda} \quad , \quad f = \frac{2V \cos\phi (\sin\theta/2)}{\lambda} = \frac{2V_x \sin\theta/2}{\lambda}$$

FIGURE A.4 DIFFERENT DOPPLER FREQUENCIES DUE TO THE PARTICLES PASSING THE MEASURING POINT IN DIFFERENT DIRECTIONS

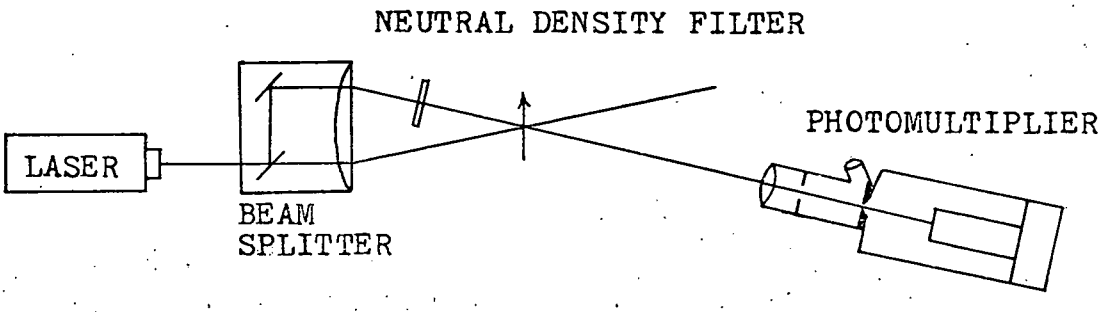

FIGURE A.5 REFERENCE BEAM MODE

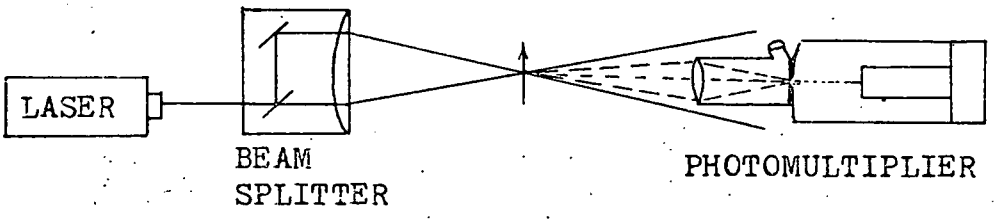

FIGURE A.6 DIFFERENTIAL DOPPLER MODE

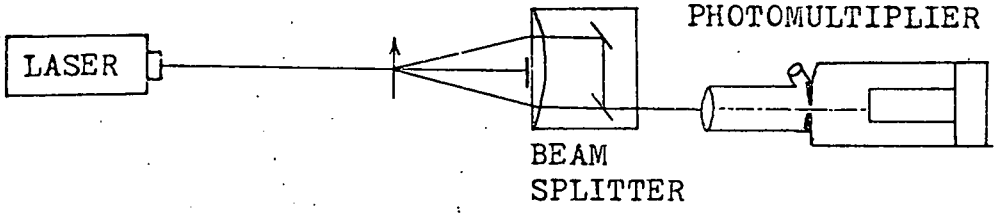

FIGURE A.7 DUAL BEAM MODE

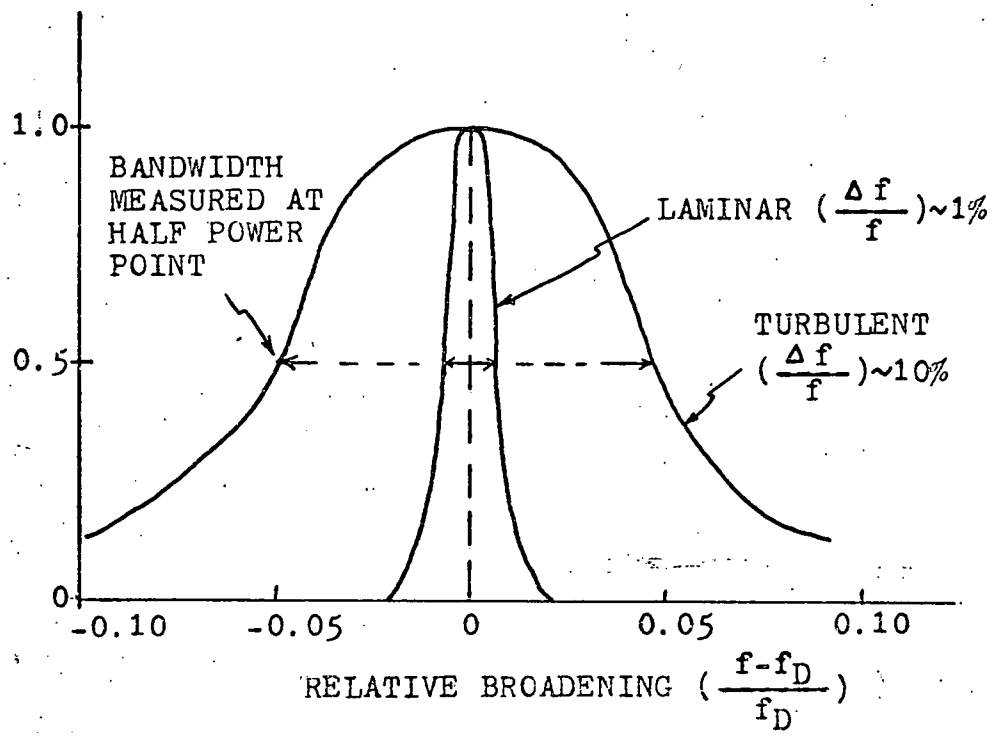

FIGURE A.8 BROADENING OF THE SIGNAL

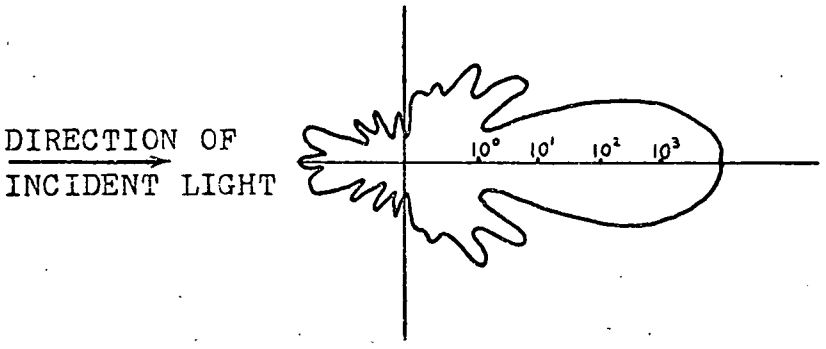

FIGURE A.9 INTENSITY DISTRIBUTION OF SCATTERED LIGHT

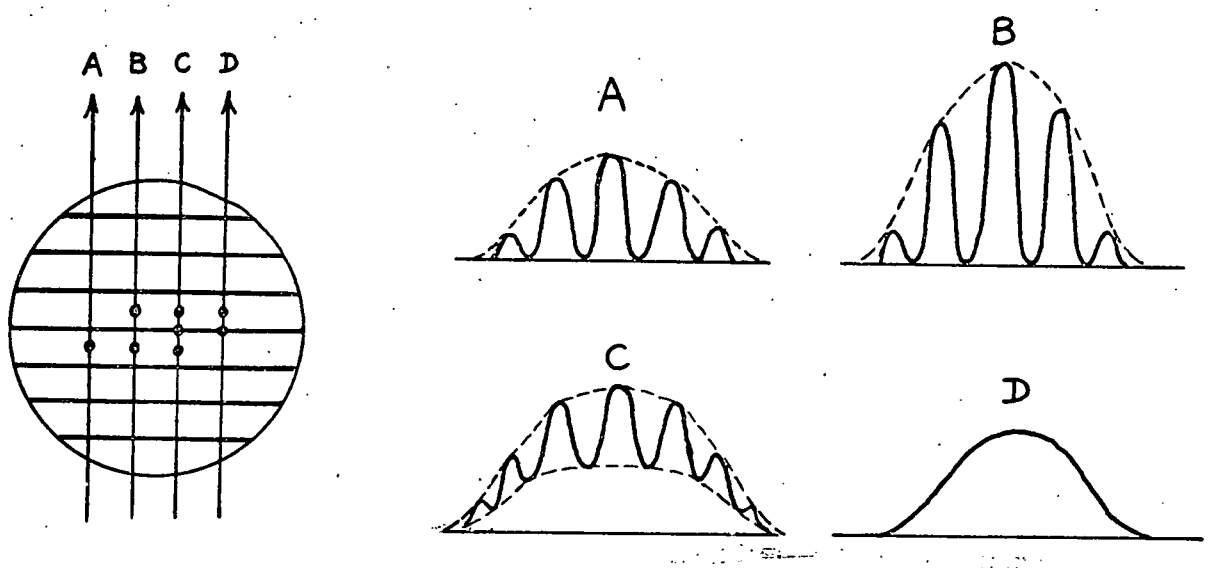

FIGURE A.10 DIFFERENT SIGNALS DUE TO THE DIFFERENT NUMBER OF PARTICLES PASSING THE MEASURING VOLUME

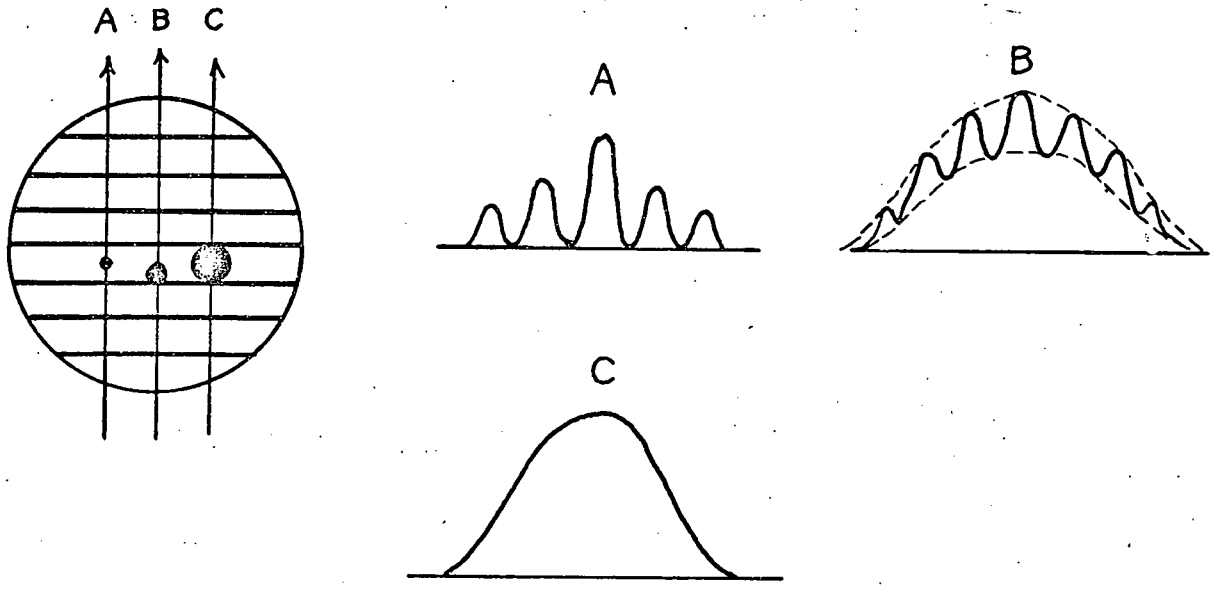

FIGURE A.11 DIFFERENT SIGNALS DUE TO THE DIFFERENT PARTICLE SIZES

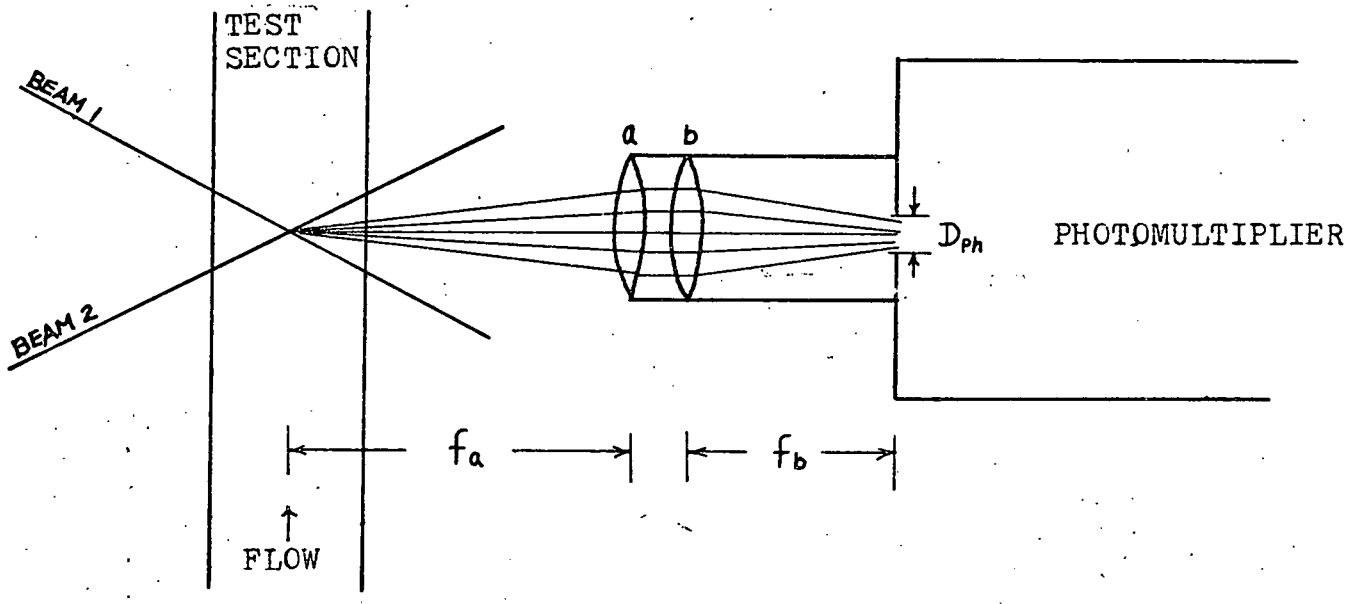

f_a and f_b are focal length of lens a and b respectively

FIGURE A.12 APERTURE SIZE IN FRONT OF PHOTOMULTIPLIER

APPENDIX B

ACTUAL MEASUREMENT POSITION

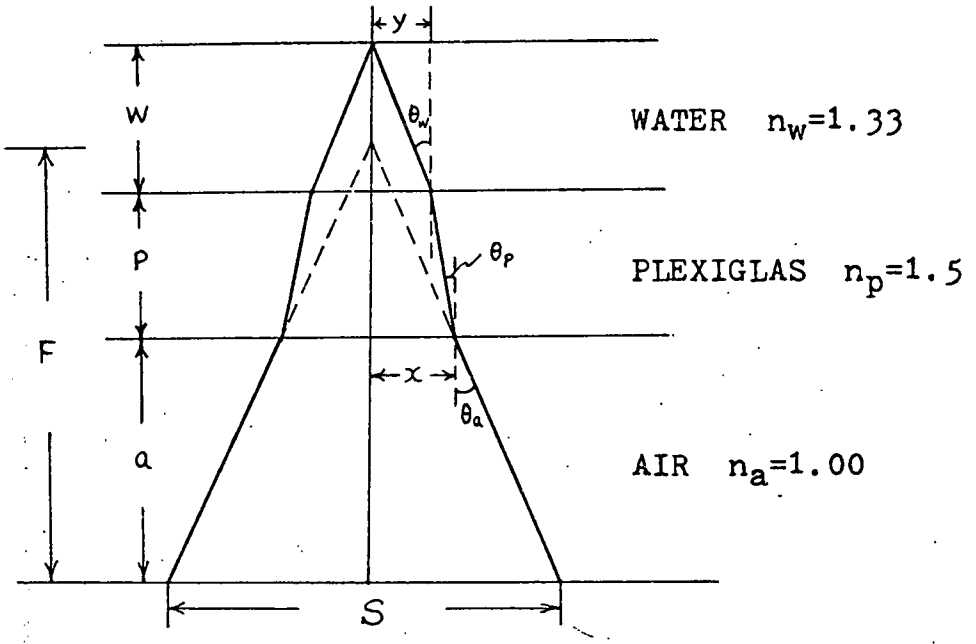

From Snell's law of refraction

$$n_w \sin\theta_w = n_p \sin\theta_p = n_a \sin\theta_a \qquad (B,1)$$

Thus θ_w, θ_p can be expressed as

$$\theta_w = \sin^{-1} \frac{\sin\theta_a}{n_w}, \quad \theta_p = \sin^{-1} \frac{\sin\theta_a}{n_p} \qquad (B,2)$$

Since $\frac{F-a}{F} = \frac{x}{S/2}$ and $y = x - p \tan\theta_p$ (B,3)

We can simplify Equation (B,2) and (B,3) to get

$$y = \frac{S}{2F} (F-a) - p \tan \theta_p \qquad (B,4)$$

Since $w = \frac{y}{\tan \theta_w}$ we can substitute Equation (B,4) into this equation to get

$$w = \frac{\frac{S}{2F}(F-a) - p\tan\theta_p}{\tan\theta_w} \qquad (B,5)$$

Equation (B,5) is an expression relating w to a. If we change a by a small distance Δa, then w is also changed by a small distance Δw. The relationship between Δw and Δa is

$$\Delta w = -\frac{\frac{S}{2F}}{\tan\theta_w}\Delta a = \frac{-S}{2F\tan\theta_w}\Delta a \qquad (B,6)$$

This relationship is used to determine the exact position of the measuring point.

Sample calculation:

In our experiment, S = 50 mm, F = 130 mm

Thus $\theta_a = 10.9°$ and $\theta_w = 8.16°$

Substitute S, F, and θ_w into Equation (B,6)

$$\Delta w = \frac{-50}{2(130)(\tan 8.16)}\Delta a = -1.34\,\Delta a$$

APPENDIX C

DATA REDUCTION PROGRAM

C.1 Principle

C.1.1 Calculation of Average Bundle Velocity

Total flow area of the bundle = 2.494 in^2 and hence average bundle velocity is

$$V_{bulk}(ft/sec) = \frac{\text{flow rate}}{\text{flow area}} = \frac{\text{FLOW RATE(GPM)} \times .1337 \frac{ft^3/min}{GPM}}{2.494\ in^2 \times \frac{1}{(12)^2}\ ft^2/in^2 \times 60 sec/min}$$

$$= (.1287) \times \text{FLOW RATE(GPM)} \qquad (C.1.1)$$

C.1.2 Relationship Between Velocity and Doppler Frequency

Since analog output of tracker is linearly proportional to the doppler frequency in a selected range and 10 volt corresponds to the maximum frequency (f_{max}) in that range, the doppler frequency is

$$f_D(KHz) = \bar{U} \times C \times \frac{f_{max}(KHz)}{10} \qquad (C.1.2)$$

where

$\bar{U}$ = average analog voltage reading in digital voltmeter corresponding to doppler frequency

C = correction factor for voltage drop in the integrating circuit. For 1 sec time constant C = 1.02

For our experiment, the relationship between velocity and doppler frequency is

$$V(\text{ft/sec}) = \frac{f_D \lambda}{2\sin(\theta/2)} = 5.497 \times 10^{-3} \times f_D(\text{KHz}) \qquad (C.1.3)$$

Consequently

$$V(\text{ft/sec}) = [U \times C \times \frac{f_{max}(\text{KHz})}{10}] \times 5.497 \times 10^{-3} \qquad (C.1.4)$$

C.1.3 Calculation of Transverse and Axial Velocities

From Eq. (C.1.4) V_1 and V_2 are

$$V_1(\text{ft/sec}) = [\bar{U}_1 \times C \times \frac{f_{max}(\text{KHz})}{10}] \times 5.497 \times 10^{-3} \qquad (C.1.5)$$

$$V_2(\text{ft/sec}) = [\bar{U}_2 \times C \times \frac{f_{max}(\text{KHz})}{10}] \times 5.497 \times 10^{-3} \qquad (C.1.6)$$

The axial and transverse velocity are

$$V_A = \frac{1}{\sqrt{2}} (V_1 + V_2) \qquad (C.1.7)$$

$$V_T = \frac{1}{\sqrt{2}} (V_1 - V_2) \qquad (C.1.8)$$

The ratios of axial and transverse velocity to bundle average velocity are obtained by dividing Eqs. (C.1.7) and (C.1.8) by Eq. (C.1.1) respectively.

C.2 Calculator Program

Since we are only interested in velocity ratios (i.e., V_A/V_{bulk}, V_T/V_{bulk}), their value can be obtained through frequency ratios and hence some calculational steps are avoided. The relationship between V_{bulk} and the equivalent bulk frequency f_{bulk} can be easily derived from Eqs. (C.1.1) and (C.1.3) as

$$f_{bulk} = 23.41 \times \text{FLOW RATE(GPM)} \qquad \text{(C.2.1)}$$

Thus

$$\frac{V_A}{V_{bulk}} = \frac{\frac{1}{\sqrt{2}}(f_1 + f_2)}{f_{bulk}}, \quad \frac{V_T}{V_{bulk}} = \frac{\frac{1}{\sqrt{2}}(f_1 - f_2)}{f_{bulk}}$$

where

$$f_1 = \bar{U}_1 \times C \times \frac{f_{max}(KHz)}{10}$$

$$f_2 = \bar{U}_2 \times C \times \frac{f_{max}(KHz)}{10}$$

The program is shown in Table C.1

This program requires as input:

$\bar{U}_1$ from digital voltmeter

$\bar{U}_2$ from digital voltmeter

f_{max} from tracker

f_{bulk} from Equation (C.2.1)

The program solves the following equations sequentially

Step 00 - 14; $f_1 = \bar{U}_1 \times 1.02 \times \frac{f_{max}}{10}$

Step 15 - 29; $f_2 = \bar{U}_2 \times 1.02 \times \frac{f_{max}}{10}$

Step 30 - 45; $\frac{V_A}{V_B} = \frac{f_1 + f_2}{\sqrt{2}\, f_{bulk}}$

Step 46 - 66; $\frac{V_T}{V_B} = \frac{f_1 - f_2}{\sqrt{2}\, f_{bulk}} \times 100$ (in %)

C.3 Sample Calculation

1. Data $\bar{U}_1$ = 6 volts $\bar{U}_2$ = 5 volts

   Small Rotameter Reading = 15%

   Frequency range = 150 KHz

2. Calculation Steps

   a. Calculate f_{bulk} = 15 x .193 x 23.41
   = 67.8

   b. Put 6, 5, 150, and 67.8 into storage 0, 1, 2, and 3 respectively

   c. Start the program

   d. Record the result

$\frac{V_A}{V_{bulk}}$ = 1.76 and $\frac{V_T}{V_{bulk}} \times 100\%$ = 16.0

TABLE C.1

CALCULATOR PROGRAM

Step No.	Code	Step No.	Code	Step No.	Code
00	14	23	16	45	1
01	41	24	46	46	54
02	61	25	41	47	14
03	75	26	61	48	56
04	60	27	60	49	15
05	62	28	47	50	57
06	46	29	11	51	41
07	41	30	54	52	61
08	16	31	14	53	75
09	46	32	56	54	64
10	41	33	15	55	61
11	61	34	56	56	64
12	60	35	41	57	47
13	47	36	61	58	41
14	10	37	75	59	17
15	15	38	64	60	47
16	41	39	61	61	41
17	61	40	64	62	61
18	75	41	47	63	60
19	60	42	41	64	60
20	62	43	17	65	46
21	46	44	47	66	1
22	41				

NOTE: Before the start of program $\bar{U}_1$, $\bar{U}_2$, f_{max}, and f_{bulk} are put into storage 0, 1, 2, and 3 respectively.

APPENDIX D

ERROR ANALYSIS

The purpose of this appendix is to estimate the errors in axial and transverse velocities from the uncertainties of LDA measurement technique and accuracy of the instrument.

D.1 General

We start with the velocity components obtained at the two axis oriented 45° about the axial direction calculated from the average frequency output of the tracker by the expression

$$\vec{V} = \frac{\vec{f}_D \times \lambda}{2 \sin(\theta/2)}$$

Therefore from the experiment we have available the following quantities and their estimated uncertainties.

$V_1 \pm \delta V_1$

$V_2 \pm \delta V_2$

(The estimated error δ is due to the factor 2, 3, 4 discussed in Section 6.3.)

$\alpha_1 \pm \varepsilon = 45° \pm 0.5°$

$\alpha_2 \pm \varepsilon = 45° \pm 0.5°$

(From experiment we determined 0.5° was the maximum uncertainty of the angle, ε.)

We now proceed to find an expression for the desired transverse and axial velocity components, V_T and V_A.

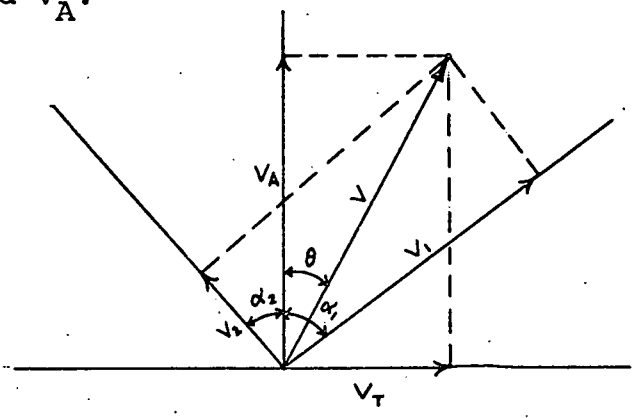

$90° > \alpha_1 > 0°$

$0° > \alpha_2 > -90°$

FIGURE D.1 VELOCITY COMPONENTS IN TWO DIFFERENT COORDINATES

From Figure D.1 we can easily obtain the following equations:

$$V_T = V \sin\theta \qquad V_1 = V \cos(\alpha_1 - \theta)$$
$$V_A = V \cos\theta \qquad V_2 = V \cos(\alpha_2 + \theta) \tag{D.1}$$

From trigonometry

$$\cos(\alpha_1 - \theta) = \cos\alpha_1 \cos\theta + \sin\alpha_1 \sin\theta$$
$$\cos(\alpha_2 + \theta) = \cos\alpha_2 \cos\theta - \sin\alpha_2 \sin\theta \tag{D.2}$$

Then:

$$V_T = \frac{V_1 \sin\theta}{\cos\alpha_1 \cos\theta + \sin\alpha_1 \sin\theta}$$

$$= \frac{V_2 \sin\theta}{\cos\alpha_2 \cos\theta - \sin\alpha_2 \sin\theta} \tag{D.3}$$

From equation (D.3) we can get

$$\tan \theta = \frac{V_1 \cos \alpha_2 - V_2 \cos \alpha_1}{V_1 \sin \alpha_2 + V_2 \sin \alpha_1} \qquad (D.4)$$

From equation (D.3) and (D.4)

$$V_T = \frac{V_1 \cos \alpha_2 - V_2 \cos \alpha_1}{\sin (\alpha_1 + \alpha_2)} \qquad (D.5)$$

Similarly,

$$V_A = \frac{V_1 \sin \alpha_2 + V_2 \sin \alpha_1}{\sin (\alpha_1 + \alpha_2)} \qquad (D.6)$$

D.2 Calculation of Errors in V_T and V_A

The errors in V_T and V_A are due to first four possible sources discussed in Section 6.3.

The method of compounding errors suggested by Wilson[19] was used here. Suppose that the final result y is related to the components X_i by the relation

$$y = F(X_1, X_2, \ldots, X_n)$$

where F is a known functional form. The small variations in X_i will alter y by the amount

$$dy = \frac{\partial F}{\partial X_1} dX_1 + \frac{\partial F}{\partial X_2} dX_2 + \ldots + \frac{\partial F}{\partial X_n} dX_n = \sum_{i=1}^{n} \frac{\partial F}{\partial X_i} dX_i$$

The square of the error will be

$$(dy)^2 = \sum_{i,j} \frac{\partial F}{\partial X_i} \frac{\partial F}{\partial X_j} dX_i \, dX_j$$

If the components dX_i, ..., dX_n are independently distributed and symmetrical with respect to positive and negative values, then $dX_i \, dX_j$ $(i \neq j)$ will vanish, on the average, so that

$$\overline{(dy)^2} = \sum_{i=1}^{n} \left(\frac{\partial F}{\partial X_i}\right)^2 \overline{(dX_i)^2} \qquad (D.7)$$

This may also be written in terms of variance as

$$\sigma^2 = \sum_{i=1}^{n} \left(\frac{\partial F}{\partial X_i}\right)^2 \sigma_i^2$$

D.2.1 Calculation of the Error in V_T and V_A due to Uncertainties in the Position of Measurement Axes ($\alpha_1 \pm \epsilon$, $\alpha_2 \pm \epsilon$)

D.2.1.1 Error due to Uncertainty in α

From Equation (D.5), differentiate V_T with respect to α_1

$$\frac{\partial V_T}{\partial \alpha_1} = [V_2 - V_1 \cos(\alpha_1 + \alpha_2)] \frac{\cos \alpha_2}{\sin^2(\alpha_1 + \alpha_2)} \quad (D.8)$$

Similarly, from equation (D.5)

$$\frac{\partial V_A}{\partial \alpha_1} = [V_2 - V_1 \cos(\alpha_1 + \alpha_2)] \frac{\sin \alpha_2}{\sin^2(\alpha_1 + \alpha_2)} \quad (D.9)$$

D.2.1.2 Error due to Uncertainty in α_2

As in D.2.1.1, we can get the following expressions

$$\frac{\partial V_T}{\partial \alpha_2} = [V_2 \cos(\alpha_1 + \alpha_2) - V_1] \frac{\cos \alpha_1}{\sin^2(\alpha_1 + \alpha_2)} \quad (D.10)$$

$$\frac{\partial V_A}{\partial \alpha_2} = [V_1 - V_2 \cos(\alpha_1 + \alpha_2)] \frac{\sin \alpha_1}{\sin^2(\alpha_1 + \alpha_2)} \quad (D.11)$$

D.2.2 Calculation of the Error in V_T and V_A due to Uncertainty in Measured Velocity Component

D.2.2.1 Error due to Uncertainty in V_1

From Equation (D.5), differentiate V_T with respect to V_1

$$\frac{\partial V_T}{\partial V_1} = \frac{\cos \alpha_2}{\sin(\alpha_1 + \alpha_2)} \quad (D.12)$$

Similarly, from (D.6)

$$\frac{\partial V_A}{\partial V_1} = \frac{\sin \alpha_2}{\sin (\alpha_1 + \alpha_2)} \tag{D.13}$$

D.2.2.2 Error due to Uncertainty in V_2

$$\frac{\partial V_T}{\partial V_2} = \frac{\sin \alpha_2}{\sin (\alpha_1 + \alpha_2)} \tag{D.14}$$

$$\frac{\partial V_A}{\partial V_2} = \frac{\sin \alpha_1}{\sin (\alpha_1 + \alpha_2)} \tag{D.15}$$

Thus, total errors are

$$(\Delta V_T)^2 = \left[\frac{\partial V_T}{\partial \alpha_1}\right]^2 (\Delta \alpha_1)^2 + \left[\frac{\partial V_T}{\partial \alpha_2}\right]^2 (\Delta \alpha_2)^2$$

$$+ \left[\frac{\partial V_T}{\partial V_1}\right]^2 (\Delta V_1)^2 + \left[\frac{\partial V_T}{\partial V_2}\right]^2 (\Delta V_2)^2$$

Divided by V_T^2 and substitute Equation (D.8), (D.10), (D.14) and

$$\alpha_1 = \alpha_2 = 45°$$

we can get the following final result

$$\left[\frac{\Delta V_T}{V_T}\right]^2 = \left[\frac{V_2}{V_1 - V_2}\right]^2 (\Delta\alpha_1)^2 + \left[\frac{V_1}{V_1 - V_2}\right]^2 (\Delta\alpha_2)^2$$

$$+ \frac{(\Delta V_1)^2}{(V_1 - V_2)^2} + \frac{(V_2)^2}{(V_1 - V_2)^2} \qquad (D.16)$$

Define $r = \frac{V_1}{V_2}$, $\Delta\alpha_1 = \Delta\alpha_2 = \varepsilon$, $\Delta V_1 = \delta V_1$, $\Delta V_2 = \delta V_2$

Equation (D.16) reduced to

$$\left[\frac{\Delta V_T}{V_T}\right]^2 = \frac{\varepsilon^2(r^2 + 1)}{(r - 1)^2} + \frac{\delta^2(r^2 + 1)}{(r - 1)^2} = \frac{(r + 1)(\varepsilon^2 + \delta^2)}{(r - 1)^2} \qquad (D.17)$$

Similarly, the total errors in V_A can be expressed as

$$\left[\frac{\Delta V_A}{V_A}\right]^2 = \frac{(r^2 + 1)(\varepsilon^2 + \delta^2)}{(r + 1)^2} \qquad (D.18)$$

D.3 Sample Calculation for Errors in V_T and V_A

The following values are used in this experiment

$\delta = 3x(0.01)^2 = 0.01732$, $\varepsilon = 0.5° = 8.727x10^{-3}$ radians

D.3.1 Error in V_T

Define $p = \frac{V_T}{V_A}$, then $r = \frac{1 + p}{1 - p}$

Equation (D.17) reduces to

$$\left[\frac{\Delta V_T}{V_T}\right]^2 = 1/2\ (1 + \frac{1}{p^2})(\varepsilon^2 + \delta^2) \qquad (D.19)$$

Typical value of $\frac{\Delta V_T}{V_T}$ for p = 0.01, 0.1, 0.2, 0.3 are

P	$\frac{\Delta V_T}{V_T}$
0.01	137%
0.1	14%
0.2	7.0%
0.3	4.8%

D.3.2 Error in V_A

Equation (D.18) also can be expressed as

$$\left(\frac{\Delta V_A}{V_A}\right)^2 = 1/2\ (1 + p^2)\ (\varepsilon^2 + \delta^2) \qquad (D.20)$$

Typical values of $\frac{\Delta V_A}{V_A}$ for p = 0.01, 0.1, 0.2, 0.3 are

P	$\frac{\Delta V_A}{V_A}$
0.01	1.4%
0.1	1.4%
0.2	1.4%
0.3	1.4%

D.4 Calculation of Errors in $\frac{V_A}{V_B}$ and $\frac{V_T}{V_B}$

Assume $X = \frac{V_A}{V_B}$, $Y = \frac{V_T}{V_B}$

Differentiate X with respect to V_A, V_B, we get

$$\frac{dX}{dV_A} = \frac{1}{V_B} \quad \text{and} \quad \frac{dX}{dV_B} = -\frac{V_A}{V_B^2}$$

Similarly,

$$\frac{dy}{dV_T} = \frac{1}{V_B} \quad \text{and} \quad \frac{dy}{dV_B} = -\frac{V_T}{V_B^2}$$

Thus, the total errors for X are

$$\left(\frac{\Delta X}{X}\right)^2 = \frac{\left(\frac{dX}{dV_A}\right)^2 (\Delta V_A)^2 + \left(\frac{dx}{dV_B}\right)^2 (\Delta V_B)^2}{X^2}$$

$$= \left(\frac{\Delta V_A}{V_A}\right)^2 + \left(\frac{\Delta V_B}{V_B}\right)^2 \qquad (D.21)$$

Similarly,

$$\left(\frac{\Delta y}{y}\right)^2 = \left(\frac{\Delta V_T}{V_T}\right)^2 + \left(\frac{\Delta V_B}{V_B}\right)^2 \qquad (D.22)$$

D.5 Sample Calculation for Errors in $\frac{V_T}{V_B}$ and $\frac{V_A}{V_B}$

D.5.1 Errors in $\frac{V_T}{V_B}$ (= y)

In Section 6.3 the error $\frac{\Delta V_B}{V_B}$ was estimated to be $+ 2\sqrt{2}\%$. Thus from equation (D.19) and equation (D.22) typical values of $\frac{\Delta y}{y}$ for p = .01, .1, .2, .3 are

P	Δy/y
0.01	140%
0.1	14%
0.2	7.5%
0.3	5.5%

Δy/y versus p is also shown in Fig. D.2.

D.5.2 Errors in $\frac{V_A}{V_B}$ (= X)

From section (D.20) and equation (D.21), typical values of ΔX/X for p = 0.01, 0.1, 0.2, 0.3 are

P	ΔX/X
0.01	3.1%
0.1	3.1%
0.2	3.2%
0.3	3.2%

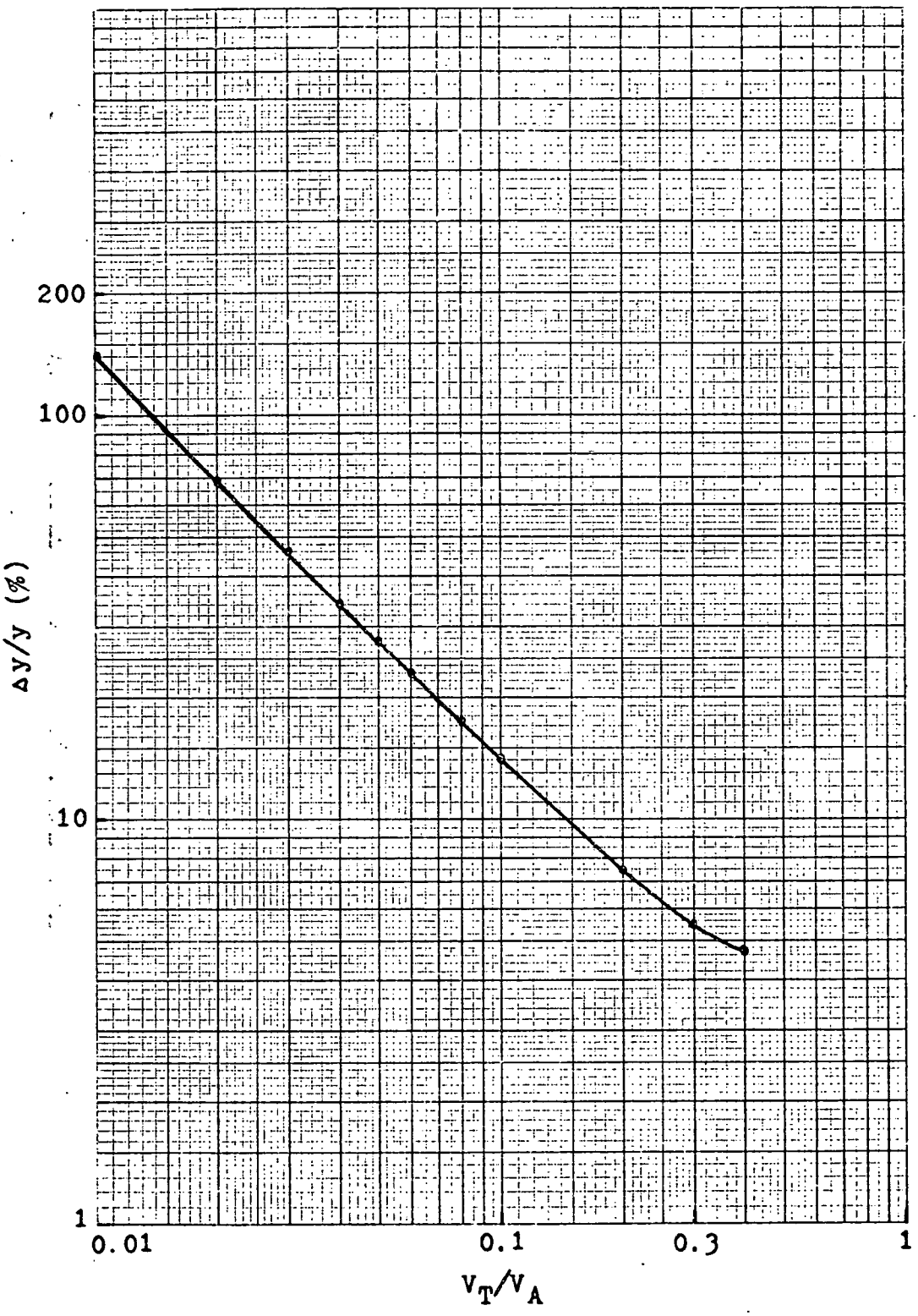

FIGURE D.2 RELATIVE ERROR IN TRANSVERSE TO BULK VELOCITY RATIO AS A FUNCTION OF TRANSVERSE TO AXIAL VELOCITY RATIO

APPENDIX E

FORMULAS FOR MEASURING VOLUME

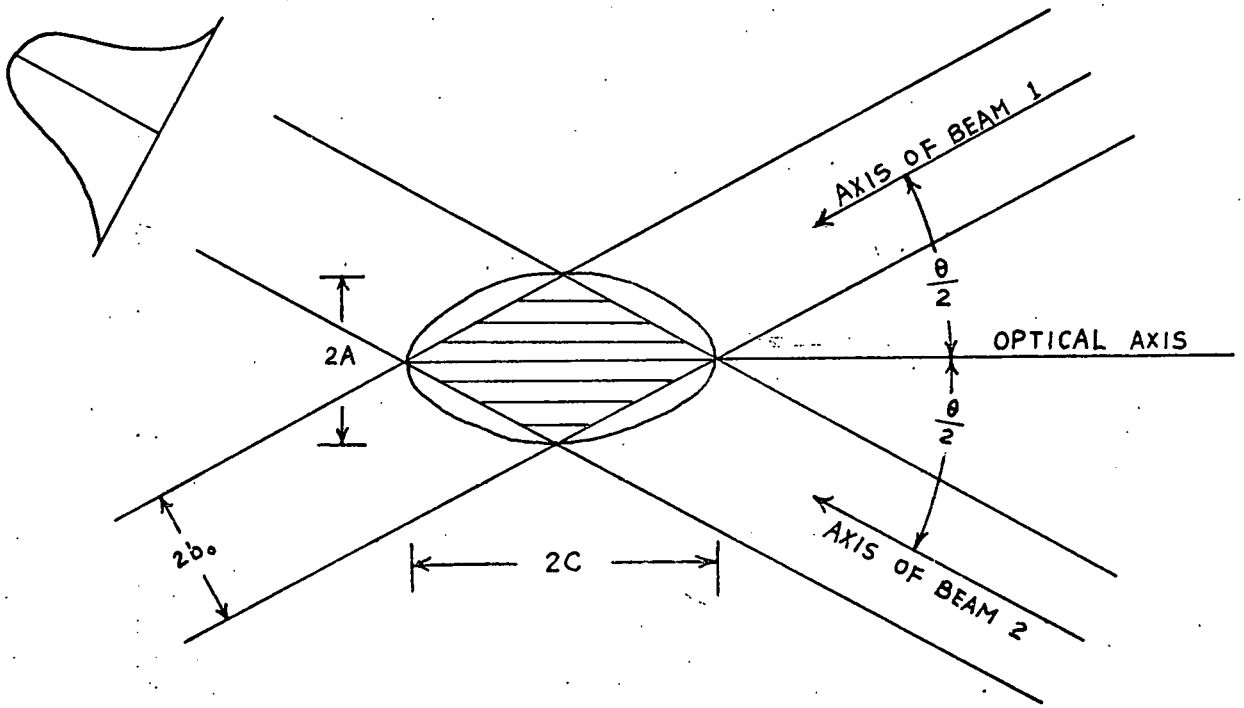

The measuring volume is approximately an ellipsoid created by the intersection of the two beams. The formulas for its shape are

small diameter	$2A = \frac{4\lambda F}{\pi D \cos \theta/2}$	width
smallest diameter	$2B = \frac{4\lambda F}{\pi D}$	height
largest diameter	$2C = \frac{4\lambda F}{\pi D \sin \theta/2}$	length
Measuring Volume	$\frac{4}{3} ABC = \frac{64(\lambda F/D)^3}{3\pi^2 \sin \theta}$	
number of fringes	$n_{fringe} = \frac{8F}{\pi D} \tan \theta/2 = \frac{4d}{\pi D}$	

where

D = diameter of laser beam, referred to e^{-2} intensity points (see detailed definition below).

F = focal length of lens focussing beam 1 and 2

θ = angle of the beam intersection

λ = wavelength of laser light

$2b_o$ = diameter of laser beam at focal point ($2b_o = \frac{4\lambda F}{\pi D}$ by diffraction theory)

Sample calculation:

In this experiment $\lambda = 6328 \times 10^{-8}$m, F = 13 cm, D = 2.0 mm, $\theta = 16.3°$

The results are:

2A = 2.08 mil = 0.053 mm

2B = 2.06 mil = 0.052 mm

2C = 14.5 mil = 0.37 mm

Measuring volume = 5.34×10^{-4} mm^3

No. of fringe = 24

Note: The laser beam usually has Gaussian intensity distribution as the sketch below

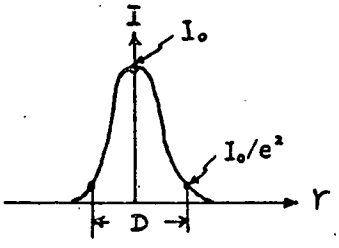

$$I(r) = I_o e^{-\frac{8r^2}{D^2}}$$

The diameter of the laser beam D is referred to the e^{-2} intensity point.

APPENDIX F

RELATIONSHIP BETWEEN VELOCITY AND PRESSURE VARIATIONS

The relationship between pressure drop p and velocity v is

$$p = f_r \frac{L}{D_e} \frac{\rho V^2}{2g_c} \qquad (F,1)$$

where

f_r = friction factor

L = length

D_e = equivalent diameter

ρ = density of the fluid

V = velocity of the fluid

g_c = conversion factor

Assume $a = \frac{f_r \rho L}{2D_e g_c}$ then we can simplify Equation (E,1) to

$$p = aV^2 \qquad (F,2)$$

If pressure has small deviation ΔP from steady value p_o then velocity also varies from V_o to $V_o + \Delta V$.
The relationship between Δp and ΔV is

$$\Delta p = 2\, a\, V_o\, \Delta V \qquad (F,3)$$

Thus root mean square value of Δp is

$$\sqrt{\frac{1}{T}\int_o^T (\Delta p)^2 dt} = 2a\, V_o \sqrt{\frac{1}{T}\int_o^T (\Delta V)^2 dt} \qquad (F,4)$$

Dividing Equation (F,6) by p_o

$$\frac{\sqrt{\frac{1}{T}\int_o^T (\Delta P)^2 dt}}{p_o} = \frac{2\sqrt{\frac{1}{T}\int_o^T (\Delta V)^2 dt}}{V_o} \qquad (F,5)$$

Thu. the velocity turbulent intensity is half of the pressure turbulent intensity.

APPENDIX G

UNCERTAINTY IN BUNDLE FLOW AREA

From Figure 2.2 we can derive the total flow area A in the 61 pin bundle

$$A = \frac{\sqrt{3}}{2} D_f^2 - 61 \times \frac{\pi}{4} \times (D_p^2 + D_w^2) \qquad (G.1)$$

where

D_f = distance across the flat

D_p = pin diameter

D_w = wire diameter

Differentiate Equation (G.1) with respect to D_f, D_p, and D_w, we have

$$\frac{dA}{dD_f} = \sqrt{3}\, D_f, \quad \frac{dA}{dD_p} = -\frac{61}{2} \pi D_p, \quad \frac{dA}{dD_w} = -\frac{61}{2} D_w \qquad (G.2)$$

From Equation (D.7) in Appendix D, the uncertainty in the flow area can be expressed as

$$(\Delta A)^2 = \left[\frac{dA}{dD_f}\right]^2 (\Delta D_f)^2 + \left[\frac{dA}{dD_p}\right]^2 (\Delta D_p)^2 + \left[\frac{dA}{dD_w}\right]^2 (\Delta D_w)^2 \qquad (G.3)$$

Substitute Equation (G.2) into Equation (G.3), we have

$$(\Delta A)^2 = (\sqrt{3} D_f)^2 (\Delta D_f)^2 + (-\frac{61}{2} \pi D_p)^2 (\Delta D_p)^2 + (-\frac{61}{2} D_w)^2 (\Delta D_w)^2 \qquad (G.4)$$

If D_f, D_p and D_w have a small variation ΔD_f, ΔD_p and ΔD_w about nominal value D_{fo}, D_{po}, D_{wo}, then flow area has a small variation ΔA about the nominal value A_o.

$$(\Delta A)^2 = (\sqrt{3}\, D_{fo})^2 (\Delta D_f)^2 + (-\tfrac{61}{2}\, \pi D_{po})^2 (\Delta D_p)^2 + (-\tfrac{61}{2}\, \pi D_{wo})^2 (\Delta D_w)^2 \qquad \text{(G.5)}$$

Divided Equation (G.5) by A_o^2, we have

$$\frac{(\Delta A)^2}{A_o^2} = \frac{(\sqrt{3} D_{fo})^2 (\Delta D_f)^2 + (-\tfrac{61}{2}\, \pi D_{po})^2 (\Delta D_p)^2 + (-\tfrac{61}{2}\, \pi D_{wo})^2 (\Delta D_w)^2}{A_o^2} \qquad \text{(G.6)}$$

Sample calculaiion:

In this experiment D_{fo} = 2.560" (See Fig. 2.4), D_{po} = 0.25", D_{wo} = 0.0625". Uncertainty in D_{fo}, D_{po} and D_{wo} was estimated to be 0.005", 0.0015", and 0.001" respectively.

Substitute D_{fo}, D_{po}, and D_{wo} into Equation (G.1) and (G.6), the uncertainty in flow area is

$$\frac{\Delta A}{A_o} \approx 2\%$$

APPENDIX H

EXPERIMENTAL PROCEDURES

The step-by-step experiment procedures are included in Section 1 "Test Sequence". The detail setup or operation of individual systems is discussed in Section 2 "Test Procedure".

H.1 Test Sequence

1. Start the pump and adjust the valves to get the desired flow rate.
2. Warm up all the electronic instruments.
3. Mix the milk for injection.
4. Set up the laser and optical unit.
5. Move the beam intersection point to the desired measuring position in the bundle by moving the carriage. Note that since water has a different index of refraction than air, a correction for the measuring position is necessary and is included in Appendix B.
6. Inject the milk into the main flow with the proper flow rate.
7. Focus the photomultiplier on the measuring point.
8. Apply the high voltage to the photomultiplier so that the anode current meter reading is 50 μA.

9. Adjust the preamplifier and tracker so that the system can follow the instantaneous velocity automatically.

10. Record the data from the readings of the digital voltmeter and RMS voltmeter.

H.2 Test Procedure

H.2.1 Laser Setup

1. Apply power to the laser and warm up for at least half hour.

2. Adjust the two pairs of horizontal and vertical knobs of the laser head until the maximum reading is shown in the laser power meter. At that time the laser power is maximum.

3. Adjust the height and direction of the laser head so that the reflected beam from the plexiglas surface of bundle is coinciding with incident beam. This step insures that the laser beam is perpendicular to the test bundle since the test bundle has been erected vertical and the carriage erected horizontal. Note the laser was normally operated without an etalon. The validity of this mode of operation was checked by observing the spectrum of the doppler signal using the etalon. No change in the doppler frequency was noted using the etalon. Further, the etalon will

decrease the laser power by about 20% and add some alignment problems. Thus no etalon was used in this experiment.

H.2.2 Mounting the Optical Unit

1. Mount the optical unit on the optical bench

2. Select the proper lens and beam separation distance for the need of the experiment. In this experiment a small focal length (13 cm) and large separation distance (50mm) was chosen in order to get a small measuring volume within the flow channel.

3. Adjust the height and set the desired orientation of the optical unit (in this experiment + 45°, - 45° from the axial was used in order to get both the axial and transverse velocity) so that the two beams intersect at the axis of the focal lens.

4. Mount the test objective at the point of beam intersection and do fine adjustment of beam intersection using the two outer screws of the optical unit. With correct intersection adjustment two overlapping spots with interference stripes can be seen on a screen placed 1 to 2 meters from the objective.

H.2.3 Mounting the Photomultiplier

1. Mount the photomultiplier on the optical bench.

2. Focus the photomultiplier on the point of measurement.

3. Move the pin-hole aperture to the beam intersection point (Note: this is an image of the measuring point)

H.2.4 Operation of the High Voltage Supply and Anode Current Meter

1. Connect both the high voltage supply and anode current meter to the photomultiplier.

2. Increase the high voltage supplied to the photomultiplier by turning the voltage control knob until the anode current meter reads approximately 50 μA. Often the high voltage must be increased to over 1000 volts to obtain a sufficient anode current meter deflection.

H.2.5 Operation of the Frequency Tracker[4]

1. Connect the signal output from photomultiplier to the tracker.

2. Adjust the signal level in the preamplifier until the needle of preamplifier level indicator is on the red mark.

3. Select the proper frequency range of the tracker so that doppler signal can easily be seen from the output of the preamplifier by an oscilloscope or spectrum analyzer.

4. Set the MAN-AUTO switch to MAN and the turning knob fully clockwise. Set the DROP-OUT DETECTION switch to IN.

5. Set the ADJUST THRESHOLD knob and IF BAND WIDTH selector to proper position (settings depend on signal to noise ratio and turbulent intensity respectively).

6. The turning knob should now be turned counterclockwise until a maximum (or first maximum) is indicated by the IF level meter. Set the IF level meter reading near the red mark and MAN-AUTO switch to AUTO. The tracker should lock on the signal.

7. The final setting of ADJUST THRESHOLD and IF BANDWIDTH depends on the maximum turbulent intensity and signal to noise ratio respectively.

H.2.6 Operation of Digital Voltmeter and RMS Voltmeter

The analog output of the tracker is simply fed to the RMS voltmeter directly and to the digital voltmeter after passing an integrating circuit with several different time constants available for selection.

H.2.7 Operation of the Hydraulic Facilities

1. Start the pump, select the proper flowmeter, and adjust the bypass valve and main line globe valve to get the desired flowrate.

2. Run the pump for at least half an hour in order to get equilibrium flow conditions.

H.2.8 Operation of the Milk Injection System

1. Mix the powdered milk with hot water in the mixer.

2. Pump the liquid milk to the large storage tank.

3. Apply the constant high pressure to inject the milk into the main flow path.

APPENDIX I
EXPLORATORY EXPERIMENTS

Several preliminary experiments were conducted to check the working condition of test loop and Laser Doppler Anemometer. The results are presented in this chapter.

I.1 Pressure Variation Measurement in Test Bundle

To prove that the inherent variation of loop flow was very low, a pressure transducer was connected at the bottom of lower plenum to monitor the pressure variation. The output voltage of the transducer was linearly proportional to the pressure. For flow rates less than 56 GPM ($Re < 8000$ at edge channel when $T = 52°F$), the turbulent intensity was found to be less than 1%. The output of the pressure transducer was recorded in X-Y plotter and shown in Figure 4.1. The equation relating pressure variation to velocity variation is included in Appendix F.

I.2 Turbulent Intensity Measurement in Rectangular Test Section

It was found that the plot of turbulent intensity in a test region versus Reynolds number was a good way to determine the transition Reynolds number of the flow.

As shown in Figure 4.2, the turbulent intensity versus Reynolds number is plotted for flow in the rectangular test section. The transition from laminar to turbulent when characterized by turbulent intensity does not appear to be a sharp transition. Fully turbulent flow defined as that flow where no further changes in turbulent intensity occur is about Reynolds number 2300 and agrees with well-known results. Note that in Fig. 4.2 both the pump and the milk injection tank were used to supply water for the rectangular test section. Since water supply from the pump was a small bypass flow from the main loop only a low flow rate could be obtained.

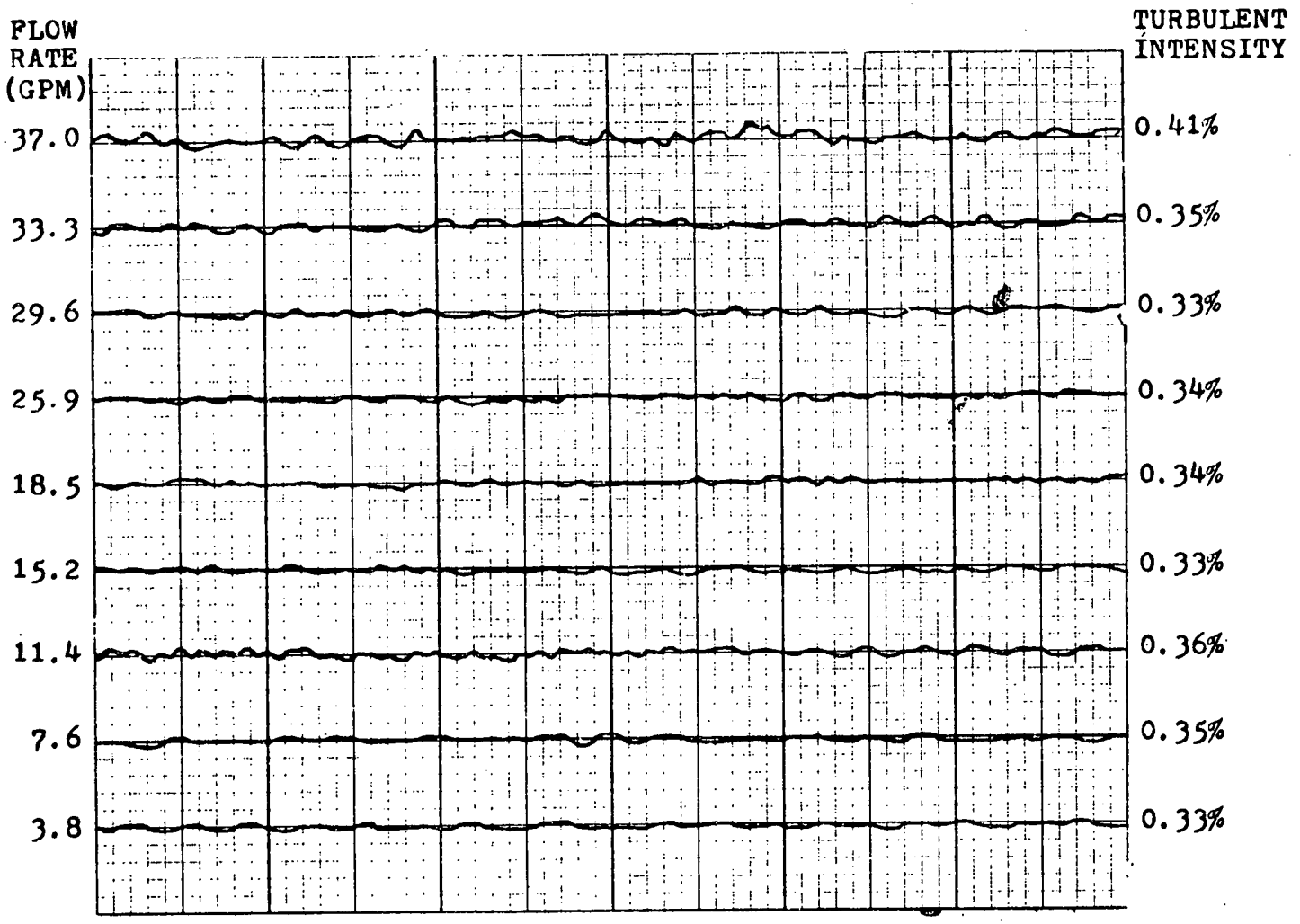

FIGURE I.1 OUTPUT OF PRESSURE TRANSDUCER

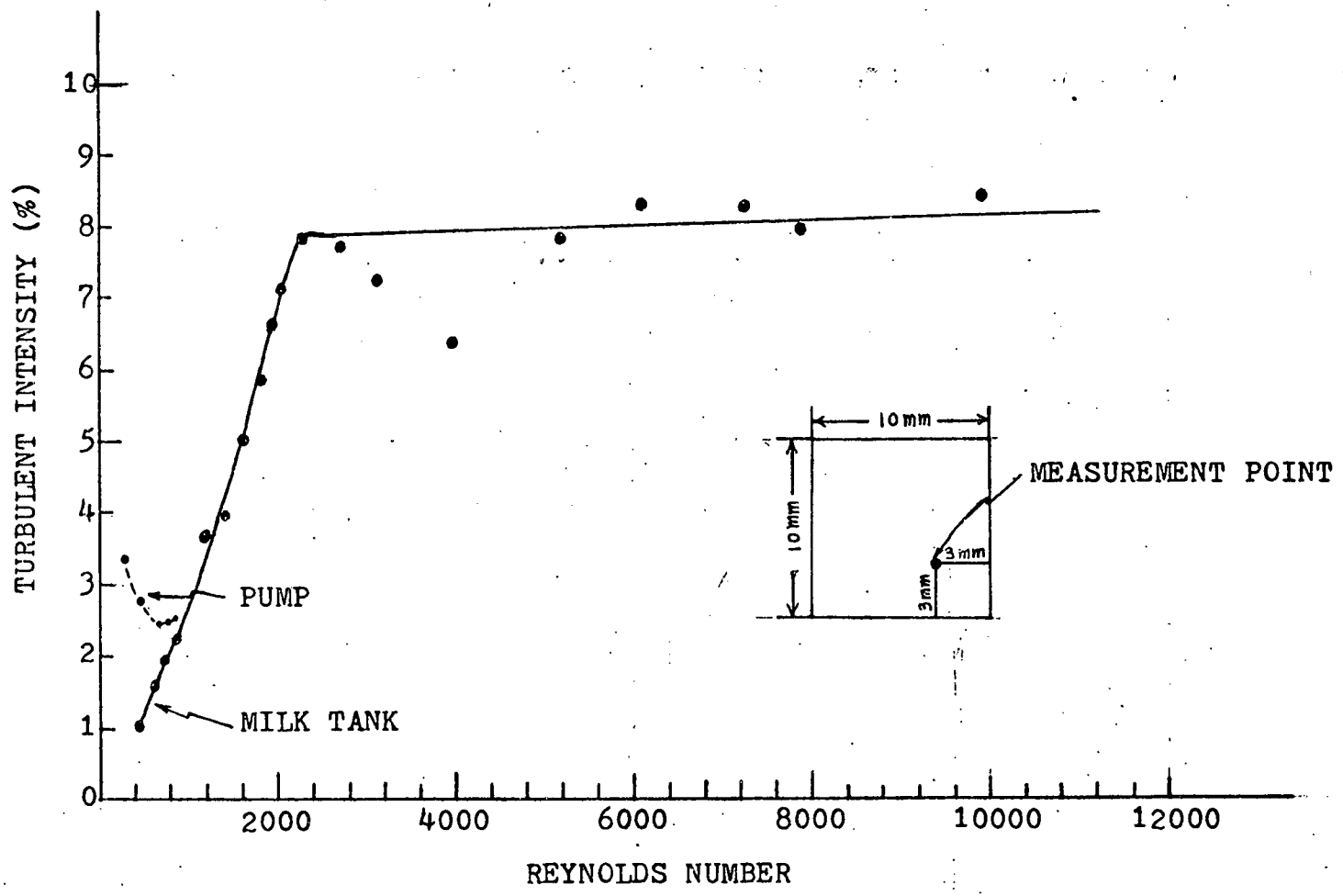

FIGURE I.2 TURBULENT INTENSITY MEASUREMENT IN THE RECTANGULAR TEST SECTION

APPENDIX J

HYDRAULIC DIAMETER FLOW SPLIT ANALYSIS*

The theoretical distribution of flow amount various subchannel types in a rod bundle has been derived by Sangster[20], who noted that the pressure losses in all subchannels are the same. This fact can be expressed by:

$$\Delta P_1 = \Delta P_2 = \Delta P_3$$

or

$$f_1 \frac{L}{D_{e1}} \frac{\rho V_1^2}{2g_c} = f_2 \frac{L}{D_{e2}} \frac{\rho V_2^2}{2g_c} = f_3 \frac{L}{D_{e3}} \frac{\rho V_3^2}{2g_c} \qquad (J.1)$$

where

f_i = friction factor for subchannel type i

D_{ei} = hydraulic diameter for subchannel type i

V_i = axial flow velocity for subchannel type i

and subscripts 1, 2, and 3 refer to the standard interior, peripheral,and corner subchannel type, respectively.

---

*This appendix was contributed by Alan Hanson

It is assumed that the friction factor can be described by the following relationship for each subchannel type:

$$f_i = \frac{C}{Re_i^M} \tag{J.2}$$

where the Reynolds number for subchannel i is defined by:

$$Re_i = \frac{\rho V_i De_i}{\mu} \tag{J.3}$$

The exponent M in equation (J.2) depends on the flow regime and typically can assume the values

M = 1.00 for turbulent flow

M = 0.25 or 0.20 for turbulent flow

The continuity equation requires that

$$W_B = N_1 W_1 + N_2 W_2 + N_3 W_3$$

or since $W = \rho AV$,

$$W_B = \rho A_B V_B = N_1 \rho A_1 V_1 + N_2 \rho A_2 V_2 + N_3 \rho A_3 V_3 \tag{J.4}$$

where

W_B = total bundle flowrate

A_B = total bundle free flow area

V_B = bundle average axial velocity

A_i = average flow area for subchannel type i

N_i = number of subchannels of type i in the bundle

N_i is related to the total number of pins in the bundle as shown in Table J.1.

Now if it is assumed that the fluid properties are the same in each subchannel, then substitution of equations (J.3) and (J.2) into equation (J.1) results in a relation between only the V_i's and De_i's which when substituted into the continuity equation (J.4) yields Sangster's flow distribution factor for the i th subchannel type:

$$Y_i = \frac{A_i De_i^{\alpha}}{\sum_{k=1}^{3} N_k A_k De_k^{\alpha}} \qquad \text{(J.5)}$$

where

$$\alpha \equiv \frac{1 + m}{2 - m}$$

and

$$Y_i \equiv W_i / W_B$$

Novendstern (21) prefers to define the flow distribution factor in terms of velocities instead of flowrates, in which case

$$X_i = \frac{A_B De_i^{\alpha}}{\sum_{k=1}^{3} N_k A_k De_k^{\alpha}} \qquad \text{(J.6)}$$

$$X_i \equiv V_i / V_B$$

Note that these two flow distribution factors are related by the relation:

$$X_i = \left(\frac{A_B}{A_i}\right) Y_i$$

The flow distribution factors are seen to be functions only of bundle geometry. To calculate them it is necessary to know A_i and De_i for each subchannel type. The De_i is defined by

$$De_i = \frac{4A_i}{S_i} \qquad (J.7)$$

where S_i = wetted perimeter of subchannel type i.

Two problems occur in the specification of flow areas and wetted perimeters in wire wrapped rod bundles. The first problem is the allocation of the wire wrap to each subchannel type. This is usually solved by assigning to each subchannel type that fraction of a wire wrap which is present in the subchannel on the average over one axial wire-wrap lead length. For example in an interior subchannel, a wire wrap is present in the subchannel over only one half of the axial lead length; thus one half wire wrap is assigned to each interior subchannel. One half of the wire-wrap cross sectional area is subtracted from the bare subchannel area, and one half of the wire-wrap perimeter is added to the bare subchannel wetted perimeter.

For the peripheral and corner subchannels the appropriate wire-wrap fractions are one-half and one-sixth, respectively. The flow areas and wetted perimeters of the various subchannel types are then given by:

$$A_1 = \frac{\sqrt{3}}{4} P^2 - 1/2 \left[\frac{\pi}{4} Dp^2\right] - 1/2 \left[\frac{\pi}{4} Dw^2\right]$$

$$A_2 = PR - 1/2 \left[\frac{\pi}{4} Dp^2\right] - 1/2 \left[\frac{\pi}{4} Dw^2\right]$$

$$A_3 = \frac{1}{\sqrt{3}} R^2 - 1/6 \left[\frac{\pi}{4} Dp\right]^2 - 1/6 \left[\frac{\pi}{4} Dw^2\right]$$

(J.8)

$$S_1 = 1/2\ (\pi Dp) + 1/2\ (\pi Dw)$$

$$S_2 = 1/2\ (\pi Dp) + 1/2\ (\pi Dw) + P$$

$$S_3 = 1/6\ (\pi Dp) + 1/6\ (\pi Dw) + \frac{2}{\sqrt{3}} R$$

where

Dp = rod diameter

Dw = wire diameter

P = rod-ro-rod pitch

R = rod-to-wall gap

(Note that the equations which describe the corner subchannels are correct only for sharp duct corners with no radii.)

The second problem is the allocation of bundle geometric tolerances among the various subchannel types. In order to accomodate fabrication tolerances and pin bowing, it is necessary to design the duct somewhat larger than would be required by a nominally-dimensioned set of straight rods. The difference between the distance across the inside flats of the actual hexagonal duct and the corresponding distance that would be required for a nominally-dimensioned set of straight, wire-wrapped rods is the diametrical tolerance, T. The existence of a diametrical tolerance makes possible a variety of pin distributions within the duct and results in "looseness". This looseness can be accomodated in the rod-to-rod pitch and the rod-to-wall gap by increasing these two dimensions over the nominal values they would have in a perfect bundle:

$$P = Dp + Dw + \Delta P$$

$$R = \frac{Dp}{2} + Dw + \Delta R \qquad \text{(J.9)}$$

If we define a looseness factor, F, as the fraction of the diametrical tolerance accomodated by the interior channels, then (1-F) is the fraction accomodated by the peripheral and corner channels. Some simple geometric calculations then show that ΔP and ΔR are given by:

$$\Delta P = FT/\sqrt{3}\ N_{ring}$$

$$\Delta R = (1-F)\ T/2 \qquad \text{(J.10)}$$

Note that the two extreme cases for tolerance distribution are:

Case 1: $F = 0$, $\Delta P = 0$, $\Delta R = T/2$

All of the tolerance is accomodated in the peripheral and corner subchannels. This configuration can be described as "compacted".

Case 2: $F = 1$, $\Delta P = T/\sqrt{3}\ N_{ring}$, $\Delta R = 0$

All of the tolerance is accomodated in the interior subchannels. This configuration can be described as "spread".

Because of the uncertainty in the rod distribution within the duct, there is a corresponding uncertainty in the flow distribution factors. Although the diametrical tolerance is generally quite small, its accomodation in the bundle can have a measurable effect on the theoretical flow distribution as can be seen in Figure J.1. This figure shows the flow distribution factors, X_i, for the MIT 61-pin bundle with a diametrical tolerance of .0195 inches in a duct with a distance across the hexagon lots of 2.560 inches. The extreme cases described above are also listed in Table J.2 for the MIT bundle.

Calculations for both laminar and turbulent flow are shown. Although the general behavior of these flow distribution factors as a function of bundle looseness is the same for laminar and turbulent flow, two obvious differences stand out, namely:

1. The magnitude of the flow maldistribution (i.e. the deviation of the flow distribution factors from unity) is substantially greater for laminar flow than for turbulent flow at any bundle loosensss.

2. The flow distribution factors are a stronger function of bundle looseness in laminar than in turbulent flow.

Novendstern has suggested that the spread configuration is most likely to occur in practice. Observation of the MIT bundle agrees with this suggestion since the pins were observed to contact the duct faces when the bundle was assembled.

TABLE J.1 NUMBERS OF INTERIOR, EDGE, AND CORNER SUBCHANNELS FOR DIFFERENT SIZES OF BUNDLE

RINGS OF PINS	TOTAL NUMBER OF PINS	N_1	N_2	N_3
1	7	6	6	6
2	19	24	12	6
3	37	54	18	6
4	61	96	24	6
5	91	150	30	6
6	127	216	36	6
7	169	294	42	6
8	217	384	48	6
N	$1+\sum_{I=1}^{N} 6(I)$	$6N^2$	6N	6

TABLE J.2 THEORETICAL FLOW DISTRIBUTION FACTORS FOR THE MIT 61-PIN BUNDLE ASSUMING A COMPACTED OR A SPREAD CONFIGURATION

		COMPACTED (F=0)	SPREAD (F=1)
ROD-TO-ROD PITCH (INCH)		0.3125	0.3153
ROD-TO-ROD GAP (INCH)		0.1972	0.1875
LAMINAR	X_1 (= V_1/V_B)	0.78	0.89
	X_2 (= V_2/V_B)	1.41	1.25
	X_3 (= V_3/V_B)	0.89	0.69
TURBULENT	X_1 (= V_1/V_B)	0.93	0.96
	X_2 (= V_2/V_B)	1.14	1.09
	X_3 (= V_3/V_B)	0.97	0.88

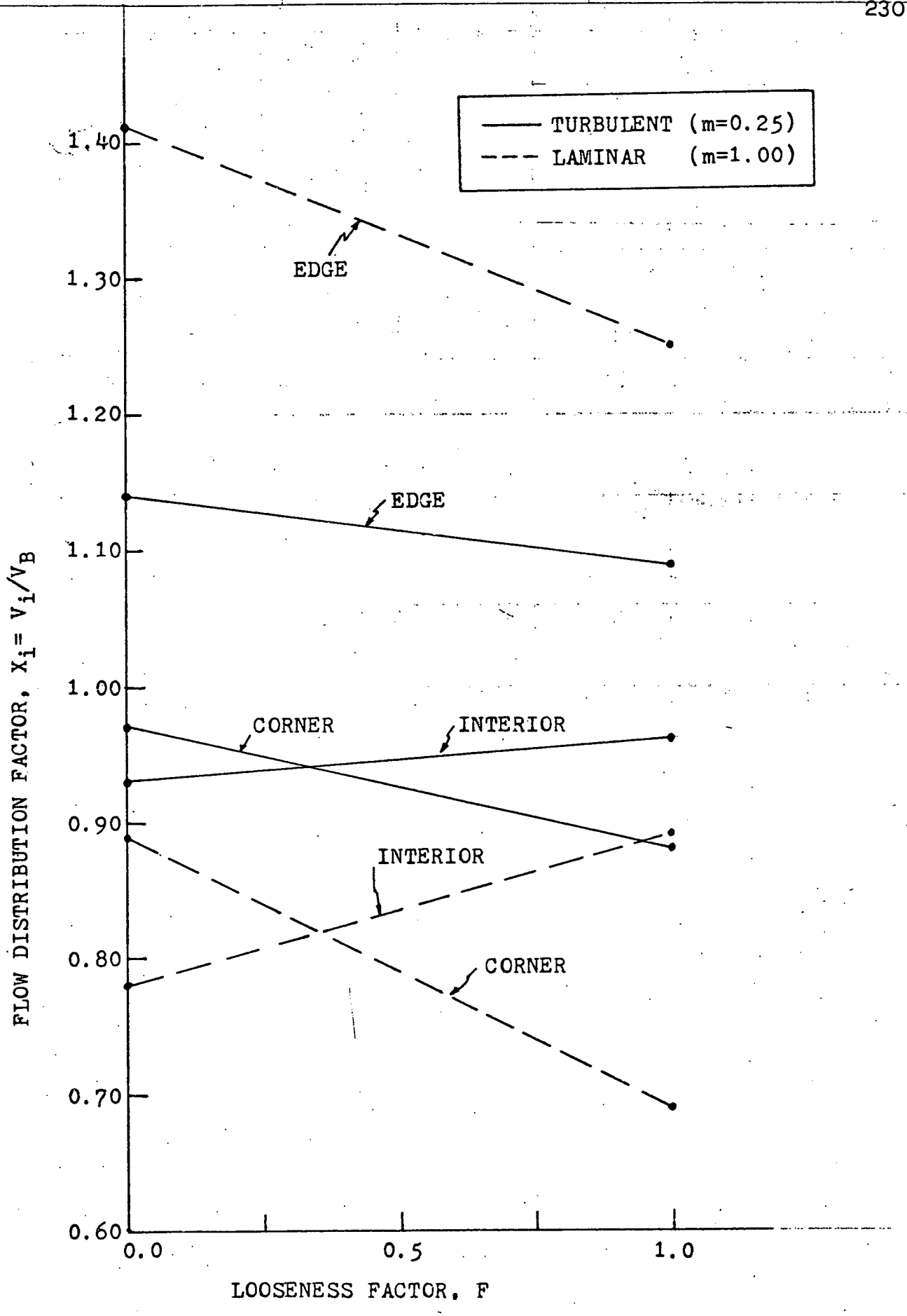

FIGURE J.1 FLOW DISTRIBUTION FACTOR ($X_i = V_i/V_B$) VERSUS LOOSENESS FACTOR (F)